https://lib.uliege.be **https://matheo.uliege.be**

1D numerical modeling of flows in a mining pumped storage reservoir

Auteur : Chabeau, Aurore
Promoteur(s) : Erpicum, Sébastien; Archambeau, Pierre
Faculté : Faculté des Sciences appliquées
Diplôme : Master en ingénieur civil des constructions, à finalité spécialisée en "civil engineering"
Année académique : 2024-2025
URI/URL : http://hdl.handle.net/2268.2/23177

Avertissement à l'attention des usagers :

Tous les documents placés en accès ouvert sur le site le site MatheO sont protégés par le droit d'auteur. Conformément aux principes énoncés par la "Budapest Open Access Initiative"(BOAI, 2002), l'utilisateur du site peut lire, télécharger, copier, transmettre, imprimer, chercher ou faire un lien vers le texte intégral de ces documents, les disséquer pour les indexer, s'en servir de données pour un logiciel, ou s'en servir à toute autre fin légale (ou prévue par la réglementation relative au droit d'auteur). Toute utilisation du document à des fins commerciales est strictement interdite.

Par ailleurs, l'utilisateur s'engage à respecter les droits moraux de l'auteur, principalement le droit à l'intégrité de l'oeuvre et le droit de paternité et ce dans toute utilisation que l'utilisateur entreprend. Ainsi, à titre d'exemple, lorsqu'il reproduira un document par extrait ou dans son intégralité, l'utilisateur citera de manière complète les sources telles que mentionnées ci-dessus. Toute utilisation non explicitement autorisée ci-avant (telle que par exemple, la modification du document ou son résumé) nécessite l'autorisation préalable et expresse des auteurs ou de leurs ayants droit.

University of Liege - Faculty of Applied Sciences

Master's thesis for the degree of Civil Construction Engineer

---

Master's thesis: 1D numerical modeling of flows in a mining pumped storage reservoir

---

Realised by:

CHABEAU Aurore s201141

Academic Advisor: Sébastien Erpicum
Co-Academic Advisor: Pierre Archambeau
Jury: Elena Pummer (NTNU), Serge Brouyère

Academic Year 2024 - 2025

ACKNOWLEDGEMENTS

I would like to express my sincere thanks to my supervisors, Sébastien ERPICUM and Pierre ARCHAMBEAU, whose expertise and wise advice have been essential in carrying out this work. Their benevolent guidance and enriching perspectives allowed me to deepen my reflection and successfully complete this project.

I would also like to extend my gratitude to all my professors throughout my academic journey for their invaluable teachings and for sharing their knowledge, which has shaped my engineering education.

I wish to express my gratitude to my parents, who have always supported and encouraged me in my study choices. A big thank you also to my loved ones for their presence and moral support throughout this journey.

RÉSUMÉ

Ce mémoire présente le développement et la validation d'un modèle numérique unidimensionnel destiné à simuler l'écoulement à surface libre dans un réseau de galeries souterraines interconnectées, utilisé comme réservoir inférieur dans une installation de pompage-turbinage souterrain (UPSH). Cette approche s'inscrit dans le cadre de la transition énergétique, avec pour ambition de valoriser des infrastructures minières abandonnées en les transformant en systèmes de stockage d'énergie renouvelable.

Le modèle repose sur les équations de Saint-Venant, résolues par une méthode des volumes finis avec un schéma temporel explicite de type Runge-Kutta d'ordre 2. Les jonctions en T sont modélisées à l'aide des multiplicateurs de Lagrange, garantissant la conservation de la masse et la continuité de la charge hydraulique.

Le réseau étudié, inspiré d'une maquette physique à l'échelle 1:100, est constitué de seize conduites interconnectées de 10 cm de diamètre, réparties autour d'un point d'injection central. Il se compose de quatre galeries principales, huit galeries secondaires et quatre galeries terminales, formant quatre sous-réseaux rectangulaires symétriques, chacun présentant un comportement hydraulique similaire grâce à cette géométrie symétrique. Quatre phases hydrauliques ont été identifiées lors du remplissage : (1) remplissage du point d'injection, (2) propagation des ondes vers les extrémités, (3) interactions entre ondes incidentes et réfléchies, et (4) stabilisation progressive vers un niveau d'eau uniforme.

Le modèle reproduit ces phénomènes, avec des erreurs moyennes inférieures à 2,6 % en régime stabilisé, calculées comme les déviations absolues moyennes entre les prédictions de hauteur d'eau du modèle et les mesures aux capteurs. Ces écarts sont à mettre en perspective avec la précision expérimentale : bien que la résolution nominale des capteurs à ultrasons soit de ±1 mm, les variations entre répétitions, les écarts initiaux entre capteurs (jusqu'à 6 mm pour certains), ainsi que les effets de traitement des données (moyennage, détection d'anomalies) introduisent une incertitude globale de l'ordre de quelques millimètres.

L'extension à l'échelle réelle démontre la transposabilité des résultats, confirmant la validité de l'approche pour des applications industrielles. Une analyse de sensibilité géométrique extensive révèle que les réseaux peuvent être adaptés à diverses contraintes spatiales tout en maintenant leurs performances hydrauliques.

Le modèle permet ainsi d'identifier les zones critiques pour le dimensionnement structurel, de mieux anticiper les efforts hydrauliques, et d'optimiser les stratégies de contrôle opérationnel. Il révèle notamment que les conduites interconnectées peuvent subir des inversions de débit fréquentes, imposant des exigences accrues en termes de résistance à la fatigue.

Le modèle constitue ainsi un outil pertinent pour l'analyse des écoulements transitoires dans les réseaux souterrains complexes et contribue au développement fiable des systèmes UPSH en tant que solution de stockage durable au service des énergies renouvelables.

ABSTRACT

This master's thesis presents the development and validation of a one-dimensional numerical model designed to simulate free-surface flow in a network of interconnected underground galleries, used as the lower reservoir in an Underground Pumped Storage Hydropower (UPSH) system. This approach aligns with the goals of the energy transition, aiming to repurpose abandoned mining infrastructures into renewable energy storage systems.

The model is based on the Saint-Venant equations, solved using a finite volume method with a second-order explicit Runge-Kutta time scheme. T-junctions are modeled using Lagrange multipliers, ensuring both mass conservation and hydraulic head continuity.

The studied network, inspired by a 1:100 scale physical model, consists of sixteen interconnected PVC pipes with a diameter of 10 cm, arranged around a central injection point. It includes four main galleries, eight secondary galleries, and four terminal galleries, forming four symmetrical rectangular sub-networks. Each sub-network exhibits similar hydraulic behavior due to this symmetric geometry. Four hydraulic phases were identified during filling: (1) filling of the injection point, (2) wave propagation toward the extremities, (3) interactions between incident and reflected waves, and (4) progressive stabilization toward a uniform water level.

The model accurately reproduces these phenomena, with average errors below 2.6% in steady-state conditions, calculated as the mean absolute deviations between model-predicted and sensor-measured water heights. These discrepancies are to be considered in light of the experimental accuracy: although the nominal resolution of the ultrasonic sensors is Âś1 mm, variations between repetitions, initial offsets between sensors (up to 6 mm in some cases), and data processing effects (smoothing, anomaly detection) introduce an overall uncertainty of a few millimeters.

The extension to full scale confirms the transferability of the results, validating the approach for industrial applications. An extensive geometric sensitivity analysis shows that the network can be adapted to various spatial constraints while maintaining its hydraulic performance.

The model thus enables the identification of critical zones for structural design, improves anticipation of hydraulic loads, and helps optimize operational control strategies. It notably reveals that the interconnected conduits are subject to frequent flow reversals, requiring enhanced fatigue resistance.

Overall, the model proves to be a relevant tool for analyzing transient flows in complex underground networks and contributes to the reliable development of UPSH systems as a sustainable energy storage solution.

CONTENTS

LIST OF FIGURES

LIST OF TABLES

NOMENCLATURE

ΔH	Head variation or loss (m)
Δt	Time step (s)
Δx	Spatial step (m)
Δx_{tank}	Spatial step for the injection point (m)
ϵ	Convergence tolerance (-)
η	Efficiency (%)
ν	Kinematic viscosity (m^2/s
θ	Central angle (rad)
$A(h)$	Wetted area (m^2)
a_1	Runge-Kutta weighting coefficient (-)
c	Speed of waves (m/s)
CFL	Courant-Friedrichs-Lewy coefficient (-)
D	Gallery diameter (m)
Fr	Froude number (-)
g	Gravitational acceleration (m/s^2)
H	Hydraulic head (m)
h	Water height (m)
h_{cr}	Critical height (m)
$h_{downstream}$	Imposed water height at the downstream end of the pipe (m)
$h_{initial}$	Initially imposed water height in the pipe (m)
$h_{upstream}$	Imposed water height at the upstream end of the pipe (m)
K	Strickler's coefficient (m$^{1/3}$/s)
$L(h)$	Length in the galleries (m)

L_{tot}	Total length of the galleries (m)
n	Manning's coefficient (s/m$^{1/3}$)
P	Wetted perimeter (m)
Pw	Power (MW)
Q	Flow rate (m^3/s)
q_l	Lateral contribution (m^2/s)
$Q_{downstream}$	Imposed flow rate at the downstream end of the pipe (m^3/s)
$Q_{initial}$	Initially imposed flow rate in the pipe (m^3/s)
Q_{mean}	Mean imposed flow rate (m^3/s)
$Q_{upstream}$	Imposed flow rate at the upstream end of the pipe (m^3/s)
R	Radius (m)
R_h	Hydraulic radius (m)
Re	Reynolds number (-)
S_0	Bottom slope (m/m)
S_f	Friction slope (m/m)
T	Water surface width (m)
t	Time (s)
t^*	Dimensionless time (-)
u	Flow velocity (m/s)
V	Volume (m^3)
Z	Elevation of free surface (m)
z	Elevation of the bottom (m)

CHAPTER 1

INTRODUCTION

Amid the ongoing energy transition, the development of efficient energy storage solutions has emerged as a major challenge in the fight against climate change. The intermittency of renewable energies such as wind and solar power requires systems capable of storing excess energy for redistribution during peak demand [Pummer and Schüttrumpf, 2018]. This issue is particularly critical as the European Union aims to achieve carbon neutrality by 2050, which implies a significant increase in the share of renewable energies in the energy mix.

Pumped storage hydropower (PSH), which emerged in Europe in the 1890s, has gradually established itself as a key energy storage technology. The principle is as follows: When there is excess of electrical energy, pumps transfer water from a lower reservoir to an upper reservoir, storing it as potential energy. When electricity demand increases, water flows in reverse through turbines, generating electrical power. Currently, reservoirs used can be rivers, natural or artificial lakes, or even the ocean. These installations can achieve complete cycle efficiencies of 70 to 85%, making them one of the most effective solutions currently available [Alvarado Montero, Niemann, and Schwanenberg, 2013]. With more than 130 GW of installed capacity worldwide, including approximately 40 GW in Europe, PSH plants play a crucial role in electrical grid stability. Modern installations can achieve unit powers exceeding 1000 MW with response times of just a few minutes, offering essential flexibility for grid management.

However, the development of new conventional plants faces increasing obstacles. Classical installations require favorable topographical conditions with significant elevation differences, often involving the flooding of entire valleys. These projects face growing opposition from local populations and increasingly strict environmental constraints [Kitsikoudis, Archambeau, Dewals, et al., 2020]. Acquisition costs and ecological impacts make it difficult to establish new sites, even as energy storage needs continue to increase.

In this context, the use of abandoned mines as lower reservoirs for underground pumped storage hydropower (UPSH) appears as a promising solution [Estanislao Pujades et al., 2016]. This approach allows for the valorization of existing infrastructure while minimizing environmental impact. Indeed, technical studies show that a medium-sized UPSH installation could avoid the emission of nearly two million tons of CO_2 over its lifetime, thus directly contributing to decarbonization objectives [Morabito et al., 2020]. The economic advantage is twofold: reduction of civil engineering costs through the use of existing cavities and contribution to the reconversion of former mining regions. Feasibility studies indicate potential investment costs 20 to 30% lower than conventional installations, although maintenance costs may be higher due to the specificities of the underground environment. A detailed analysis of the life cycle and return on investment is necessary for each site, taking into account particularly the costs related to ventilation equipment and water treatment [Pummer and Schüttrumpf, 2018].

Whether using existing mine cavities or creating new ones, UPSH systems must maximize the ratio between water volume and reservoir volume for economic reasons, while allowing rapid operational changes [Pummer and Schüttrumpf, 2018]. This creates significant challenges in hydraulic engineering, particularly regarding the behavior of water in interconnected gallery networks, a system fundamentally different from conventional surface reservoirs.

A critical challenge in UPSH systems is the management of air pressure in the underground galleries. Unlike surface reservoirs where water freely displaces air into the atmosphere, underground chambers have limited air exchange capacity. As water fills underground chambers during turbine operation, the entrapped air must be effectively managed through ventilation systems to prevent pressure build-up that would otherwise impede water flow, reduce system efficiency, and potentially cause structural damage [Menendez et al., 2019]. Studies show that inadequate ventilation can reduce electricity production by up to 12.5% depending on the configuration of ventilation shafts.

Additionally, the complex geometry of mine galleries gives rise to unique hydrodynamic phenomena during rapid water level changes. The narrow passages between chambers, abrupt direction changes, and eventually variable cross-sections lead to complex wave propagation patterns including reflection phenomena, undular bores, and pressure transients [Pummer and Schüttrumpf, 2018]. These effects must be carefully analyzed to ensure operational safety and efficiency.

The presence of sediments and water quality are also major issues, potentially affecting machine efficiency and requiring adapted maintenance strategies.

Despite these challenges, UPSH technology offers significant potential for expanding energy storage capacity in regions without suitable topography for conventional PSH. Belgium, with its rich mining history and relatively flat landscape, represents an ideal candidate for such installations, with abandoned mines and quarries that could be converted into underground reservoirs.

Regulatory aspects add an additional layer of complexity. The conversion of mining sites is governed by specific legislation concerning safety, ground stability, and groundwater protection. In Belgium, these projects fall within the framework of the policy for rehabilitating abandoned industrial sites and must comply with European environmental standards, particularly the Water Framework Directive.

This thesis aims to develop a numerical model for analyzing flows in UPSH gallery networks, with a particular focus on the specific hydraulic behaviors that arise in these complex systems. Through numerical modeling and analysis, we seek to provide insights that will contribute to the technical feasibility assessment and design optimization of future UPSH installations.

CHAPTER 2

PREVIOUS WORK AND STUDY FOUNDATIONS

I Background to previous work

Underground pumped storage hydropower (UPSH) has been conceptually explored since the early 20th century. The first patent for such a system attributed to R.A. Fessenden in 1917, who proposed "placing the lower reservoir, not on the surface of the earth, but subterraneously, so as to have a high negative gravitation potential with reference to the earth's surface" [Pummer and Schüttrumpf, 2018].

Despite its long conceptual history, few UPSH plants have progressed beyond preliminary studies. Early geological investigations were conducted in the Netherlands in the 1980s, examining the limestone rock of South Limberg for potential underground reservoirs at depths of approximately 1000 m [Morabito et al., 2020]. In Belgium, the Smart-Water project collected tools and information across socio-legal, economic, hydraulic, and hydrogeologic domains to identify potential underground sites in the Walloon region for energy storage use [Estanislao Pujades et al., 2016; Morabito et al., 2020].

Similar feasibility investigations have been conducted worldwide: Singapore evaluated the Bukit Timah granite quarry for a 370 MW UPSH plant [Morabito et al., 2020]; Germany studied the Prosper-Haniel coal mine, addressing challenges related to rock stability, porosity, and water composition [Morabito et al., 2020; Alvarado Montero, Niemann, and Schwanenberg, 2013]; the United States examined ten potential sites in Minnesota for creating caverns that could serve as lower reservoirs [Morabito et al., 2020]; and the Mount Hope project in New Jersey proposed using an iron mine as a lower reservoir but never advanced beyond planning stages [Morabito et al., 2020]. Recent interest has also emerged in Australia (Bendigo project), Estonia (Muuga project), and Finland (Callio project) [Morabito et al., 2020].

The Belgian context offers significant potential for the development of underground pumped storage hydropower (UPSH), largely due to its extensive network of abandoned mines and quarries, remnants of a once-thriving mineral processing industry. While Belgium lacks the topographical relief necessary for large-scale conventional pumped storage hydropower (PSH), it possesses numerous underground cavities that could be repurposed as lower reservoirs for UPSH systems. Currently, the country operates only two conventional PSH facilities: Coo-Trois-Ponts (1164 MW, 5 GWh capacity) and Plate-Taille (144 MW, 0.796 GWh capacity), both commissioned in the 1970s-80s, with roundtrip efficiencies of 75% and 70% respectively [Morabito et al., 2020].

Among Belgium's many abandoned mines, a legacy of nearly 150 years of extractive activity, the Martelange slate mine stands out as a particularly promising case study. It is located in the southeast, near the border with the Grand Duchy of Luxembourg. Originally exploited in the 19th century, the Martelange site was once a major center for high-quality slate extraction used in construction. The mine comprises a complex system of deep, interconnected chambers and galleries, some reaching depths over 100 meters. Its slate substrate presents favorable geological characteristics: low permeability, excellent structural stability, and high resistance to pressure and cyclic loads properties that are essential for the safe and efficient operation of an underground reservoir. With nine interconnected chambers totaling approximately 550 000 m^3 in volume and depths that enable substantial hydraulic head differences, the Martelange site provides an ideal pilot case. It is well suited to demonstrate the technical and economic feasibility of underground pumped storage [Estanis Pujades, Orban, Archambeau, et al., 2018].

II Reference experimental device

This master's thesis builds upon the thesis of Sara Ceresetti [Ceresetti, 2023], who developed and conducted experimental studies on a physical model of an underground pumped storage system. Her work focused primarily on the hydraulic behavior of interconnected galleries during filling operations, with only a small focus on emptying, providing essential experimental data for numerical model validation.

The system was designed with the following key characteristics:

- Power capacity: $Pw = 300\,\mathrm{MW}$.
- Head difference: $\Delta H = 500\,\mathrm{m}$.
- Gallery diameter: $D = 10\,\mathrm{m}$ (chosen based on typical tunnel boring machine capabilities).
- Total gallery length: $L_{tot} = 31.92\,\mathrm{km}$.
- System efficiency: $\eta = 75\%$.
- Operating flow rate: $Q = 81.55\,\mathrm{m}^3/\mathrm{s}$.
- Total storage volume: $V_{storage} = 2\,348\,623.86\,\mathrm{m}^3$.

The gallery network was arranged in a rectangular configuration to optimize space utilization, with a slight slope of 0.023% to facilitate ventilation at the highest points. The design maintained free surface flow conditions to avoid pressure effects on the surrounding rock mass.

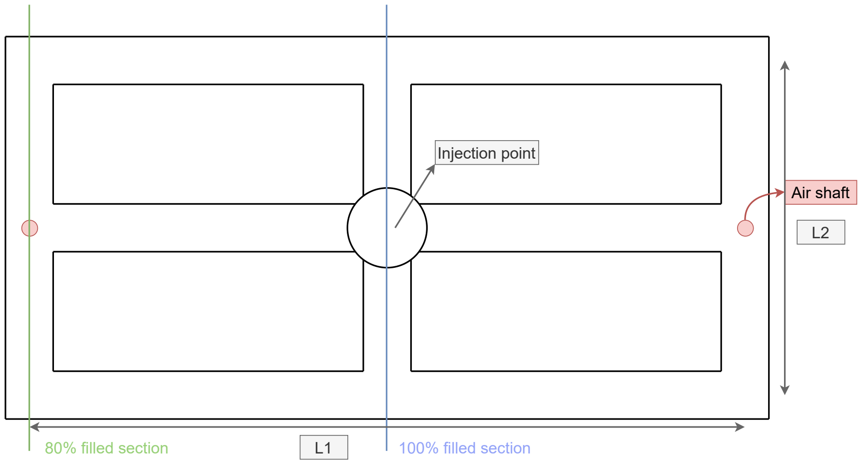

Figure 2.1: Scheme of a duct filled with water

The physical model was constructed at a 1:100 scale relative to the proposed full-scale facility. It consisted of PVC pipes with a 10 cm diameter arranged in a 4 m x 2 m network. Flow rates ranged from 0.5 L/s to 2.6 L/s for filling tests. The laboratory model accurately replicated the geometry of the full-scale system, with one notable modification: the absence of slope in the pipes, which would have been difficult to implement at the laboratory scale (requiring a rise of just 0.46 mm).

Here is an image of the model created by Sara Ceresetti at the hydraulic laboratory.

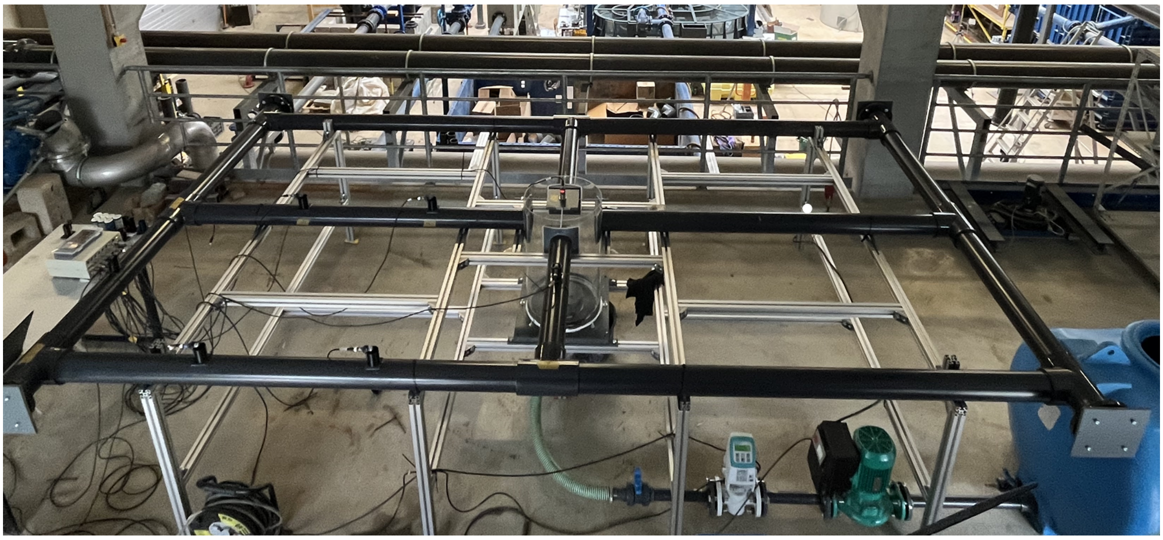

Figure 2.2: Laboratory setup [Ceresetti, 2023]

For the injection point, a cylindrical area with a diameter of 40 cm was designed, equipped with an anti-surge device to ensure uniform water distribution and to limit wave formation that could have interfered with the measurements.

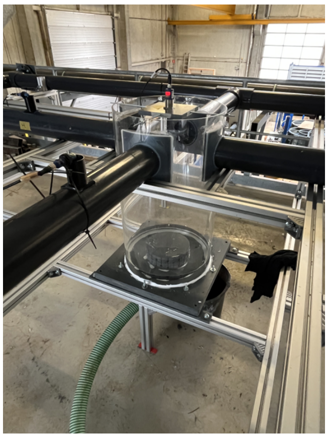

Figure 2.3: Image of the tank for the injection zone with the anti-removal device [Ceresetti, 2023]

Finally, here are the main dimensions of the model.

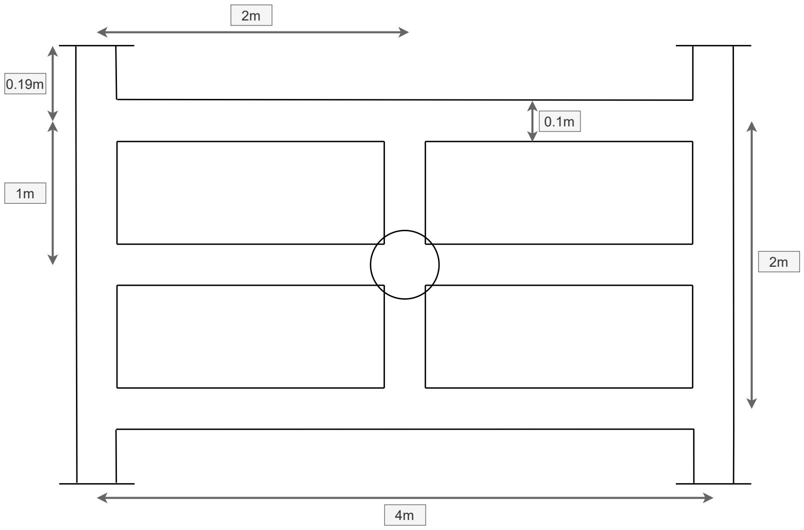

Figure 2.4: Laboratory setup dimensions

III Instrumentation and data acquisition

Sara Ceresetti used precise instrumentation to measure water levels and flow rates.

III.1 Measurement of water heights

Seven ultrasonic sensors were strategically installed on the laboratory model:

- Six pico+35/WK/I sensors were positioned above the pipes to measure water levels along the main flow path.
- One vnp-35/IU/TC sensor was placed above the injection zone to monitor the water level at the inlet.

Here is the location of the sensors on the laboratory model.

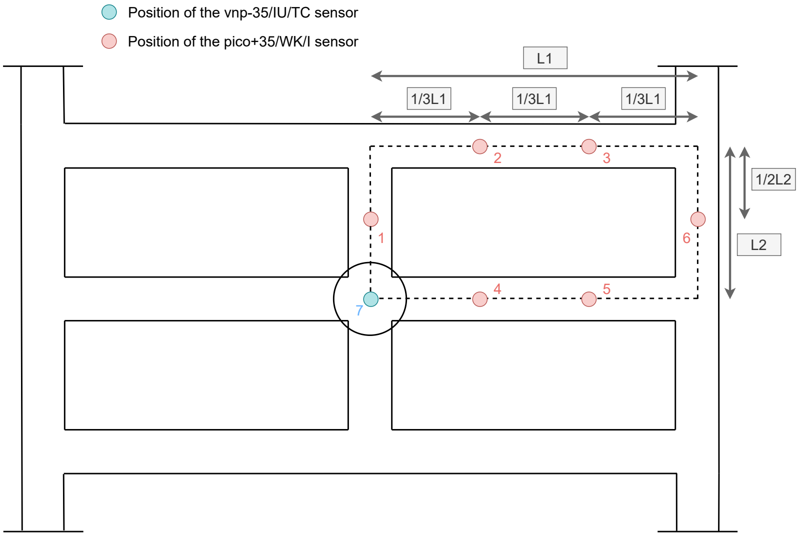

Figure 2.5: Position of the sensors

All sensors were carefully calibrated and mounted on custom-designed 3D-printed holders, ensuring stable and precise positioning above the pipes through 4 cm diameter openings. This setup allowed accurate water level measurements while maintaining proper ventilation within the pipes.

Several measurement challenges were addressed in the experimental setup. Ultrasonic sensors emit a cone-shaped beam rather than a perfectly straight line, introducing inherent uncertainty in the measurements. Instead of detecting a single point, the sensor returns an average distance over the surface within the cone. Consequently, the bottom of the circular pipe cannot be directly measured, especially at low water levels, as the beam reflects off the water surface before reaching the true bottom.

The vertical resolution of the sensors and their physical placement also contributed to measurement uncertainty. Even with millimeter-level positioning accuracy, small deviations (e.g., 3-4 mm) significantly affected water level readings, particularly in differential analyses.

Water level determination was especially challenging when pipes were nearly empty due to both the conical beam geometry and limited sensor resolution. Nonetheless, the data consistently indicated the presence of residual water, showing that the pipes were not completely drained.

Calibration involved establishing a linear relationship between the sensor's electrical output (in volts) and known distances, using reference measurements (e.g., $(x_1, v_1), (x_2, v_2), (x_3, v_3)$). This allowed accurate conversion of the signal into distance values.

Importantly, this calibration process is distinct from the sensor's Z-axis alignment. Even with perfect geometric placement, the conical emission pattern prevents direct measurement of the lowest point in the pipe. This offset must be corrected during data processing.

III.2 Flow measurement

An electromagnetic flow meter operating on Faraday's law principles was used to measure the water flow introduced into the system. This device allowed flow measurements with an accuracy of 0.2% ± 1 mm/s, within a range of 0 to 3 L/s.

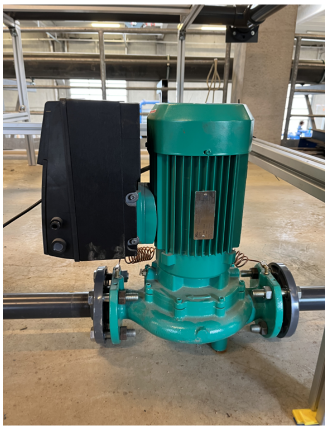

Figure 2.6: Image of the pump [Ceresetti, 2023]

III.3 Data acquisition and processing

Data were recorded at a frequency of 100 Hz for water levels and 10 Hz for flow rate.

Sara Ceresetti conducted various laboratory tests during her master's thesis. She selected three simulations for each of the following flow rates: $Q_{mean} = 0.5 L/s$, $Q_{mean} = 1.35 L/s$, $Q_{mean} = 1.87 L/s$, and $Q_{mean} = 2.50 L/s$.

I was able to retrieve the raw results obtained in the laboratory by Sara Ceresetti. I then had to apply the same method she used in her code to process the experimental data.

The primary method for outlier elimination was the my_movmean() function, which implements a moving average technique with outlier detection:

1. For each data point, the method considers a window of neighboring points (of size *window*) and calculates the mean and standard deviation.
2. If a point deviates from the mean by more than *lim* standard deviations (default *lim* = 1), it is considered an outlier and replaced by the window mean.
3. The method treats points at the beginning, middle, and end of the sample differently:
    - For points in the middle, a centered window is used.
    - For points at the beginning, the window is shifted to the right.
    - For points at the end, the window is shifted to the left.
4. A counter matrix is created in parallel, indicating with a "1" the positions where outliers have been detected and replaced.

This approach allows for a smoothed signal while preserving true trends in the data, eliminating outlier peaks that may arise from experimental disturbances.

For calculating the average of the three simulations conducted for each flow rate, the sample_avg() function was employed. This function:

1. Detects maximum values for each time point among the three simulations.

2. Applies selective filtering if the difference between maximum and minimum values exceeds a threshold (*lim_1* = 1 by default).
3. Uses hierarchical processing:
   - If a value is identified as potentially outlying, the two other values are examined.
   - If the difference between the two remaining values is smaller than a second, stricter threshold (*lim_2* = 0.5 by default), their average is used.
   - If the difference between the two remaining values is also large, the lower value is retained.
4. For normal cases where the difference between values is not significant, a simple average of the three values is calculated.

This method ensures a representative average that is not unduly influenced by occasional outliers in any of the simulations.

After eliminating outliers and calculating averages, several additional analyses were performed:

1. Temporal alignment: The data was time-shifted to ensure that the start of significant hydraulic phenomena coincided across different simulations.
2. Normalization: Water heights were converted from millimeters to meters to facilitate comparison with numerical simulations.

The various experimental result curves can be found in the appendix A.

IV Current thesis scope

Building on Sara Ceresetti's work, the present study focuses on the development of a numerical model validated by experimental results obtained in the laboratory. The main objectives include:

- Development of a finite volume numerical model.
- Validation against experimental data.
- Investigation of flow regime transitions.
- Analysis of wave propagation phenomena.

The numerical approach employs the finite volume method to solve the Navier-Stokes equations, with particular attention to:

- Accurate representation of free surface flows in partially filled galleries.
- Treatment of wave propagation and reflection in complex geometries.
- Implementation of appropriate boundary conditions.

This approach aims to complement and expand upon Sara Ceresetti's experimental work by developing a modeling tool capable of predicting the hydraulic behavior of large-scale underground pumped-storage systems. In doing so, it contributes to the advancement of this promising energy storage technology.

CHAPTER 3

THEORETICAL FOUNDATIONS AND NUMERICAL SOLUTION METHODS

I Mathematical modelling of flows

I.1 Development of Saint Venant equations for our case

The Saint-Venant equations, named after French mathematician Adhémar Jean Claude Barré de Saint-Venant (1797-1886), constitute a system of hyperbolic partial differential equations that describe one-dimensional unsteady open channel flow. The Saint-Venant equations are used to describe how water flows in open channels or pipes that are not completely full. They take into account how the water level and speed change over time and along the length of the channel. These equations are derived from the principles of conservation of mass and momentum, applied to a control volume of fluid under the following key assumptions:

1. **The flow is one-dimensional:** Variations in the flow across the channel (width and depth) are neglected; only changes along the length of the channel are considered.
2. **The pressure distribution is hydrostatic:** Vertical accelerations are assumed to be negligible, so pressure increases linearly with depth.
3. **The channel slope is small:** This allows for the simplification of gravitational terms.
4. **The channel bed is stable and impermeable**: No erosion or deposition.
5. **The flow is continuous:** No sudden additions or losses of mass occur, except where explicitly modeled (e.g., inflows or outflows).
6. **The fluid is incompressible and homogeneous:** Water density is constant, and there is no variation in composition.

The conservative general form of Saint-Venant equations is:

$$\begin{cases} \iint \left(\frac{\partial A}{\partial t} + \frac{\partial Q}{\partial x}\right) dxdt = 0 \\ \iint \left(\frac{\partial Q}{\partial t} + \frac{\partial(\beta \bar{u} Q + g\cos\theta P_w)}{\partial x} - g\cos\theta \left(P_x - hl_b \frac{\partial(-h_b(x))}{\partial x}\right) + gA(S_f - \sin\theta)\right) dxdt = 0 \end{cases} \tag{I.1}$$

Where:

$$P_w = \int_{-h_b}^{h_s} (h_s - z) l(x,z) dz \quad \text{Hydrostatic pressure force term} \tag{I.2}$$

$$P_x = \int_{-h_b}^{h_s} (h_s - z)\frac{\partial l(x,z)}{\partial x} dz \quad \text{Pressure Gradient Contribution due to geometry variation} \tag{I.3}$$

It is assumed that there is no lateral inflow ($q_L = 0$) and that all loss components (friction and viscosity) are combined into a general term S_f.

For the first equation:

- $\frac{\partial A}{\partial t}$ represents temporal variation of wet section.
- $\frac{\partial Q}{\partial x}$ corresponds to spatial variation of flow.

For the second equation:

- $\frac{\partial Q}{\partial t}$ represents the flow time variation (local acceleration).
- $\frac{\partial(\beta \overline{u} Q)}{\partial x}$ is the convective term where β is a Boussinesq coefficient that takes into account the non-uniformity of the velocity profile.
- $\frac{\partial(g\cos\theta P_w)}{\partial x}$ is the hydrostatic pressure gradient where P_w is the hydrostatic thrust.
- $g\cos\theta P_x$ is the ressure force due to variation in channel geometry. It comes from the reaction of the banks.
- $g\cos\theta h l_b \frac{\partial(-h_b(x))}{\partial x}$ is the pressure force applied to the bottom of the channel.
- gAS_f are the frictional forces, where S_f is the friction slope.
- $gA\sin\theta$ is the weight component projected in the direction of flow, where θ is the angle of the bottom of the channel with the horizontal. This term therefore depends on the bottom slope.

It is possible to highlight the free surface slope using Leibniz for the term $\frac{\partial P_w}{\partial x}$:

$$\frac{\partial P_w}{\partial x} = \frac{\partial}{\partial x}\int_{-h_b}^{h_s} \left[(h_s - \zeta)l\right] d\zeta = \int_{-h_b}^{h_s} \frac{\partial\left[(h_s - \zeta l\right]}{\partial x} d\zeta - h l_b \frac{\partial(-h_b)}{\partial x} \tag{I.4}$$

Let us then group the terms $\frac{\partial P_w}{\partial x}$, $hl_b\frac{\partial(-h_b)}{\partial x}$ and P_x.

$$\frac{\partial P_w}{\partial x} + hl_b\frac{\partial(-h_b)}{\partial x} - P_x = \int_{-h_b}^{h_s} \frac{\partial\left[(h_s-\zeta)l\right]}{\partial x} d\zeta - \int_{-h_b}^{h_s} (h_s - \zeta)\frac{\partial l}{\partial x} d\zeta = \int_{-h_b}^{h_s} \frac{\partial(h_s-\zeta)}{\partial x} l d\zeta = \frac{\partial h_s}{\partial x} A \tag{I.5}$$

Finally, the total contributions from the hydrostatic pressure term, the bank reaction, the bottom pressure, and the bed slope give:

$$g\left(\frac{\partial P_w}{\partial x} + hl_b\frac{\partial(-h_b)}{\partial x} - P_x\right) cos\theta - gAsin\theta = gA\left(\frac{\partial h_s}{\partial x} cos\theta - sin\theta\right) = gA\frac{\partial Z}{\partial x} \tag{I.6}$$

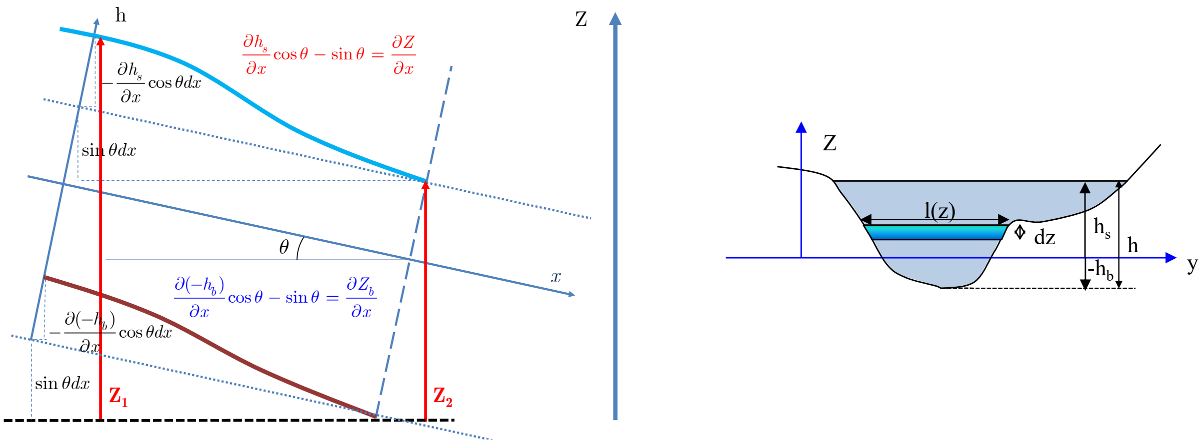

Figure 3.1: Highlighting the free surface slope [Pirotton, 2022]

Finally, here is the partially non-conservative formulation implemented in the numerical code.

$$\begin{cases} \frac{\partial A}{\partial t} + \frac{\partial Q}{\partial x} = 0 \\ \frac{\partial Q}{\partial t} + \frac{\partial (\frac{Q^2}{A})}{\partial x} + gA\frac{\partial Z}{\partial x} + gAS_f = 0 \end{cases} \tag{I.7}$$

Why the non-conservative form of the momentum equation works well?

The partially non-conservative formulation implemented in the numerical code offers several advantages. While conservation forms are generally preferred for capturing hydraulic jumps and shocks, the non-conservative form expressed directly in terms of free surface elevation proves advantageous in many scenarios.

When testing a still lake condition, the non-conservative formulation performs exceptionally well. Since discharge is zero, the first two terms of the equation vanish. With no flow velocity, friction terms disappear as well, leaving only the pressure term. When variables are expressed in terms of surface elevation, a horizontal water surface identically satisfies the equation, ensuring perfect numerical balance.

In contrast, the fully conservative formulation contains separate terms for pressure gradients and bed slopes. Without careful coordinated discretization of these terms, maintaining a perfectly still water surface becomes numerically challenging.

One might question the accuracy of non-conservative formulations for hydraulic jumps, which theoretically require conservation forms to capture discontinuities properly. However, for moderate jumps (which represent most real-world situations in our study), the error introduced by the non-conservative approach remains acceptably small. The advantages in numerical stability and accuracy for slowly varying flows generally outweigh the small inaccuracies that might occur at sharp transitions.

I.2 Flow regimes and transitions

Froude number and flow regimes

The Froude number is a dimensionless parameter that characterizes the local flow regime. It is defined as the ratio between the flow velocity and the speed of shallow surface gravity waves:

$$Fr = \frac{u}{c} = \frac{Q}{\sqrt{\frac{gA^3}{T}}} \tag{I.8}$$

where u is the flow velocity, $c = \sqrt{gh}$ is the wave celerity, Q is the discharge, A the wetted cross-sectional area, and T the top width of the water surface. Physically, the Froude number compares the speed of the water to the speed at which surface disturbances propagate. This provides an intuitive way to understand how information (such as a change in boundary conditions or a local disturbance) travels through the system.

Depending on the value of Fr, the flow falls into one of three categories:

- $Fr < 1$: Subcritical (slow) flow.
- $Fr = 1$: Critical flow.
- $Fr > 1$: Supercritical (rapid) flow.

In subcritical flow ($Fr < 1$), gravitational forces dominate over inertial effects. The flow velocity is lower than the wave celerity, meaning that disturbances can travel both upstream and downstream. Mathematically, the Saint-Venant equations for this regime feature two characteristic lines: $C^+ = u + c$, which moves downstream, and $C^- = u - c$, which moves upstream. As information propagates in both directions, the flow is influenced by both upstream and downstream conditions. In numerical modeling, this implies that one boundary condition (typically the discharge) must be imposed at the upstream end, and one (usually the water depth) at the downstream end.

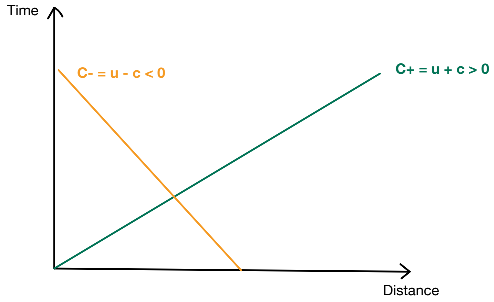

Figure 3.2: Characteristic lines in subcritical flow ($Fr < 1$): information propagates both upstream and downstream.

In contrast, supercritical flow ($Fr > 1$) is dominated by inertial forces, with a flow velocity greater than the wave celerity. In this case, both characteristics C^+ and C^- travel downstream, and no information can propagate upstream. Consequently, the flow is entirely controlled by upstream conditions. For numerical simulations, both boundary conditions (e.g., discharge and water depth) must be specified at the upstream end, while no boundary condition is required downstream. The same equation for the water surface slope applies, but the denominator becomes negative, indicating a qualitatively different behavior.

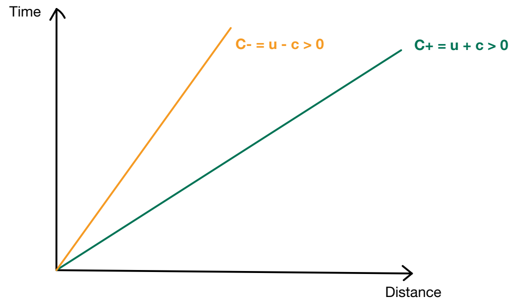

Figure 3.3: Characteristic lines in supercritical flow ($Fr > 1$): all information propagates downstream.

The water surface profile for gradually varied flow in this regime can be described by:

$$\frac{dh}{dx} = \frac{S_0 - S_f}{1 - Fr^2}$$

where S_0 is the bed slope and S_f is the friction slope.

Understanding the direction in which information travels through the domain is essential for the correct application of boundary conditions. It also explains why transitions between flow regimes, such as at hydraulic jump, must be handled carefully in numerical schemes. The governing dynamics and control mechanisms change fundamentally between subcritical and supercritical flows.

Hydraulic jump

The hydraulic jump represents an important phenomenon in open channel hydraulics. It occurs as an abrupt transition from supercritical flow to subcritical flow, where the water surface rises dramatically over a short distance. This phenomenon typically manifests when a fast-moving, shallow stream encounters conditions that force it to slow down and deepen. Such conditions include a change in channel slope, an obstruction, or downstream control structures like gates or stilling basins.

From a physical perspective, the hydraulic jump serves as a natural mechanism for energy dissipation. The high-velocity supercritical flow approaching the jump possesses considerable kinetic energy, which transforms into potential energy and heat through intense turbulence during the transition. This process is accompanied by significant air entrainment, surface rollers, and chaotic mixing patterns, creating a visibly turbulent region.

Before the jump, in the supercritical region, the flow exhibits high velocity with relatively low depth and pressure. After passing through the jump, the flow characteristics reverse dramatically: velocity decreases, while both water depth and pressure increase substantially. This transformation enables the flow to adapt to downstream conditions in a manner consistent with the principles of momentum conservation.

The relationship between the water depths on either side of the jump, known as conjugate depths, can be derived analytically through momentum conservation principles. For rectangular channels, this relationship is expressed as:

$$\frac{h_2}{h_1} = \frac{1}{2}\left(\sqrt{1 + 8Fr_1^2} - 1\right) \tag{I.9}$$

where h_1 represents the upstream supercritical depth, h_2 denotes the downstream subcritical depth, and $Fr_1 = \frac{u_1}{\sqrt{\frac{gA_1}{T}}}$ is the upstream Froude number, with u_1 being the approach velocity and A_1 the upstream cross-sectional area.

The hydraulic jump exhibits several important characteristics that make it valuable in hydraulic engineering. It transforms unstable supercritical flow into stable subcritical flow, providing a mechanism for flow control. The process involves substantial specific energy loss, making hydraulic jumps effective for energy dissipation downstream of spillways and outlet works. The intensity of the jump correlates directly with the upstream Froude number: higher values produce more violent and effective energy dissipation. Finally, the jump's position is not fixed but depends dynamically on downstream conditions. If the downstream depth exceeds the required conjugate depth, the jump migrates upstream, while insufficient downstream depth causes the jump to move downstream or potentially disappear altogether.

In hydraulic design, engineers often intentionally create and position hydraulic jumps to protect downstream channels from erosive high-velocity flows, making them essential features in stilling basins and other hydraulic structures.

II Numerical methods of resolution

II.1 Spatial discretization - finite volume method

The finite volume method (FVM) represents a powerful numerical approach for solving partial differential equations, particularly well-suited for fluid mechanics problems. Its fundamental principle lies in discretizing the computational domain into elementary control volumes, where conservation equations are rigorously integrated.

The finite volume method is particularly suited for modeling flows in mining galleries. This method is based on a fundamental physical principle: the conservation of quantities (mass, momentum) in control volumes. The basic principle consists of dividing the study domain, in our case the galleries, into a set of elementary volumes. For each volume, we focus not on point values of variables such as water height or velocity, but on their average values over the volume. This approach is particularly relevant as it corresponds to the physical reality of our problem: we are interested in the global evolution of flow in each gallery section.

The temporal evolution of these quantities is calculated by evaluating the fluxes crossing the interfaces between neighboring volumes. These fluxes represent the exchanges of mass and momentum between volumes. For example, if we consider a given volume, the increase in water height in this volume during a time interval is directly related to the difference between the incoming and outgoing water flux during this interval.

A major advantage of this method is its ability to naturally handle discontinuities in the flow. In our case, these discontinuities appear particularly during the propagation of the wave front during gallery filling. The finite volume method, unlike other numerical approaches, does not require special treatment to handle these discontinuities as it relies on an integral formulation of conservation equations.

Mesh type

The first step is to divide the domain into different volumes, which will form the mesh. The mesh can be either regular or irregular, offering great flexibility in terms of the shapes of domains that can be discretized into finite volumes.

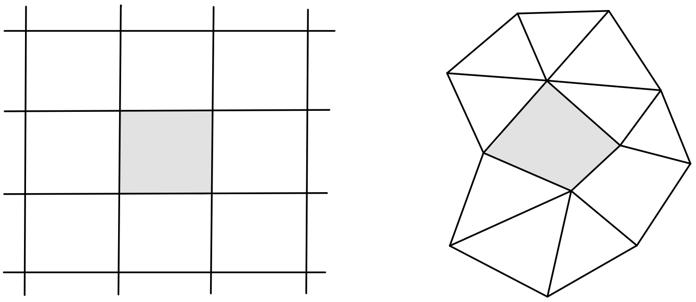

Figure 3.4: Mesh type

The idea here is to maintain a regular mesh as much as possible. However, at the reservoir level, the mesh is different from that of the pipes.

Types of finite volumes

After the mesh is generated, it is essential to define the type of control volume and, as a result, determine the location of the unknowns. Like the mesh, the control volumes must be continuous and encompass the entire modeling domain, but their shape can vary without restriction. There are various families of finite volume methods, depending on how the control volumes are defined and how the unknowns are positioned. The most common methods are cell-centered, vertex-centered and cell-vertex approaches.

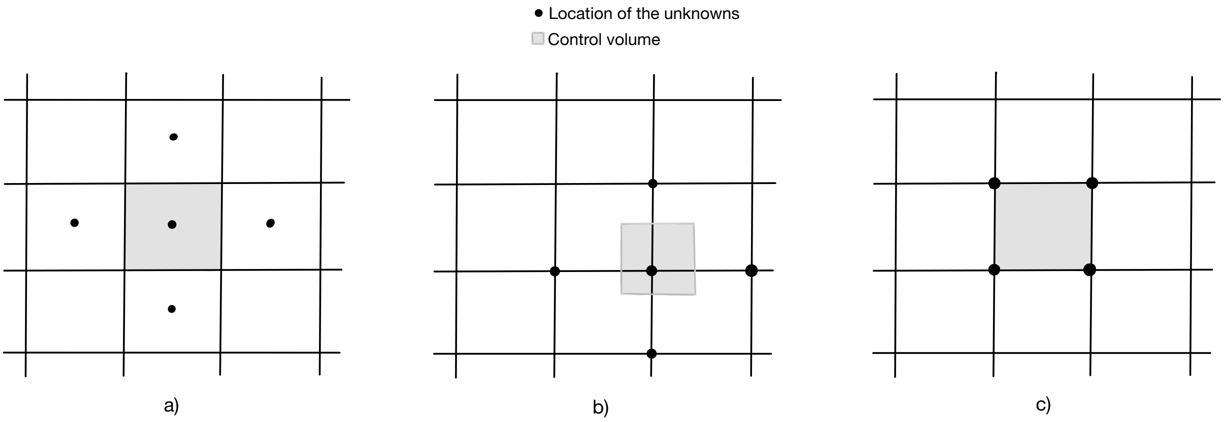

Figure 3.5: Type of control volumes - a) "cell-centered", b) "vertex-centered", c) "cell-vertex"

In the cell-centered approach, the unknowns are positioned at the center of each mesh cell, with the control volume being identical to the mesh cell itself. This method is widely adopted due to its straightforward implementation and natural conservation of fluxes across cell interfaces. The direct correspondence between mesh and control volumes makes it particularly intuitive to understand and implement. However, this method may require special treatment for boundary conditions, as the unknowns are not directly located on the domain boundaries. This method was adopted in the present study.

The vertex-centered method positions the unknowns at the mesh vertices, with control volumes constructed around these mesh nodes, typically by connecting cell centers to edge midpoints. This approach generally provides higher accuracy for smooth solutions and handles boundary conditions more naturally since unknowns are located directly on the boundaries. It's particularly well-suited for unstructured meshes and complex geometries. However, the implementation is more complex than the cell-centered approach, requiring additional geometric calculations, especially for control volume construction in three dimensions. The method demands careful consideration of how to construct control volumes, particularly at domain boundaries and irregular mesh regions.

The cell-vertex method represents a hybrid approach where unknowns are stored at vertices but control volumes are defined as the mesh cells themselves. Values at cell centers are typically computed by averaging the vertex values, combining aspects of both previous approaches. This method offers a good compromise between accuracy and implementation complexity, performing well with both structured and unstructured meshes. While it can be more computationally expensive than simpler approaches and requires careful treatment of averaging procedures, it provides flexibility in handling various types of problems.

II.2 Time discretization - Runge-Kutta 22 method

The Runge-Kutta 22 method (RK22) is a second-order accurate predictor-corrector scheme used in this implementation for temporal integration. This method offers a good compromise between computational efficiency and numerical accuracy. The scheme can be expressed as follows:

For a system of differential equations of the form:

$$\frac{dy}{dt} = f(t, y) \tag{II.1}$$

The RK22 method advances the solution from time step n to $n + 1$ using two stages:

$$y^* = y^n + \Delta t f(t^n, y^n) \text{ (predictor)} \tag{II.2}$$

$$y^{n+1} = y^n + \Delta t[(1 - a_1)f(t^n, y^n) + a_1 f(t^n + \Delta t, y^*)] \text{ (corrector)} \tag{II.3}$$

where:

- y^n is the solution at time step n.
- y^* is the intermediate prediction.
- y^{n+1} is the solution at the next time step.
- a_1 is the scheme weighting parameter (set to 0.5 for optimal accuracy).
- Δt is the time step determined by the CFL condition.

Physically, the RK22 method can be understood as an improvement over the simple Euler scheme, using a two-step prediction-correction logic. In the predictor step, the solution is advanced forward in time using the initial slope (or rate of change) given by $f(t^n, y^n)$, which corresponds to assuming the system evolves with constant velocity during Δt. However, in real physical systems, the dynamics often evolve during the time step due to changing forces or fluxes. Therefore, a corrector step is introduced: we re-evaluate the slope at the predicted point $(t^n + \Delta t, y^*)$ and take a weighted average of the two slopes (initial and predicted). This approach more accurately captures the average behavior of the system during the time interval and leads to second-order temporal accuracy.

This idea is particularly important in systems governed by conservation laws, such as mass and momentum conservation, where the dynamics are driven by spatial fluxes and source terms that can vary significantly over time. The RK22 scheme offers a physically intuitive way to account for these evolving influences by incorporating feedback from the system's predicted state before finalizing the update. This makes the method more robust and reliable for unsteady problems.

In our numerical model, this scheme is applied to both the mass and momentum conservation equations. For the mass conservation equation:

$$A^* = A^n - \frac{\Delta t}{\Delta x}(Q^n_{i+1/2} - Q^n_{i-1/2}) \tag{II.4}$$

$$A^{n+1} = A^n - \frac{\Delta t}{\Delta x}[(1-a_1)(Q^n_{i+1/2} - Q^n_{i-1/2}) + a_1(Q^*_{i+1/2} - Q^*_{i-1/2})] \tag{II.5}$$

And similarly for the momentum equation:

$$Q^* = Q^n - \frac{\Delta t}{\Delta x}(F^n_{i+1/2} - F^n_{i-1/2}) + \Delta t S^n \tag{II.6}$$

$$Q^{n+1} = Q^n - \frac{\Delta t}{\Delta x}[(1-a_1)(F^n_{i+1/2} - F^n_{i-1/2}) + a_1(F^*_{i+1/2} - F^*_{i-1/2})] + \Delta t[(1-a_1)S^n + a_1 S^*] \tag{II.7}$$

where F represents the flux terms, which include the convective term $(\frac{Q^2}{A})$ and the pressure term $(gA\frac{\partial Z}{\partial x})$. S is the source term which includes the friction term (gAJ).

This implementation has several advantages:

- Second-order temporal accuracy when a_1 = 0.5.
- Strong stability properties due to the predictor-corrector structure.
- Efficient computation with only two stages per time step.
- Natural handling of source terms and boundary conditions.

The weighting parameter of the predictor-corrector scheme (a1)

The parameter a_1 controls the relative contribution of the predictor and the corrector in the Runge-Kutta scheme. A value of a_1 close to 1 favors the corrector, which can lead to better numerical stability at the expense of precision. Conversely, a lower value of a_1 can improve precision at the cost of stability. The choice of a_1 should be balanced based on the specific needs of the simulation. For RK22, a value of a_1 = 0.5 will be used to achieve maximum precision. This is used for unsteady calculations. On the other hand, for RK21, a_1 = 1 will be used, where maximum dissipation occurs. This scheme is used for steady-state solutions.

The Courant-Friedrichs-Lévy (CFL) number

The CFL (Courant-Friedrichs-Lewy) condition must be respected to ensure scheme stability. The CFL is mathematically defined as follows:

$$\Delta t \leq \text{CFL} \frac{\Delta x}{\max(|v| + \sqrt{g\frac{A}{T}})} \tag{II.8}$$

where:

- Δt is the time step.
- Δx is the mesh size.
- v is the water velocity.
- $\sqrt{gA/T}$ is the wave propagation speed.

The time step must not be too large. Concretely: a water particle must not cross more than one mesh cell in one time step. Thus, the CFL determines the relationship between the time step, the spatial step, and the maximum velocity of the flow. A smaller CFL ensures better numerical stability but may require smaller time steps, which increases the computation time. A larger CFL may speed up convergence, but it can also compromise the stability of the solution. The choice of CFL depends on the balance between accuracy and computational efficiency.

Physically, the CFL number can be interpreted as the ratio between two velocities: the numerical velocity (i.e., how fast information can travel across the computational grid per time step), and the physical velocity (i.e., how fast waves or particles actually move in the real system).

More precisely:

- The physical speed corresponds to the flow velocity |v| combined with the wave propagation speed $\sqrt{gA/T}$, representing the fastest way information can travel through the system.
- The numerical speed is given by the grid resolution divided by the time step $\Delta x/\Delta t$, which represents how quickly the scheme updates information across cells.

The CFL number is then:

$$CFL = \frac{\text{physical speed}}{\text{numerical speed}} \tag{II.9}$$

If CFL > 1, the physical information travels faster than the scheme can handle, potentially skipping cells and causing instability. If CFL < 1, the scheme updates faster than the physical process, ensuring stability but possibly requiring many small time steps.

Therefore, the CFL number reflects a balance between stability, accuracy, and computational efficiency. It ensures that the numerical method respects the causality of wave propagation in the physical system.

II.3 Type of reconstruction

In the cell-centered finite volume approach, solution variables are stored at the centers of control volumes. However, to compute fluxes across cell interfaces, we need to determine variable values at these interfaces. This process is known as reconstruction, where we extrapolate the cell-centered values to obtain interface values.

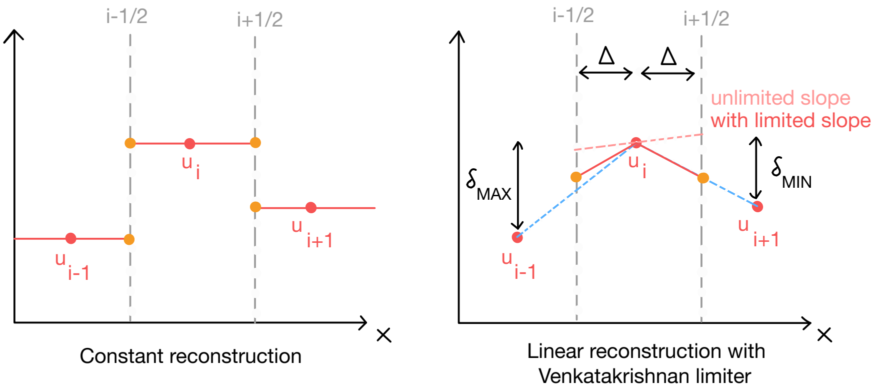

Figure 3.6: Illustration of constant and linear reconstruction (without limited slope) methods for approximating interface values from cell-centered data

Our implementation supports two types of reconstruction methods: constant and limited linear reconstruction.

In constant reconstruction, the solution value is considered uniform within each control volume, equal to the value at the cell center:

$$u_{i-\frac{1}{2},right} = u_i = u_{i+\frac{1}{2},left} \tag{II.10}$$

This method is first-order accurate and preserves the mean value of the solution within each cell.

For higher accuracy, we implement a limited linear reconstruction approach that uses the Venkatakrishnan limiter. The basic linear reconstruction takes the form:

$$u_{i-\frac{1}{2},right} = u_i - \frac{\Delta x}{2} \cdot slope_i \quad \text{and} \quad u_{i+\frac{1}{2},left} = u_i + \frac{\Delta x}{2} \cdot slope_i \tag{II.11}$$

Where the slope is calculated based on neighboring cell values and then limited to prevent unphysical oscillations.

The Venkatakrishnan slope limiter is designed to prevent non-physical oscillations in numerical schemes while preserving high-order accuracy in smooth regions. It modifies the computed slope based on local extrema and a regularization parameter.

1. Computation of the unlimited slope The unlimited slope is first computed using the centered difference between neighboring cell values:

$$\text{slope} = \frac{u_{i+1} - u_{i-1}}{2\Delta x} \tag{II.12}$$

2. Definition of local extremes To control the magnitude of the slope, we define the following local extrema:

- Maximum allowable increase:

$$\delta_{\text{max}} = \max(u_i, u_{i-1}, u_{i+1}) - u_i \tag{II.13}$$

- Maximum allowable decrease:

$$\delta_{\text{min}} = u_i - \min(u_i, u_{i-1}, u_{i+1}) \tag{II.14}$$

3. Projected slope increment The absolute increment that would result from applying the unlimited slope is estimated as:

$$\Delta = \left|\text{slope} \cdot \frac{\Delta x}{2}\right| \tag{II.15}$$

4. Limiting function The Venkatakrishnan limiter uses a smooth function to modulate the slope based on local gradients:

$$\phi(\delta, \Delta) = \frac{\delta \cdot (\delta + 2\Delta) + \epsilon}{\delta \cdot (\delta + \Delta) + 2\Delta^2 + \epsilon} \tag{II.16}$$

where ϵ is a small regularization parameter, typically chosen as:

$$\epsilon^3 = (\kappa \Delta x)^3 \tag{II.17}$$

with κ being a small positive constant (e.g., related to mesh resolution).

5. Final limited slope The final limited slope is then computed by applying the most restrictive (i.e., smallest) limiter to the original slope:

$$\text{slope}_{\text{limited}} = \text{slope} \cdot \min\left(\phi(\delta_{\text{min}}, \Delta), \phi(\delta_{\text{max}}, \Delta)\right) \tag{II.18}$$

This limiter ensures that sharp gradients are preserved where appropriate, while preventing overshoots or undershoots in the solution near discontinuities or extrema.

This limiter has several advantages. It produces smoother limiting compared to traditional minmod or superbee limiters. It also maintains second-order accuracy in smooth regions, preventing the creation of new extrema in the solution. Additionally, it includes a parameter (ϵ) that can be tuned to adjust the amount of limiting applied.

Special care is taken at domain boundaries, where not all neighboring cells are available for reconstruction: constant reconstruction is applied to prevent extrapolation errors.

The reconstruction process is implemented in the Reconstruction function.

The function returns a 2D array containing the reconstructed left and right states at each interface.

The choice of reconstruction method impacts both the accuracy and stability of the numerical solution:

- Constant reconstruction offers robust stability at the cost of higher numerical diffusion and first-order accuracy.
- Limited linear reconstruction with the Venkatakrishnan limiter achieves second-order accuracy in smooth regions while maintaining stability near discontinuities, resulting in sharper resolution of solution features.

Given the regularity of the mesh and the need for stability in challenging flow regimes, a constant reconstruction was chosen. This provides a robust first-order method that remains reliable even in the presence of sharp transitions. This reconstruction achieves first-order accuracy, which provides sufficient resolution for the current application.

II.4 Explicit, implicit, and hybrid solving schemes

In the numerical resolution of the Saint-Venant equations using the finite volume method, time discretization is a key component that strongly influences both the stability and accuracy of the solution. Three main families of time integration schemes are commonly used: explicit, implicit, and hybrid schemes.

An explicit scheme determines the solution at the next time step t^{n+1} only based on known values at the current time t^n and, if needed, at previous time levels (t^{n-1}, t^{n-2}, ...). In other words, the future state of the system is computed directly from the present, without requiring the solution of any algebraic system. This approach is straightforward to implement and computationally efficient per time step. However, its main limitation lies in the stability condition it imposes, known as the Courant-Friedrichs-Lewy (CFL) condition. This condition restricts the maximum time step allowed for stability based on the flow velocity u, wave celerity c, and mesh size Δx, typically requiring $\Delta t \leq \frac{\Delta x}{u+c}$. As a result, explicit schemes may require very small time steps, particularly in cases with shallow depths or fine spatial resolution.

In contrast, implicit schemes calculate the solution at t^{n+1} using not only the known values at previous time levels, but also unknown variables at the new time level itself. This leads to the formulation of a system of equations (often non linear and coupled) that must be solved at each time step. Although more complex to implement and computationally more demanding per iteration, implicit schemes offer the significant advantage of being unconditionally stable under certain conditions. They are particularly well suited to stiff systems or slow transients, where larger time steps are desirable without compromising the stability of the solution.

Hybrid schemes aim to combine the advantages of both explicit and implicit methods. A common example is the Runge-Kutta family of methods, which employ multi-stage, predictor-corrector approaches to improve accuracy while retaining an explicit formulation. In particular, the second-order explicit Runge-Kutta method is widely used in finite volume models for shallow water flows. At each time step, the computation proceeds in several stages. First, the numerical fluxes are evaluated at the interfaces between control volumes. These fluxes are based on average values of the conserved variables in adjacent cells and must be accurately reconstructed, as they directly influence the precision and stability of the solution. Then, for each control volume, a flux balance is performed by comparing incoming and outgoing fluxes, while also incorporating source terms such as bottom slope and friction. Finally, the average values of the conserved variables are updated based on this balance. Special care is required to ensure that certain physical constraints are respected during the update, such as the non-negativity of water depth and the conservation of mass and momentum.

The spatial accuracy of the scheme depends on the method used for flux reconstruction at cell interfaces. A first-order method assumes piecewise constant values, which introduces numerical diffusion. To reduce this while avoiding spurious oscillations near sharp gradients (e.g., hydraulic jumps), second-order reconstructions are often employed. These methods, which may involve slope limiters, offer a good compromise between accuracy and stability.

CHAPTER 4

NUMERICAL MODEL OF A SINGLE PIPE

The initial implementation of the numerical model focuses on simulating flow dynamics within a single pipe configuration, which serves as the foundation for the more complex interconnected gallery network. This approach allows for validation of core numerical methods and boundary condition handling before extending to the full system.

I Implemented functions

The following figures illustrate the geometric variables used for circular and rectangular cross-sections.

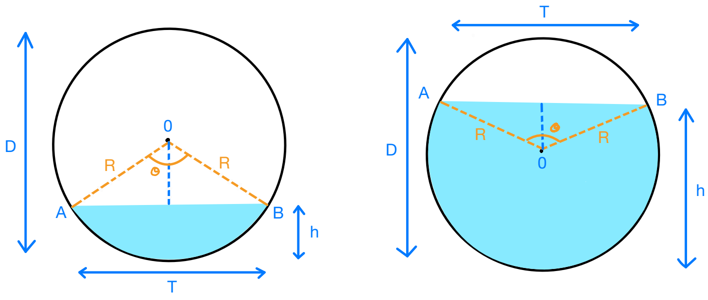

Figure 4.1: Schematic representation of geometric parameters in a circular cross-section

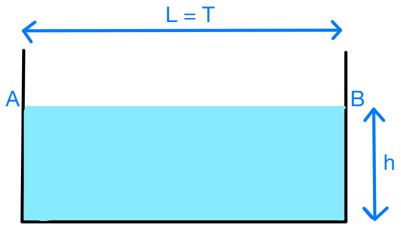

Figure 4.2: Schematic representation of geometric parameters in a rectangular cross-section

I.1 Function calculate_wetted_area

This function calculates the wetted area from a given water height. For rectangular sections:

$$A = L \cdot h \tag{I.1}$$

For circular sections, three cases are considered:

- If $h \leq 0$: $A = 0$.
- If $h \geq D$: $A = \pi R^2$.
- Otherwise:

For $h \leq R$:

$$\theta = 2 \arccos\left(\frac{R - h}{R}\right) \tag{I.2}$$

$$A = \frac{R^2}{2}(\theta - \sin\theta) \tag{I.3}$$

For $h > R$:

$$\theta = 2 \arccos\left(\frac{R - (2R - h)}{R}\right) \tag{I.4}$$

$$A = \pi R^2 - \frac{R^2}{2}(\theta - \sin\theta) \tag{I.5}$$

I.2 Function calculate_wetted_perimeter_from_A

This function computes the wetted perimeter from a given area. For rectangular sections:

$$P = L + 2h \tag{I.6}$$

For circular sections, after recovering h using Newton-Raphson:

For $h \leq R$:

$$\theta = 2 \arccos\left(\frac{R - h}{R}\right) \tag{I.7}$$

$$P = R\theta \tag{I.8}$$

For $h > R$:

$$\theta = 2 \arccos\left(\frac{R - (2R - h)}{R}\right) \tag{I.9}$$

$$P = 2\pi R - R\theta \tag{I.10}$$

I.3 Function calculate_top_width_from_A

For rectangular sections:

$$T = L \tag{I.11}$$

For circular sections, after recovering h using Newton-Raphson:

For $h \leq R$:

$$\theta = 2 \arccos\left(\frac{R - h}{R}\right) \tag{I.12}$$

$$T = 2R\sin\left(\frac{\theta}{2}\right) \tag{I.13}$$

For $h > R$:

$$\theta = 2\arccos\left(\frac{R-(2R-h)}{R}\right) \tag{I.14}$$

$$T = 2R\sin\left(\frac{\theta}{2}\right) \tag{I.15}$$

I.4 Functions "h_Newton_Raphson" ans "find_h_from_area_NR"

In hydraulic calculations for circular pipes, a fundamental challenge is determining the water height h from a given wetted area A. For a pipe of radius R, this relationship is governed by geometric considerations that vary depending on whether the water level is above or below the pipe's center.

When the water height h is less than or equal to the radius R (lower half of the pipe), the wetted area A is given by:

$$A = \frac{R^2}{2}(\theta - \sin\theta) \tag{I.16}$$

where $\theta = 2 \cdot \arccos(\frac{R-h}{R})$ is the central angle.

For water heights above the pipe's center ($h > R$), the wetted area becomes:

$$A = \pi R^2 - \frac{R^2}{2}(\theta - \sin\theta) \tag{I.17}$$

with $\theta = 2 \cdot \arccos(\frac{R-(2R-h)}{R})$.

Since these equations cannot be analytically inverted to solve for h, we employ the Newton-Raphson method, an iterative technique for finding roots of equations.

The core idea of the Newton-Raphson method is based on linear approximation. If we have a function $f(x)$ and want to find a value x such that $f(x)$ = 0, the method works by:

1. Starting with an initial approximation x_0.
2. Finding the tangent line to the function at x_0.
3. Computing the x-intercept of this tangent line (where it crosses the x-axis).
4. Using this intercept as the next approximation x_1.
5. Iterating this process until convergence.

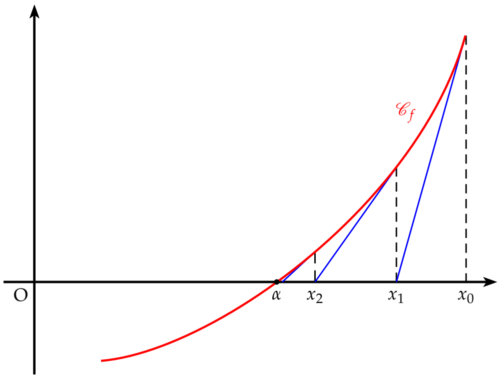

Figure 4.3: Newton-Raphson algorithm

1. **Initial approximation:**

   For small heights ($A \leq \pi R^2/2$), we can approximate the circular arc with a parabola:

   $$h \approx \left(\frac{3}{4\sqrt{2}}\right)^{2/3} \cdot A^{2/3} \cdot R^{-1/3} \tag{I.18}$$

   For large heights ($A > \pi R^2/2$), we use the symmetry of the problem and consider the complementary segment:

   $$h = 2R - \left(\frac{3}{4\sqrt{2}}\right)^{2/3} \cdot (\pi R^2 - A)^{2/3} \cdot R^{-1/3} \tag{I.19}$$

   This parabolic approximation provides a good starting point for the iteration process.

   The detailed derivations of these approximations are provided in Appendix B.

2. **The Newton-Raphson method** finds a root of function $f(h)$ through successive approximations:

   $$h_{n+1} = h_n - \frac{f(h_n)}{f'(h_n)} \tag{I.20}$$

   In our case, we define $f(h)$ as the difference between calculated and target areas:

   $$f(h) = \begin{cases} \frac{R^2}{2}(\theta - sin\theta) - A & \text{if } h \leq R \\ \pi R^2 - \frac{R^2}{2}(\theta - sin\theta) - A & \text{if } h > R \end{cases} \tag{I.21}$$

   The derivative $f'(h)$ if $h \leq R$ is:

   $$f'(h) = \frac{R^2}{\sqrt{2Rh - h^2}}\,(1 - cos(\theta)) \tag{I.22}$$

   And the derivative $f'(h)$ if $h > R$ is:

   $$f'(h) = \frac{R^2}{\sqrt{2R(2R-h) - (2R-h)^2}}(1 - \cos\theta) \tag{I.23}$$

   The detailed derivations of these derivatives are provided in Appendix B.

3. **Numerical stability considerations:**
    - Implementation of boundary protections: h is constrained between a small tolerance value and $2R$ − tolerance.
    - Step size limitation: The Newton-Raphson update Δh is limited to $\pm 0.1R$.
    - Division by zero protection: A minimum threshold is set for the derivative.
    - Convergence criteria:

$$|f(h)| < \text{tolerance or } |h_{n+1} - h_n| < \text{tolerance} \tag{I.24}$$

   The method's convergence is demonstrated through the normalized height-area relationship (h/D vs A/D^2), showing:
    - At $A/D^2 = 0$: $h/D = 0$ (empty pipe).
    - At $A/D^2 = 0.5$: $h/D = 0.5$ (half-full pipe).
    - At $A/D^2 \approx 0.785$ ($\pi/4$): $h/D = 1$ (full pipe).

4. Here is **the graph** showing the evolution of the normalized height (h/D) as a function of the normalized wetted area (A/D^2).

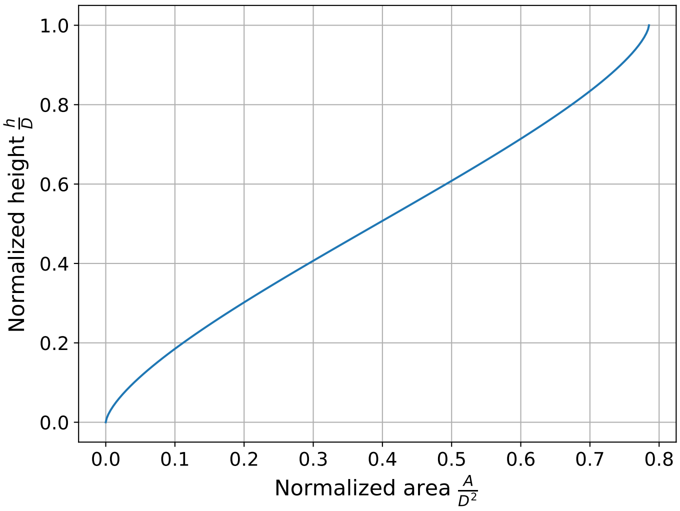

Figure 4.4: Evolution of the normalized height (h/D) as a function of the normalized wetted area (A/D^2)

II Governing equations

The one-dimensional flow in the pipe is governed by the Saint-Venant equations, consisting of mass and momentum conservation equations integrated over the gallery flow cross-section:

$$\begin{cases} \frac{\partial A}{\partial t} + \frac{\partial Q}{\partial x} = 0 \\ \frac{\partial Q}{\partial t} + \frac{\partial (\frac{Q^2}{A})}{\partial x} + gA\frac{\partial Z}{\partial x} + gAS_f = 0 \end{cases} \tag{II.1}$$

where:

- A is the wetted cross-sectional area.
- Q is the flow rate.
- g is gravitational acceleration.
- Z is the free surface elevation.
- S_f is the friction slope.

III Numerical discretization

Due to the circular shape of the section, it is not feasible to work with water depth and specific flow, as the width is variable. The two key variables for analysis are the section and the total flow rate. Consequently, the equations will be discretized as outlined below.

The equations are discretized using a finite volume approach with a two-step Runge-Kutta scheme for temporal integration. The spatial domain is divided into N control volumes, and the variables are evaluated at cell centers. The discretized mass conservation equation takes the form:

$$\frac{A_i^{n+1} - A_i^n}{\Delta t} + \frac{Q_{i+1/2}^n - Q_{i-1/2}^n}{\Delta x} = 0 \tag{III.1}$$

Similarly, the discretized momentum equation is:

$$\frac{Q_i^{n+1} - Q_i^n}{\Delta t} + \frac{(\frac{Q^2}{A})_{i+1/2}^n - (\frac{Q^2}{A})_{i-1/2}^n}{\Delta x} + \frac{g}{2}\frac{\frac{(A^2)_{i+1/2}^n - (A^2)_{i-1/2}^n}{A_{i+1/2}^n - A_{i-1/2}^n}(Z_{i+1/2}^n - Z_{i-1/2}^n)}{\Delta x} + g \cdot A_i^n \cdot S_f = 0 \tag{III.2}$$

The index 'i' denotes the spatial step, while the index 'n' refers to the time step.

The head loss is determined using Manning's formula. The Manning's coefficient will be a calibratable parameter, as its value is unknown. Since the pipes are made of PVC, this coefficient can be estimated.

Here is the Manning's equation:

$$Q = \frac{1}{n} \cdot R_H^{2/3} \cdot \sqrt{S_f} \tag{III.3}$$

We can then calculate the head loss using this equation by isolating S_f:

$$S_f = \frac{n^2}{R_H^{4/3}} \cdot \frac{Q^2}{A^2} \tag{III.4}$$

IV Flux evaluation

The numerical fluxes at cell interfaces are evaluated using a flux-splitting approach based on the local flow characteristics. This evaluation takes into account the flow direction (left to right or right to left).

For a given interface $i + 1/2$, we must evaluate two types of fluxes:

1. The mass flux.
2. The momentum flux.

The choice of which side of the interface to use for evaluation depends on the flow direction at the left and right edges:

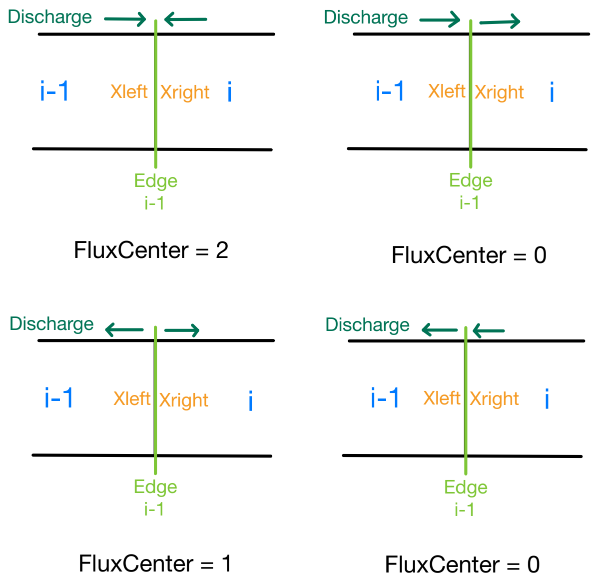

Figure 4.5: Flow direction at the edges

Then, for each term:

- Convective terms (Q and $\frac{Q^2}{A}$): Evaluated from upstream side.
- Pressure term ($gA\frac{\partial Z}{\partial x}$): Evaluated from downstream side.

This upwind/downwind selection is implemented through the FluxCenter parameter which determines how to evaluate the fluxes at cell interfaces based on flow direction.

Here are the equations used for each case.

If FluxCenter = 0 and both upstream and downstream discharges are positive:

$$Q^n_{calc,Edge\ i} = Q^n_{Edge\ i,left} \tag{IV.1}$$

$$Qu^n_{calc,Edge\ i} = \frac{(Q^n_{Edge\ i,left})^2}{A^n_{Edge\ i,left}} \tag{IV.2}$$

$$A^n_{calc,Edge\ i} = A^n_{Edge\ i,right} \tag{IV.3}$$

$$\left(A^n_{calc,Edge\ i}\right)^2 = \left(A^n_{Edge\ i,right}\right)^2 \tag{IV.4}$$

$$Z^n_{calc,Edge\ i} = z^n_{Edge\ i,right} + h^n_{Edge\ i,right} \tag{IV.5}$$

If FluxCenter = 0 and both upstream and downstream discharges are negative:

$$Q^n_{calc,Edge\ i} = Q^n_{Edge\ i,right} \tag{IV.6}$$

$$Qu^n_{calc,Edge\ i} = \frac{(Q^n_{Edge\ i,right})^2}{A^n_{Edge\ i,right}} \tag{IV.7}$$

$$A^n_{calc,Edge\ i} = A^n_{Edge\ i,left} \tag{IV.8}$$

$$\left(A^n_{calc,Edge\ i}\right)^2 = \left(A^n_{Edge\ i,left}\right)^2 \tag{IV.9}$$

$$Z^n_{calc,Edge\ i} = z^n_{Edge\ i,left} + h^n_{Edge\ i,left} \tag{IV.10}$$

If FluxCenter = 1 (contradiction of signs with downstream positive and upstream negative):

$$Q^n_{calc,Edge\ i} = 0.5 \cdot \left(Q^n_{Edge\ i,left} + Q^n_{Edge\ i,right}\right) \tag{IV.11}$$

$$Qu^n_{calc,Edge\ i} = 0.5 \left(\frac{(Q^n_{Edge\ i,left})^2}{A^n_{Edge\ i,left}} + \frac{(Q^n_{Edge\ i,right})^2}{A^n_{Edge\ i,right}}\right) \tag{IV.12}$$

$$A^n_{calc,Edge\ i} = 0.5 \left(A^n_{Edge\ i,left} + A^n_{Edge\ i,right}\right) \tag{IV.13}$$

$$\left(A^n_{calc,Edge\ i}\right)^2 = 0.5 \left(\left(A^n_{Edge\ i,left}\right)^2 + \left(A^n_{Edge\ i,right}\right)^2\right) \tag{IV.14}$$

$$Z^n_{calc,Edge\ i} = 0.5 \left((z^n_{Edge\ i,left} + h^n_{Edge\ i,left}) + (z^n_{Edge\ i,right} + h^n_{Edge\ i,right})\right) \tag{IV.15}$$

If FluxCenter = 2 (contradiction of signs with upstream positive and downstream negative):

If $MAX\left(Q^n_{Edge\ i,left}; Q^n_{Edge\ i,right}\right) = Q^n_{Edge\ i,left}$:

$$Q^n_{calc,Edge\ i} = Q^n_{Edge\ i,left} \tag{IV.16}$$

$$Qu^n_{calc,Edge\ i} = \frac{(Q^n_{Edge\ i,left})^2}{A^n_{Edge\ i,left}} \tag{IV.17}$$

$$A^n_{calc,Edge\ i} = A^n_{Edge\ i,right} \tag{IV.18}$$

$$\left(A^n_{calc,Edge\ i}\right)^2 = \left(A^n_{Edge\ i,right}\right)^2 \tag{IV.19}$$

$$Z^n_{calc,Edge\ i} = z^n_{Edge\ i,right} + h^n_{Edge\ i,right} \tag{IV.20}$$

If $MAX\left(Q^n_{Edge\ i,left}; Q^n_{Edge\ i,right}\right) = Q^n_{Edge\ i,right}$:

$$Q^n_{calc,Edge\ i} = Q^n_{Edge\ i,right} \tag{IV.21}$$

$$Qu^n_{calc,Edge\ i} = \frac{(Q^n_{Edge\ i,right})^2}{A^n_{Edge\ i,right}} \tag{IV.22}$$

$$A^n_{calc,Edge\ i} = A^n_{Edge\ i,left} \tag{IV.23}$$

$$\left(A^n_{calc,Edge\ i}\right)^2 = \left(A^n_{Edge\ i,left}\right)^2 \tag{IV.24}$$

$$Z^n_{calc,Edge\ i} = z^n_{Edge\ i,left} + h^n_{Edge\ i,left} \tag{IV.25}$$

V Loss terms

The loss terms represent the source/sink contributions in both the mass and momentum equations. In our case:

1. Mass loss terms:

$$LossOfMass_i = 0 \tag{V.1}$$

as there are no lateral inflows or outflows in our system.

2. Momentum loss terms:

$$LossOfMomentum_i = gA_i^n S_f \Delta x \tag{V.2}$$

where:

- S_f is the friction slope, computed using Manning's formula:

$$S_f = \frac{n^2 Q_i |Q_i|}{A_i^2 R_h^{4/3}} \tag{V.3}$$

- $R_h = \frac{A}{P}$ is the hydraulic radius.
- n is Manning's roughness coefficient.

VI Global resolution algorithm: general algorithm structure

The numerical algorithm developed for solving the Saint-Venant equations follows a structured approach divided into several main steps.

VI.1 Main steps

1. Initialization
    - Definition of geometric parameters (length, section, slope)
    - Initialization of hydraulic variables:
        - Initial water depth.
        - Initial flow rate.
        - Initial wetted area: calculated from $h_{initial}$.
    - Definition of numerical parameters:
        - CFL.
        - $a_1 = 0.5$ (RK weighting coefficient).
        - Δx (spatial step).
2. Time loop

    For each time step, until a stopping criterion is met:

(a) **Adaptive time step calculation:**

$$\Delta t = CFL\frac{\Delta x}{\max(|u| + c)} \tag{VI.1}$$

where u is the local velocity and c the wave celerity.

(b) **Two-stage Runge-Kutta scheme:**

- Predictor step: computation of A^* and Q^*.
- Variable reconstruction at interfaces.
- Evaluation of fluxes and source terms.
- Corrector step: computation of A^{**} and Q^{**}.
- Linear combination for final solution.

(c) **Solution update:**

- Update of variables A, Q and h.
- Application of boundary conditions.
- Convergence calculation.

VI.2 Stopping criteria

The algorithm stops if one of the following conditions is met:

1. **Time criterion:**

$$t_{current} \geq t_{max} = N_{save} \cdot \Delta t_{save} \tag{VI.2}$$

2. **Iterative criterion:**

$$n_{steps} \geq n_{max} = 10^{10} \tag{VI.3}$$

3. **Convergence criterion:**

$$\epsilon = \max(\epsilon_A, \epsilon_Q) \leq \epsilon_{max} = 10^{-5} \tag{VI.4}$$

where:

$$\epsilon_A = \max|A^{n+1} - A^n| \tag{VI.5}$$

$$\epsilon_Q = \max|Q^{n+1} - Q^n| \tag{VI.6}$$

CHAPTER 5

NUMERICAL MODEL VALIDATION FOR A SINGLE PIPE

I Water surface profiles theory

The calculation of water surface profiles is essential for understanding flow behavior in open channels or partially filled pipes. Before proceeding with the validation of our numerical model, it is important to establish the theoretical framework that will serve as a basis for comparison.

I.1 Critical and uniform flow depths

For a circular pipe with zero slope, two characteristic depths are particularly important:

Uniform depth

The uniform depth is the water height obtained under the assumption that the friction slope S_f equals the bed slope S_0. This height can be determined using Manning's formula:

$$u = \frac{Q}{A} = K \cdot R_H^{2/3} \cdot \sqrt{S_0} \tag{I.1}$$

Where:

- A is the flow cross-sectional area.
- Q is the flow rate.
- K is the Strickler roughness coefficient.
- R_h is the hydraulic radius.
- S_0 is the channel slope.

For a horizontal pipe ($S_0 = 0$), the uniform depth becomes infinite:

$$h_u = \infty \tag{I.2}$$

This result indicates that, theoretically, a zero-slope channel would need to be infinitely deep to maintain uniform flow, which is a mathematical consequence of the equation rather than a physically realizable state.

Critical depth

The critical depth occurs when the Froude number equals unity ($Fr = 1$):

$$Fr = \frac{u}{c} = \sqrt{\frac{Q^2 \cdot T}{g \cdot A^3}} = 1 \tag{I.3}$$

Where:

- Q is the flow rate.
- T is the top width of the water surface.
- g is the gravitational acceleration.
- A is the flow cross-sectional area.

Physically, critical flow represents a condition where the flow velocity exactly equals the wave celerity. At this state, disturbances cannot propagate upstream, creating a hydraulic control section. This is a crucial concept for understanding flow transitions and hydraulic structures.

For circular pipes, the geometry complicates the determination of critical depth. Using relations between geometric parameters:

$$\theta = 2 \cdot \arccos\left(\frac{R-h}{R}\right) \text{ if } h < R \tag{I.4}$$

$$T = 2 \cdot R \cdot \sin\left(\frac{\theta}{2}\right) \tag{I.5}$$

$$A = \frac{R^2}{2} \cdot (\theta - \sin\theta) \tag{I.6}$$

For our experimental setup with $D = 0.1$ m, the critical depths for different flow rates are:

- For $Q = 0.5 \cdot 10^{-3}$ m^3/s: $h_{cr} = 0.011$ m.
- For $Q = 1.35 \cdot 10^{-3}$ m^3/s: $h_{cr} = 0.018$ m.
- For $Q = 1.87 \cdot 10^{-3}$ m^3/s: $h_{cr} = 0.021$ m.
- For $Q = 2.5 \cdot 10^{-3}$ m^3/s: $h_{cr} = 0.025$ m.

I.2 Gradually varied flow equation

The water surface profile in a channel or partially filled pipe follows the gradually varied flow equation:

$$\frac{dh}{dx} = \frac{S_0 - S_f}{1 - Fr^2} \tag{I.7}$$

Where:

- h is the water depth.
- x is the longitudinal distance.
- S_0 is the channel slope.

- S_f is the friction slope.
- Fr is the Froude number.

This equation is derived from the principles of energy conservation along the flow path. The numerator $(S_0 - S_f)$ represents the balance between gravitational forces (slope) and frictional resistance. The denominator $(1 - Fr^2)$ accounts for the influence of the flow regime on the water surface profile.

The friction slope S_f is derived from Manning's equation:

$$S_f = \frac{1}{K^2} \cdot \frac{Q^2}{A^2} \cdot \left(\frac{A}{P}\right)^{-4/3} \tag{I.8}$$

I.3 Flow regime classification

Based on the Froude number, flow regimes are classified as:

- Subcritical Flow ($Fr < 1$): Slow flow controlled from downstream.
- Supercritical Flow ($Fr > 1$): Rapid flow controlled from upstream.
- Mixed Flow: Contains both subcritical and supercritical regions with a hydraulic jump.

The sign of the denominator $(1 - Fr^2)$ in the gradually varied flow equation changes between subcritical and supercritical flow, resulting in fundamentally different behavior of the water surface profile.

I.4 Hydraulic jump treatment

When a hydraulic jump occurs, the relationship between upstream and downstream depths follows:

$$\frac{h_2}{h_1} = \frac{1}{2}\left(-1 + \sqrt{1 + 8 \cdot Fr_1^2}\right) \tag{I.9}$$

where h_1 is the upstream supercritical depth, h_2 is the downstream subcritical depth, and Fr_1 is the upstream Froude number.

The hydraulic jump serves as a natural mechanism for energy dissipation. The high-velocity supercritical flow approaching the jump possesses considerable kinetic energy, which transforms into potential energy and heat through intense turbulence during the transition. This process is accompanied by significant air entrainment, surface rollers, and chaotic mixing patterns.

II Steady-state test cases

To validate the numerical model, a series of steady-state test cases were performed comparing numerical results with analytical solutions. These tests cover various flow conditions and pipe geometries to verify the model's ability to correctly simulate different hydraulic phenomena.

While tests were conducted for both rectangular and circular pipes, we focus here on the circular pipe results, as they are more relevant to our study of underground galleries. Results for rectangular pipes can be found in Appendix C.

II.1 Circular pipes

The treatment of circular pipes introduces additional complexity due to the non-linear relationship between water depth and hydraulic parameters like wetted area, wetted perimeter, and top width. These geometric relationships were carefully implemented in the code and tested through a similar series of steady-state cases.

Still lake case

Parameters: Length: 10 m, Radius: 0.4 m, $\Delta x = 0.1$ m, Slope: 0%, CFL = 0.15, $K = 100\ \mathrm{m}^{1/3}/\mathrm{s}$.
Boundary conditions: $Q_{\text{upstream}} = 0\ \mathrm{m}^3/\mathrm{s}$, $Q_{\text{downstream}} = 0\ \mathrm{m}^3/\mathrm{s}$.
Initial conditions: $Q_{\text{initial}} = 0\ \mathrm{m}^3/\mathrm{s}$, $h_{\text{initial}} = 0.7$ m.

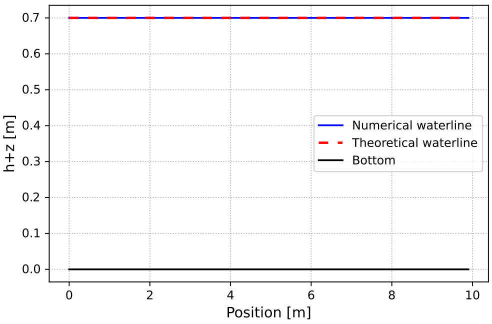

Figure 5.1: Profiles of water surface elevation along the pipe: case of a still lake in a circular pipe

As with the rectangular case, the theoretical solution is a horizontal water line with zero discharge. The numerical model reproduces this behavior with excellent precision. The discharge is conserved to within $10^{-6}\ \mathrm{m}^3/\mathrm{s}$ throughout the pipe. The notable difference compared to the rectangular case lies in the calculation of the wetted area and wetted perimeter, which are more complex for a circular section. Nevertheless, the model correctly handles these geometric calculations, as evidenced by the perfect agreement (0.00% error).

Downstream subcritical flow

Parameters: Length: 10 m, Radius: 0.15 m, Δx = 0.1 m, Slope: 0%, CFL = 0.15, $K = 100$ $\mathrm{m}^{1/3}/\mathrm{s}$.
Boundary conditions: $Q_{\text{upstream}} = 0.025\ \mathrm{m}^3/\mathrm{s}$, $h_{\text{downstream}} = 0.2$ m.
Initial conditions: $Q_{\text{initial}} = 0.025\ \mathrm{m}^3/\mathrm{s}$, $h_{\text{initial}} = 0.2$ m.

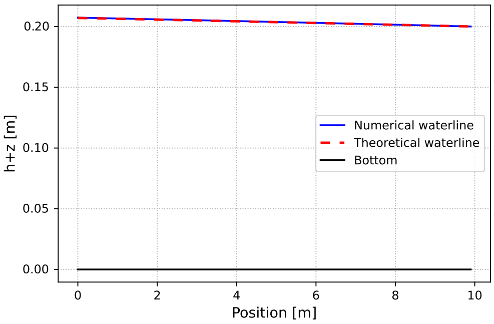

Figure 5.2: Profiles of water surface elevation along the pipe: case of a downstream subcritical flow in a circular pipe

For this circular pipe case with downstream subcritical flow, the numerical results show a water surface with a slight downward slope, driven by friction effects. The numerical simulation demonstrates excellent agreement with the theoretical water surface profile, with average relative error of just 0.08%. The discharge is consistently maintained at 0.025 m^3/s throughout the pipe with a variation of less than 10^{-6}.

This case demonstrates the model's ability to handle flow in circular sections, which involves more complex geometric calculations for the wetted perimeter and hydraulic radius. The gradual increase in water depth moving upstream is consistent with the expected backwater curve for subcritical flow with downstream control.

Downstream supercritical flow

Parameters: Length: 10 m, Radius: 0.2 m, $\Delta x = 0.1$ m, Slope: 1%, CFL = 0.15, $K = 100\ \mathrm{m}^{1/3}/\mathrm{s}$.
Boundary conditions: $Q_{\text{upstream}} = 0.1\ \mathrm{m}^3/\mathrm{s}$, $h_{\text{upstream}} = 0.2$ m.
Initial conditions: $Q_{\text{initial}} = 0.1\ \mathrm{m}^3/\mathrm{s}$, $h_{\text{initial}} = 0.2$ m.

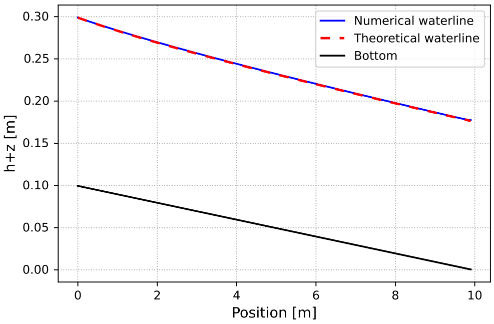

Figure 5.3: Profiles of water surface elevation along the pipe: case of a downstream supercritical flow in a circular pipe

In supercritical flow conditions (Froude number > 1), upstream boundary conditions govern the entire profile since disturbances cannot propagate upstream. As in the rectangular case, the influence of friction leads to a progressive decrease in energy and hence a slightly non-horizontal water surface.

The main distinction here lies in the circular geometry, which introduces nonlinearities in the hydraulic radius and wetted perimeter.

Despite these geometric complexities, the model accurately captures the flow behavior. The discharge remains constant at 0.1 m^3/s with a relative variation below 10^{-6}, illustrating the robustness of mass conservation. The simulated water surface aligns very well with the theoretical profile.

Additional circular pipe configurations

Tests for upstream subcritical flow and upstream supercritical flow in circular pipes showed similar excellent agreement with theoretical solutions. The average relative errors were consistently below 0.25%, demonstrating the model's high accuracy for circular geometries.

Flow Regime	**Max. Rel. Error**	**Avg. Rel. Error**	**Max. Abs. Error**	**Avg. Abs. Error**
Still Lake	0.00%	0.00%	0.000000 m	0.000000 m
Subcritical (downstream)	0.13%	0.08%	0.000271 m	0.000160 m
Subcritical (upstream)	0.13%	0.08%	0.000271 m	0.000161 m
Supercritical (downstream)	0.56%	0.23%	0.000985 m	0.000413 m
Supercritical (upstream)	0.56%	0.22%	0.000984 m	0.000412 m

Table 5.1: Error analysis for different flow regimes in circular pipes

Interestingly, the circular pipe cases showed even lower average errors than the rectangular cases. This is possibly due to the smoother transitions in geometric parameters with changing water depth in circular sections and to the fact that the conditions imposed to the flow are not exactly the same.

II.2 Hydraulic jump case

A test case involving a hydraulic jump was conducted to evaluate the model's ability to handle flow regime transitions:

Parameters: Length: 10 m, Width: 0.2 m, $\Delta x = 0.1$ m, Slope: 1%, CFL = 0.15, $K = 100\ \mathrm{m}^{1/3}/\mathrm{s}$.
Boundary conditions: $Q_{\text{upstream}} = 0.1\ \mathrm{m}^3/\mathrm{s}$, $h_{\text{upstream}} = 0.1$ m, $h_{\text{downstream}} = 0.6$ m.
Initial conditions: $Q_{\text{initial}} = 0.1\ \mathrm{m}^3/\mathrm{s}$, $h_{\text{initial}} = 0.5$ m.

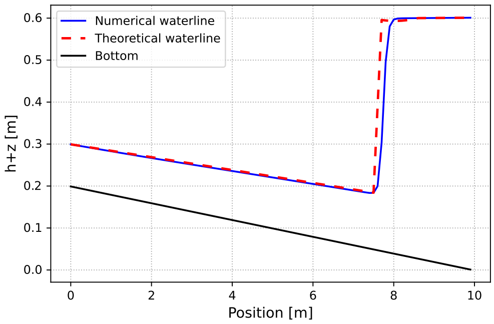

Figure 5.4: Evolution of water surface elevation along the pipe, illustrating a hydraulic jump in a rectangular conduit

This configuration creates a supercritical flow upstream that transitions to subcritical flow downstream through a hydraulic jump. The hydraulic jump represents an abrupt transition between these flow regimes, with strong local gradients. During this transition, a significant amount of kinetic energy is converted to potential energy and dissipated through turbulence.

The hydraulic jump found by the waterline calculation is located at position $x = 7.6$ m. The position and amplitude of the hydraulic jump were correctly reproduced by the model, with a well-defined transition between the two flow regimes. The model demonstrated its ability to handle discontinuities without generating excessive numerical oscillations, thanks to the appropriate use of the numerical scheme. The discharge is maintained at 0.1 m^3/s with a precision of 10^{-6} throughout the pipe.

While the maximum relative error appears high (55.48%), this is due to the theoretical waterline being drawn vertically at the jump location, whereas the numerical solution exhibits a smoother transition. This smoother profile is a consequence of the discretization method (finite volume), and not of the mesh size, since the same mesh resolution (0.1 m) is used for both the simulation and the theoretical waterline calculation. The average relative error of 2.60% provides a better measure of the overall accuracy of the solution.

This test case is particularly important as it demonstrates the model's ability to handle mixed flow regimes and abrupt transitions, which are likely to occur during the transient filling and emptying phases of underground pumped storage systems.

III Dam break unsteady flow

The dam break problem represents a fundamental test case for validating numerical models in unsteady, rapidly varying flow conditions. This section presents the results of the numerical model for an instantaneous dam break scenario and compares them with the analytical solution derived by Ritter [Erpicum, 2003].

III.1 Problem description

Parameters: Length: 50 000 m, Width: 1000 m, Slope: 0%, CFL = 0.1.
Boundary conditions: $Q_{\text{upstream}} = 0\ \text{m}^3/\text{s}$, $Q_{\text{downstream}} = 0\ \text{m}^3/\text{s}$.
Initial conditions: $Q_{\text{initial}} = 0\ \text{m}^3/\text{s}$ everywhere, upstream water depth (left of dam): 250 m, downstream water depth (right of dam): 0 m.
Dam location: $x =$ 25 000 m.

The dam is assumed to break instantaneously at $t = 0$ s, releasing water into the initially dry downstream channel. This highly transient scenario tests the model's ability to handle rapidly varying flows with steep gradients and wave propagation.

III.2 Ritter's analytical solution

Ritter (1892) derived an analytical solution for the idealized dam break problem under the following assumptions:

1. Horizontal, frictionless channel.
2. Rectangular cross-section with constant width.

3. Initially still water.
4. Instantaneous and complete removal of the dam.
5. Neglecting convective acceleration terms.
6. Dry bed downstream of the dam.

Under these assumptions, the water surface profile after the dam break is given by:

$$h(x,t) = \begin{cases} h_0 & \text{if } x \leq x_{dam} - c_0 t \\ \frac{1}{9g}\left(2c_0 - \frac{x - x_{dam}}{t}\right)^2 & \text{if } x_{dam} - c_0 t < x < x_{dam} + 2c_0 t \\ 0 & \text{if } x \geq x_{dam} + 2c_0 t \end{cases} \tag{III.1}$$

Where:

- h_0 is the initial upstream water depth.
- $c_0 = \sqrt{gh_0}$ is the wave celerity corresponding to the initial water depth.
- x_{dam} is the position of the dam.
- g is the gravitational acceleration.

The water velocity in the rarefaction wave region is:

$$u(x,t) = \frac{2}{3}\left(c_0 + \frac{x - x_{dam}}{t}\right) \tag{III.2}$$

This analytical solution identifies three distinct regions:

1. An undisturbed region upstream of the rarefaction wave where the depth remains constant at h_0.
2. A rarefaction wave region where the depth decreases smoothly according to a parabolic profile.
3. A dry bed region where the depth is zero.

The Ritter solution describes a rarefaction wave propagating upstream at speed c_0 and a wave front advancing downstream at speed $2c_0$. At the dam location ($x = x_{dam}$), the water depth is exactly $\frac{4}{9}h_0$.

III.3 Numerical results and analysis

The simulation was run for a total duration of 240 seconds, with results saved at t = 10, 40, 70, 100, 130, 160, 190, 220 and 240 seconds. To assess the influence of numerical parameters, four different configurations were tested: constant and linear reconstruction, each with spatial steps of $\Delta x = 10$ m and $\Delta x = 100$ m. This section presents the results obtained with the finer spatial discretization ($\Delta x = 10$ m), while those corresponding to the coarser grid ($\Delta x = 100$ m) are provided in Appendix D.

Constant reconstruction with $\Delta x = 10$ m

Figures 5.5 and 5.6 show the water height and discharge profiles at different times using constant reconstruction and $\Delta x = 10$ m:

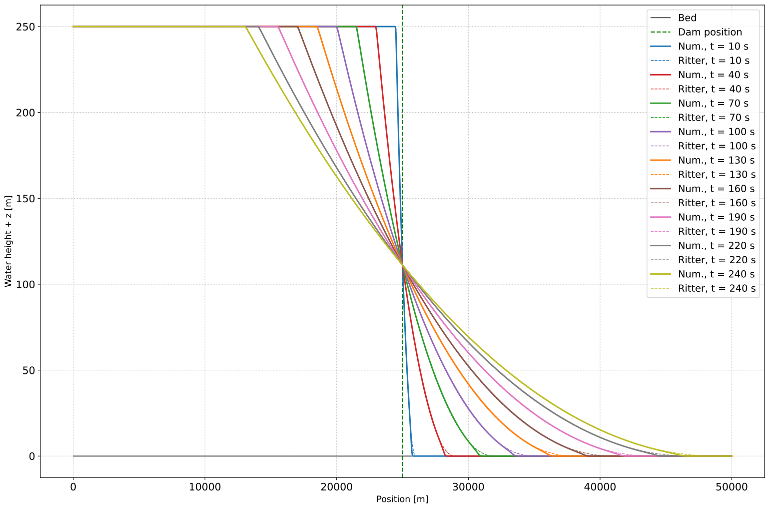

Figure 5.5: Comparison between the numerical solution and Ritter's analytical solution for water height at different times, using constant reconstruction and $\Delta x = 10$ m

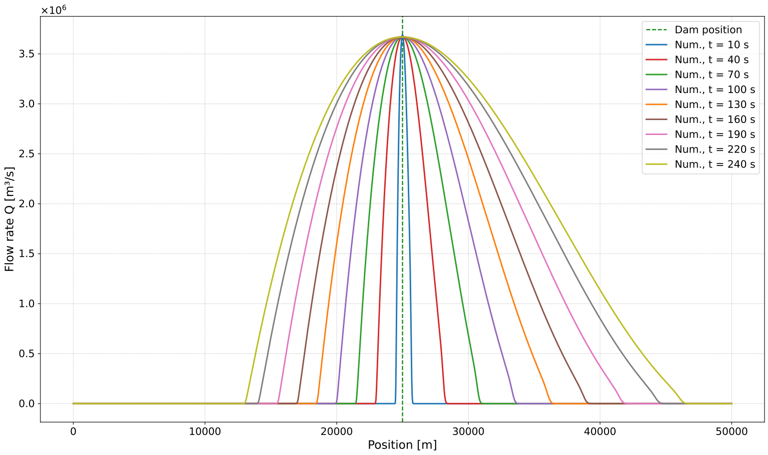

Figure 5.6: Comparison between the numerical solution and Ritter's analytical solution for discharge at different times, using constant reconstruction and $\Delta x = 10$ m

With the finer spatial resolution of $\Delta x = 10$ m, the numerical model produces significantly improved results compared to the coarser grid (see Appendix D). The transitions between the three flow regions (namely the undisturbed upstream, the rarefaction wave and the wavefront) are captured with greater precision. The rarefaction wave profile more closely follows the analytical parabolic shape, showing good agreement in the intermediate region. Additionally, the wavefront is represented more sharply, with reduced numerical diffusion and a clearer discontinuity. The water depth at the dam location ($x = 25000$ m) consistently maintains the theoretically expected value of $\frac{4}{9}h_0 \approx 111.1$ m throughout the simulation. The discharge is maintained with a variation of less than 10^{-6} m^3/s across all regions.

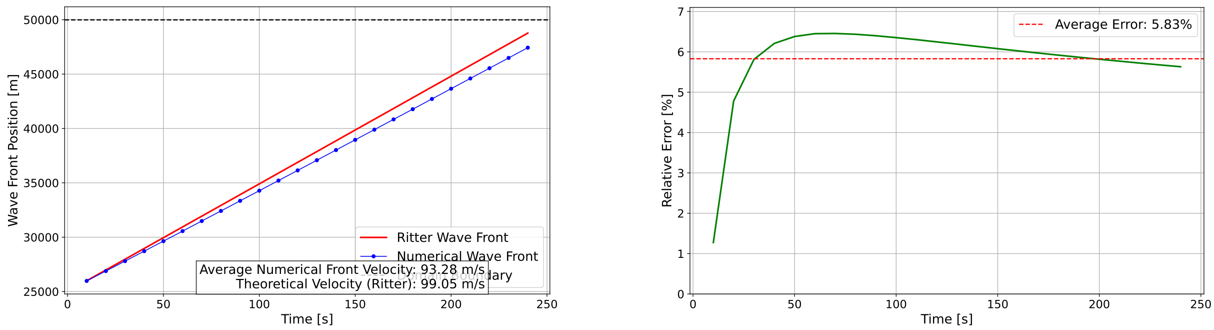

Figure 5.7: Comparison between the position of the wavefront calculated numerically and with Ritter's method, along with the error in this position with constant reconstruction and $\Delta x = 10$ m

The wavefront tracking analysis in Figure 5.7 shows that the average numerical front velocity is 93.28 m/s, which is 5.83% slower than the theoretical velocity of 99.05 m/s predicted by Ritter's solution. This difference, while still present, represents a significant improvement over the coarser grid results. The error generally increases with time as the accumulated effect of numerical diffusion slows the wavefront propagation.

The constant reconstruction maintains monotonic profiles but introduces noticeable numerical diffusion, particularly near discontinuities. This is evident in the slightly rounded wavefront and the gradual rather than sharp transition at the leading edge of the rarefaction wave. Nevertheless, the overall wave structure and propagation characteristics are well captured.

Linear reconstruction with $\Delta x = 10$ m

The combination of finer spatial resolution ($\Delta x = 10$ m) and higher-order reconstruction (linear) provides the most accurate results, as shown in Figures 5.8 and 5.9:

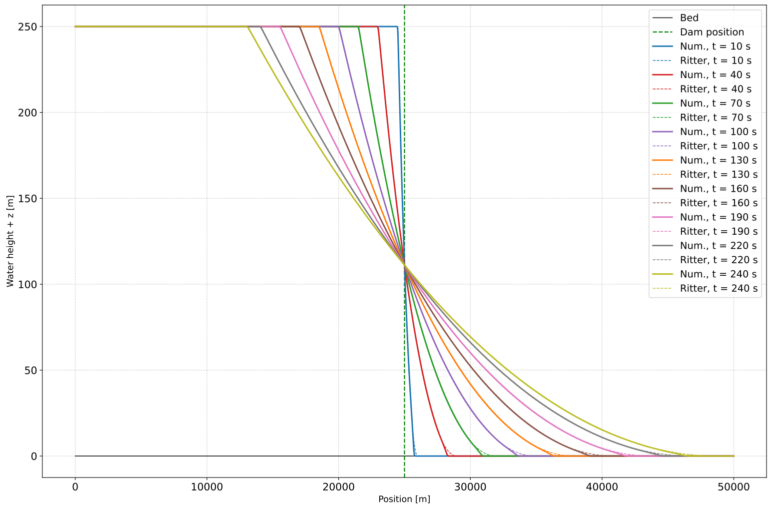

Figure 5.8: Comparison between the numerical solution and Ritter's analytical solution for water height at different times, using linear reconstruction and $\Delta x = 10$ m

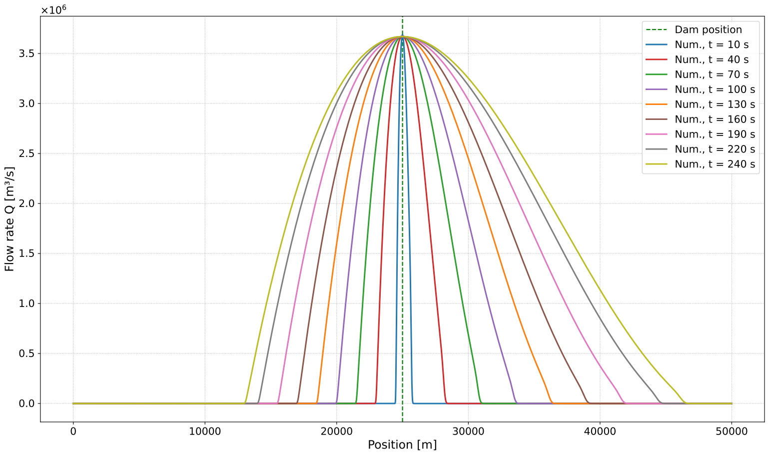

Figure 5.9: Comparison between the numerical solution and Ritter's analytical solution for discharge at different times, using linear reconstruction and $\Delta x = 10$ m

This configuration provides the most accurate representation of the rarefaction wave profile, with excellent agreement to the analytical parabolic shape. It also offers the sharpest resolution of the wavefront, minimizing the smoothing of the discontinuity. Among all tested setups, it shows the closest match with the analytical solution across all three flow regions. The model tracks the wavefront position with high precision and maintains a nearly perfect representation of the water depth at the dam location, corresponding to the theoretical value of $\frac{4}{9}h_0$.

The linear reconstruction significantly reduces numerical diffusion compared to the constant reconstruction case, resulting in sharper representation of steep gradients. This effect is particularly evident at the boundaries between flow regions, where transitions are captured more crisply. The finer spatial resolution ensures that these improvements translate to overall better accuracy rather than introducing numerical oscillations.

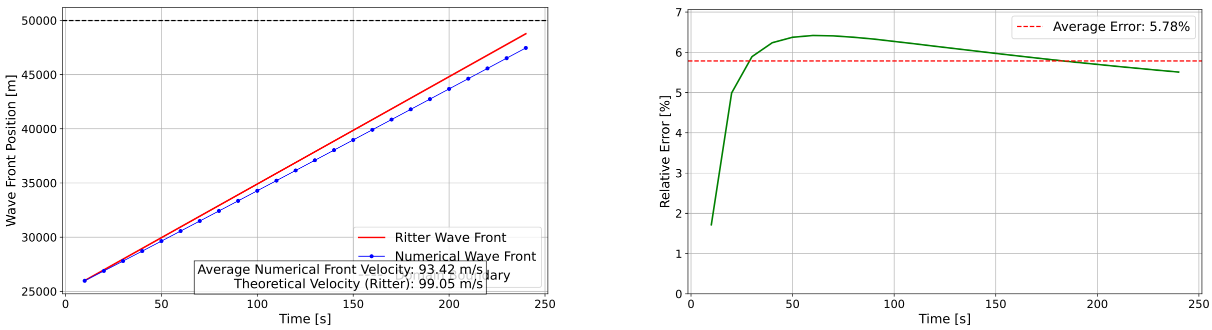

Figure 5.10: Comparison between the position of the wavefront calculated numerically and with Ritter's method, along with the error in this position with linear reconstruction and $\Delta x = 10$ m

Figure 5.10 confirms the superior performance of this configuration. The average error in wavefront position is further reduced to 5.78%, with an average numerical front velocity of 93.42 m/s. The combination of finer spatial resolution and higher-order reconstruction provides the best performance for capturing the complex wave dynamics of the dam break problem.

Comparative analysis of numerical schemes

To better understand the influence of numerical parameters, Table 5.2 compares key metrics across all four tested configurations:

Configuration	Average Front Velocity	Theoretical Velocity	Average Error
Constant, $\Delta x = 100$ m	91.33 m/s	99.05 m/s	7.07%
Linear, $\Delta x = 100$ m	91.32 m/s	99.05 m/s	7.06%
Constant, $\Delta x = 10$ m	93.28 m/s	99.05 m/s	5.83%
Linear, $\Delta x = 10$ m	93.42 m/s	99.05 m/s	5.78%

Table 5.2: Summary of wavefront propagation characteristics for different numerical schemes

Several key observations emerge from this comparative analysis:

- **Impact of spatial resolution**: Reducing the grid size from $\Delta x = 100$ m to $\Delta x = 10$ m yields a significant improvement in accuracy, reducing the wavefront position error by approximately 1.3 %. This confirms the importance of adequate spatial resolution for capturing sharp gradients and wave propagation phenomena.
- **Effect of reconstruction order**: For the same spatial resolution, linear reconstruction offers a slight improvement over constant reconstruction. The benefit is more pronounced for the finer grid ($\Delta x = 10$ m), where the higher-order method can better leverage the additional spatial information without introducing oscillations.
- **Diminishing returns**: The difference between constant and linear reconstruction is relatively small compared to the effect of refining the spatial grid. This suggests that for practical applications, ensuring adequate spatial resolution should be prioritized over increasing the order of the reconstruction scheme.
- **Numerical diffusion**: All configurations underestimate the wavefront velocity to some degree, which is a characteristic effect of numerical diffusion. This phenomenon artificially smears sharp discontinuities, effectively slowing the propagation of shock fronts. The effect is reduced, but not eliminated, with finer grids and higher-order schemes.

Physical interpretation of results

The dam break test case provides valuable insights into the model's ability to handle complex transient phenomena that are relevant to the simulation of underground pumped storage systems:

1. **Initial wave formation**: In the early stages (t = 10s), the numerical model captures the characteristic shape of the dam break wave with remarkable accuracy. The water depth at the dam location (x = 25,000 m) closely approximates the theoretical value of $\frac{4}{9} \cdot 250$ m $\approx$ 111.1 m prescribed by Ritter's solution, confirming the model's ability to accurately represent the initial dynamics of the dam break.
2. **Progressive wave propagation**: As time advances, two distinct wave phenomena are clearly visible: a rarefaction wave propagates upstream at a speed of $c_0 = \sqrt{gh_0}$ and a bore front advances downstream at about twice that speed ($2c_0$). The numerical model maintains excellent agreement with the analytical solution throughout the simulation period, accurately tracking both phenomena.

3. **Preservation of key features**: The numerical model consistently preserves the key theoretical features of the dam break wave, including:
    - The constant water depth in the undisturbed upstream region.
    - The parabolic profile in the rarefaction wave zone.
    - The sharp front propagating at a speed approaching the theoretical value of $2c_0$.
    - The characteristic depth of $\frac{4}{9}h_0$ at the original dam location.
4. **Reservoir drawdown**: The simulations clearly show the progressive drainage of the upstream reservoir, with water depths gradually decreasing over time at locations between the upstream wave and the dam site. The rate of drawdown aligns well with theoretical expectations, reflecting proper mass conservation in the numerical model.
5. **Energy transfer**: The dam break phenomenon involves a complex transfer of potential energy (initially stored in the elevated water column) to kinetic energy (in the form of the advancing wave and associated flow velocities). The numerical model correctly captures this energy transformation process, as evidenced by the discharge profiles that show maximum values near the wavefront.

These observations confirm that the numerical model can accurately simulate rapid transients, wave propagation, and energy transfer processes. These are essential capabilities for modeling the hydraulic behavior of underground gallery networks during filling and emptying operations, where similar wave phenomena will occur at a smaller scale.

III.4 Conclusion

The steady-state and unsteady tests conducted demonstrate that the developed numerical model is capable of accurately reproducing various flow conditions in pipes of different geometries. The main validated results are:

1. Mass conservation (constant discharge to within 10^{-6} m^3/s).
2. Correct prediction of water depths in steady-state conditions.
3. Appropriate handling of different section geometries (rectangular and circular).
4. Ability to correctly model transitions between flow regimes (hydraulic jump).
5. Accurate representation of rapidly varying unsteady flows, as demonstrated by the dam break test case and its excellent agreement with Ritter's analytical solution.

The dam break validation case, in particular, provides strong evidence of the model's ability to handle highly transient flows with steep gradients and wave propagation phenomena. The close agreement between numerical results and theoretical predictions across multiple time steps confirms the accuracy of both the spatial discretization method and temporal integration scheme.

These results confirm the reliability of the model for both steady-state and unsteady simulations and provide a solid foundation for the analysis of more complex flows in transient conditions, including the simulation of flow in interconnected gallery networks that is the primary focus of this thesis.

CHAPTER 6

NUMERICAL MODEL OF INTERCONNECTED GALLERIES

I Network configuration and flow conventions

The hydraulic network model consists of interconnected pipes with various junction types. This section presents the configuration of the network, identification of components and flow direction conventions adopted in the numerical model.

I.1 Pipe identification

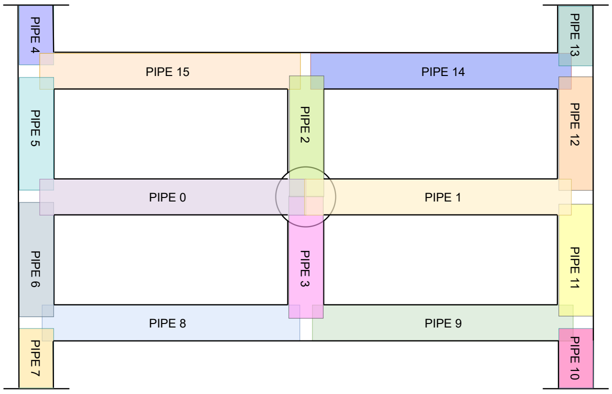

Figure 6.1: Identification of pipes in the numerical model. The network consists of 16 circular pipes arranged in a rectangular configuration

Figure 6.1 shows the numbering scheme used for the 16 pipes in the network model. The pipes are arranged in a rectangular configuration, connecting at various T-junctions and the central tank of the injection point. This configuration replicates the physical layout of Sara Ceresetti's laboratory model at a scale of 1:100 relative to the proposed full-scale underground pumped storage facility.

I.2 Junction types

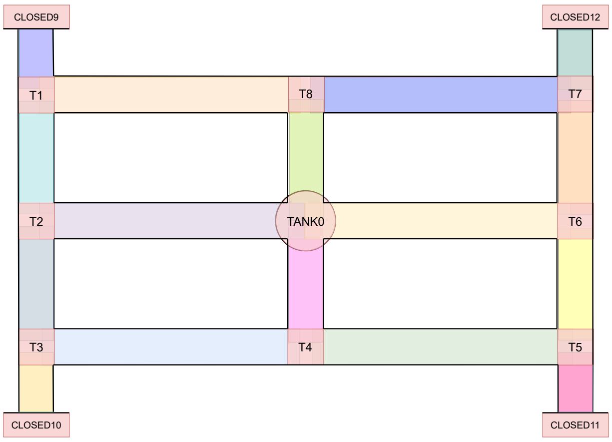

Figure 6.2: Junction types in the numerical model. T-junctions (T1-T8) connect three pipes, closed sections (CLOSED9-CLOSED12) closing a pipe, and the central tank (TANK0) connects four pipes

The network contains different types of junctions connecting the pipes, as shown in Figure 6.2:

- T-junctions (T1, T2, T3, T4, T5, T6, T7, T8): Connecting three pipes.
- Closed sections (CLOSED9, CLOSED10, CLOSED11, CLOSED12): Closing a pipe.
- Tank (TANK0): Central reservoir connecting to pipes 0, 1, 2, and 3.

Each junction type requires special treatment in the numerical model to ensure conservation of mass and continuity of water surface elevation across connected pipes.

I.3 Flow direction convention

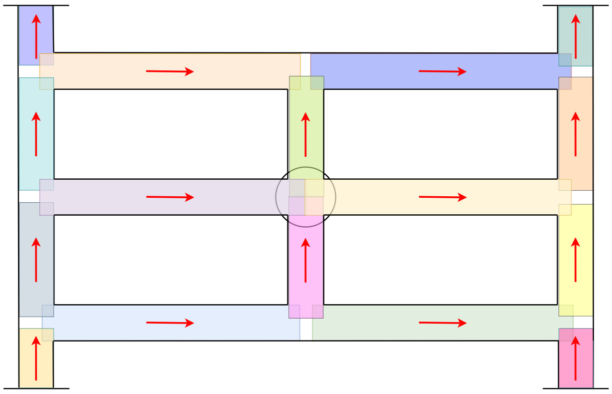

Figure 6.3: Flow direction convention in the numerical model. Red arrows indicate the positive flow direction for each pipe

The flow direction convention is critical for the proper implementation of boundary conditions and junction treatments in the numerical model. As illustrated in Figure 6.3, positive flow is defined as:

- Horizontal pipes: Flow from left to right is positive.
- Vertical pipes: Flow from bottom to top is positive.

This convention determines the sign of the flow rate in the mathematical model, affecting mass conservation at junctions and the interpretation of boundary conditions.

It has important implications for the interactions between pipes and junction points:

- When the tank of an injection point is positioned to the right or below a pipe, the flow from the reservoir into the pipe will have a negative sign, indicating that water is moving against the positive direction convention.
- Conversely, when the tank of an injection point is positioned to the left or above a pipe, the flow from the reservoir into the pipe will have a positive sign, as water moves in alignment with our defined positive direction.

This convention is consistently applied throughout the model for all types of junctions, including injection points, T-junctions and bends. It allows for a coherent representation of flow directions across the entire network of interconnected galleries.

II Implementation of the injection point

The injection point represents a critical boundary condition in the hydraulic model, serving as the water source within the pipe network system. Implementing this feature required careful consideration of both physical realism and numerical stability.

II.1 Flow rate integration

First, it was necessary to incorporate the pump flow rates measured in Sara Ceresetti's laboratory experiments into the numerical code to enable proper comparison with experimental results. Using a constant flow rate throughout the simulation would have been inappropriate, as shown for $Q_{mean} = 1.87$ L/s on Figure 6.4.

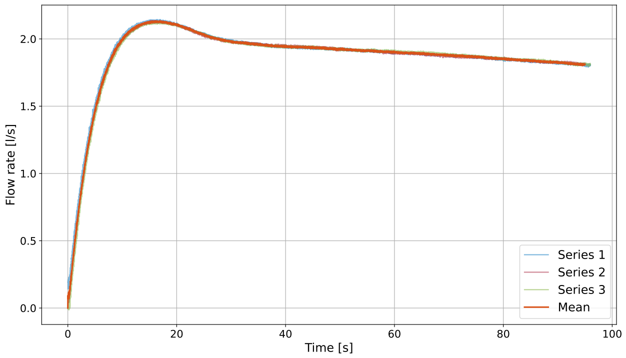

Figure 6.4: Evolution of the experimental flow rate over time for $Q_{mean} = 1.87$ L/s

II.2 Anti-vortex device consideration

A key physical element in the experimental setup was an 11cm tall anti-vortex device placed at the bottom of the injection point reservoir. This device affects the water dynamics, particularly during the early filling stages. To account for this feature, I adjusted the simulation to begin when the water level in the injection point reservoir reached the top of this anti-vortex device. Based on flow rate integration, this occurs at different times depending on the flow rate.

- 0.01 seconds for $Q_{mean} = 0.55$ L/s.
- 3.92 seconds for $Q_{mean} = 1.35$ L/s.
- 1.47 seconds for $Q_{mean} = 1.87$ L/s.
- 1.93 seconds for $Q_{mean} = 2.5$ L/s.

It is important to note that since sensor 7 is located at the center of the injection point, it does not always reflect the actual water level. When the water level is below the height of the anti-vortex device, the sensor still detects the top of the device rather than the true water surface. This explains the initial constant plateau observed in the experimental measurements at the beginning of the filling process. This phenomenon must be considered when comparing numerical results with experimental data.

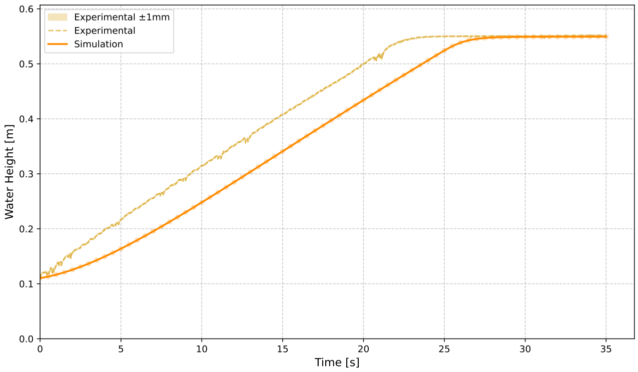

Figure 6.5: Comparison between experimental and numerical water height at sensor 7 with $Q_{mean} = 1.87$ L/s, with the simulation starting when the water reaches the top of the anti-vortex device

Figure 6.5 shows improved agreement after accounting for the anti-vortex device, but discrepancies still remain in the rate of water level rise and timing of features. This suggested that additional physical phenomena needed to be considered to fully reconcile the numerical model with experimental observations.

II.3 Water height relationship analysis

Despite these adjustments, an interesting phenomenon was discovered: the relationship between the water height measured at sensor 7 and the water height calculated through flow rate integration was not the identity function that had been expected.

Using the trapezoidal method, the water height can be estimated by integrating the flow rate over time as follows:

Given a time series of flow rates Q_0, Q_1, ..., Q_n sampled every Δt seconds, the total volume up to time t_n is computed as:

$$V_n = \sum_{i=0}^{n-1} \frac{Q_i + Q_{i+1}}{2} \cdot \Delta t \tag{II.1}$$

The corresponding water height is then given by:

$$h_n = \frac{V_n}{A} = \frac{V_n}{\Delta x_{\text{tank}} \cdot \text{Width}_{\text{tank}}} \tag{II.2}$$

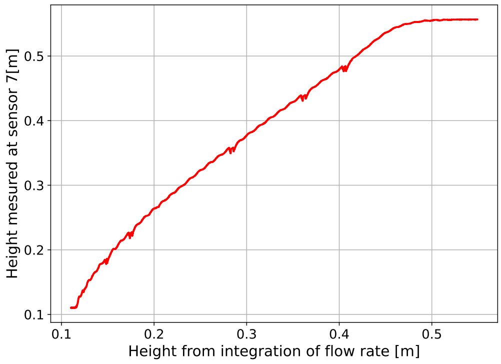

Figure 6.6: Non-linear relationship between the height measured at sensor 7 and the height obtained by integrating the flow rate with $Q_{mean} = 1.87$ L/s

The comparative analysis between directly measured water height (sensor 7) and theoretically calculated height (from flow rate integration) reveals significant insights into the hydraulic behavior of the system. As illustrated in Figure 6.6, a clear discrepancy exists between these two measurements, particularly during the transient phase of the flow.

The observed deviation indicates that the water height directly measured by sensor 7 consistently exceeds the theoretical height calculated through simple volumetric principles. This phenomenon can be attributed to several dynamic hydraulic effects that are not captured by basic volume integration calculations:

- **Surface waves**: The injection of water generates surface waves that propagate through the system, causing the water level to fluctuate around the mean value predicted by volume integration.
- **Local turbulence**: The complex interaction between the inflowing water and the tank geometry creates turbulence patterns that affect the local water level distribution.
- **Sensor position**: The ultrasonic sensor measures the water level at a specific point, which may not be representative of the average level across the entire tank during dynamic filling conditions.

The relationship gradually approaches the ideal 1:1 correlation (where measured height would equal calculated height) as the system progresses toward steady state, suggesting that these dynamic effects diminish as the flow stabilizes.

II.4 Time shift adjustment

To address these issues, a time shift was applied to the experimental data. This effectively started the simulation when the water surface in the reservoir was just slightly below the water surface level in the adjacent pipes. This adjustment helped synchronize the simulated and experimental results more effectively.

The time shift values, determined through iterative testing to achieve best agreement with experimental data, were:

- 66.22 seconds for $Q_{mean} = 0.55$ L/s.
- 27.83 seconds for $Q_{mean} = 1.35$ L/s.
- 22.00 seconds for $Q_{mean} = 1.87$ L/s.
- 17.11 seconds for $Q_{mean} = 2.5$ L/s.

Note that these time shifts are inversely proportional to the flow rate, which is physically consistent. At higher flow rates, the initial filling phase progresses more rapidly, requiring smaller time shifts to synchronize the results.

II.5 Geometric conversion for numerical implementation

One of the key challenges in implementing the injection point was reconciling the typically cylindrical geometry of real-world tanks with the requirements of the numerical scheme. To address this, a geometric transformation is employed that preserves the volume while simplifying the calculations:

1. The tank is conceptually divided into four equal sections, with each section connecting to a pipe.
2. Each quarter-tank is then converted into an equivalent rectangular cell with the same volume.
3. This rectangular representation allows for straightforward calculation of wetted area, hydraulic radius, and other parameters needed for the Saint-Venant equations.

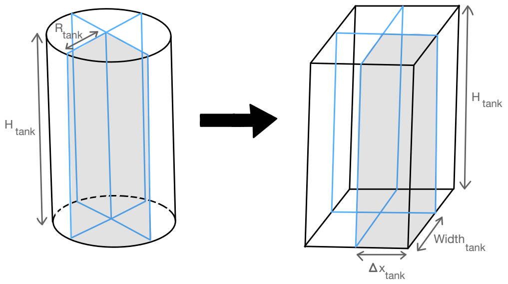

Figure 6.7: Transformation of the tank cross-section from a quarter-circle to a rectangle

The volume conversion is handled in the code through the following relationship:

$$V_{quarter\ tank} = \frac{\pi R_{tank}^2 H_{tank}}{4} = \Delta x_{tank} \cdot Width_{tank} \cdot H_{tank} \tag{II.3}$$

where Δx_{tank} is the length of the equivalent rectangular cell, $Width_{tank}$ is the width and H_{tank} is the distance between the bottom of the injection point and the bottom of the pipes.

This transformation preserves the total volume of the tank while allowing the numerical scheme to represent it using the same computational approach as the pipes. The parameter Δx_{tank} becomes a calibration parameter that can be adjusted to fine-tune the model's response, as will be discussed in the sensitivity analysis.

II.6 Water level synchronization in the tank

To maintain hydraulic consistency across the central injection tank, a synchronization mechanism was implemented to ensure uniform water levels throughout the reservoir. Since the tank is numerically divided into four quarter-sections, each connected to a different pipe, it is essential to maintain the same water elevation across all sections to represent the physical reality of a single, unified reservoir.

After each time step calculation, the volumes of all tank sections are averaged using the following procedure:

$$V_{avg} = \frac{1}{N}\sum_{i=1}^{N} V_i \tag{II.4}$$

where V_{avg} is the average volume of the tank, N is the number of connected pipes (4 in this case), and V_i is the volume of each tank section.

This averaged volume is then redistributed to all tank sections, ensuring that each quarter maintains the same water level. The corresponding wetted areas are recalculated based on this uniform volume distribution. This synchronization step is performed within the `synchronize_boundary_conditions` function after the main pipe calculations in each time step, maintaining the physical constraint of a single, coherent reservoir while preserving the numerical efficiency of the sectioned approach.

III Sensitivity analysis

Prior to implementing the full network with T-junctions, a comprehensive sensitivity analysis was conducted using only the four pipes directly connected to the central tank (PIPE0, PIPE1, PIPE2, and PIPE3). For this analysis, the pipes were extended to ten meters in length to minimize the influence of boundary conditions and to approximate flow behavior in an infinitely long pipe, with closed-end boundary conditions applied at their downstream ends. This preliminary stage was crucial for calibrating key model parameters and understanding fundamental flow dynamics before tackling the more complex complete network.

Three key parameters were investigated:

- Initial water height (h_{min}), the thin layer of water initially present in pipes.
- Strickler's friction coefficient (K), controlling energy losses in the pipe system.
- Injection point cell length (Δx_{tank}), influencing the tank-pipe interface dynamics.

For clarity, this section primarily presents results for the flow rate $Q_{\text{mean}} = 1.87 \cdot 10^{-3}$ m^3/s. Results for the other three flow rates are available in Appendix F.

III.1 Initial water height

The parameter h_{min} represents the minimal water depth initially present in all pipes at simulation start. This corresponds to the residual water typically remaining in experimental pipes between tests, as observed in the laboratory measurements.

Sensor	**Minimum (m)**	**Maximum (m)**	**Mean (m)**	**Std. Dev. (m)**
Sensor 1	0.0003	0.0056	0.0038	0.0013
Sensor 2	0.0001	0.0045	0.0028	0.0011
Sensor 3	0.0006	0.0035	0.0025	0.0009
Sensor 4	-0.0005	0.0040	0.0021	0.0011
Sensor 5	-0.0004	0.0037	0.0024	0.0010
Sensor 6	0.0002	0.0036	0.0028	0.0010
Global	-0.0005	0.0056	0.0027	0.0012

* Values calculated from the first 100 points or first 20 seconds of data

Table 6.1: Initial water heights measured across experimental sensors

The Table 6.1 presents key statistical values of the initial water height observed across all tested flow rates, providing a reference for selecting relevant testing ranges.

Five different values for $h_{\min}$ were tested: 0.001 m, 0.002 m, 0.003 m, 0.004 m, and 0.005 m.

Figure 6.8 shows the results for $Q_{mean} = 1.87 \cdot 10^{-3}$ m^3/s.

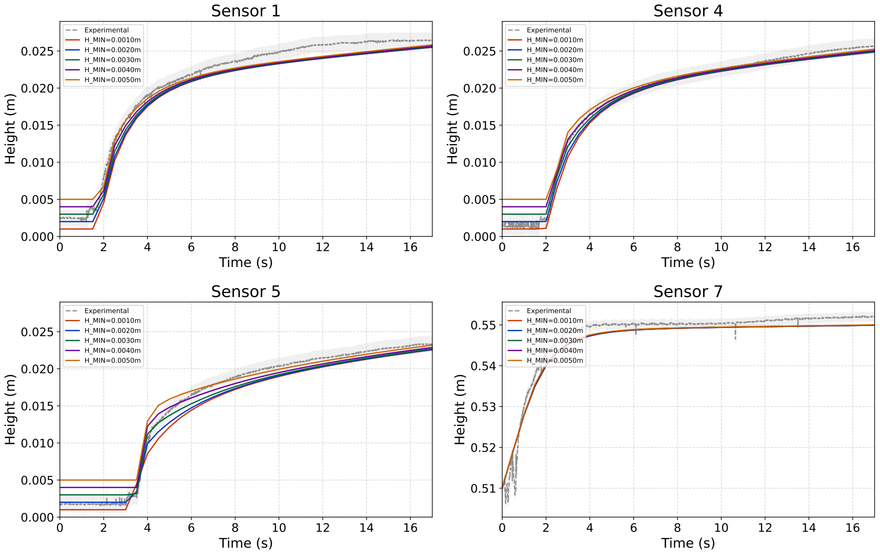

Figure 6.8: Comparison of water height evolution at different sensors for various h_{min} values ($Q_{mean} = 1.87 \cdot 10^{-3} m^3/s$, $K = 90 m^{1/3}/s$, $\Delta x_{tank} = 0.2 m$)

The analysis revealed several important observations:

- **Wave dynamics:** Smaller $h_{\min}$ values (0.001-0.002 m) tended to produce earlier wave arrivals accompanied by smoother water level rises, whereas larger values caused the waves to arrive later and led to more abrupt increases.
- **Spatial sensitivity:** The effect of $h_{\min}$ increased with distance from the reservoir. At more distant sensors, differences between various $h_{\min}$ values were more pronounced in both timing and wave amplitude.
- **Long-term convergence:** Despite differences in initial wave dynamics, all simulations eventually converged toward similar steady-state water levels, indicating that $h_{\min}$

primarily affects transient behavior rather than equilibrium conditions.

Analysis across all flow rates showed similar trends, with varying sensitivities. As the flow rate increases, the wavefront arrives earlier at all sensors, and the differences in wave timing and amplitude between h_{min} values become more pronounced, especially at sensors farther from the tank.

The optimal h_{min} values determined through comparison with experimental data were:

- For $Q_{\text{mean}} = 0.55 \cdot 10^{-3}$ m^3/s: $h_{\text{min}} = 0.002$ m.
- For $Q_{\text{mean}} = 1.35 \cdot 10^{-3}$ m^3/s: $h_{\text{min}} = 0.001$ m.
- For $Q_{\text{mean}} = 1.87 \cdot 10^{-3}$ m^3/s: $h_{\text{min}} = 0.003$ m.
- For $Q_{\text{mean}} = 2.50 \cdot 10^{-3}$ m^3/s: $h_{\text{min}} = 0.003$ m.

III.2 Friction coefficient

The Strickler coefficient K (related to Manning's coefficient $n = 1/K$) characterizes friction losses in the pipes. Five different values were tested: 70, 80, 90, 100, and 110 m$^{1/3}$/s.

Figure 6.9 shows the results for Q_{mean} = 1.87 · 10^{-3} m^3/s.

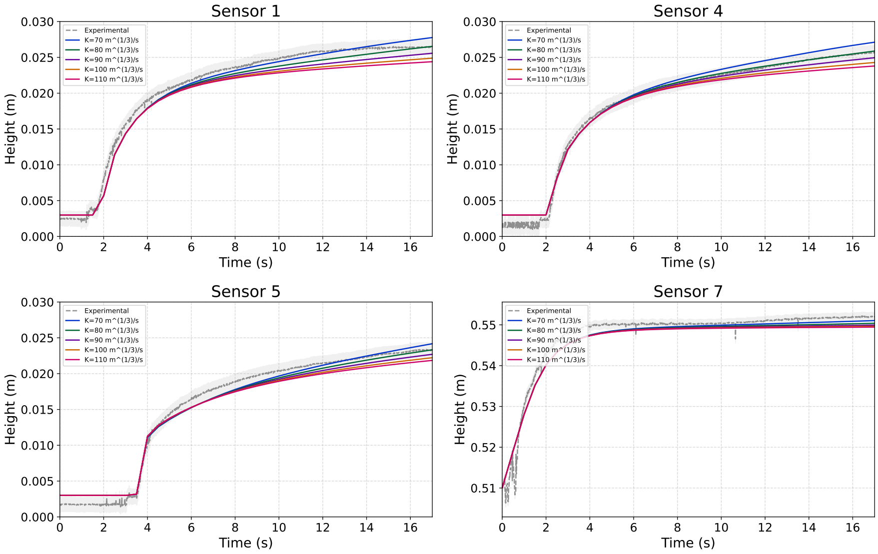

Figure 6.9: Comparison of water height evolution at different sensors for various Strickler coefficient values ($Q_{mean} = 1.87 \cdot 10^{-3} m^3/s$, $h_{min} = 0.003m$, $\Delta x_{tank} = 0.2m$)

Several notable observations emerged from the analysis:

- **Wave height and timing:** Lower K values (higher friction) resulted in slower wave propagation but higher wave peaks. For example, at sensor 4, the peak reached approximately 0.027 m with $K = 70$ m$^{1/3}$/s compared to about 0.023 m with $K = 110$ m$^{1/3}$/s at t = 17s. This behavior occurs because increased friction slows down the flow, causing water to accumulate more at the wave front, resulting in a wave with greater height but lower propagation speed.

- **Equilibrium water levels:** Higher friction consistently produced higher steady-state water depths throughout the network, due to the steeper hydraulic gradients required to convey the same flow rate against greater resistance.
- **Flow rate dependency:** The model's sensitivity to friction increased with flow rate. At the lowest flow rate ($Q_{\text{mean}} = 0.55 \cdot 10^{-3}$ m^3/s), friction effects were minimal, while at higher flow rates, the same variation in K produced much more significant differences in wave dynamics and water levels.

This progressive increase in sensitivity with flow rate aligns with hydraulic theory, as friction forces scale approximately with velocity squared. Despite these variations, a value of $K = 90$ m$^{1/3}$/s was chosen as a compromise, since $K = 70$ m$^{1/3}$/s provided the best fit for flow rates below or equal to 1.87 L/s, while $K = 100$ m$^{1/3}$/s was optimal for $Q = 2.5$ L/s. This value of K provides the best overall agreement with experimental data across all flow rates and represents a physically realistic value for smooth PVC pipes.

III.3 Injection point cell length

The parameter Δx_{tank} represents the length of the computational cell used to model each quarter of the central tank. Six different values were tested: 0.05 m, 0.1 m, 0.15 m, 0.2 m, 0.25 m, and 0.3 m.

Figure 6.10 shows the results for Q_{mean} = 1.87 · 10^{-3} m^3/s.

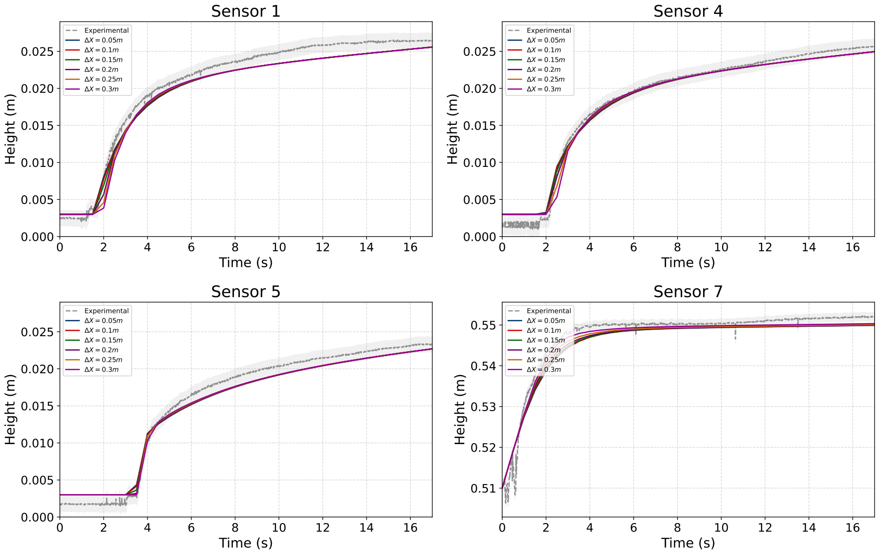

Figure 6.10: Comparison of water height evolution at different sensors for various Δx_{tank} values ($Q_{mean} = 1.87 \cdot 10^{-3} m^3/s$, $h_{min} = 0.003m$, $K = 90m^{1/3}/s$)

Analysis revealed that:

- **Hydraulic slope effects:** Δx_{tank} directly controls the free surface slope between the reservoir and the pipes through its role in the numerical discretization. In the finite volume formulation, the mass conservation equation includes the term:

$$\text{RHS}_{\text{Mass}} = -\frac{1}{\Delta x_i}(\text{Balance}_Q + \text{Source}_{\text{mass}})$$

Larger Δx_{tank} values (0.25-0.3 m) create gentler free surface slopes, which reduce the initial outflow from the reservoir to the pipes. This occurs because the numerical gradient calculation $\frac{\partial h}{\partial x} \approx \frac{\Delta h}{\Delta x}$ becomes smaller when Δx increases for the same water level difference. A gentler slope results in lower driving pressure gradients, causing reduced discharge rates from the tank into the connected pipes.

Conversely, smaller Δx_{tank} values produce steeper numerical gradients, leading to higher initial discharge rates and faster wave propagation. However, this also causes the water level in the reservoir to rise more slowly initially, as more water flows out into the pipe network.

The physical interpretation is that Δx_{tank} acts as a numerical parameter controlling the effective hydraulic resistance between the tank and pipe interface. Larger values create a more gradual transition, delaying the outflow and allowing water to accumulate higher in the reservoir before significant flow begins. As a result, the water level in the pipes tends to be higher after a few seconds when Δx_{tank} is large, but the initial wave propagation is delayed.

- **Long-term convergence:** After the initial transient phase (beyond ≈ 8 seconds), the water level curves for different values of Δx_{tank} remain very close, with only slight differences. This indicates that this parameter primarily influences the dynamics of the early waves but has a limited impact on long-term equilibrium conditions.
- **Flow rate dependency:** Similar conclusions can be drawn across all four flow rates tested. However, at higher flow rates, the difference in water height at the reservoir becomes more pronounced. For lower flow rates, the variations in water height for different Δx_{tank} values are nearly overlapping, showing little sensitivity. In contrast, at higher flow rates, the impact of Δx_{tank} is more noticeable.

The value $\Delta x_{\text{tank}} = 0.2$ m offered the best overall compromise across different flow rates. Interestingly, this value closely approximates the physical reservoir radius (0.19 m), suggesting a consistent relationship between real geometry and its numerical representation.

III.4 Parameter selection for complete network model

Based on this comprehensive sensitivity analysis, the following parameters were selected for the full network model:

- Strickler coefficient: $K = 90$ m$^{1/3}$/s (consistent across all flow rates).
- Injection point cell length: $\Delta x_{\text{tank}} = 0.2$ m (consistent across all flow rates).
- Initial water height: flow-rate dependent, as specified above.

This parameter set provided the best overall agreement with experimental data while maintaining physical consistency with the laboratory apparatus.

The results obtained for a flow rate of $Q_{\text{mean}} = 1.87$ L/s are presented below.

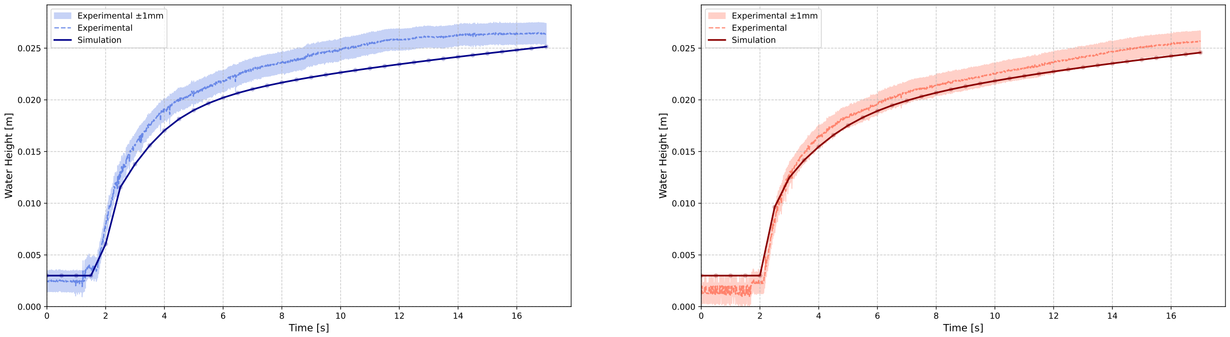

Figure 6.11: Evolution of water height over time at sensors 1 (on the left) and 4 (on the right) with a time delay of 22 seconds, $h_{min} = 0.003$ m, $\Delta x_{tank} = 0.2$m, $K = 90 m^{1/3}/s$ and a mean flow rate of $1.87 \cdot 10^{-3} m^3/s$

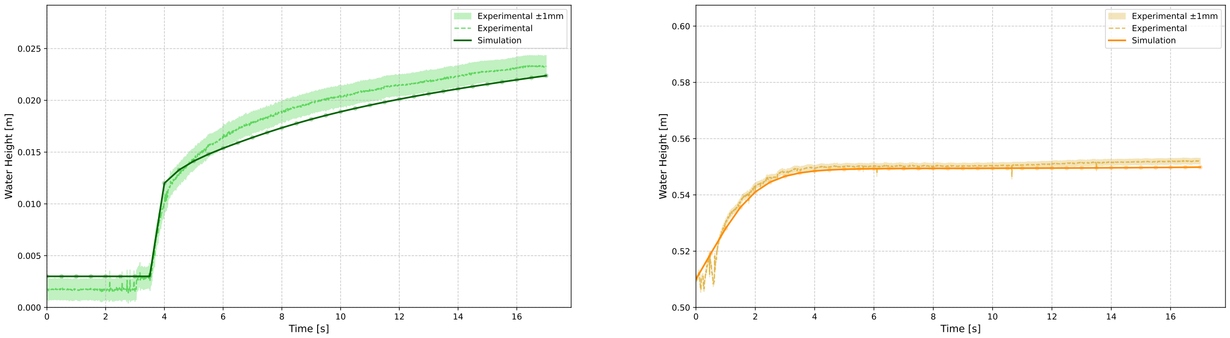

Figure 6.12: Evolution of water height over time at sensors 5 (on the left) and 7 (on the right) with a time delay of 22 seconds, $h_{min} = 0.003$ m, $\Delta x_{tank} = 0.2$m, $K = 90 m^{1/3}/s$ and a mean flow rate of $1.87 \cdot 10^{-3} m^3/s$

The comparison shows good agreement between experimental and numerical results for the sensors directly connected to the tank (sensors 1, 4, 5, and 7). It can be seen that:

- The model correctly captures the timing of the initial wave arrival at each sensor location.
- The rate of water level rise is well reproduced.
- At sensor 7 (in the tank), the model successfully tracks the water level evolution, confirming proper implementation of the time-varying inflow condition.

These results confirm that the basic flow transmission from the tank to adjacent pipes is correctly modeled. The next step is to implement the proper treatment of T-junctions to capture the complex wave dynamics throughout the entire network.

IV Implementation of the T junctions

IV.1 Mathematical formulation

The implementation of T-junctions is a critical aspect of the hydraulic network model, as these connection points present unique challenges for numerical simulation. At each T-junction, two fundamental physical principles must be simultaneously satisfied:

1. **Conservation of mass**: The net flow entering and leaving a junction must sum to zero, following the principle that water cannot be created or destroyed at junction points.
2. **Continuity of water surface elevation**: The water surface elevation (or hydraulic head) must be equal across all pipes connected to the junction, reflecting physical reality.

These requirements can be viewed as constraints on the numerical solution. When the numerical scheme advances independently in each pipe, the resulting flow rates and water levels at junctions generally do not automatically satisfy these constraints. Therefore, we need a corrective method to adjust these values while minimizing deviation from the originally calculated results.

The Lagrangian multipliers method provides a mathematical framework to solve these constrained optimization problems. The approach allows us to find solutions that are closest to the original calculations while satisfying the physical constraints at junctions.

Mass conservation using Lagrangian multipliers

For a junction with n connected pipes, the mass conservation constraint is expressed as:

$$\sum_{i=1}^{n} Q_i = 0 \tag{IV.1}$$

where Q_i represents the flow rate in pipe i, with positive values for inflow and negative values for outflow.

To enforce this constraint while minimizing changes to the computed values, we formulate the following constrained optimization problem:

$$\text{Minimize: } \sum_{i=1}^{n} \frac{1}{2}(Q_i^{\text{new}} - Q_i)^2 \tag{IV.2}$$

$$\text{Subject to: } \sum_{i=1}^{n} Q_i^{\text{new}} = 0 \tag{IV.3}$$

This means we want to find new flow rates Q_i^{new} that satisfy mass conservation while being as close as possible to the originally calculated values Q_i in a least-squares sense.

In our implementation, we solve this system using matrix operations by constructing the following linear system:

$$\begin{bmatrix} 1 & 1 & \cdots & 1 & 0 \\ 1 & 0 & \cdots & 0 & 1 \\ 0 & 1 & \cdots & 0 & 1 \\ \vdots & \vdots & \ddots & \vdots & \vdots \\ 0 & 0 & \cdots & 1 & 1 \end{bmatrix} \begin{bmatrix} \lambda \\ Q_1^{\text{new}} \\ Q_2^{\text{new}} \\ \vdots \\ Q_n^{\text{new}} \end{bmatrix} = \begin{bmatrix} 0 \\ Q_1 \\ Q_2 \\ \vdots \\ Q_n \end{bmatrix} \tag{IV.4}$$

Water surface elevation continuity

The second physical constraint at junctions is the continuity of water surface elevation or hydraulic head. For a T-junction connecting three pipes, we require that all water surfaces align at the same elevation:

$$H_1 = H_2 = H_3 \tag{IV.5}$$

The hydraulic head H_i at any point combines three components:

$$H_i = z_i + h_i + \frac{Q_i^2}{2gA_i^2} \tag{IV.6}$$

where z_i is the pipe bottom elevation, h_i is the water depth (dependent on wetted area A_i), and the final term represents kinetic energy (omitted when energy considerations are disabled). This last term, representing kinetic energy, is excluded from the current implementation, as energy-based corrections are not considered.

This constraint poses a significant challenge due to two non-linear relationships:

- The complex geometric relationship between water depth and wetted area in circular pipes.
- The inverse square relationship between wetted area and velocity.

Similar to the mass conservation problem, we formulate an optimization problem:

$$\text{Minimize: } \sum_{i=1}^{n} \frac{1}{2}(A_i^{\text{new}} - A_i)^2 \tag{IV.7}$$

$$\text{Subject to: } H_i - H_j = 0 \quad \forall \text{ connected pipe pairs } (i, j) \tag{IV.8}$$

However, due to the non-linear nature of this constraint, an iterative approach is required.

Iterative solution method The implementation uses the following steps to solve this constrained optimization problem:

1. **Initialization:** Start with initial estimates of the wetted areas A_i for each pipe connected to the junction.
2. **Water depth computation:** For each wetted area A_i, compute the corresponding water depth h_i using the Newton-Raphson method described in Section I.4.
3. **Constraint formulation:** For each adjacent pipe pair (i, j), enforce continuity of hydraulic head at the junction:
    - Without energy term:

      $$z_i + h_i = z_j + h_j$$

    - With energy term (if `energy = True`):

      $$z_i + h_i + \frac{v_i^2}{2g} = z_j + h_j + \frac{v_j^2}{2g}, \quad \text{where } v_i = \frac{Q_i}{A_i}$$

4. **Local linearization:** The constraints linking the pipes are nonlinear functions of the wetted areas due to the complex relationships $h(A)$ and $v(A) = Q/A$. To solve the system at each iteration, a Newton-type method is employed, requiring construction of a linear approximation of the constraint equations around the current state. This involves computing the Jacobian matrix of the constraints with respect to the wetted areas, where each Jacobian term represents how a small change in wetted area affects the water surface elevation (or total head).
5. **Derivative computation:**
   - The derivative of water depth with respect to wetted area is computed numerically using central differences:

     $$\frac{\partial h_i}{\partial A_i} \approx \frac{h(A_i + \epsilon) - h(A_i - \epsilon)}{2\epsilon} \tag{IV.9}$$

     where ϵ is a small perturbation parameter.
   - When the energy term is included, the analytical derivative of the kinetic energy term is added:

     $$\frac{\partial}{\partial A_i} \left(\frac{Q_i^2}{2gA_i^2} \right) = -\frac{Q_i^2}{gA_i^3} \tag{IV.10}$$
6. **System construction:** All equations are assembled into a linear system of the form $\mathbf{Ax} = \mathbf{b}$, where:
   - The first n equations correspond to wetted area updates,
   - The remaining equations enforce head continuity constraints via Lagrange multipliers.
7. **Solution and update:** The linear system is solved to compute the area corrections ΔA_i. The wetted areas are updated as $A_i^{new} = A_i^{old} + \Delta A_i$, and new water depths are computed. This iterative process continues until the maximum correction becomes smaller than a specified tolerance, indicating convergence.

IV.2 Implementation details

The implementation of the junction treatment consists of two key functions:

1. **junction_q_lagrangemult**: This function handles mass conservation at junctions by applying Lagrangian multipliers to balance the flows.
2. **junction_wse_head_lagrangemult**: This function ensures conservation of hydraulic head across connected pipes.

For each junction in the network, we follow these steps:

1. Identify all connected pipes and their respective positions (upstream or downstream).
2. Collect initial flow rates and wetted areas for each pipe at the junction.
3. Apply the Lagrangian multiplier method to enforce mass conservation.
4. Apply the Lagrangian multiplier method to enforce water surface elevation continuity.
5. Update the simulation matrices with the corrected values.

For the T-junctions, we enforce two continuity conditions: between pipes 1 and 2, and between pipes 1 and 3. This ensures that all three pipes have the same water surface elevation at the junction.

Boundary conditions at closed pipe ends are handled by setting the boundary value of the flow rate to zero. The water surface elevation is then allowed to adjust based on neighboring conditions, preserving mass conservation and physical plausibility.

The junction treatment is applied at each time step after the standard numerical scheme has computed preliminary values. This corrective approach ensures that the physical constraints are satisfied at all junctions throughout the simulation. This lead to a more accurate representation of the complex hydraulic behavior in the interconnected gallery network.

IV.3 Pipe length adjustment for T-junction volume compensation

Before implementing the complete network model, a geometric correction was applied to account for T-junction volumes and prevent overestimation of the total network volume.

In the laboratory setup, pipe lengths were measured from center-to-center distances between T-junctions. However, direct implementation of these distances would lead to volume overestimation. The model would account for both the full cylindrical volume of each pipe segment and the additional volume of T-junctions at each connection point.

To address this issue, the precise volume of each T-junction was calculated using geometric analysis (detailed derivation provided in Appendix G). For pipes with radius $R = 0.05$ m, the T-junction volume is:

$$V_T = R^3 \left(\pi + \frac{8}{3}\right) = 0.000726032 \text{ m}^3$$

Each T-junction volume was divided equally among the three connecting pipes, and converted to an equivalent pipe length:

$$\Delta L_T = \frac{V_T}{3\pi R^2} = 0.0308 \text{ m}$$

The original pipe lengths were then adjusted according to their junction connectivity:

- Pipes connecting two T-junctions: $L_{\text{adjusted}} = L_{\text{original}} - 2 \cdot R + 2\Delta L_T$
- Pipes connecting one T-junction: $L_{\text{adjusted}} = L_{\text{original}} - R + \Delta L_T$

where the $-R$ and $-2R$ terms account for the pipe radius overlap at junction centers.

This correction ensures that the total network volume matches the physical laboratory setup and maintains accurate mass conservation throughout the simulation.

V Final results

Here are the final results obtained with a mean flow rate of 1.87 L/s.

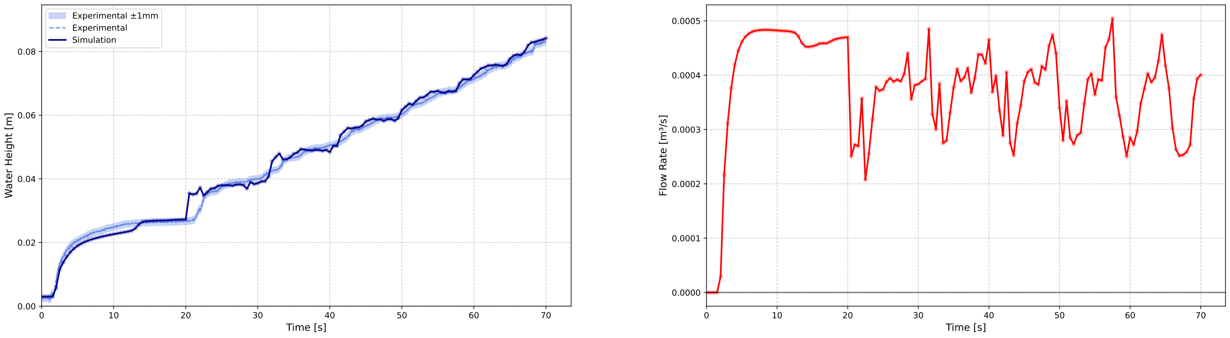

Figure 6.13: Evolution of water height and flow rate over time at sensor 1 with a time delay of 22 seconds, $h_{min} = 0.003$ m, $\Delta x_{tank} = 0.2$m, $K = 90m^{1/3}/s$ and a mean flow rate of $1.87 \cdot 10^{-3}m^3/s$

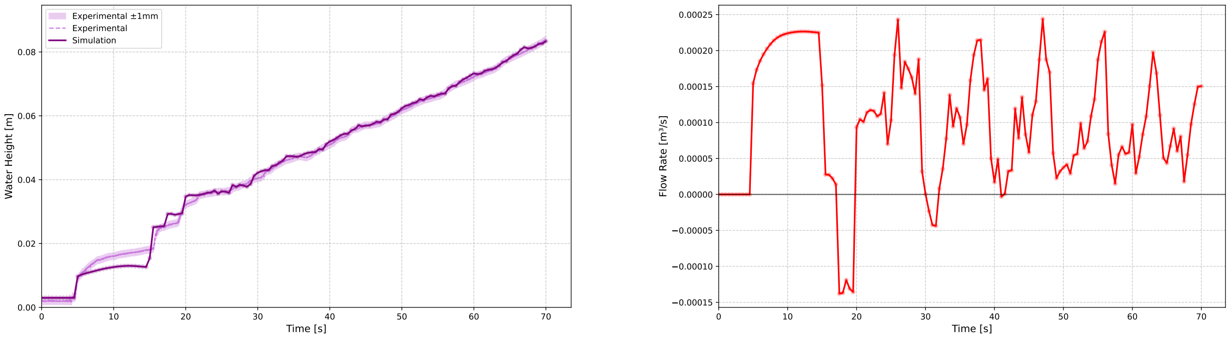

Figure 6.14: Evolution of water height and flow rate over time at sensor 2 with a time delay of 22 seconds, $h_{min} = 0.003$ m, $\Delta x_{tank} = 0.2$m, $K = 90m^{1/3}/s$ and a mean flow rate of $1.87 \cdot 10^{-3}m^3/s$

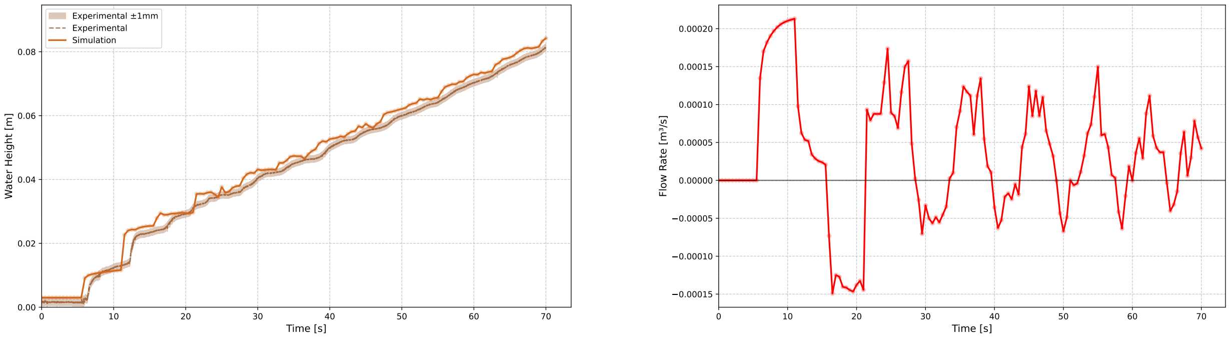

Figure 6.15: Evolution of water height and flow rate over time at sensor 3 with a time delay of 22 seconds, $h_{min} = 0.003$ m, $\Delta x_{tank} = 0.2$m, $K = 90m^{1/3}/s$ and a mean flow rate of $1.87 \cdot 10^{-3}m^3/s$

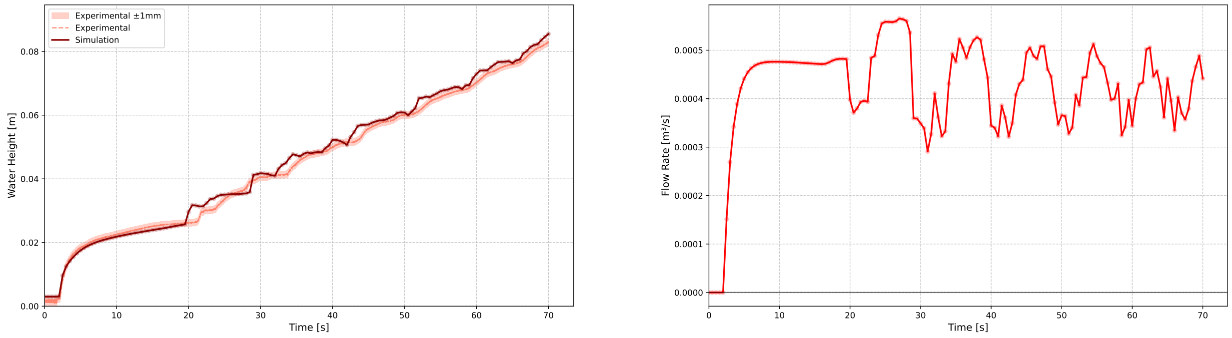

Figure 6.16: Evolution of water height and flow rate over time at sensor 4 with a time delay of 22 seconds, $h_{min} = 0.003$ m, $\Delta x_{tank} = 0.2$m, $K = 90 m^{1/3}/s$ and a mean flow rate of $1.87 \cdot 10^{-3} m^3/s$

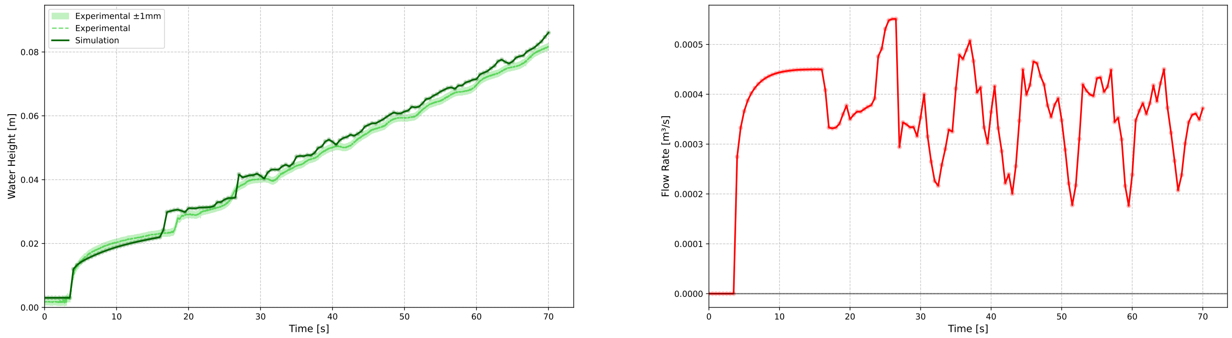

Figure 6.17: Evolution of water height and flow rate over time at sensor 5 with a time delay of 22 seconds, $h_{min} = 0.003$ m, $\Delta x_{tank} = 0.2$m, $K = 90 m^{1/3}/s$ and a mean flow rate of $1.87 \cdot 10^{-3} m^3/s$

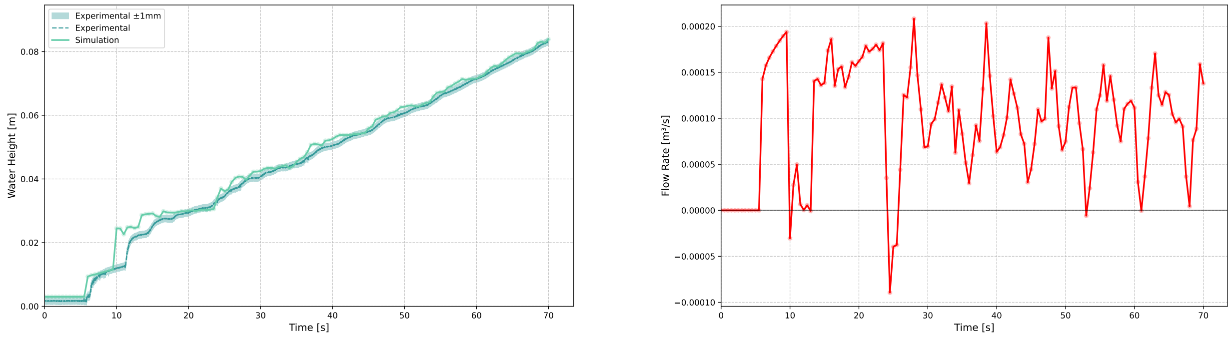

Figure 6.18: Evolution of water height and flow rate over time at sensor 6 with a time delay of 22 seconds, $h_{min} = 0.003$ m, $\Delta x_{tank} = 0.2$m, $K = 90 m^{1/3}/s$ and a mean flow rate of $1.87 \cdot 10^{-3} m^3/s$

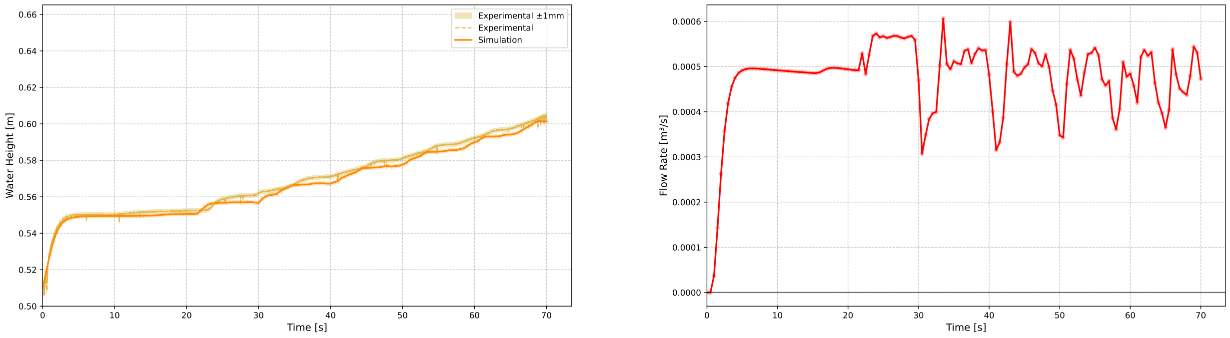

Figure 6.19: Evolution of water height and flow rate over time at sensor 7 with a time delay of 22 seconds, $h_{min} = 0.003$ m, $\Delta x_{tank} = 0.2$m, $K = 90 m^{1/3}/s$ and a mean flow rate of $1.87 \cdot 10^{-3} m^3/s$

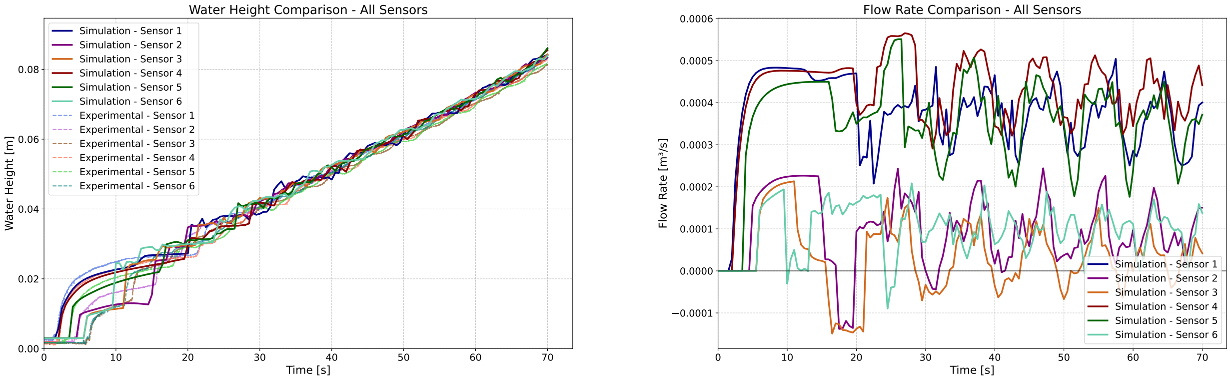

Figure 6.20: Evolution of water height and flow rate over time at all sensors with a time delay of 22 seconds, $h_{min} = 0.003$ m, $\Delta x_{tank} = 0.2$m, $K = 90 m^{1/3}/s$ and a mean flow rate of $1.87 \cdot 10^{-3} m^3/s$

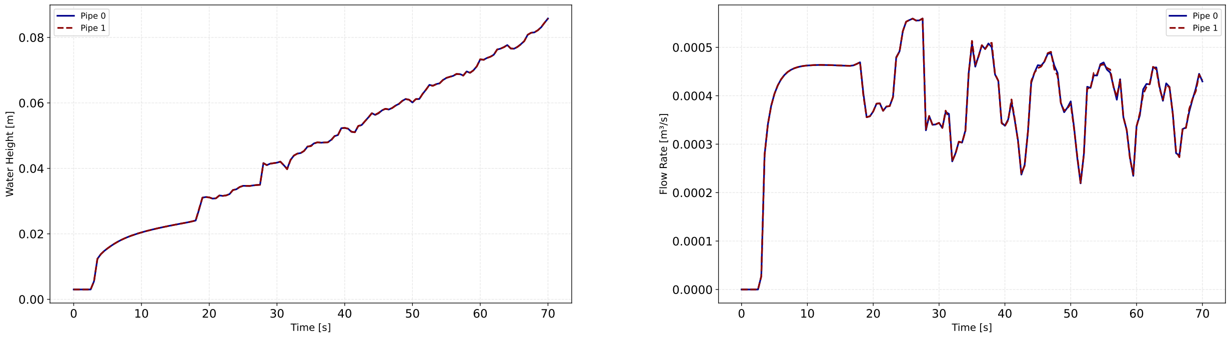

Figure 6.21: Evolution of water height and flow rate over time at the middle of pipes 0 and 1 with a time delay of 22 seconds, $h_{min} = 0.003$ m, $\Delta x_{tank} = 0.2$m, $K = 90 m^{1/3}/s$ and a mean flow rate of $1.87 \cdot 10^{-3} m^3/s$

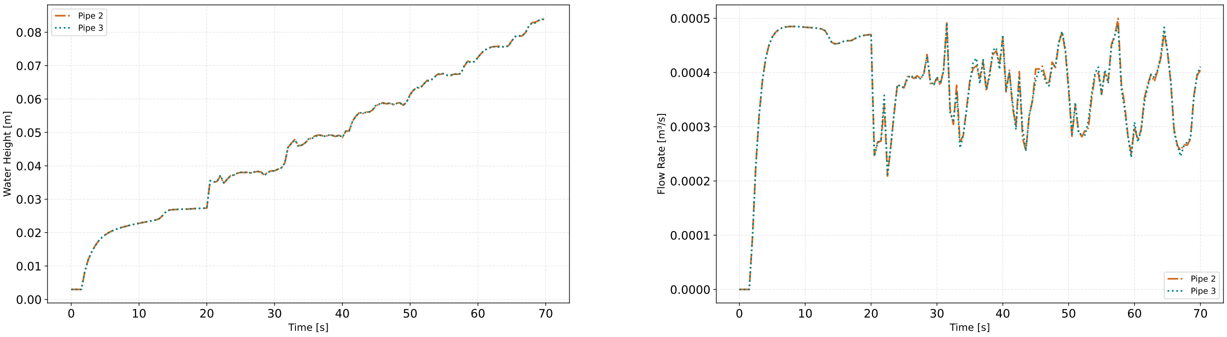

Figure 6.22: Evolution of water height and flow rate over time at the middle of pipes 2 and 3 with a time delay of 22 seconds, $h_{min} = 0.003$ m, $\Delta x_{tank} = 0.2$m, $K = 90 m^{1/3}/s$ and a mean flow rate of $1.87 \cdot 10^{-3} m^3/s$

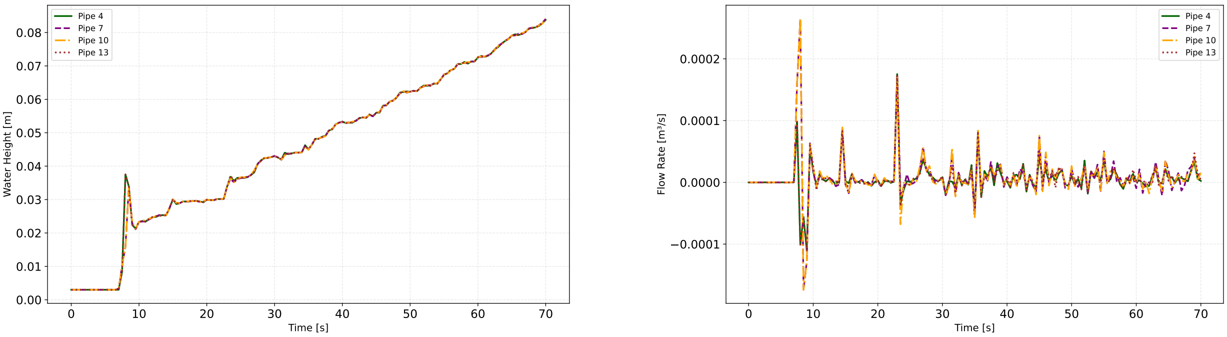

Figure 6.23: Evolution of water height and flow rate over time at the middle of pipes 4, 7, 10 and 13 with a time delay of 22 seconds, $h_{min} = 0.003$ m, $\Delta x_{tank} = 0.2$m, $K = 90 m^{1/3}/s$ and a mean flow rate of $1.87 \cdot 10^{-3} m^3/s$

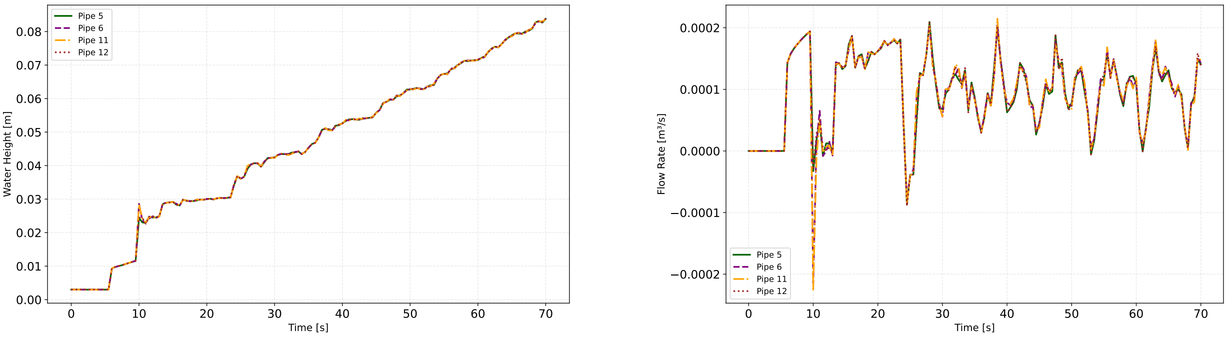

Figure 6.24: Evolution of water height and flow rate over time at the middle of pipes 5, 6, 11 and 12 with a time delay of 22 seconds, $h_{min} = 0.003$ m, $\Delta x_{tank} = 0.2$m, $K = 90 m^{1/3}/s$ and a mean flow rate of $1.87 \cdot 10^{-3} m^3/s$

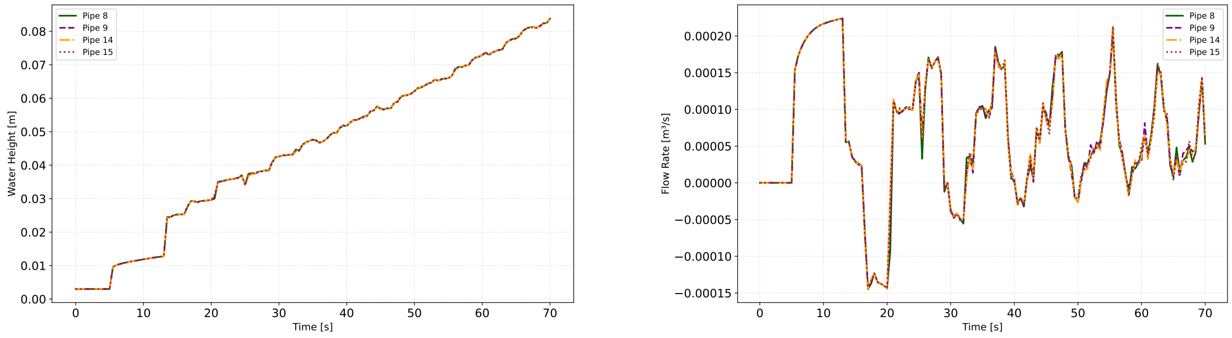

Figure 6.25: Evolution of water height and flow rate over time at the middle of pipes 8, 9, 14 and 15 with a time delay of 22 seconds, $h_{min} = 0.003$ m, $\Delta x_{tank} = 0.2$m, $K = 90 m^{1/3}/s$ and a mean flow rate of $1.87 \cdot 10^{-3} m^3/s$

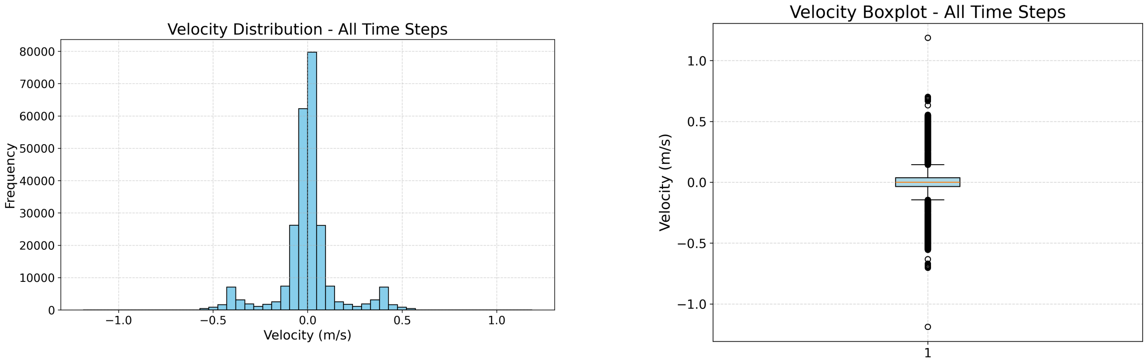

Figure 6.26: Histogram and boxplot of the velocity for all time steps with a time delay of 22 seconds, $h_{min} = 0.003$ m, $\Delta x_{tank} = 0.2$m, $K = 90 m^{1/3}/s$ and a mean flow rate of $1.87 \cdot 10^{-3} m^3/s$

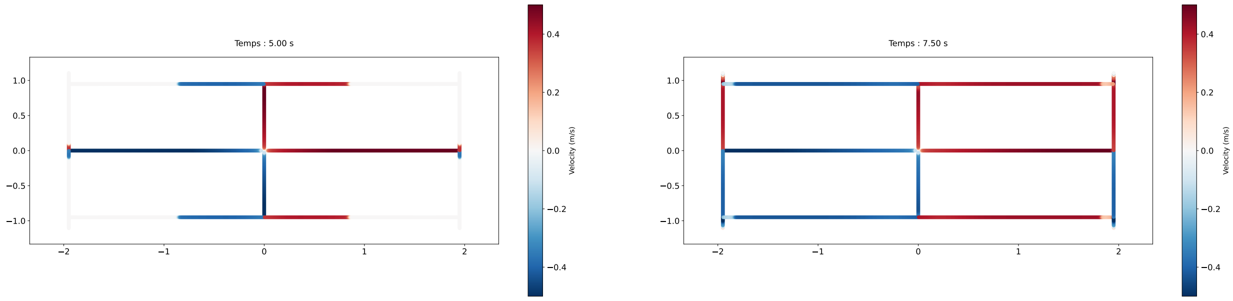

Figure 6.27: Value of the velocity in the network at time t=5s and t=7.5s with a time delay of 22 seconds, $h_{min} = 0.003$ m, $\Delta x_{tank} = 0.2$m, $K = 90 m^{1/3}/s$ and a mean flow rate of $1.87 \cdot 10^{-3} m^3/s$

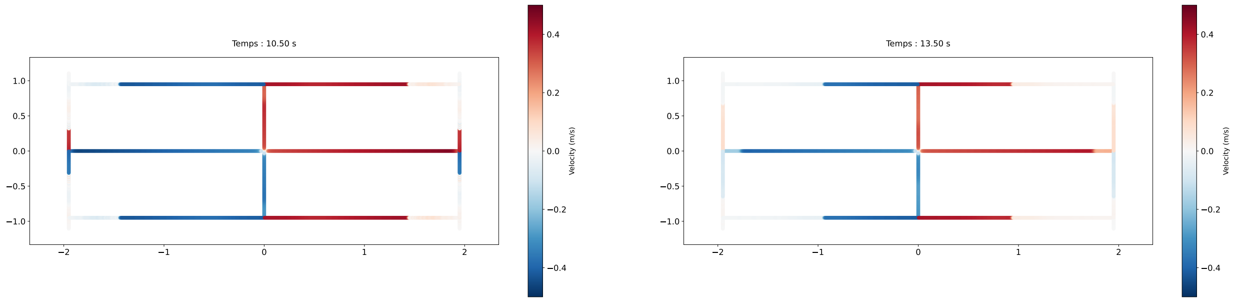

Figure 6.28: Value of the velocity in the network at time t=10.5s and t=13.5s with a time delay of 22 seconds, $h_{min} = 0.003$ m, $\Delta x_{tank} = 0.2$m, $K = 90 m^{1/3}/s$ and a mean flow rate of $1.87 \cdot 10^{-3} m^3/s$

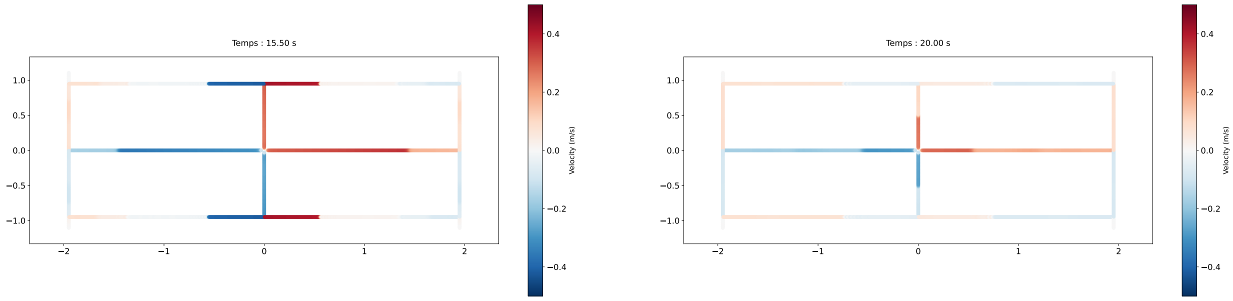

Figure 6.29: Value of the velocity in the network at time t=15.5s and t=20s with a time delay of 22 seconds, $h_{min} = 0.003$ m, $\Delta x_{tank} = 0.2$m, $K = 90 m^{1/3}/s$ and a mean flow rate of $1.87 \cdot 10^{-3} m^3/s$

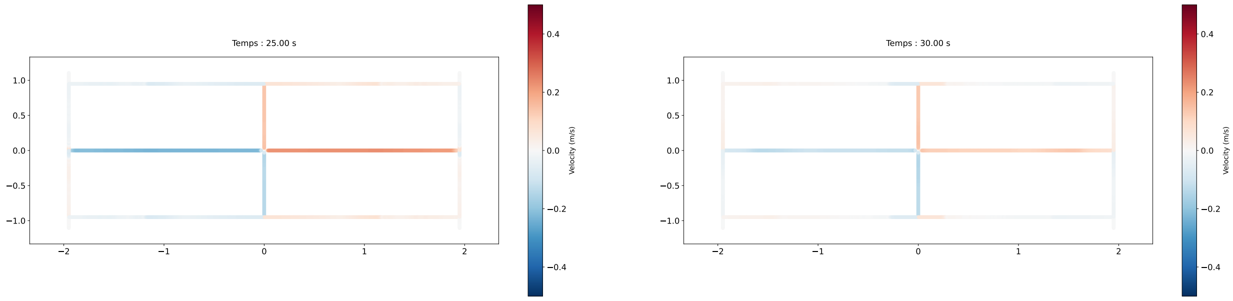

Figure 6.30: Value of the velocity in the network at time t=25s and t=30s with a time delay of 22 seconds, $h_{min} = 0.003$ m, $\Delta x_{tank} = 0.2$m, $K = 90 m^{1/3}/s$ and a mean flow rate of $1.87 \cdot 10^{-3} m^3/s$

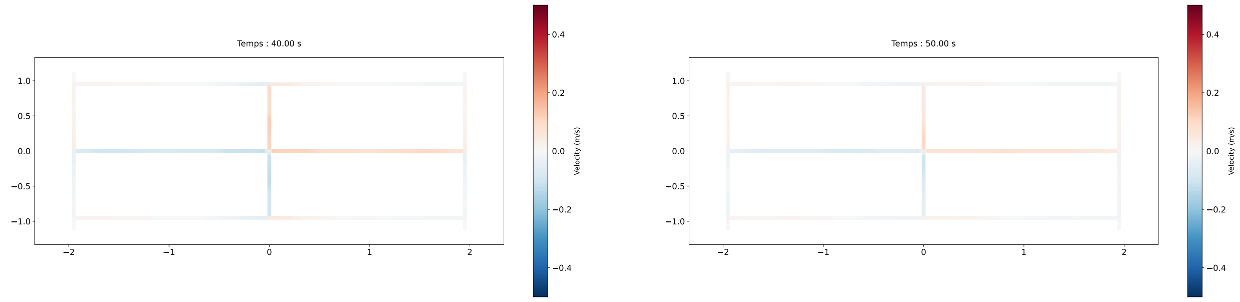

Figure 6.31: Value of the velocity in the network at time t=40s and t=50s with a time delay of 22 seconds, $h_{min} = 0.003$ m, $\Delta x_{tank} = 0.2$m, $K = 90 m^{1/3}/s$ and a mean flow rate of $1.87 \cdot 10^{-3} m^3/s$

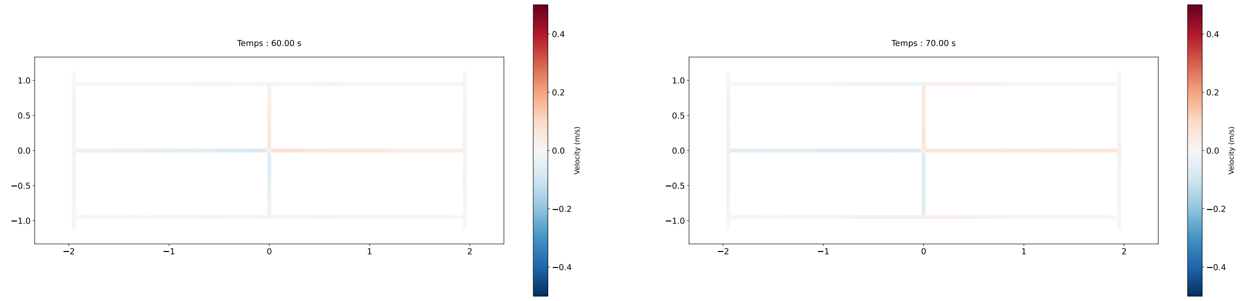

Figure 6.32: Value of the velocity in the network at time t=60s and t=70s with a time delay of 22 seconds, $h_{min} = 0.003$ m, $\Delta x_{tank} = 0.2$m, $K = 90 m^{1/3}/s$ and a mean flow rate of $1.87 \cdot 10^{-3} m^3/s$

VI Interpretation of results and hydraulic analysis

This section provides a comprehensive interpretation of the numerical results, examining the complex hydraulic behavior observed in the interconnected gallery network during filling operations.

VI.1 Overview of network hydraulic response

The numerical simulations reveal that underground gallery networks exhibit complex hydraulic characteristics during transient filling operations. The network demonstrates a sequence of distinct hydraulic regimes, each characterized by unique flow patterns, water level distributions and energy dissipation mechanisms.

This behavior arises from the combined influence of several factors:

- Geometric constraints imposed by the pipe network configuration.
- Wave propagation and reflection phenomena at junctions and boundaries.
- Transient flow disturbances caused by interactions between incident and reflected waves.
- Energy dissipation through friction losses along pipe walls.

VI.2 Detailed analysis of four-stage hydraulic evolution

Time is expressed in dimensionless form to enable scale-independent analysis. The total process duration is set to $t_{\text{ref}} = 92$ s and the dimensionless time is defined as $t^* = t/t_{\text{ref}}$.

Phase 1: Injection point filling ($t^* = 0$ to $t^* \approx 0.25$)

The first phase corresponds to the gradual filling of the injection point. At a mean injection flow rate of $Q_{\text{mean}} = 1.87$ L/s, this phase lasts approximately 23 seconds. During this time, water remains confined within the central injection chamber and no flow reaches the rest of the network.

This initial phase was simulated separately and is not included in the main results presented here. Instead, the state of the system at the end of this phase, when the injection point is nearly full, is used to initialize the full network simulation. Therefore, in all plots above, simulation time $t = 0$ s corresponds to $t = 22$ s in the laboratory experiment, marking the moment when water almost starts entering the pipe system.

This approach avoids simulating the quasi-static filling phase again, while ensuring that the dynamic simulation starts from realistic and physically consistent initial conditions.

Phase 2: Initial filling until water reaches terminal junctions (T1, T3, T5, T7) ($t^* \approx 0.25$ to $t^* \approx 0.32$)

Water is injected from the central injection point, initiating a pressure wave that propagates radially into the four main conduits (pipes 0-3). At $t^* \approx 0.25$ (t = 0 seconds for this simulation), the system is hydraulically symmetric. However, due to differences in pipe lengths, the wave fronts reach the downstream junctions (T2, T4, T6, and T8) at different times. This phase ends when the wave reaches the outermost T-junctions: T1, T3, T5, and T7.

At each T-junction, the incident pressure wave undergoes both reflection and transmission as a result of flow redistribution. A portion of the wave propagates into the downstream branches (transmission), while the remainder reflects back upstream along the incoming conduit (reflection).

The timing of wave propagation across the network reflects the varying lengths of the conduits. Around $t^* \approx 0.27$ (t ≈ 3 seconds for this simulation), water reaches the first T-junctions (T4 and T8) via the shorter branches (pipes 2 and 3). By $t^* \approx 0.29$ (t ≈ 4.8 seconds for this simulation), the wave has propagated through the longer pipes (0 and 1), reaching the second set of junctions (T2 and T6). Peak velocities are observed in pipes 0 to 3, reaching 0.521 m/s in pipes 2 and 3 at $t^* \approx 0.29$ (t ≈ 4.5 seconds for this simulation) and 0.555 m/s in pipes 0 and 1 at $t^* \approx 0.3$ (t ≈ 5.5 seconds for this simulation). These represent the highest velocities recorded in the inner conduits during the entire simulation. They occur specifically at the downstream T-junctions, shortly after the advancing flow reaches these terminal points and begins to split into the lateral branches. Finally, at approximately $t^* = 0.32$ (t ≈ 7 seconds for this simulation), the wave front reaches the outermost junctions (T1, T3, T5, and T7), as indicated by notable rises in water level, flow rate and velocity in the corresponding pipes (4, 7, 10, and 13).

Due to the four-fold symmetry of the network, which creates four identical rectangular sub-networks, the following analysis focuses on one representative sub-network comprising pipes 1, 2, 12, 13, and 14. The pipes in the three remaining sub-networks occupy geometrically equivalent positions and therefore exhibit identical hydraulic behavior.

It is important to note that water reaches the terminal junctions via pipe 12 slightly earlier than through pipe 14. This timing difference can be explained by the hydraulic paths involved. The flow feeding pipe 12 originates from pipe 1, which is one of the longest conduits directly connected to the reservoir. During the initial phase, this pipe carries the full discharge from the reservoir divided by 4, without prior division at T-junctions. As a result, the velocity in this path is initially higher, allowing water to travel longer distances more quickly. In contrast, the flow reaching pipe 14 passes through pipe 2, also directly connected to the reservoir but shorter in length. While this might suggest a faster path, the downstream water must travel a longer total distance through interconnecting pipes after experiencing flow division at junctions T8, resulting in lower velocities and delayed arrival. It is also worth noting that due to the symmetry of the network, the total hydraulic path length from the reservoir to any terminal junction (T1, T3, T5, T7) is the same, regardless of the route taken. Therefore, the observed differences in arrival time are not due to geometric distance, but rather to differences in local flow rates and wave propagation speeds.

As the pressure fronts arrive at the dead-end pipes, reflections are initiated almost immediately, generating reverse waves that begin to propagate back toward the reservoir. These reflections play a significant role in shaping the subsequent flow behavior.

Graphical sensor data confirm these dynamics. Sensors 1 and 4, followed closely by sensor 5, display sharp increases in water level within the time interval preceding $t^* = 0.28$ (t = 4 seconds for this simulation). In contrast, sensors 2, 3, and 6 start responding later, around $t^* = 0.29$ to 0.32 (t = 5 to 7 seconds for this simulation), confirming the delayed arrival of the wave at the terminal junctions. Flow rate variations are tightly correlated with changes in water height and velocity, reinforcing the transient nature of this phase. In the dead-end pipe 13, both flow and water height exhibit sudden changes around the end of this phase, clearly marking the onset of reflection.

The formation of reflected waves in the dead-end branches around $t^* = 0.32 - 0.33$ (t = 7-8 seconds for this simulation) leads to secondary wave activity throughout the network. These reflected waves interact with the incoming flow, producing interference patterns and flow reversals particularly visible in the interconnecting pipes.

From an engineering standpoint, these findings highlight critical considerations. The downstream ends of pipes 0 to 3 experience high velocities, resulting in elevated shear stresses, making these locations priority zones for protective measures such as erosion-resistant linings.

Phase 3: Complex wave interference and multi-directional flow ($t^* \approx 0.32$ to $t^* \approx 0.62$)

Following the initial wave propagation and the arrival of pressure fronts at the terminal junctions, the network enters its most hydraulically complex phase. This period is characterized by the simultaneous interaction of multiple incident and reflected waves travelling through various conduits. The overlapping of these waves gives rise to intricate interference patterns that define the dynamic behavior of the system between approximately $t^* = 0.32$ (t = 7 seconds for this simulation) and $t^* = 0.62$ (t = 35 seconds for this simulation).

As reflected waves return from dead-end pipes, they begin to interact with newly incoming flow from the reservoir. The highest velocity values recorded during the entire simulation occur in the interconnecting pipes. At $t^* = 0.33$ (t = 8 seconds for this simulation), the absolute maximum velocity of ± 1.188 m/s is reached in the interconnecting pipe 12 in the representative sub-network, specifically at the terminal T-junctions. This reflects the intense bidirectional flow reversals that characterize the complex wave interference phase. Moreover, dead-end pipe 13 show significant velocity spikes (up to 0.703 m/s) at its entrance point, confirming its role as strong wave reflectors that generate substantial momentum changes during reflection events. The junctions in the network, which had previously served as points of simple redirection, now become active mixing zones where energy redistribution takes place. These interactions produce rapid pressure fluctuations and initiate partial reflections that further complicate the flow dynamics.

Several wave phenomena are observed during this phase:

- Constructive interference occurs when pressure waves from different directions arrive in phase, amplifying the local pressure and creating significant peaks, particularly near junctions and terminal sections.
- Destructive interference, in contrast, takes place when waves are out of phase, leading to partial cancellation and damping of oscillations.

These complex interactions result in diverse hydraulic behaviors across the network. The interconnecting pipes (such as pipe 12 and 14 in the representative sub-network) exhibit repeated reversals in flow direction, which occur when local pressure increases are strong enough to push the flow in the opposite direction. In contrast, the primary injection conduits (pipes 1 and 2 in the representative sub-network) maintain a consistent flow direction despite undergoing pressure fluctuations, indicating that the incoming flow from the injection point continues to dominate. The dead-end pipe 13, meanwhile, act as strong reflectors, contributing the most significant reflected waves to the system.

Despite the apparent hydraulic chaos, the network preserves its fundamental symmetry. Flow increases in pipe 1 are mirrored by decreases in its symmetric counterpart, and similar balancing behavior is observed between pipe 2 and its symmetric equivalent. The absolute magnitudes of these changes remain symmetrical, suggesting uniform energy distribution and confirming the system's well-balanced design.

Graphical data further validate these dynamics. Pipe 12 shows clear signs of bidirectional flow between $t^* = 0.35$ (t = 10 seconds for this simulation) and $t^* = 0.48$ (t = 22 seconds for this simulation), confirming the presence of wave-induced reversals. Pipe 14 displays more gradual, sawtooth-like oscillations compared to pipe 12, which can be attributed to its greater length and the longer time required for pressure waves to complete a round trip. The mirrored dynamics between the primary pipes persist, although now superimposed with localized reflections from secondary branches.

From an engineering standpoint, this phase raises important concerns. The alternating flow patterns, especially the very high velocities recorded at the terminal T-junctions of interconnecting pipes like pipe 12, impose significant cyclic loading on the junctions, increasing the risk of fatigue and necessitating robust mechanical design. Moreover, this period should be avoided for any operational switching, as the system is still experiencing substantial hydraulic instability.

In conclusion, this phase represents the peak of hydraulic complexity within the network. The combination of intense wave reflections, interference, and multi-directional flows disperses energy throughout the system in a chaotic yet structured manner. Over time, these oscillations are progressively attenuated by energy dissipation mechanisms, gradually leading the network toward a more stable flow regime.

Phase 4: Energy dissipation and approach to quasi-steady state (> $t^* \approx 0.62$)

After the peak of wave activity and flow reversals observed during the previous phase, the network gradually enters a phase of hydraulic stabilization. From approximately $t^* = 0.62$ (t = 35 seconds for this simulation) onward, the amplitude of oscillations diminishes noticeably as residual energy is dissipated. This marks the transition into a regime where friction effects become dominant and both water level and flow progressively stabilize across the system.

The damping of oscillatory motion is governed by energy dissipation mechanisms that work to reduce flow variability. The primary mechanism in the current model is distributed friction losses along pipe walls, modeled using Manning's formula, which are proportional to the square of velocity and thus particularly effective during phases with high-velocity fluctuations. It should be noted that the current numerical model does not explicitly account for minor losses at junctions and geometric transitions, which would contribute additional energy dissipation in real systems through turbulence formation. These mechanisms would be frequency-sensitive in reality: high-frequency components would be damped more rapidly than low-frequency oscillations, leading to a gradual smoothing of flow and water surface elevation curves over time. Furthermore, the wall friction distributed along the entire pipe network contributes to steady, uniform energy dissipation, facilitating the approach to equilibrium.

Graphical outputs from the simulation confirm this trend. Flow rates and water levels begin to stabilize in all conduits and velocity profiles lose their earlier oscillatory character. Interference patterns fade, and directional flow becomes consistent across the network. While minor fluctuations persist due to residual wave reflections, their magnitudes are sufficiently small to be considered negligible for operational purposes.

From an engineering perspective, this phase marks a safe operational window. The attainment of quasi-steady conditions implies that the system can now tolerate changes in flow rate or initiate turbine operations without triggering significant transients. However, it is important to note that structural design margins must still account for the peak dynamic loads observed in earlier phases, particularly during the wave interference and reflection stages, rather than the more stable conditions of this phase.

In conclusion, the network reaches a state of hydraulic equilibrium between approximately $t^* = 0.78$ (50 seconds for this simulation) and $t^* = 0.89$ (60 seconds for this simulation). This stable regime is essential for the reliable and efficient operation of full-scale Underground Pumped Storage Hydropower systems, as it ensures that dynamic wave effects have dissipated and the system exhibits predictable hydraulic behavior suitable for operational control.

VI.3 Quantitative validation against experimental data

Quantitative error analysis (Table 6.2) provides deeper insight into model performance. During Period 1, sensor 2 exhibits the highest mean absolute error (MAE), reaching 22.54% (4.10 mm), closely followed by sensor 6 with an MAE of 22.18% (2.73 mm). In contrast, Period 2 shows significantly lower error values, with sensor 3 recording the highest MAE at just 2.55%.

It is important to note that the time intervals used for computing these errors are not fixed but vary by sensor and flow rate. For each sensor, Period 1 errors were evaluated over a specific time window selected just before the return peak of the first wave, capturing the initial transient response of the system. This window was chosen manually based on the wave arrival time at each sensor, which depends on both sensor location and the imposed inflow rate. Period 2 errors were then calculated over a later time interval corresponding to the quasi-steady period, once transient oscillations had mostly dissipated.

This tailored approach allows for a more accurate and representative comparison between measured and simulated water levels in both dynamic and steady-state conditions. The intervals used for the current case (with a flow rate of $1.87 \cdot 10^{-3}$ L/s) range approximately from 7-22 seconds for Period 1 and from 45-70 seconds for Period 2, depending on the sensor position.

Sensor	Period	MAE (mm)	RMSE (mm)	Max Error (mm)	MAE (%)
1	1	1.52	2.34	8.05	5.58
1	2	0.76	0.92	2.75	0.91
2	1	4.10	4.14	5.54	22.54
2	2	0.31	0.37	1.36	0.37
3	1	1.58	1.61	2.03	11.32
3	2	2.07	2.16	4.01	2.55
4	1	1.23	1.65	5.35	4.63
4	2	1.18	1.32	3.39	1.42
5	1	2.10	2.77	6.83	8.69
5	2	1.99	2.06	3.50	2.44
6	1	2.73	5.14	12.74	22.18
6	2	0.88	1.04	2.25	1.05
7	1	1.81	1.83	2.22	0.33
7	2	2.96	3.05	4.32	0.49

Table 6.2: Error metrics comparing simulation and experiment for $Q = 1.87\,\mathrm{L/s}$

The error analysis reveals several key trends:

- Errors are consistently larger during Period 1 (transient regime) than Period 2 (quasi-steady regime), reflecting the greater challenge of modeling complex wave interactions.
- Period 2 errors remain below 3% across all sensors, indicating excellent model performance during the uniform filling regime.

Several factors contribute to the observed discrepancies between numerical and experimental results:

- **Experimental uncertainties**: The experimental data in Appendix A underwent significant processing including outlier detection and selective averaging, which reduced apparent variability between test repetitions. However, even after this smoothing, variations of 2-3 mm between experimental series remain visible during transient phases. More importantly, the initial water height measurements (Table 6.1) show standard deviations of 0.0009-0.0013 m across sensors, with some sensors exhibiting ranges of up to 6.1 mm (sensor 1: 0.0003-0.0056 m). These variations, combined with the ± 1 mm ultrasonic sensor accuracy, sensor alignment issues and surface ripples contribute to measurement uncertainty.

- **Junction modeling limitations**: The one-dimensional approach simplifies the three-dimensional flow patterns that occur at pipe intersections.
- **Energy loss approximations**: No explicit minor loss coefficients were included in the numerical model. However, such losses are inherently present in the physical laboratory setup due to friction and turbulence at junctions and bends, potentially contributing to discrepancies between simulated and measured energy dissipation.
- **Geometric simplifications**: Small differences between the physical model and its numerical representation, particularly at the tank-pipe interface and the T-junctions.

Analysis of the error distribution reveals that the largest discrepancies consistently occur at sensors located downstream of T-junctions (sensors 2, 3, and 6), which exhibit significantly higher errors compared to those placed in pipes directly connected to the injection point. At T-junctions, Lagrange multipliers are used to enforce mass conservation and impose a common water surface elevation across all connected conduits. While this method is mathematically robust for ensuring continuity and consistency, it does not fully capture the complex three-dimensional flow phenomena that occur at such junctions in reality. The assumption of a single water level at the junction is consistent with the conservation of hydraulic head (here simplified to piezometric height, since velocity terms are neglected) and enables a coherent numerical representation of the system. However, the actual flow behavior at these intersections involves flow separation, secondary currents, and energy losses that are inherently three-dimensional and cannot be adequately represented by the one-dimensional Saint-Venant equations employed in this model. This limitation is particularly evident during the transient phases when rapid flow changes and wave interactions intensify the three-dimensional effects at junction points.

Despite these limitations, the close agreement, particularly during Period 2, confirms the model's capability to accurately represent the dominant hydraulic processes in the gallery network.

VI.4 Design and operational insights for UPSH systems

The numerical simulations provide valuable insights into the hydraulic behavior of underground pumped storage hydropower (UPSH) systems, particularly regarding the differentiated roles of the various gallery types. Each category of conduit exhibits distinct dynamic responses during transient and quasi-steady phases.

This table presents the number of zero-crossings observed in each pipe. A zero-crossing indicates a change in the direction of flow velocity, corresponding to a transition from positive to negative values or vice versa.

Pipe	0	1	2	3	4	5	6	7	8	9	10	11	12	13	14	15
Zero-crossings	0	0	0	0	313	122	144	312	204	195	311	130	114	279	190	188

Table 6.3: Number of flow reversals (zero-crossings) for each pipe

The main conduits (pipes 0-3), directly connected to the central reservoir, act as high-throughput channels and maintain a consistent flow direction throughout the simulation. However, they experience pronounced oscillations in both velocity and water surface elevation, particularly during the initial transient phases. So, these zones should be prioritized for reinforcement and erosion protection.

In contrast, the corner dead-end pipes (pipes 4, 7, 10, and 13) exhibit the highest number of flow reversals, as illustrated in Table 6.3. These pipes act as strong reflectors: when wave fronts reach these terminations, they produce substantial pressure surges due to abrupt momentum changes. The interconnecting pipes leading to these dead-end sections generally experience high velocities at the T-junctions where they connect. These areas should therefore be considered for erosion protection to ensure long-term structural integrity. With over 300 flow reversals recorded during a single filling cycle, these conduits are particularly susceptible to cyclic fatigue loading, necessitating fatigue-resistant design specifications and materials capable of withstanding repeated stress cycles. Consequently, they are key targets for structural monitoring, fatigue assessment, and environmental management.

The interconnecting pipes (5, 6, 8, 9, 11, 12, 14, 15) play a more dynamic role, redistributing flow between main branches and frequently undergoing partial or complete flow reversals during phases 3 and 4. This fluctuating behavior contributes significantly to energy dissipation within the system. Accordingly, they require design strategies that accommodate flexibility and fatigue resistance to withstand repeated cyclic loading. Furthermore, the terminal T-junctions must be protected against erosion due to the elevated velocities and associated shear stresses.

A particularly noteworthy observation during phases 3 and 4 is the synchronized behavior of wave reflections in the four primary conduits (pipes 0-3). Numerical results demonstrate that reflected waves consistently return from these four pipes simultaneously and depart uniformly once the wave fronts reconvene at the central reservoir. This coordinated interaction is hydraulically significant, as it reflects an optimal network geometry that promotes uniform reservoir filling. Such symmetry ensures balanced flow redistribution, enhances filling efficiency, and prevents preferential paths that could cause uneven water levels or hinder system performance. Overall, this behavior confirms that the rectangular layout offers well-balanced hydraulic properties, making it especially well-suited for UPSH applications where fast and uniform filling is critical to operational efficiency.

The simulations also highlight the system's sensitivity to variations in injection flow rate. As flow increases, both wave speed and amplitude rise, accelerating propagation and amplifying pressure oscillations. While higher inflows reduce the time needed to reach quasi-steady conditions, due to increased frictional damping, they also induce higher peak loads, presenting structural design challenges. Thus, while faster filling improves operational efficiency, it also intensifies hydraulic aggressiveness during early transients.

These conditions generate wall shear stresses capable of exceeding the critical Shields threshold for sediment mobilization, particularly in unlined galleries containing fine-grained material. In addition, abrupt flow redirection at T-junctions and turbulence zones can create local hotspots of hydraulic stress. Among all components, the dead-end and interconnecting pipes are most susceptible to intense flow reversals and should be carefully considered in design and monitoring strategies.

To assess the potential for erosion, the Shields criterion can be used [Dewals, 2023]. The critical shear stress τ_c for the initiation of particle motion is estimated as:

$$\tau_c = \theta_c(\rho_s - \rho)gd$$

is the dimensionless Shields parameter (typically 0.03-0.06 for non-cohesive materials), ρ_s and ρ are sediment and water densities respectively, and d is particle diameter. Actual wall shear stress can be approximated by:

$$\tau = \rho g R_h S_f$$

where R_h is the hydraulic radius and S_f the friction slope. This formulation provides a means to evaluate whether local flow conditions might exceed the critical threshold for erosion, particularly in unlined sections of the network. However, further analysis would be required to confirm whether this threshold is reached under typical operating velocities.

Based on these findings, several operational recommendations can be formulated. First, it is advisable to delay any operational mode transitions for at least 6 to 7 minutes (or 40-50 seconds in the model timeframe) to allow for full hydraulic stabilization. Flow changes should be introduced progressively through ramp control strategies to minimize transient loads. In addition, air management systems must be integrated to prevent overpressurization during rapid filling events. Finally, sensor deployment should focus on key hydraulic nodes (T-junctions, tank interfaces and dead-end conduits), where flow dynamics are most complex and potential risks are concentrated.

Together, these insights contribute to a better understanding of hydraulic behavior in underground storage systems and provide practical guidance for both the design and operation of future UPSH installations.

VI.5 Conclusion

UPSH systems leveraging abandoned mines must be treated as dynamic hydraulic circuits rather than static reservoirs. The wave-induced phenomena, including pressure surges, standing waves and flow reversals necessitate adaptive control, robust design and tailored operational protocols to ensure safety, efficiency and longevity.

CHAPTER 7

FROM LABORATORY VALIDATION TO FULL-SCALE MODELING: SCALING STRATEGY AND NUMERICAL SENSITIVITY ANALYSIS

This chapter represents a critical transition from experimental validation to practical engineering application, examining the numerical model's computational characteristics and demonstrating its capability for real-world UPSH system analysis.

The chapter addresses fundamental questions essential for practical implementation: How do the hydraulic phenomena identified in laboratory experiments translate to full-scale systems? How does spatial and temporal discretization affect solution accuracy?

I Theoretical framework for scale transition

I.1 Froude similarity principles and implementation

The scaling process involved a two-step application of Froude similarity. First, Froude similarity was used to design the laboratory model based on a conceptual full-scale system. Then, an inverse Froude scaling was applied to the laboratory results in order to simulate and analyze the system at full scale. This bidirectional approach enabled a direct comparison between laboratory-scale and full-scale behaviors, ensuring that the fundamental hydraulic phenomena were consistently reproduced and could be confidently extrapolated to real-world conditions.

Initial scaling: Full-scale to laboratory design

The laboratory model development began with a conceptual full-scale UPSH system designed for practical implementation in abandoned mining facilities. This reference system, featuring 10-meter diameter galleries in a 400 m x 200 m network configuration, represented realistic dimensions for underground pumped storage applications while remaining within feasible construction and operational parameters.

To enable experimental validation within laboratory constraints, Froude similarity principles were applied to scale this full-scale concept down to manageable laboratory dimensions.

The 1:100 geometric scaling factor was selected based on laboratory space limitations and instrumentation capabilities.

Validation scaling: Laboratory to full-scale application

After validating the numerical model against laboratory-scale experimental data, the same Froude similarity principles were applied in reverse to simulate the system at full scale. This inverse scaling process consisted of transforming the laboratory configuration, originally derived from a conceptual full-scale design, back into full-scale conditions by adjusting geometric parameters, flow rates and friction coefficients accordingly.

By applying the validated model to the full-scale configuration, the approach confirms its ability to accurately reproduce the hydraulic behavior of real-world systems. This two-step scaling method ensures physical consistency throughout the modeling process and reinforces the reliability of the laboratory-to-field extrapolation. Moreover, it highlights the model's versatility for application to various full-scale configurations beyond the one used in the physical experiment, offering a robust framework for future design and analysis.

Comprehensive parameter scaling and physical considerations

The application of Froude similarity requires systematic scaling of all dimensional quantities to maintain dynamic similarity between laboratory and full-scale systems. Each parameter must be scaled according to its fundamental dimensional relationship to ensure that the relative importance of different physical effects remains constant across scales.

Geometric scaling forms the foundation of the similarity analysis, with all length dimensions scaled by the factor $\lambda_L = 100$:

$$L_{real} = L_{lab} \cdot 100 \tag{I.1}$$

This includes pipe diameters, network dimensions, junction geometries and all other spatial characteristics of the system.

Temporal scaling derives from the need to preserve the relative timing of hydraulic events across scales:

$$T_{real} = T_{lab} \cdot \sqrt{100} = T_{lab} \cdot 10 \tag{I.2}$$

This scaling ensures that the durations of key transient phenomena, such as wave travel, reflection and interference remain consistent in proportion between laboratory and full-scale systems.

Velocity scaling ensures that characteristic flow speeds remain consistent across scales:

$$V_{real} = V_{lab} \cdot \sqrt{100} = V_{lab} \cdot 10 \tag{I.3}$$

This scaling guarantees that velocities observed in the full-scale system correctly reflect those measured in the laboratory model.

Discharge scaling accounts for both velocity and cross-sectional area scaling:

$$Q_{real} = Q_{lab} \cdot 100^{2.5} = Q_{lab} \cdot 100000 \tag{I.4}$$

This reflects the fact that discharge scales with the flow area ($\propto \lambda_L^2$) and flow velocity ($\propto \lambda_L^{0.5}$), leading to a total scaling factor of $\lambda_L^{2.5}$.

Friction coefficient scaling requires particular attention due to the empirical nature of Manning's formula. The dimensional analysis of Manning's equation reveals that the Strickler coefficient must scale according to:

$$K_{real} = K_{lab} \cdot 100^{1/6} \approx K_{lab} \cdot 2.15 \tag{I.5}$$

For the laboratory model with $K_{lab} = 90$ m$^{1/3}$/s, this yields $K_{real} = 194$ m$^{1/3}$/s for the full-scale system. While this value appears high compared to typical field conditions, it represents the theoretically correct scaling relationship required for perfect dynamic similarity. This apparent discrepancy highlights the limitations of empirical friction formulations when applied across vastly different scales.

The systematic application of these scaling relationships helps preserve the key hydraulic behaviors governing UPSH systems during the transition from laboratory to full scale, thereby increasing confidence that the numerical model remains valid when applied to real-world configurations.

I.2 Full-scale system configuration and geometric scaling

The full-scale network retains the same topology as the laboratory model, with all dimensions scaled according to the established relationships. This ensures that key geometric features, such as junction layout, relative pipe lengths and overall connectivity are consistently represented in the full-scale application.

The resulting full-scale configuration represents realistic dimensions for underground gallery systems that could be implemented in abandoned mining facilities:

- **Pipe diameter**: 10 m.
- **Network dimensions**: 400 m x 200 m.
- **Total pipe length**: approximately 1.8 km of interconnected galleries.
- **Central reservoir capacity**: 51.7 m height capacity.
- **Initial water depth**: 0.3m.
- **Operating mean flow rate**: 187 m^3/s.

This configuration represents a realistic scale for underground mining galleries that could be repurposed for UPSH applications, matching typical tunnel boring machine capabilities and structural feasibility constraints.

II Full-scale hydraulic behavior and phase preservation

The application of proper scaling relationships to the validated numerical model produces full-scale results that demonstrate the preservation of fundamental hydraulic phenomena across scales. This section presents comprehensive analysis of the full-scale hydraulic behavior and confirms the persistence of the characteristic four-phase evolution identified in laboratory experiments.

II.1 Full-scale simulation results

Figures 7.1 through 7.5 present the complete hydraulic evolution at the middle of pipes for different pipe groups in the full-scale network, revealing the scaled manifestation of the complex flow dynamics observed in laboratory experiments.

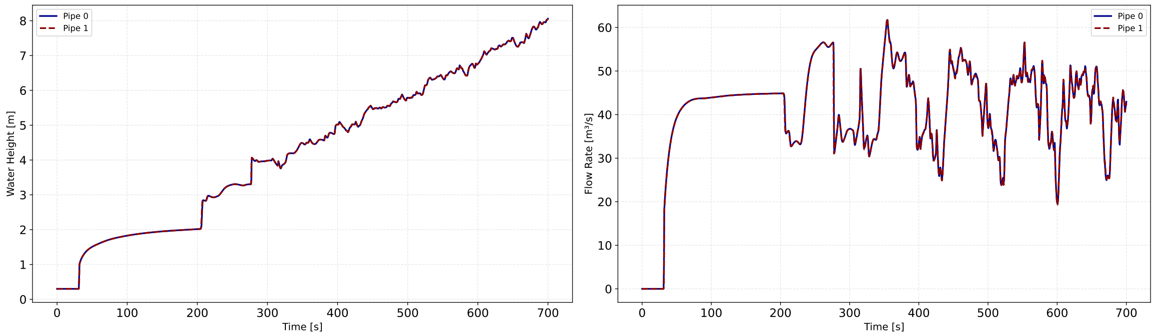

Figure 7.1: Evolution of water height and flow rate over time at the middle of pipes 0 and 1

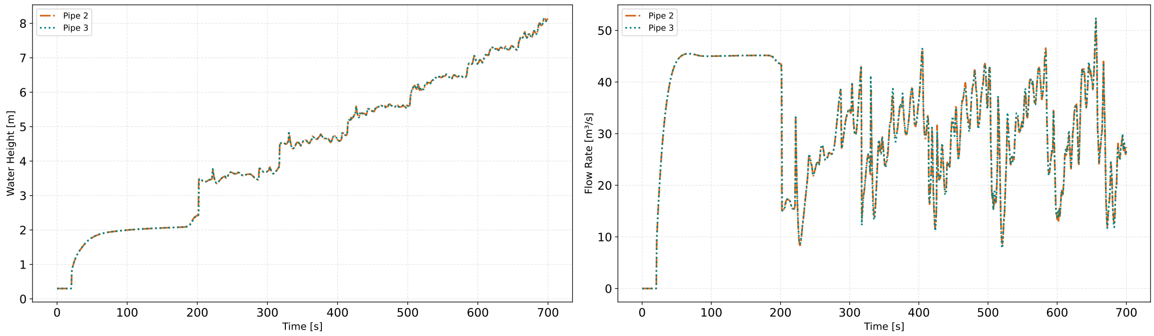

Figure 7.2: Evolution of water height and flow rate over time at the middle of pipes 2 and 3

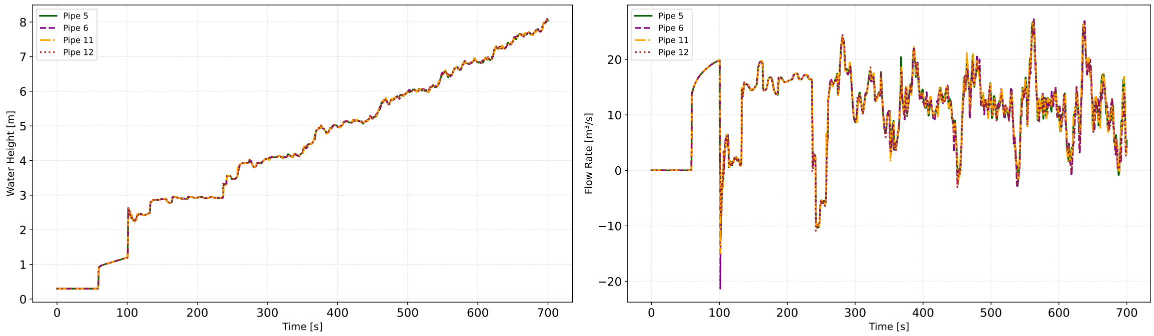

Figure 7.3: Evolution of water height and flow rate over time at the middle of pipes 5, 6, 11 and 12

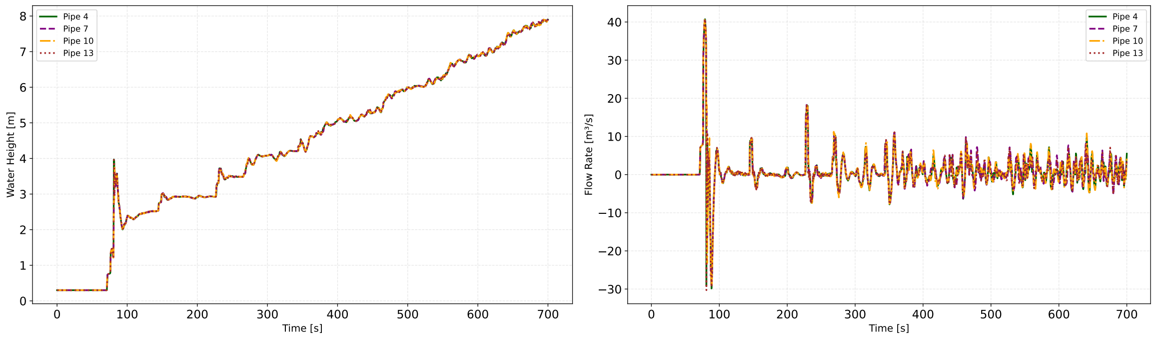

Figure 7.4: Evolution of water height and flow rate over time at the middle of pipes 4, 7, 10 and 13

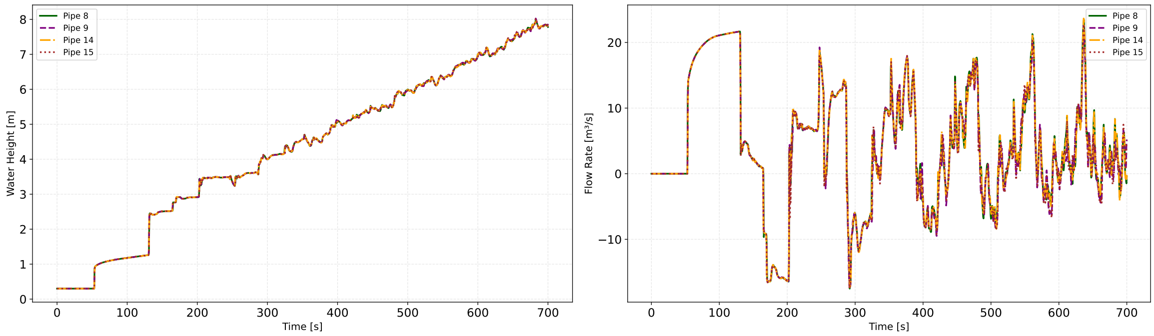

Figure 7.5: Evolution of water height and flow rate over time at the middle of pipes 8, 9, 14 and 15

II.2 Dimensionless phase analysis and scale-independent behavior

The analysis of full-scale results using dimensionless time coordinates confirms the preservation of the characteristic four-phase hydraulic evolution identified in laboratory experiments. By expressing time in dimensionless form as $t^* = t/t_{ref}$ where $t_{ref} = 920$ s, including the initial 220 s reservoir filling period, represents the total process duration.The temporal dynamics of hydraulic phenomena can be directly compared across different scales.

The four-phase hydraulic evolution identified in laboratory experiments is perfectly preserved in the full-scale simulations:

- Phase 1: Initial filling of injection reservoir ($t^* = 0$ to $t^* \approx \frac{230}{920} = 0.25$).
- Phase 2: Propagation of wave front toward network extremities ($t^* \approx 0.25$ to $t^* \approx \frac{294}{920} = 0.32$).
- Phase 3: Complex interactions between incident and reflected waves ($t^* \approx 0.32$ to $t^* \approx \frac{350}{920} = 0.62$).
- Phase 4: Gradual stabilization toward uniform water level ($t^* > 0.62$).

The identical dimensionless timing of these phases between laboratory and full-scale simulations demonstrates that the fundamental hydraulic phenomena and their temporal evolution are perfectly scale-independent when proper Froude scaling is applied. This confirms the validity of the numerical model for full-scale applications and validates the use of laboratory experiments for predicting the complete hydraulic behavior of real-world UPSH installations.

III Sensitivity analysis of spatial and temporal steps

A sensitivity study was carried out to evaluate the influence of spatial step size Δx and Courant-Friedrichs-Lewy (CFL) number on numerical accuracy and computational efficiency. Four values of Δx (0.2 m, 0.5 m, 1.0 m and 5.0 m) and four CFL values (0.1, 0.2, 0.3 and 0.4) were tested to guide optimal settings for practical engineering use.

III.1 Spatial step analysis

To test the influence of this parameter, all other parameters are kept constant and remain identical for each spatial step, with the CFL coefficient fixed at 0.2.

Table 7.1 summarizes the computational cost associated with each spatial resolution. As expected, larger Δx values significantly reduce computation time due to fewer mesh points and larger allowable time steps.

Δx [m]	Time step count [-]	Simulation time [s]
0.2	166368	54060
0.5	66465	12960
1.0	33235	6480
5.0	7179	4260

Table 7.1: Simulation cost as a function of spatial resolution

Figure 7.6 illustrates water height and discharge profiles for pipes 5, 6, 11 and 12. Visually, only $\Delta x = 5.0$ m shows a significant deviation. The three finer steps (0.2 m, 0.5 m, 1.0 m) yield very similar results, indicating low sensitivity in this range.

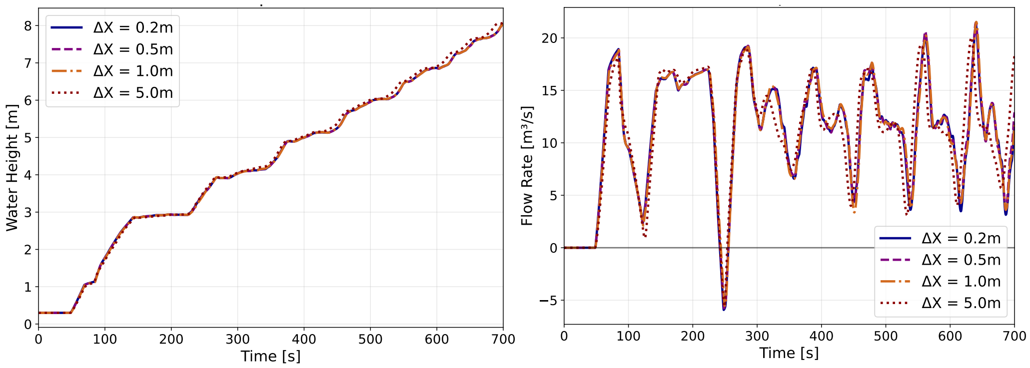

Figure 7.6: Evolution of water height and flow rate at the center of pipes 5, 6, 11, and 12 as a function of Δx

A quantitative error analysis confirms these trends. Table 7.2 shows that relative errors remain below 1-2% for $\Delta x \leq 1.0$ m. $\Delta x = 5.0$ m introduces significantly higher discrepancies, particularly for flow rate.

Water Height Error [%]					Flow Rate Error [%]					Velocity Error [%]				
Pipe/Δx	0.2m	0.5m	1.0m	5.0m	Pipe/Δx	0.2m	0.5m	1.0m	5.0m	Pipe/Δx	0.2m	0.5m	1.0m	5.0m
P0	0.00	0.16	0.38	2.48	P0	0.00	0.30	0.71	4.00	P0	0.00	0.98	0.42	4.47
P1	0.00	0.39	0.39	2.47	P1	0.00	0.30	0.70	3.99	P1	0.00	1.00	0.42	4.46
P2	0.00	0.80	0.80	3.75	P2	0.00	1.50	1.50	6.59	P2	0.00	2.04	0.86	8.37
P3	0.00	0.83	0.83	3.75	P3	0.00	1.45	1.45	6.65	P3	0.00	2.06	0.86	8.38
P4	0.00	0.65	0.65	2.35	P4	0.00	2.13	2.13	5.07	P4	0.00	1.65	0.96	3.92
P5	0.00	0.24	0.24	1.66	P5	0.00	1.81	1.81	8.63	P5	0.00	0.60	0.32	1.82
P6	0.00	0.24	0.24	1.67	P6	0.00	1.88	1.88	8.40	P6	0.00	0.59	0.33	1.79
P7	0.00	0.65	0.65	2.29	P7	0.00	2.11	2.11	4.98	P7	0.00	1.64	0.94	3.86
P8	0.00	0.23	0.23	1.48	P8	0.00	1.04	1.04	5.02	P8	0.00	0.60	0.30	1.15
P9	0.00	0.24	0.24	1.50	P9	0.00	1.01	1.01	5.04	P9	0.00	0.61	0.28	1.16
P10	0.00	0.63	0.63	2.30	P10	0.00	2.05	2.05	5.00	P10	0.00	1.61	0.95	3.86
P11	0.00	0.63	0.63	2.34	P11	0.00	1.78	1.78	8.60	P11	0.00	0.56	0.31	1.79
P12	0.00	0.63	0.63	2.34	P12	0.00	1.79	1.79	8.54	P12	0.00	0.58	0.33	1.82
P13	0.00	0.26	0.26	1.48	P13	0.00	2.06	2.06	5.10	P13	0.00	1.63	0.94	3.92
P14	0.00	0.26	0.26	1.50	P14	0.00	1.04	1.04	4.99	P14	0.00	0.67	0.67	1.16
P15	0.00	0.26	0.26	1.50	P15	0.00	1.02	1.02	5.02	P15	0.00	0.65	0.65	1.16

Table 7.2: Relative errors (%) in water height, flow rate and velocity for different spatial step Δx for each pipe, using $\Delta x = 0.2m$ as reference

In conclusion, the choice of $\Delta x = 0.5$ m offers a good compromise between accuracy and efficiency, reducing computational cost by nearly 75% compared to $\Delta x = 0.2$ m with negligible error increase.

III.2 Temporal step analysis via CFL variation

To test the influence of this parameter, all other parameters are kept constant and remain identical for each spatial step, with Δx = 0.5 m fixed.

A separate analysis varied the CFL number from 0.1 to 0.4. Since the time step is calculated as $\Delta t = \mathrm{CFL} \cdot \Delta x / c$, this directly controls temporal resolution.

Table 7.3 summarizes the computational cost associated with each CFL value. As expected, larger CFL values significantly reduce computation time by allowing larger time steps, resulting in fewer iterations required for the simulation.

CFL [-]	Time step count [-]	Simulation time [s]
0.1	132262	21900
0.2	66465	12960
0.3	44515	10440
0.4	33788	8640

Table 7.3: Simulation cost as a function of CFL coefficient

Figure 7.7 shows that CFL values 0.1 and 0.2 yield nearly identical results. In contrast, CFL = 0.3 and 0.4 introduce visible oscillations and noticeable deviations in water height and discharge curves.

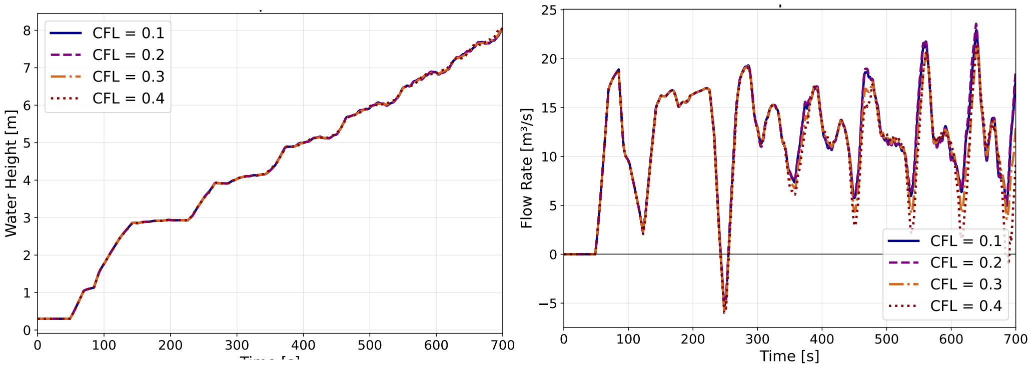

Figure 7.7: Evolution of water height and flow rate at the center of pipes 5, 6, 11, and 12 as a function of CFL

Water Height Error [%]					Flow Rate Error [%]					Velocity Error [%]				
Pipe/CFL	0.1	0.2	0.3	0.4	Pipe/CFL	0.1	0.2	0.3	0.4	Pipe/CFL	0.1	0.2	0.3	0.4
P0	0.0	0.02	0.03	0.17	P0	0.0	0.09	0.13	0.80	P0	0.0	0.02	0.04	0.14
P1	0.0	0.02	0.02	0.11	P1	0.0	0.09	0.13	1.1	P1	0.0	0.02	0.03	0.20
P2	0.0	0.07	0.05	0.31	P2	0.0	0.40	0.33	1.7	P2	0.0	0.10	0.07	0.28
P3	0.0	0.07	0.05	0.27	P3	0.0	0.42	0.32	1.3	P3	0.0	0.11	0.08	0.23
P4	0.0	0.28	0.60	1.2	P4	0.0	1.3	2.3	4.3	P4	0.0	0.31	0.61	1.1
P5	0.0	0.10	0.30	0.71	P5	0.0	0.95	3.5	6.8	P5	0.0	0.14	0.46	0.87
P6	0.0	0.11	0.30	0.52	P6	0.0	1.0	3.7	7.0	P6	0.0	0.14	0.47	0.87
P7	0.0	0.30	0.62	1.0	P7	0.0	1.5	2.4	4.1	P7	0.0	0.35	0.63	1.1
P8	0.0	0.23	0.23	0.42	P8	0.0	0.55	2.0	3.0	P8	0.0	0.09	0.32	0.52
P9	0.0	0.07	0.23	0.39	P9	0.0	0.49	1.9	3.7	P9	0.0	0.10	0.30	0.59
P10	0.0	0.25	0.60	1.1	P10	0.0	1.1	2.3	4.1	P10	0.0	0.30	0.61	1.1
P11	0.0	0.10	0.30	0.61	P11	0.0	1.0	3.4	6.0	P11	0.0	0.15	0.45	0.81
P12	0.0	0.11	0.30	0.55	P12	0.0	1.2	3.7	7.3	P12	0.0	0.16	0.47	0.90
P13	0.0	0.29	0.62	1.1	P13	0.0	1.4	2.4	4.4	P13	0.0	0.33	0.64	1.1
P14	0.0	0.07	0.23	0.46	P14	0.0	0.60	2.0	4.1	P14	0.0	0.11	0.32	0.62
P15	0.0	0.07	0.23	0.44	P15	0.0	0.47	1.9	4.2	P15	0.0	0.09	0.31	0.66

Table 7.4: Relative errors (%) in water height, flow rate, and velocity for different CFL values, using CFL = 0.1 as reference

In conclusion, CFL values above 0.2 degrade solution quality. Therefore, CFL = 0.2 is retained as the preferred value, providing a good balance between accuracy and computational time.

IV Conclusion

This chapter bridges the gap between laboratory validation and full-scale engineering application. By leveraging Froude similarity principles in both forward and inverse directions, the numerical model was shown to preserve the essential dynamics of underground pumped storage hydropower (UPSH) systems across scales. The four characteristic hydraulic phases observed experimentally were reproduced at full scale, confirming the model's physical consistency and applicability for real-world systems.

The sensitivity analysis highlights the balance between numerical accuracy and computational efficiency in full-scale UPSH system simulations.

On the spatial side, the results for $\Delta x =$ 0.2m, 0.5m, and 1.0m are nearly indistinguishable, with overlapping profiles and relative errors below 2%. Only the coarsest resolution ($\Delta x =$ 5.0m) introduces significant deviations, especially in sensitive conduits. Given this, $\Delta x =$ 1m emerges as the best compromise, offering accuracy comparable to finer grids while reducing computational time by up to 92%.

On the temporal side, varying the CFL number confirms that higher CFL values (0.3-0.4) lead to numerical instabilities and oscillatory behavior, particularly in discharge results. CFL values of 0.1 and 0.2 produce nearly identical outcomes, validating the stability of the scheme. Given its shorter computation time, CFL = 0.2 is selected as the preferred time discretization setting.

In summary, the combination of $\Delta x = 1$ m and $CFL = 0.2$ offers an efficient configuration, providing engineering-grade accuracy with manageable computational demands. This configuration would be suitable for full-scale simulations and the practical design of UPSH systems.

CHAPTER 8

GEOMETRIC PARAMETER SENSITIVITY ANALYSIS

One of the primary advantages of numerical modeling over physical experimentation lies in the ability to investigate the influence of geometric parameters on system behavior. While laboratory experiments are constrained by the physical model geometry, numerical simulations enable rapid evaluation of multiple configurations, detailed analysis at any spatial location and comprehensive parameter sensitivity studies. This capability is particularly valuable for UPSH systems, where the geometric constraints of existing mining cavities necessitate adaptive design approaches.

This chapter examines one critical geometric parameter: pipe spacing. The analysis focuses on measurements taken at the midpoint of each conduit, which provides several methodological advantages: it minimizes boundary effects from complex three-dimensional flow patterns at junctions, captures representative hydraulic conditions within each pipe segment, ensures consistent measurement methodology across different configurations and leverages the highest accuracy region of the one-dimensional model away from junction complexities.

For this chapter, an initial water height of 0.05 m and a Strickler coefficient of 90 $\mathrm{m}^{1/3}/\mathrm{s}$ were used, as these values appear to be more realistic than those given by Froude similarity. All other parameters were kept in Froude similarity. The average flow rate of $1.87 \cdot 100^{2.5}$ L/s was considered. A spatial discretization of $\Delta x = 0.5$m and a Courant number of 0.2 were applied.

I Effect of pipe spacing on flow dynamics

The investigation of pipe spacing effects examines how network compactness influences hydraulic behavior. Four configurations were analyzed with varying horizontal spacing:

- Real model: 200 m x 400 m network (baseline configuration).
- Modified model 1: 150 m x 400 m network (25% reduction in horizontal spacing).
- Modified model 2: 100 m x 400 m network (50% reduction in horizontal spacing).
- Modified model 3: 70 m x 400 m network (65% reduction in horizontal spacing).

All configurations maintained constant pipe diameter (10 m) and a mean flow rate of 187 m^3/s, scaled from laboratory conditions.

I.1 Hydraulic response patterns

The analysis reveals distinct behavioral patterns across different pipe groups within the network, each responding uniquely to spacing variations based on their hydraulic function and geometric sensitivity.

Primary flow pipes (pipes 0-3)

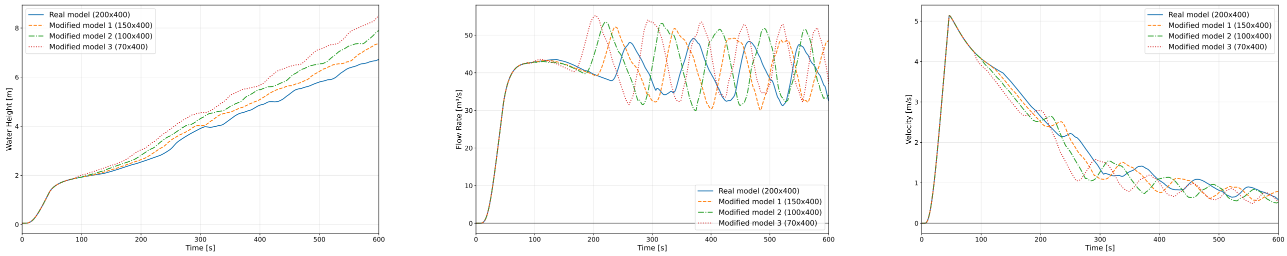

(a) Water depths (b) Flow rates (c) Velocities

Figure 8.1: Hydraulic behavior comparison at the middle of pipes 0 and 1 across different network spacings

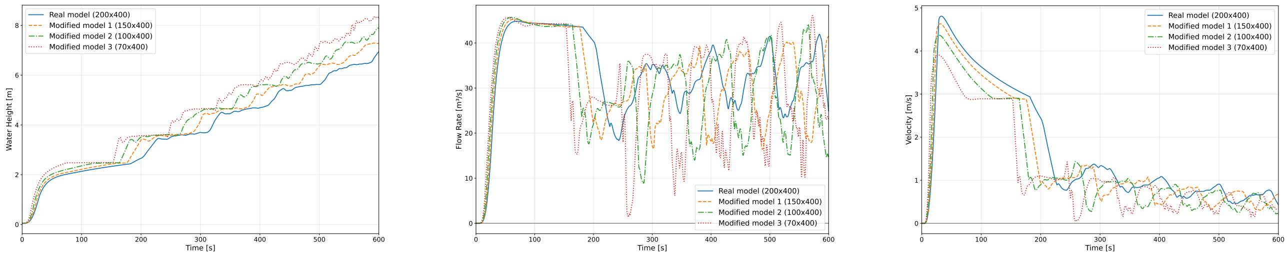

(a) Water depths (b) Flow rates (c) Velocities

Figure 8.2: Hydraulic behavior comparison at the middle of pipes 2 and 3 across different network spacings

The primary conduits demonstrate fundamentally different responses to spacing modifications depending on their orientation, revealing the critical influence of geometric constraints on hydraulic behavior.

The primary conduits can be divided into two distinct groups based on their orientation and length: the long horizontal pipes (0 and 1), which maintain their physical dimensions regardless of spacing, and the short vertical pipes (2 and 3), whose effective lengths change with network compactness. This classification implies the markedly different hydraulic responses observed in these two groups.

Here are the observations for pipes 0 and 1.

Stability across configurations: Long pipes (0 and 1) exhibit a high degree of stability across all configurations, with similar overall velocity profiles and peak values around 5 m/s. However, a closer look reveals slight phase shifts between curves for velocity and flow rate, particularly during the transient phase. Additionally, the flow rate oscillates around a higher mean value in more compact networks.

Wave propagation effects: This behavior stems from the fact that, although the geometry of pipes 0 and 1 remains unchanged, the overall network compactness affects how quickly pressure waves propagate and reflect within the system. In more compact configurations, the water reaches downstream junctions faster, reducing the delay between wave emissions and reflections. This leads to earlier interactions and slightly advanced oscillation phases.

Flow redistribution influence: Moreover, the higher mean flow rate in compact networks reflects a more efficient redistribution of flow: the reduced hydraulic resistance in shorter interconnecting paths allows more water to be directed through pipes 0 and 1. As a result, even if their geometry is constant, the overall network dynamics cause these pipes to carry a slightly greater sustained flow, particularly during quasi-steady phases.

Initial velocity peak consistency: The initial velocity peaks in pipes 0 and 1 remain unchanged across all spacing configurations, which is expected since these peaks occur when water first reaches the downstream T-junctions, before the influence of the modified interconnecting pipe lengths can manifest. This timing independence confirms that the initial wave propagation characteristics are controlled by the main conduit geometry rather than the overall network configuration.

However, short pipes show distinctly different and more complex behavior, with clear variations in their hydraulic response across spacing configurations. Several key observations emerge from the detailed analysis:

Initial peak behavior and wave arrival timing: The initial velocity peaks in pipes 2 and 3 demonstrate a clear relationship with network compactness. As the pipe spacing becomes smaller, the magnitude of these initial velocity peaks decreases. This phenomenon occurs because the downstream T-junctions are reached more quickly in compact networks due to reduced pipe lengths. Since maximum velocity is achieved precisely when water reaches these terminal junctions, the shorter travel distances result in lower peak velocities as the flow has less time to accelerate and build momentum before encountering the junction resistance.

Velocity plateau formation: The characteristic velocity plateau around 2.9 m/s in pipes 2 and 3 results from a specific wave reflection sequence that creates a temporary hydraulic equilibrium. When the initial pressure wave reaches junctions T4 and T8, it undergoes partial reflection back toward the reservoir while simultaneously transmitting energy into the outer pipes toward the dead-end terminals (pipes 4, 7, 10, 13).

The plateau begins when this first reflected wave from T4 and T8 returns to the central reservoir, temporarily stabilizing the water level in pipes 2 and 3. During this plateau period, the system maintains hydraulic equilibrium until the second reflected wave, originating from the dead-end pipes (4, 7, 10, 13), completes its return journey to the reservoir area. The plateau duration is therefore determined by the time difference between these two wave reflection events.

In compact networks, the shortened distances between T4/T8 and the reservoir create a significant time gap between the arrival of the first reflected wave (from T4/T8) and the second reflected wave (from dead-ends 4, 7, 10, 13), resulting in a pronounced and sustained plateau. However, in the baseline configuration (200x400m), the wave travel times are such that both reflected waves arrive at the reservoir almost simultaneously, eliminating the temporal separation needed for plateau formation. Consequently, the water level continues to rise steadily without the stabilizing effect of the intermediate wave reflection, preventing the characteristic plateau from developing.

Enhanced flow stabilization: In compact networks with shorter pipe lengths, velocities in pipes 2 and 3 tend to stabilize more rapidly toward zero or near-zero values following the initial transient phase. This accelerated stabilization reflects the reduced system inertia and enhanced energy dissipation that characterize compact configurations. The shorter pipe lengths reduce the total fluid mass in motion, allowing for quicker response to changing hydraulic conditions and faster achievement of equilibrium states.

Flow direction variations: A particularly important observation is the increased frequency of flow changes (while maintaining positive overall flow) in more compact networks. As spacing decreases, pipes 2 and 3 exhibit more frequent variations in discharge, creating a more dynamic and oscillatory flow pattern. This increased variability reflects the enhanced wave interaction frequency that develops when reflection points are closer together, creating more complex interference patterns between incident and reflected waves.

Water level rise characteristics: The analysis reveals that water levels rise more rapidly in compact networks, which is physically consistent with the reduced total network volume when interconnecting pipes are shortened. This faster filling behavior has important implications for operational control and system response times, as operators must account for accelerated system dynamics in compact configurations.

This geometric sensitivity principle establishes a fundamental understanding for the entire network analysis: pipes whose dimensions are modified by spacing changes will exhibit altered hydraulic behavior, while those maintaining constant dimensions preserve their baseline characteristics. The contrasting behavior between short and long pipes provides clear evidence of this principle and demonstrates the selective impact of geometric modifications on system performance.

Interconnecting pipes (pipes 5, 6, 11, 12)

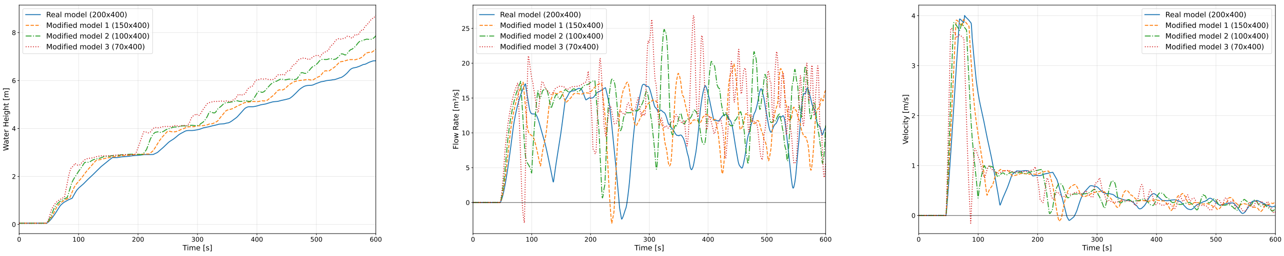

(a) Water depths

(b) Flow rates

(c) Velocities

Figure 8.3: Hydraulic behavior comparison at the middle of pipes 5, 6, 11 and 12 across different network spacings

The short interconnecting pipes demonstrate moderate but systematic sensitivity to spacing variations, exhibiting behavior that directly reflects their role as dynamic flow redistributors within the network.

Flow redistribution dynamics: As the network becomes more compact, pipes 5, 6, 11 and 12 exhibit more pronounced oscillations during transient phases. This results from the altered wave propagation patterns in compact networks, where shorter distances create more frequent wave interactions and reflections, leading to more dynamic flow redistribution and more frequent bidirectional flow events.

Amplified wave interactions: Shorter pipe lengths in compact configurations reduce the time it takes for pressure waves to travel between junctions. This means pipes 5, 6, 11, and 12 are subjected to more rapid and overlapping wave arrivals from multiple sources: reflected waves at the terminal dead-ends (pipes 4, 7, 10, 13), transmitted waves from the main conduits, and secondary reflections from various junction points. This converging wave activity intensifies local velocity variations and makes the flow more dynamic.

Role in network connectivity and regulation: In compact layouts, reduced hydraulic resistance in these interconnecting pipes facilitates more efficient internal flow redistribution. They serve as internal regulators, redistributing flow between different branches of the network and helping to balance pressure differences across the system. This flow redistribution capability reduces local pressure concentrations and contributes to overall system stability by providing flexible pathways for hydraulic energy dissipation during transient phases.

Terminal dead-end pipes (pipes 4, 7, 10, 13)

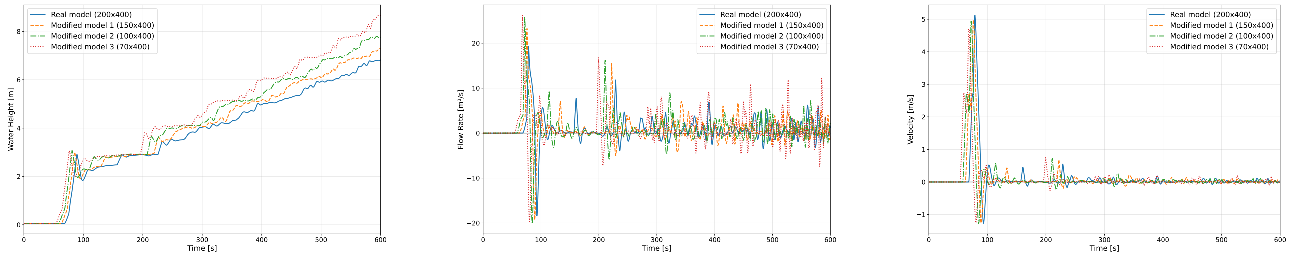

(a) Water depths (b) Flow rates (c) Velocities

Figure 8.4: Hydraulic behavior comparison at the middle of pipes 4, 7, 10 and 13 across different network spacings

These pipes behave consistently across all spacing configurations. As the main sources of wave reflections, they play a crucial role in shaping the overall dynamics of the network.

Initial peak characteristics: An interesting observation in the terminal dead-end pipes is the contrasting behavior between flow rate and velocity peaks during the initial wave arrival. The most compact network (70x400m) exhibits the highest initial flow rate peak but shows the lowest velocity peak among all configurations.

This phenomenon is explained by the significant differences in wetted cross-sectional areas at the moment of peak flow arrival. As observed in the water depth graphs, the baseline configuration (200x400m) reaches a lower water level peak compared to compact networks during the initial wave arrival. Given the large pipe diameter (10m), even small variations in water depth result in substantial changes in wetted cross-sectional area due to the circular geometry.

Therefore, while compact networks deliver higher peak flow rates to the terminal pipes, they also achieve higher water levels and consequently larger wetted areas. The baseline configuration, despite receiving lower peak flow rates, maintains smaller wetted areas due to lower water accumulation. Since velocity is governed by $V = Q/A$, the smaller cross-sectional area in the baseline configuration more than compensates for the reduced flow rate, resulting in higher velocities despite lower discharge values.

Stable reflection patterns: Each terminal pipe exhibits a characteristic two-phase response: first, a strong inflow of water at high velocity, followed by a flow reversal as the reflected waves travel back toward the reservoir. This pattern stays the same because the physical shape and size of these pipes don't change. However, in more compact networks, changes in flow rate, velocity and water level happen sooner since the water reaches these pipes faster through shorter connecting pipes.

Wave generation role: These pipes are the primary origins of reflected waves that create complex wave interference patterns in the connecting pipes. Their steady and predictable behavior provides a reliable source of wave energy that drives the network's dynamics.

Impact on system damping: While the response of each terminal pipe remains stable, the timing of the reflected waves depends on the network's compactness. In more compact networks, waves return quicker and interact more often with other parts of the system, increasing oscillations in the connecting pipes. This shows how a stable local behavior can still significantly affect the overall system through changes in timing and wave interactions.

Peripheral interconnecting conduits (pipes 8, 9, 14, 15)

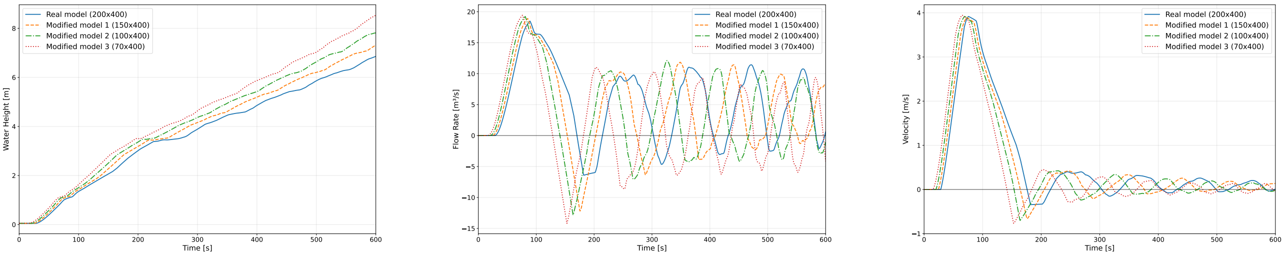

(a) Water depths (b) Flow rates (c) Velocities

Figure 8.5: Hydraulic behavior comparison at the middle of pipes 8, 9, 14 and 15 across different network spacings

The peripheral interconnecting conduits demonstrate consistent behavior patterns across all spacing configurations, with several distinctive characteristics that differentiate them from other pipe groups in the network.

Bidirectional flow characteristics: A key distinguishing feature of pipes 8, 9, 14 and 15 is their oscillation around zero flow rate, indicating frequent flow direction reversals. This contrasts markedly with the other interconnecting pipes (5, 6, 11, 12), which oscillate around positive flow values while maintaining a predominantly unidirectional character. The flow reversal analysis confirms this behavior, with these peripheral pipes experiencing between 3587 and 7901 flow reversals depending on the configuration, representing some of the highest reversal frequencies in the entire network.

Peak flow reversal in moderate compactness: The flow reversal data (Table I.1) reveals a non-monotonic relationship with spacing, where moderately compact configurations (100x400 m and 150x400 m) exhibit the highest number of flow reversals (7000-7900), while both the most compact (70x400 m) and baseline (200x400 m) configurations show fewer reversals (3500-5700). In very compact or highly extended layouts, wave interactions either happen too quickly to sustain oscillations or are too delayed and damped, leading to fewer reversals.

Velocity response and energy dissipation: Although initial velocity peaks are comparable across all spacings ($\approx$ 4 m/s), the rate at which velocities decay differs significantly. In compact networks, where distances between wave reflection points are reduced, velocities are damped more rapidly. This accelerated damping results from more frequent wave collisions and higher cumulative energy losses at junctions, making peripheral pipes effective sites for hydraulic energy dissipation.

Accelerated water level rise: In all configurations, water levels in these pipes rise steadily, but more rapidly in compact networks due to the smaller total volume to fill. The reduced pipe lengths allow water to reach peripheral sections faster, contributing to quicker transitions toward steady-state conditions.

Role and contribution to stability: Peripheral interconnecting pipes act as dynamic regulators at the network's edges. Instead of conveying constant flow, they adjust to pressure imbalances by varying their flow direction and magnitude. This flexible response helps redistribute momentum, absorb pressure surges and prevent localized build-up. While their behavior appears unstable, it plays a stabilizing role by dampening oscillations and supporting overall hydraulic equilibrium.

I.2 Velocity field evolution and statistical analysis

The velocity distribution analysis reveals systematic changes in flow characteristics as network compactness increases. The baseline real model exhibits a concentrated velocity distribution centered around zero, with most velocities contained within ±5 m/s and occasional extremes reaching up to ± 35 m/s during intense transient events.

Analysis of the velocity histograms (Figures I.1-I.3) shows clear trends with increasing compactness. Modified model 1 (150 m x 400 m) displays a symmetric distribution extending to approximately ±30 m/s, indicating that moderate spacing reduction maintains significant wave activity during transient phases. Modified model 2 (100 m x 400 m) demonstrates improved velocity concentration with extremes limited to approximately ±20 m/s, representing about 33% reduction in peak velocities compared to the less compact configuration.

The most compact configuration (modified model 3, 70 m x 400 m) exhibits the most controlled velocity distribution, with velocities predominantly confined within ±10 m/s. This represents approximately 67% reduction in velocity extremes compared to the moderately spaced networks, indicating substantial improvement in flow stability through geometric optimization.

This systematic velocity reduction reflects enhanced energy dissipation mechanisms in compact networks. Shortened distances between reflection points create more frequent wave-wall and wave-junction interactions, each contributing to energy dissipation through viscous effects. The improved hydraulic connectivity in compact spacing also enables more efficient pressure equilibration, reducing the pressure gradients that drive high-velocity flows.

I.3 Quantitative comparison with baseline configuration

To quantify the effect of network compactness, each configuration was compared to the baseline case (200x400m) by calculating the mean absolute differences in flow rate and velocity over time for each pipe group (Table 8.1). These differences highlight how geometric changes influence system dynamics.

Pipe Group	**150x400 vs 200x400**		**100x400 vs 200x400**		**70x400 vs 200x400**	
	Flow Rate (m^3/s)	**Velocity (m/s)**	**Flow Rate (m^3/s)**	**Velocity (m/s)**	**Flow Rate (m^3/s)**	**Velocity (m/s)**
Primary (0-3)	2.1	0.18	3.2	0.24	4.8	0.31
Interconnecting (5,6,11,12)	1.8	0.15	2.6	0.19	3.9	0.28
Terminal (4,7,10,13)	2.3	0.19	3.1	0.23	4.2	0.29
Peripheral (8,9,14,15)	1.9	0.16	2.8	0.21	4.1	0.27

Table 8.1: Mean absolute differences in flow rate and velocity compared to the 200x400m baseline configuration

Progressive deviation with network compactness: Across all pipe groups, the observed deviations grow systematically as the network becomes more compact. This trend reflects the increasing impact of shortened interconnecting pipes on wave dynamics and flow redistribution. However, it is essential to clarify that these are not errors in the conventional sense, but rather expected differences arising from the altered timing and shape of hydraulic signals.

Origin of deviations: phase shifts in flow and velocity: The key source of these deviations lies in the phase shift introduced by shorter pipe lengths. In compact networks, pressure waves and reflected signals travel more quickly, leading to earlier changes in velocity and discharge. As a result, even if the general flow patterns remain similar, time-aligned comparisons with the baseline configuration highlight larger discrepancies, particularly during transient phases.

These phase shifts are most pronounced in the primary and interconnecting pipes, where flow is strongly influenced by network geometry. Shorter pipes reduce hydraulic inertia and delay, causing more rapid responses that diverge temporally from those of the baseline network. The deviations observed are therefore not modeling errors, but rather physical consequences of geometric modification.

Flow rate more sensitive than velocity: Flow rate deviations tend to be larger than velocity deviations. This reflects the fact that flow rate integrates both velocity and pipe cross-section area, making it more sensitive to temporal shifts and redistribution effects. Velocity, in contrast, is locally constrained by continuity and adapts more smoothly across configurations.

I.4 Physical interpretation and engineering implications

The effects of spacing can be interpreted through wave propagation principles. Reduced spacing shortens wave travel times between junctions, accelerating hydraulic dynamics and increasing wave interference frequency. This results in enhanced energy dissipation and explains the improved velocity stability observed in compact configurations.

Greater hydraulic connectivity at smaller spacing also promotes faster pressure equilibration. Shorter distances between branches facilitate quicker resolution of pressure imbalances, leading to lower pressure gradients and more stable flow patterns.

From an engineering perspective, these findings show that network compactness can be increased without compromising core hydraulic performance. The 67% reduction in velocity extremes achieved under maximum compaction translates into lower dynamic loads, improved structural safety margins, and more predictable operation.

The geometric sensitivity highlighted by this analysis offers practical guidance for adapting UPSH systems to varied underground constraints. These findings demonstrate that UPSH systems remain viable across various aspect ratios, with the understanding that optimal performance results from careful consideration of both geometric proportions and appropriate flow rate selection for each configuration.

In conclusion, UPSH systems demonstrate strong hydraulic resilience across varied geometries. The consistent behavior of pipes confirms system robustness, while clear links between geometry and hydraulic response enable reliable scaling from model to full scale. Geometric optimization improves energy dissipation, limits velocity extremes and enhances operational predictability, supporting more efficient designs, stronger economic viability and broader implementation. This study provides a quantifiable basis for the confident deployment of UPSH systems in complex underground settings.

CHAPTER 9

CONCLUSION

This thesis has successfully developed and validated a comprehensive numerical modeling framework for analyzing water flows in interconnected mine galleries used for Underground Pumped Storage Hydropower (UPSH) systems. Through rigorous mathematical modeling, experimental validation, and extensive parametric analysis, this research provides crucial insights that advance the technical feasibility of transforming abandoned mines into valuable energy storage facilities, addressing one of the most pressing challenges in the renewable energy transition.

The core achievement of this work lies in the creation of a one-dimensional finite volume numerical model that correctly predicts water movement through complex interconnected pipe networks. Built upon the Saint-Venant equations with a second-order Runge-Kutta temporal integration scheme, the model incorporates advanced junction treatment using Lagrangian multipliers to ensure mass conservation and water surface elevation continuity at critical connection points. This mathematical framework has been rigorously validated against laboratory experiments conducted on a 1:100 scale physical model, demonstrating good agreement with errors consistently below 3% during quasi-steady periods and acceptable discrepancies during complex transient phases.

This research provides detailed analysis and characterization of four distinct hydraulic phases that occur during gallery network filling: filling of the injection point, wave propagation through the network reaching terminal junctions, complex wave interference creating intricate patterns with bidirectional flows, and finally energy dissipation leading to quasi-steady uniform filling. This four-phase behavior reveals that underground gallery networks function as dynamic hydraulic circuits rather than passive storage volumes, exhibiting complex wave phenomena including pressure surges, standing waves, and flow reversals that must be carefully considered in system design and operation.

The comprehensive parameter sensitivity analysis has revealed the relative importance of key design variables for system performance. The friction coefficient significantly influences wave propagation speed and equilibrium water levels. Initial water depth affects transient wave dynamics but has minimal impact on steady-state conditions, while injection point geometry controls tank-pipe interface hydraulics and early-phase flow distribution. These findings provide engineers with quantitative guidance for optimizing UPSH system design while maintaining operational safety and efficiency.

Scaling analysis using Froude similarity principles successfully demonstrated the applicability of laboratory findings to full-scale installations. The full-scale model, featuring 10 m diameter pipes in a 400 m x 200 m network, confirmed that fundamental hydraulic phenomena are preserved at larger scales. This validation provides confidence in applying laboratory-derived insights to real-world UPSH installations while identifying specific areas where scaling limitations must be considered.

The extensive geometric optimization studies revealed remarkable flexibility in network design, demonstrating that pipe spacing can be significantly reduced without compromising hydraulic performance. This geometric adaptability significantly enhances the potential for repurposing diverse abandoned mining facilities, as the hydraulic performance remains robust across a wide range of geometric constraints imposed by existing infrastructure.

From an engineering perspective, this research addresses several critical challenges for UPSH implementation. The accurate prediction of pressure wave magnitudes and timing enables proper structural design for peak hydraulic loads, identification of high-stress zones requiring protective measures and establishment of safe operational protocols. Understanding the four-phase hydraulic behavior provides crucial insights for operational control, including identification of stable periods for safe mode transitions and optimization of filling strategies to minimize energy losses.

The economic significance of this work extends beyond technical performance optimization. The demonstrated geometric flexibility enables adaptation to existing mining infrastructure without major modifications, potentially reducing capital costs by 20-30% compared to conventional pumped storage installations. The predictive capabilities developed provide design confidence that reduces engineering uncertainties and associated safety margins, further contributing to economic viability. For Belgium, with its extensive network of abandoned mines and topography unsuitable for conventional pumped storage, UPSH represents a particularly attractive pathway for expanding energy storage capacity.

While this research provides a solid foundation for UPSH hydraulic design, certain limitations must be acknowledged. The one-dimensional approach, while computationally efficient and suitable for long gallery sections, cannot fully capture three-dimensional flow patterns at junctions where complex vortices and recirculation zones develop. The model does not account for air-water interactions, which can be significant in underground systems where trapped air compression creates additional hydraulic resistance. Additionally, the numerical scheme introduces slight artificial dissipation that can attenuate rapid oscillations, as observed in the dam break validation where wave front propagation was marginally slower than analytical predictions.

These limitations suggest several promising directions for future research. A hybrid modeling approach combining efficient one-dimensional methods for straight sections with detailed three-dimensional analysis at complex junctions would improve accuracy while maintaining computational efficiency. Integration of air dynamics modeling would enable more realistic representation of underground filling processes, particularly important for rapid operational cycling. Coupling hydraulic analysis with rock mechanics would provide comprehensive assessment of structural stability under repeated loading cycles. Field-scale validation at sites such as the proposed Martelange installation would provide crucial full-scale verification and operational experience.

The broader significance of this research extends well beyond technical hydraulic analysis. As global renewable energy deployment accelerates, the intermittency challenges of wind and solar power create urgent demand for large-scale energy storage solutions. Underground Pumped Storage Hydropower offers a promising pathway for expanding storage capacity in regions lacking suitable topography for conventional systems, while simultaneously repurposing abandoned industrial infrastructure in an environmentally responsible manner. This alignment with circular economy principles represents more than technological innovation. It embodies sustainable development approaches that transform industrial heritage into renewable energy assets.

The numerical modeling framework developed in this thesis successfully bridges the gap between theoretical hydraulic analysis and practical engineering implementation. The tools and insights provided enable engineers to approach UPSH development with more confidence, armed with predictive capabilities necessary for safe, efficient and economical system design. The comprehensive understanding of complex hydraulic phenomena, validated through rigorous experimental comparison and extended through parametric analysis, establishes a robust foundation for transforming abandoned mining infrastructure into critical components of sustainable energy systems.

As the energy transition continues to accelerate, the ability to repurpose existing infrastructure while creating valuable storage capacity becomes increasingly important. This research demonstrates that with proper understanding and engineering analysis, the mines that once powered industrial growth can be reimagined to support clean energy integration, creating resilient infrastructure while preserving environmental heritage. The transformation of industrial relics into energy storage assets represents a powerful example of how technical innovation can serve both economic and environmental objectives, contributing to a more sustainable energy future built upon the foundations of our industrial past.

APPENDIX A

EXPERIMENTAL DATA

I Experimental graphs at $Q_{mean} = 0.55L/s$

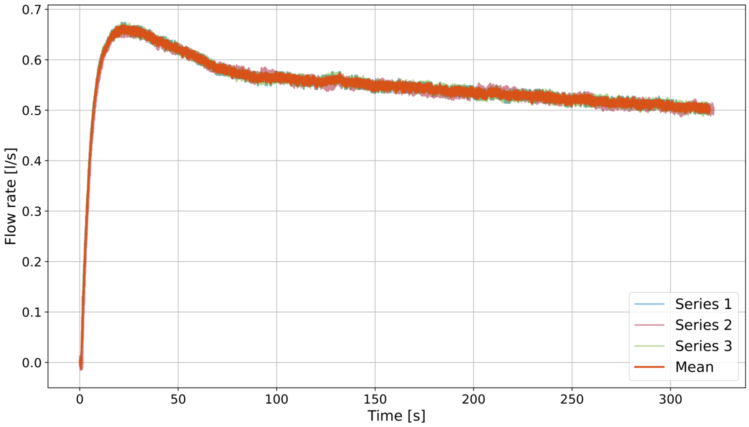

Figure A.1: Evolution of the experimental flow rate over time for $Q_{mean} = 0.5L/s$

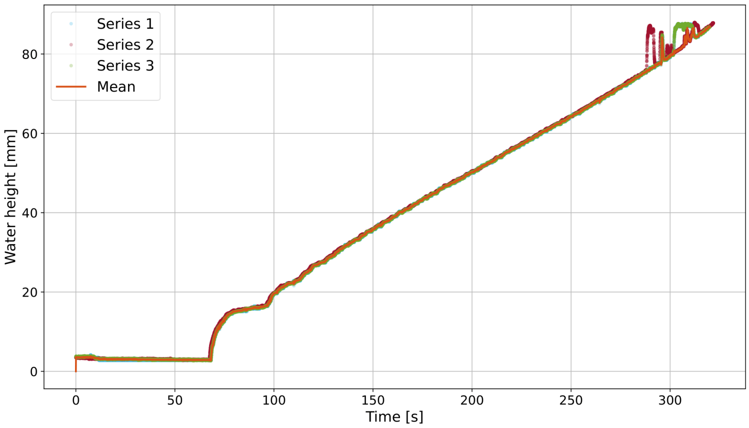

Figure A.2: Evolution of the water height over time at sensor 1 for $Q_{mean} = 0.5L/s$

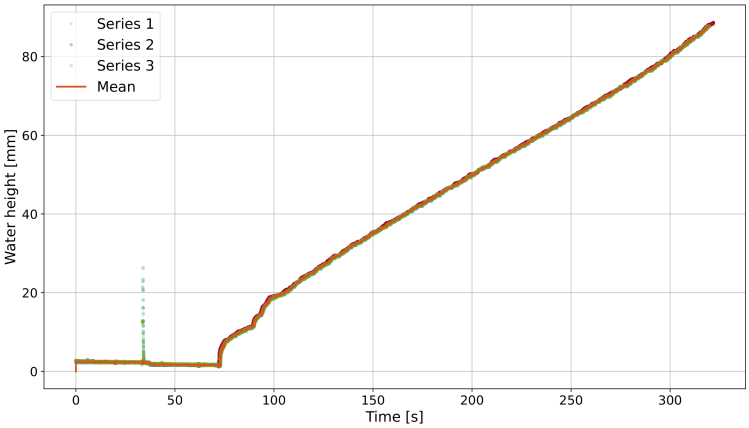

Figure A.3: Evolution of the water height over time at sensor 2 for $Q_{mean} = 0.5L/s$

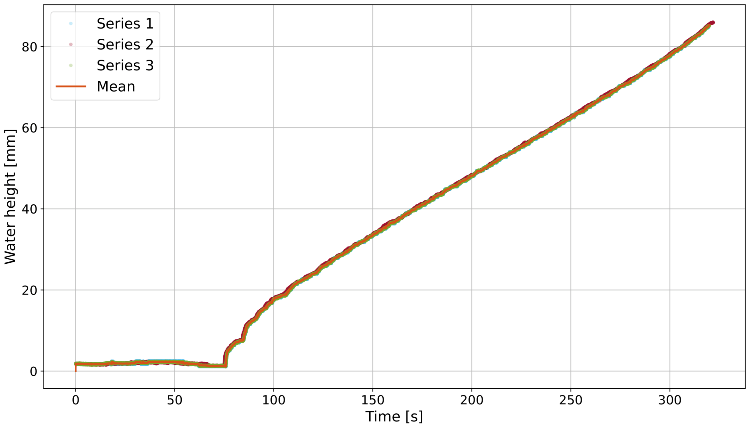

Figure A.4: Evolution of the water height over time at sensor 3 for $Q_{mean} = 0.5L/s$

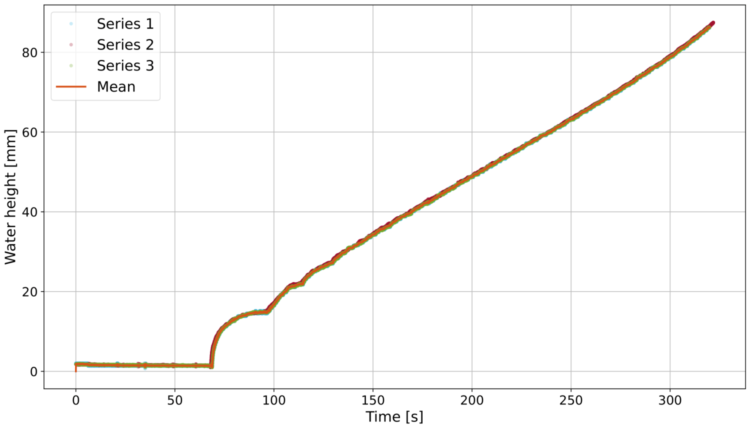

Figure A.5: Evolution of the water height over time at sensor 4 for $Q_{mean} = 0.5L/s$

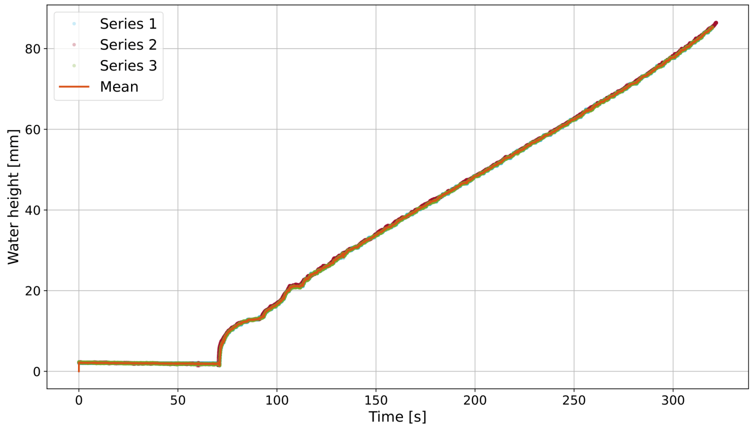

Figure A.6: Evolution of the water height over time at sensor 5 for $Q_{mean} = 0.5L/s$

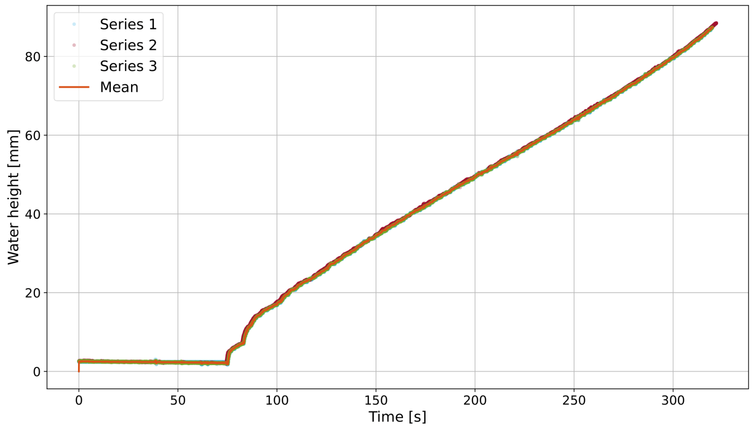

Figure A.7: Evolution of the water height over time at sensor 6 for $Q_{mean} = 0.5L/s$

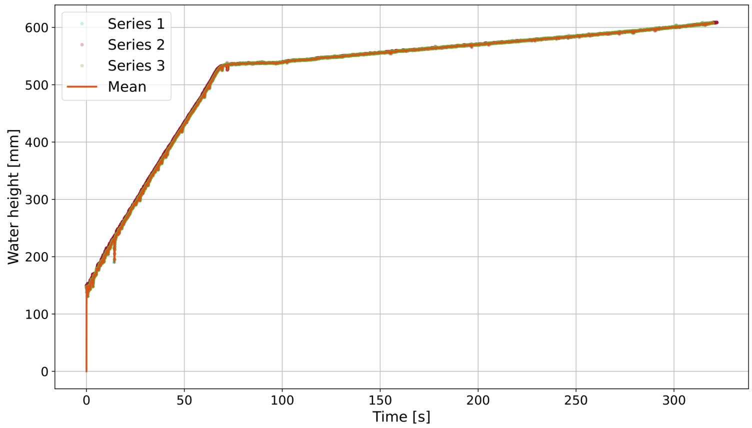

Figure A.8: Evolution of the water height over time at sensor 7 for $Q_{mean} = 0.5L/s$

II Experimental graphs at $Q_{mean} = 1.35L/s$

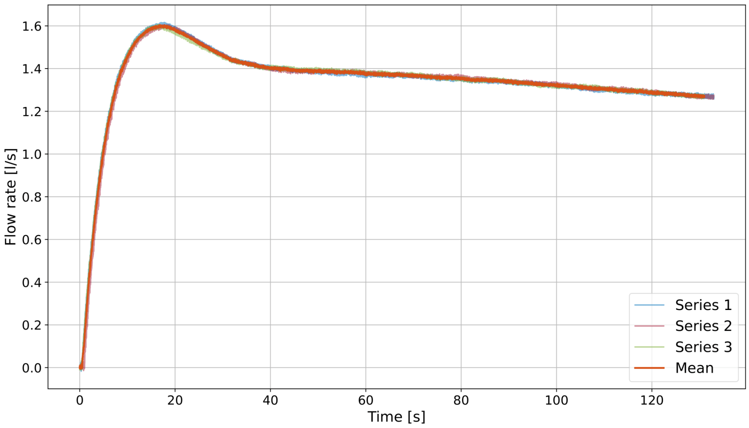

Figure A.9: Evolution of the experimental flow rate over time for $Q_{mean} = 1.35L/s$

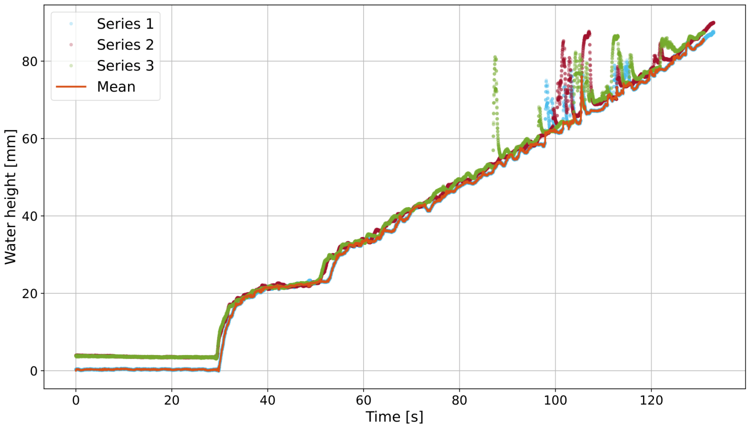

Figure A.10: Evolution of the water height over time at sensor 1 for $Q_{mean} = 1.35L/s$

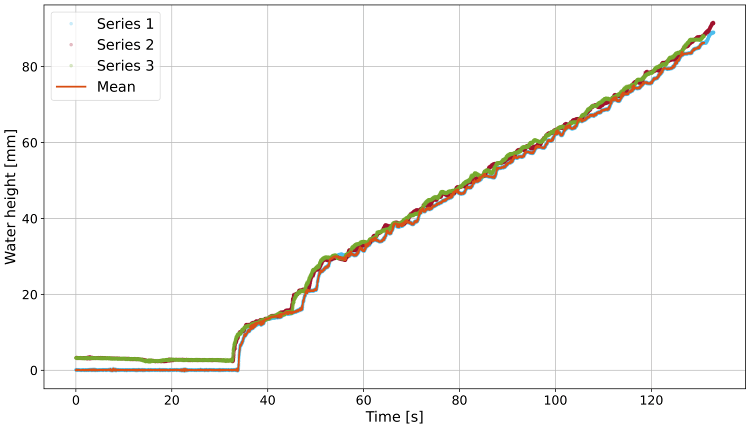

Figure A.11: Evolution of the water height over time at sensor 2 for $Q_{mean} = 1.35L/s$

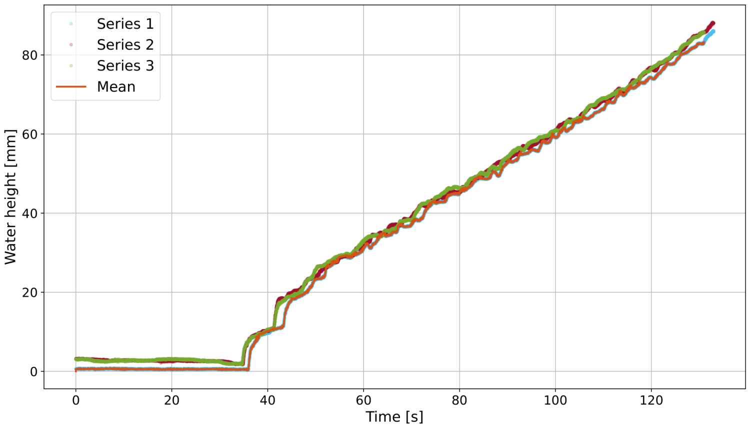

Figure A.12: Evolution of the water height over time at sensor 3 for $Q_{mean} = 1.35L/s$

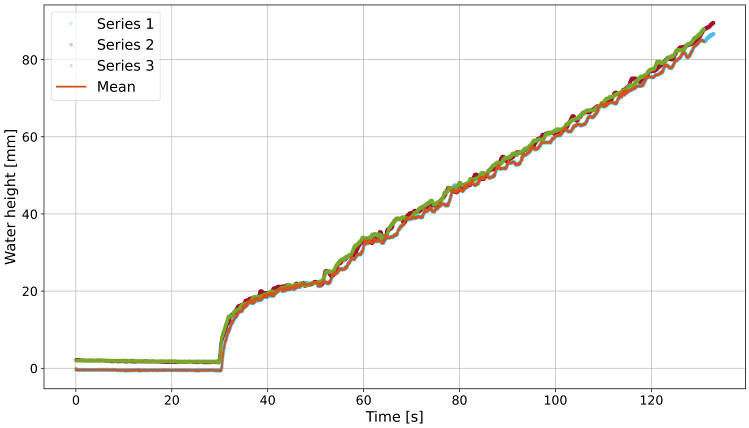

Figure A.13: Evolution of the water height over time at sensor 4 for $Q_{mean} = 1.35L/s$

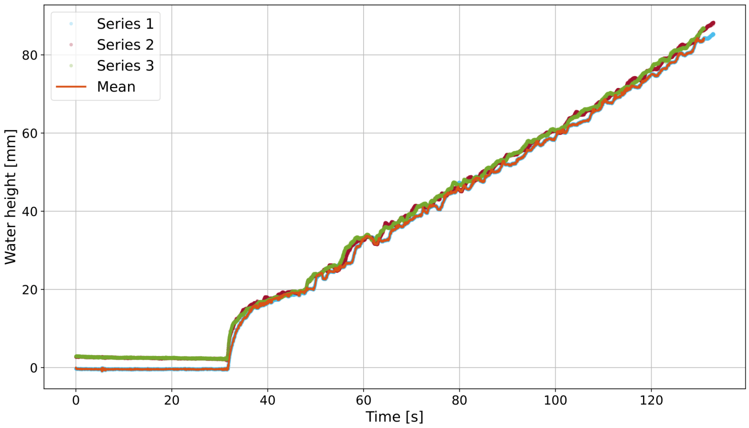

Figure A.14: Evolution of the water height over time at sensor 5 for $Q_{mean} = 1.35L/s$

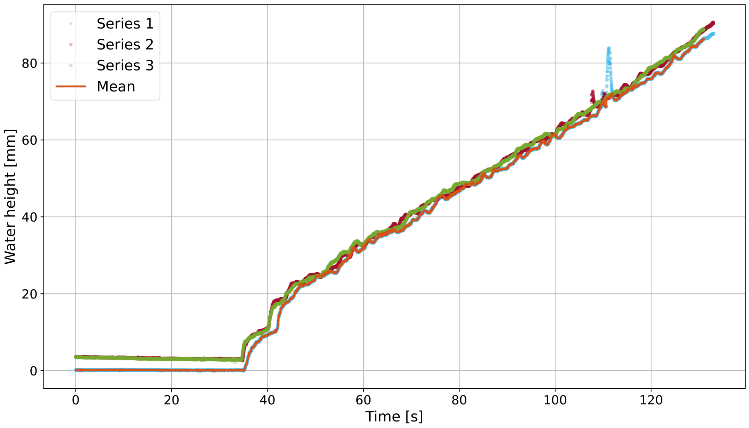

Figure A.15: Evolution of the water height over time at sensor 6 for $Q_{mean} = 1.35L/s$

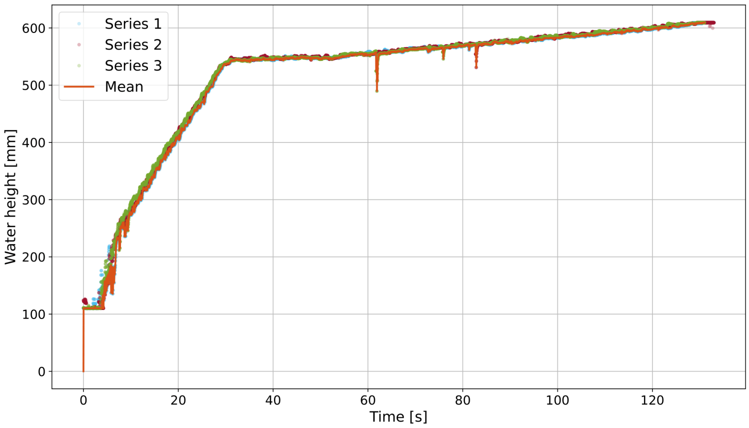

Figure A.16: Evolution of the water height over time at sensor 7 for $Q_{mean} = 1.35L/s$

III Experimental graphs at $Q_{mean} = 1.87L/s$

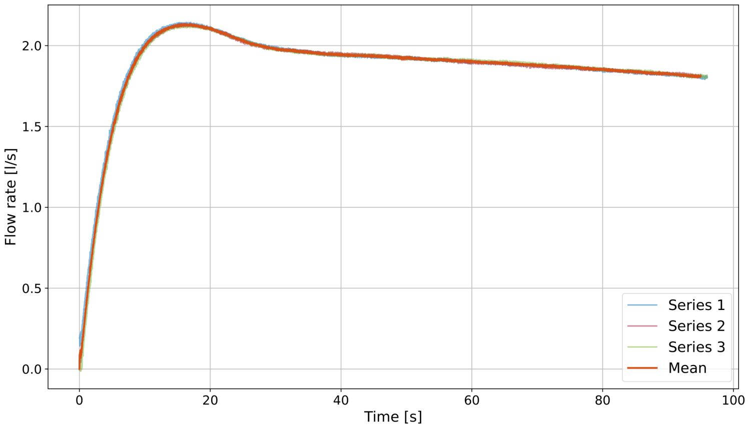

Figure A.17: Evolution of the experimental flow rate over time for $Q_{mean} = 1.87L/s$

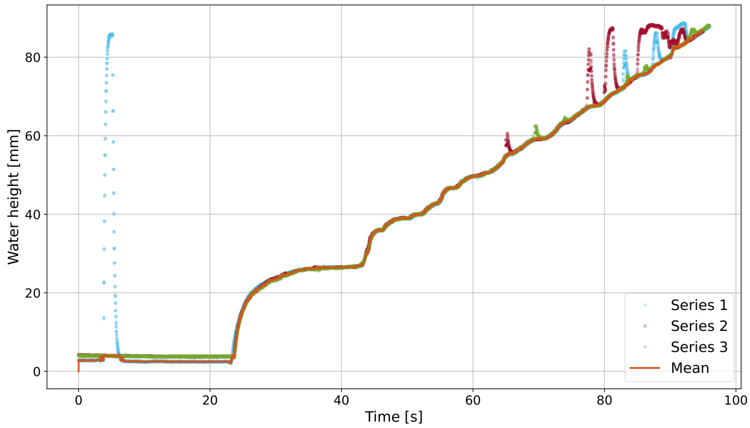

Figure A.18: Evolution of the water height over time at sensor 1 for $Q_{mean} = 1.87L/s$

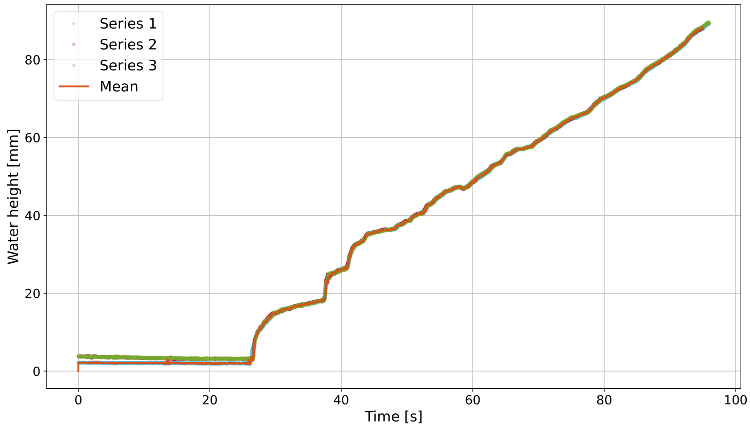

Figure A.19: Evolution of the water height over time at sensor 2 for $Q_{mean} = 1.87L/s$

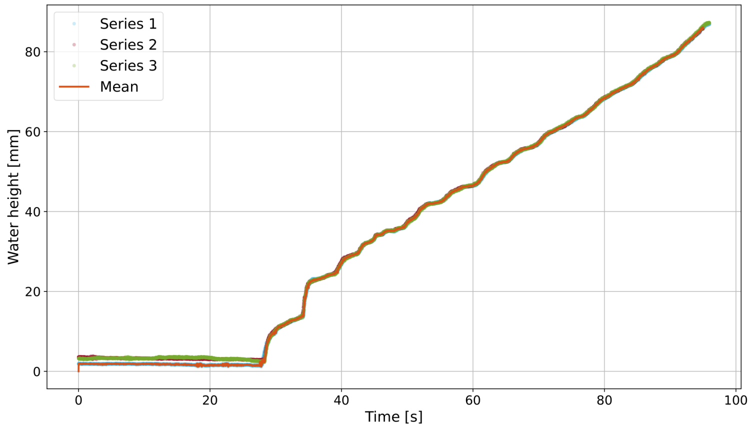

Figure A.20: Evolution of the water height over time at sensor 3 for $Q_{mean} = 1.87L/s$

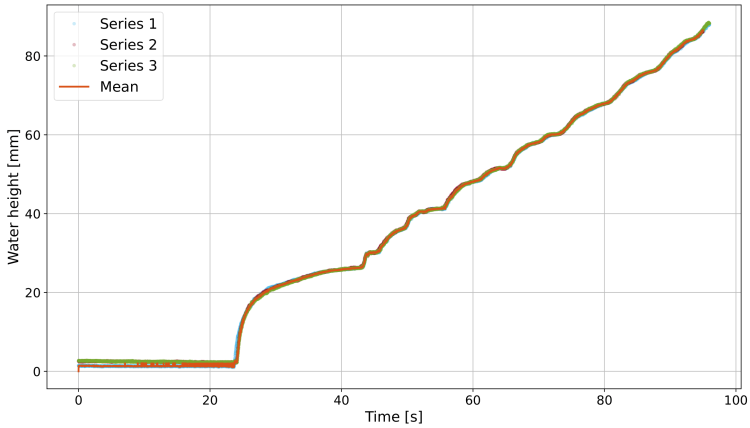

Figure A.21: Evolution of the water height over time at sensor 4 for $Q_{mean} = 1.87L/s$

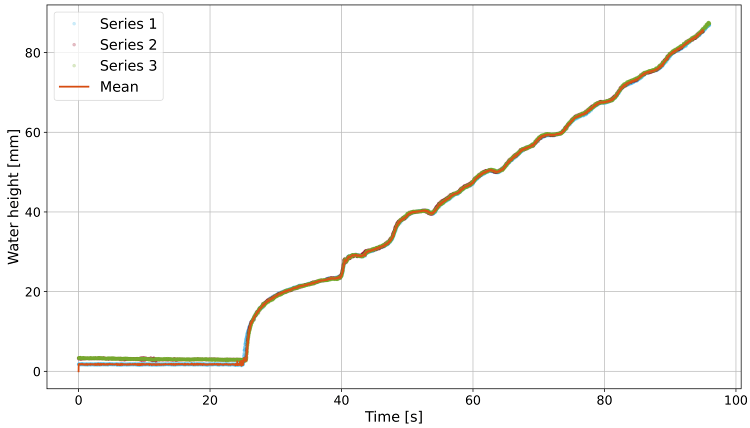

Figure A.22: Evolution of the water height over time at sensor 5 for $Q_{mean} = 1.87L/s$

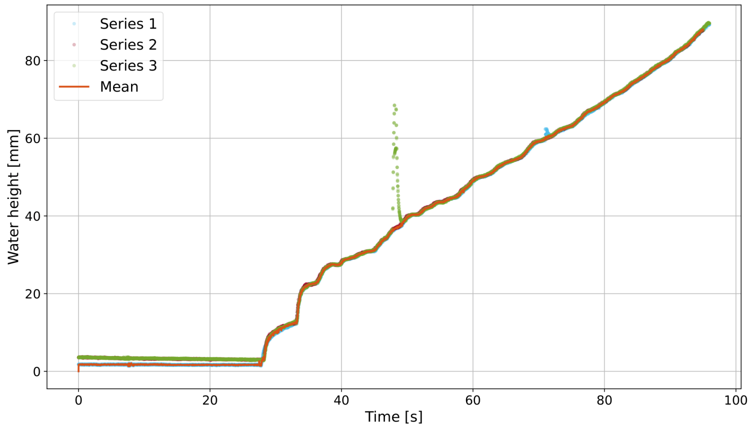

Figure A.23: Evolution of the water height over time at sensor 6 for $Q_{mean} = 1.87L/s$

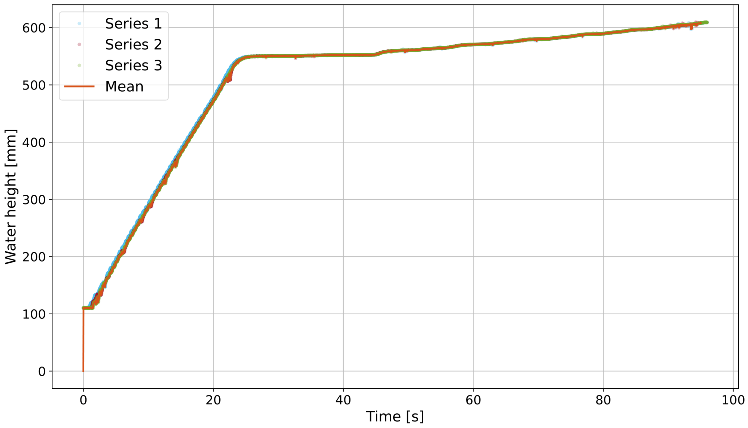

Figure A.24: Evolution of the water height over time at sensor 7 for $Q_{mean} = 1.87L/s$

IV Experimental graphs at $Q_{mean} = 2.50L/s$

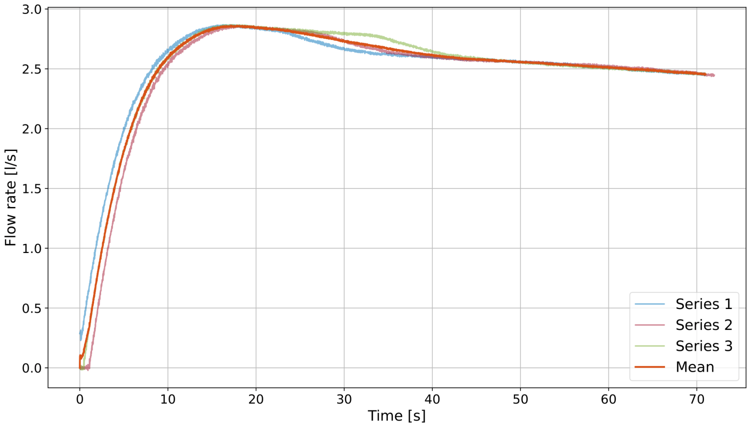

Figure A.25: Evolution of the experimental flow rate over time for $Q_{mean} = 2.5L/s$

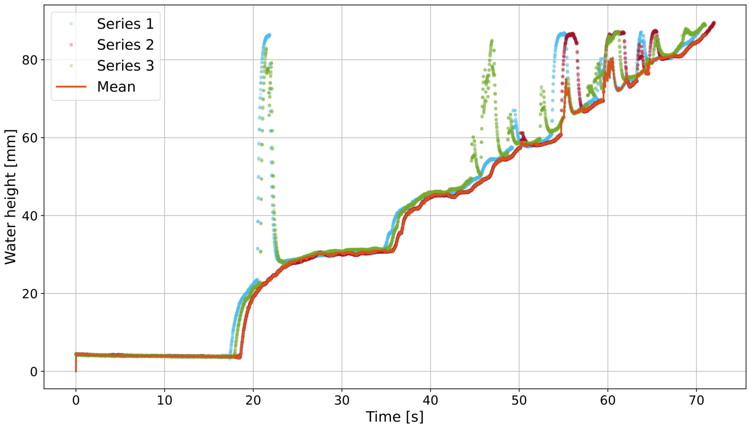

Figure A.26: Evolution of the water height over time at sensor 1 for $Q_{mean} = 2.5L/s$

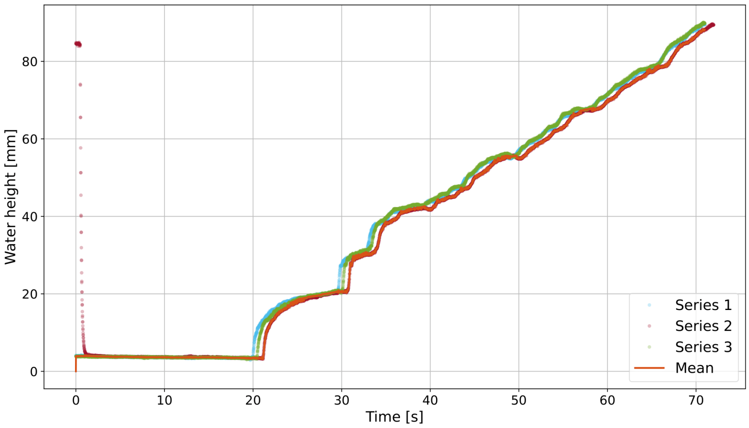

Figure A.27: Evolution of the water height over time at sensor 2 for $Q_{mean} = 2.5L/s$

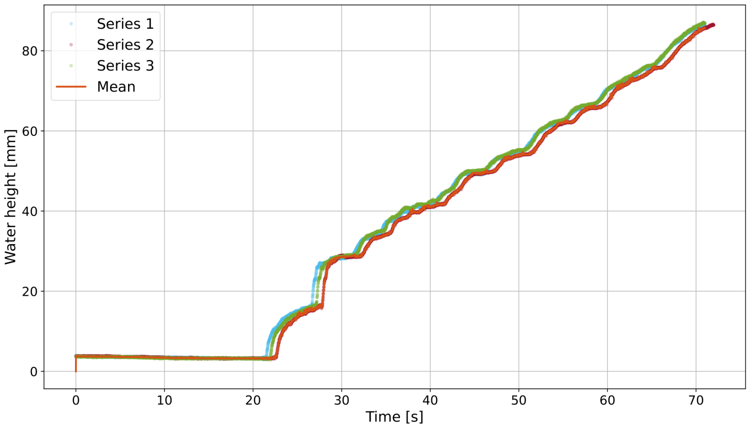

Figure A.28: Evolution of the water height over time at sensor 3 for $Q_{mean} = 2.5L/s$

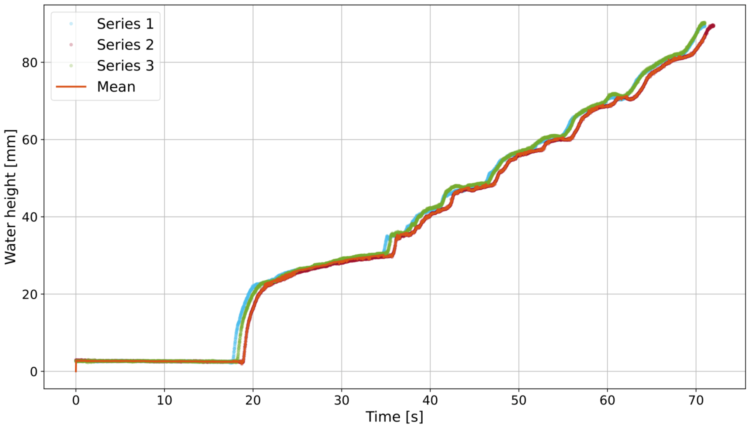

Figure A.29: Evolution of the water height over time at sensor 4 for $Q_{mean} = 2.5L/s$

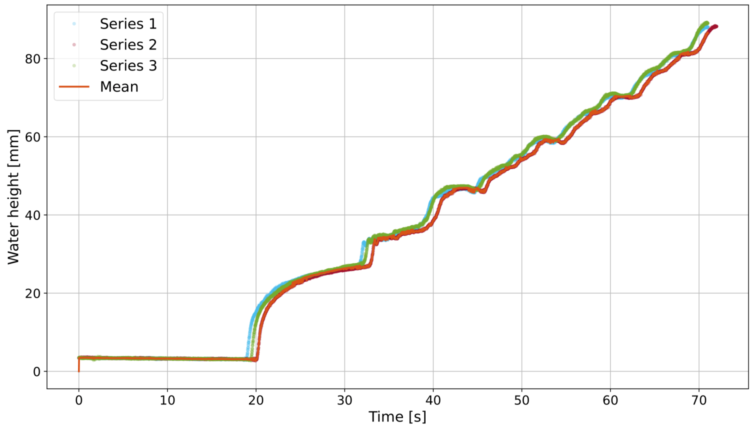

Figure A.30: Evolution of the water height over time at sensor 5 for $Q_{mean} = 2.5L/s$

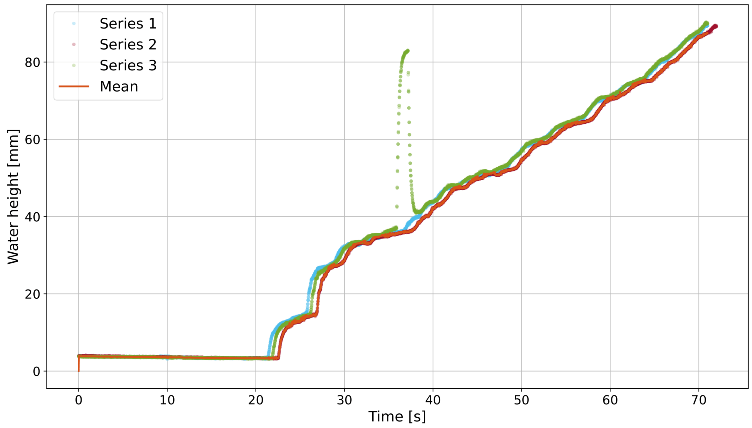

Figure A.31: Evolution of the water height over time at sensor 6 for $Q_{mean} = 2.5L/s$

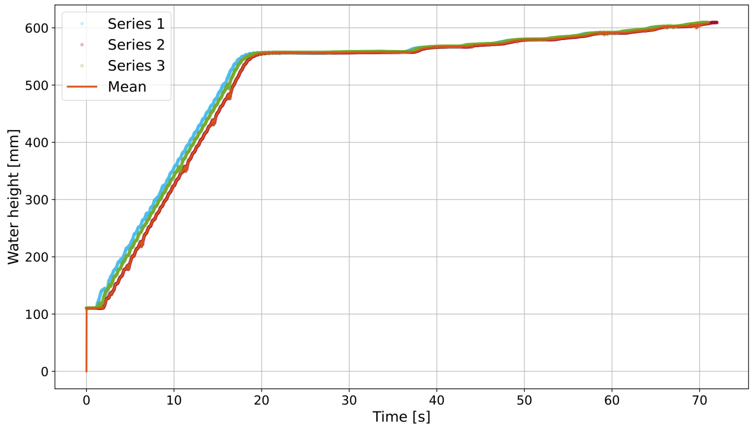

Figure A.32: Evolution of the water height over time at sensor 7 for $Q_{mean} = 2.5L/s$

APPENDIX B

DETAILED DERIVATIONS FOR THE NEWTON-RAPHSON METHOD

I Derivation of initial approximations

I.1 Small heights approximation

For small heights (when $A \leq \pi R^2/2$), we approximate the circular arc with a parabola.

We have the following geometric relationships:

- For a point (x, y) on the circle:
$$x^2 + y^2 = R^2 \tag{I.1}$$

- At height h:
$$y = R - h \tag{I.2}$$

- Finding the width L at height h:
$$x^2 + (R-h)^2 = R^2 \tag{I.3}$$
$$x^2 = R^2 - (R-h)^2 = R^2 - (R^2 - 2Rh + h^2) \tag{I.4}$$
$$x^2 = 2Rh - h^2 \tag{I.5}$$

- For $h \ll R$ (small heights approximation):
$$x^2 \approx 2Rh \tag{I.6}$$
$$L = 2x \approx 2\sqrt{2Rh} = 2R\sqrt{\frac{2h}{R}} \tag{I.7}$$

- Area approximation using parabolic shape:
$$A \approx \frac{2}{3} L \cdot h \text{ (area of a parabola)} \tag{I.8}$$

$$A \approx \frac{2}{3}\left(2R\sqrt{\frac{2h}{R}}\right) \cdot h \tag{I.9}$$

$$A \approx \frac{4}{3}R \cdot h \cdot \sqrt{\frac{2h}{R}} \tag{I.10}$$

$$A \approx \frac{4\sqrt{2}}{3}R \cdot h^{3/2} \cdot \frac{1}{\sqrt{R}} \tag{I.11}$$

- Solving for h:

$$h^{3/2} \approx \frac{3}{4\sqrt{2}} \cdot A \cdot \frac{\sqrt{R}}{R} \tag{I.12}$$

$$(h^{3/2})^{2/3} = h \approx \left(\frac{3}{4\sqrt{2}} \cdot A \cdot \frac{\sqrt{R}}{R}\right)^{2/3} \tag{I.13}$$

$$h \approx \left(\frac{3}{4\sqrt{2}}\right)^{2/3} \cdot A^{2/3} \cdot R^{-1/3} \tag{I.14}$$

I.2 Large heights approximation

For large heights (when $A > \pi R^2/2$), we use the symmetry of the problem and consider the complementary segment:

- Defining the complementary height:

$$h' = 2R - h \tag{I.15}$$

- Area of the complementary segment:

$$\pi R^2 - A \approx \frac{4\sqrt{2}}{3}R \cdot (h')^{3/2} \cdot \frac{1}{\sqrt{R}} \tag{I.16}$$

$$(h')^{3/2} \approx \frac{3}{4\sqrt{2}} \cdot (\pi R^2 - A) \cdot \frac{\sqrt{R}}{R} \tag{I.17}$$

- Final expression for h:

$$h = 2R - \left(\frac{3}{4\sqrt{2}}\right)^{2/3} \cdot (\pi R^2 - A)^{2/3} \cdot R^{-1/3} \tag{I.18}$$

II Derivation of derivatives for Newton-Raphson method

II.1 Derivative for $h \leq R$

The derivative $f'(h)$ if $h \leq R$ is:

$$f'(h) = \left[\frac{R^2}{2}(\theta - \sin\theta) - A\right]' = \frac{R^2}{2}\left(\frac{\partial\theta}{\partial h} - \cos\theta \cdot \frac{\partial\theta}{\partial h}\right) \tag{II.1}$$

We need to calculate $\frac{\partial\theta}{\partial h}$:

$$\frac{\partial\theta}{\partial h} = \frac{\partial\left(2\arccos(\frac{R-h}{R})\right)}{\partial h} \tag{II.2}$$

Using the chain rule and the derivative of arccos:

$$\frac{d}{dx}\arccos(x) = \frac{-1}{\sqrt{1-x^2}} \tag{II.3}$$

We get:

$$\frac{\partial\theta}{\partial h} = 2 \cdot \frac{-1}{\sqrt{1-\left(\frac{R-h}{R}\right)^2}} \cdot \frac{-1}{R} \tag{II.4}$$

$$\frac{\partial\theta}{\partial h} = \frac{2}{R\sqrt{1-\frac{R^2-2Rh+h^2}{R^2}}} \tag{II.5}$$

$$\frac{\partial\theta}{\partial h} = \frac{2}{R\sqrt{\frac{2Rh-h^2}{R^2}}} \tag{II.6}$$

$$\frac{\partial\theta}{\partial h} = \frac{2}{\sqrt{2Rh-h^2}} \tag{II.7}$$

Substituting back:

$$f'(h) = \frac{R^2}{2}\left(\frac{2}{\sqrt{2Rh-h^2}} - \cos\theta \cdot \frac{2}{\sqrt{2Rh-h^2}}\right) \tag{II.8}$$

$$f'(h) = \frac{R^2}{\sqrt{2Rh-h^2}}(1-\cos\theta) \tag{II.9}$$

II.2 Derivative for $h > R$

For $h > R$, the derivative follows a similar pattern but with the complementary angle:

$$f'(h) = \left[\pi R^2 - \frac{R^2}{2}(\theta - \sin\theta) - A\right]' \tag{II.10}$$

$$f'(h) = -\frac{R^2}{2}\left(\frac{\partial\theta}{\partial h} - \cos\theta \cdot \frac{\partial\theta}{\partial h}\right) \tag{II.11}$$

Using the new angle $\theta' = 2\arccos\left(\frac{h-R}{R}\right)$ and following similar steps:

$$f'(h) = \frac{R^2}{\sqrt{2R(2R-h)-(2R-h)^2}}(1-\cos\theta') \tag{II.12}$$

APPENDIX C

ADDITIONAL STEADY-STATE RESULTS

I Rectangular pipes

I.1 Still lake case

Parameters: Length: 10 m, Width: 0.2 m, Δx = 0.1 m, Slope: 0%, CFL = 0.15, $K = 100$ m$^{1/3}$/s.
Boundary conditions: $Q_{\text{upstream}} = 0$ m^3/s, $Q_{\text{downstream}} = 0$ m^3/s.
Initial conditions: $Q_{\text{initial}} = 0$ m^3/s, $h_{\text{initial}} = 0.7$ m.

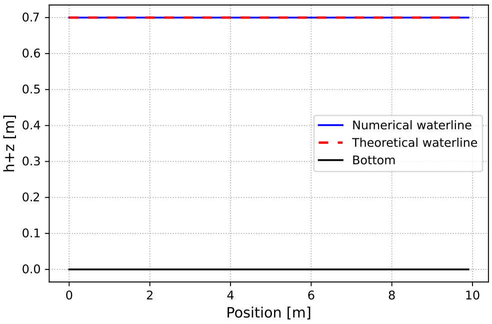

Figure C.1: Profiles of water surface elevation and discharge along the pipe: case of a still lake in a rectangular pipe

I.2 Non-zero slope lake case

Parameters: Length: 10 m, Width: 0.2 m, Δx = 0.1 m, Slope: 2%, CFL = 0.15, $K = 100$ m$^{1/3}$/s.
Boundary conditions: $Q_{\text{upstream}} = 0$ m^3/s, $Q_{\text{downstream}} = 0$ m^3/s.
Initial conditions: $Q_{\text{initial}} = 0$ m^3/s, $H_{\text{initial}} = z + h = 1$ m.

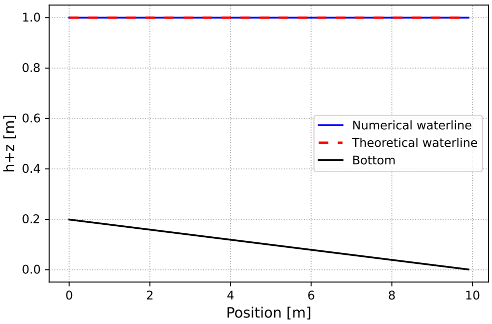

Figure C.2: Profiles of water surface elevation and discharge along the pipe: case of a non-zero slope lake in a rectangular pipe

I.3 Downstream subcritical flow

Parameters: Length: 10 m, Width: 0.2 m, Δx = 0.1 m, Slope: 0%, CFL = 0.15, $K = 100$ m$^{1/3}$/s.
Boundary conditions: $Q_{\text{upstream}} = 0.05$ m^3/s, $h_{\text{downstream}} = 0.2$ m.
Initial conditions: $Q_{\text{initial}} = 0.05$ m^3/s, $h_{\text{initial}} = 0.2$ m.

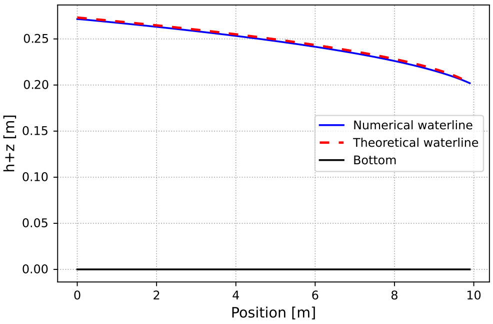

Figure C.3: Profiles of water surface elevation and discharge along the pipe: case of a downstream subcritical flow in a rectangular pipe

I.4 Upstream subcritical flow

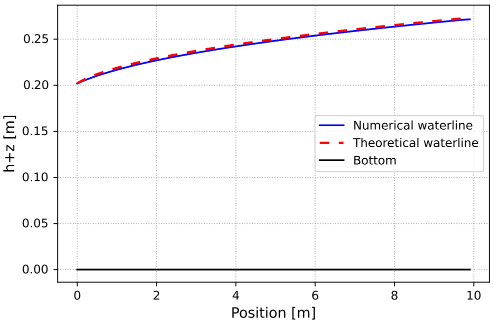

Figure C.4: Profiles of water surface elevation and discharge along the pipe: case of a upstream subcritical flow in a rectangular pipe

I.5 Downstream supercritical flow

Parameters: Length: 10 m, Width: 0.2 m, $\Delta x = 0.1$ m, Slope: 1%, CFL = 0.15, $K = 100\ \mathrm{m}^{1/3}/\mathrm{s}$.
Boundary conditions: $Q_{\text{upstream}} = 0.06\ \mathrm{m}^3/\mathrm{s}$, $h_{\text{upstream}} = 0.2$ m.
Initial conditions: $Q_{\text{initial}} = 0.06\ \mathrm{m}^3/\mathrm{s}$, $h_{\text{initial}} = 0.2$ m.

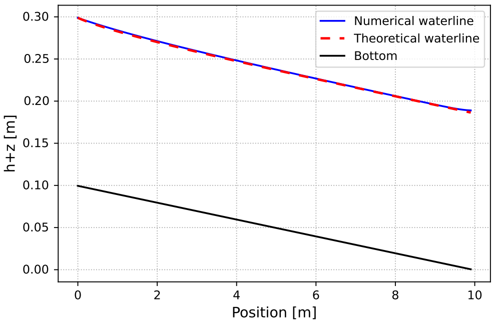

Figure C.5: Profiles of water surface elevation and discharge along the pipe: case of a downstream supercritical flow in a rectangular pipe

I.6 Upstream supercritical flow

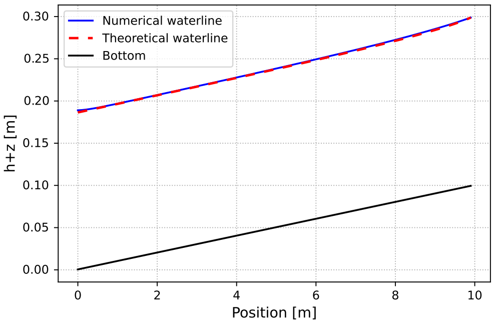

Figure C.6: Profiles of water surface elevation and discharge along the pipe: case of a upstream supercritical flow in a rectangular pipe

II Circular pipes

II.1 Upstream subcritical flow

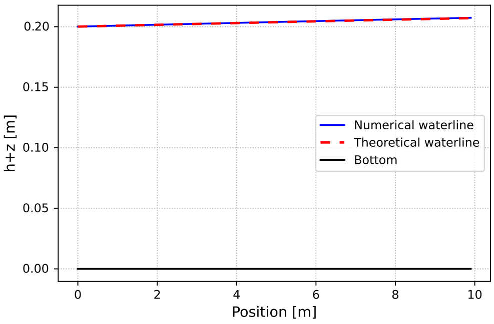

Figure C.7: Profiles of water surface elevation and discharge along the pipe: case of a upstream subcritical flow in a circular pipe

II.2 Upstream supercritical flow

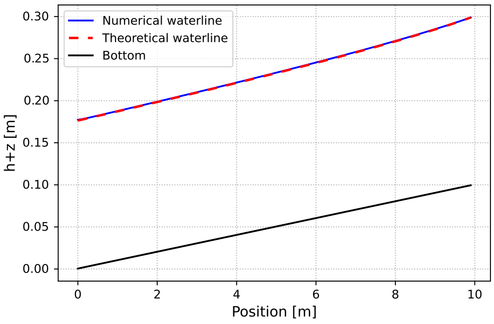

Figure C.8: Profiles of water surface elevation and discharge along the pipe: case of a upstream supercritical flow in a circular pipe

APPENDIX D

ADDITIONAL DAM BREAK RESULTS WITH COARSER GRID

I Constant reconstruction with $\Delta x = 100$ m

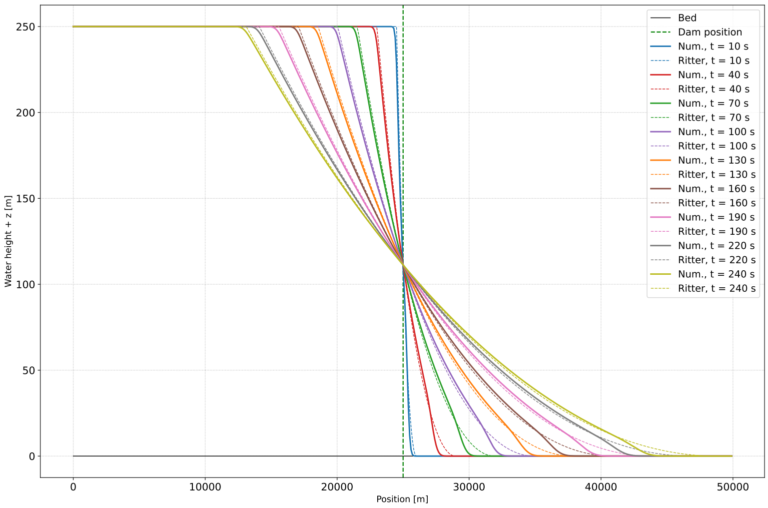

Figure D.1: Comparison between the numerical solution and Ritter's analytical solution for water height at different times, using constant reconstruction and $\Delta x = 100$ m.

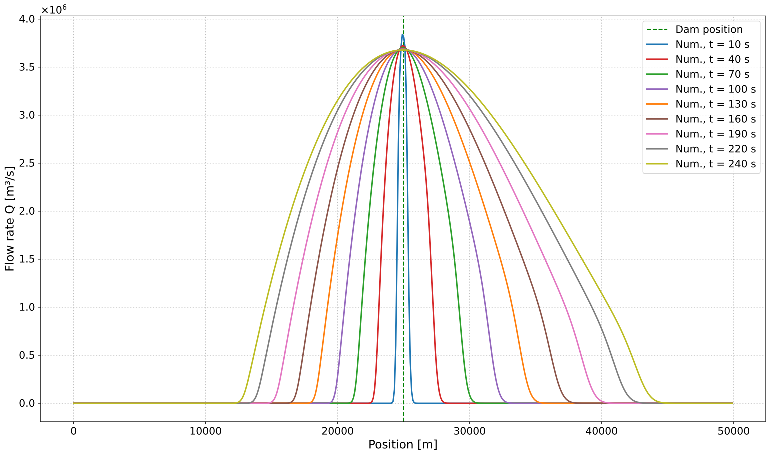

Figure D.2: Comparison between the numerical solution and Ritter's analytical solution for discharge at different times, using constant reconstruction and $\Delta x = 100$ m.

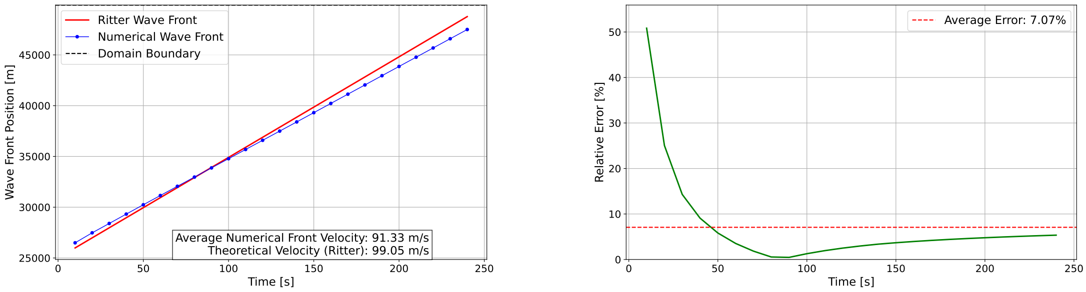

Figure D.3: Comparison between the position of the wavefront calculated numerically and with Ritter's method, along with the error in this position with constant reconstruction and $\Delta x = 100$ m.

II Linear reconstruction with $\Delta x = 100$ m

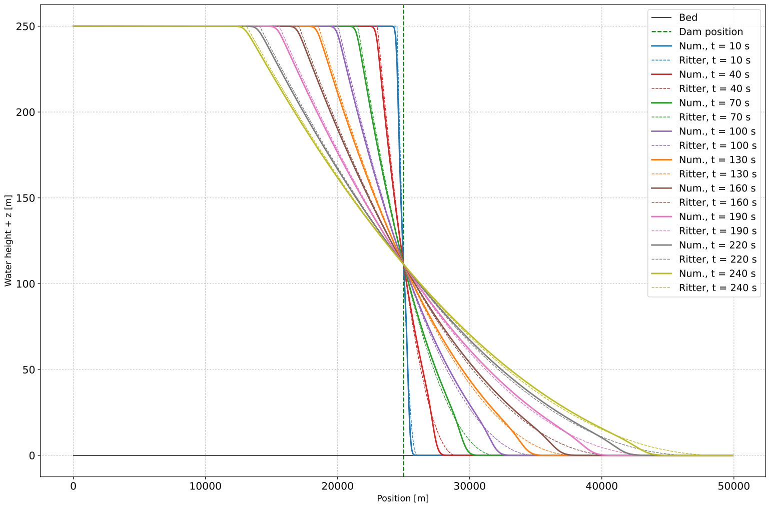

Figure D.4: Comparison between the numerical solution and Ritter's analytical solution for water height at different times, using linear reconstruction and $\Delta x = 100$ m.

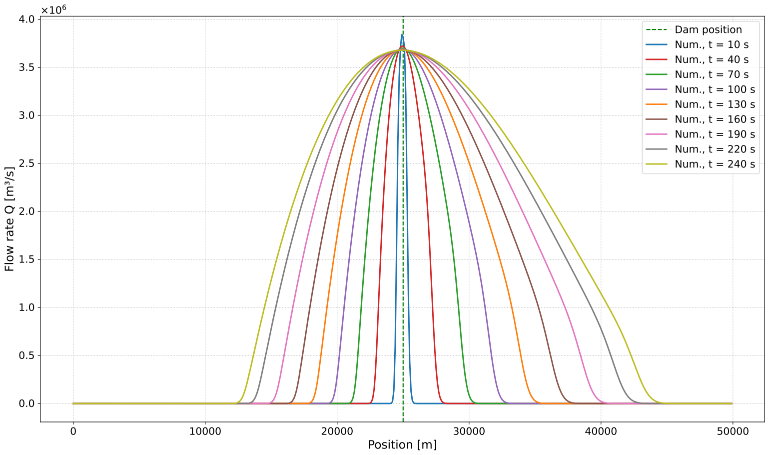

Figure D.5: Comparison between the numerical solution and Ritter's analytical solution for discharge at different times, using linear reconstruction and $\Delta x = 100$ m.

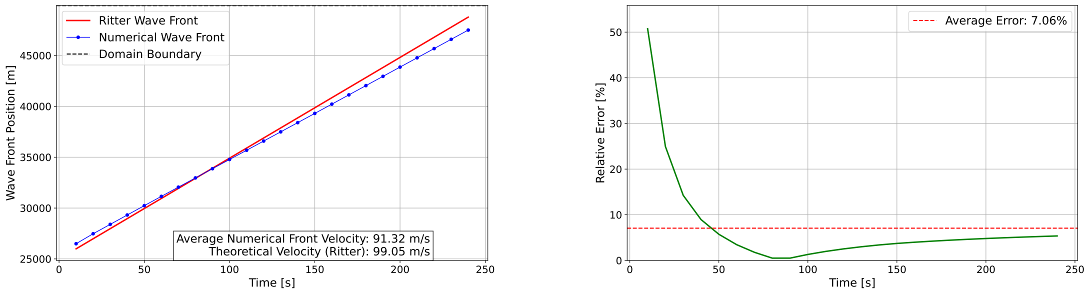

Figure D.6: Comparison between the position of the wavefront calculated numerically and with Ritter's method, along with the error in this position with linear reconstruction and $\Delta x = 100$ m.

APPENDIX E

SENSITIVITY ANALYSIS

I Initial water height sensitivity

Figures E.1 through E.4 show the sensitivity of the model to the initial water height parameter (h_{min}) for each of the four flow rates tested.

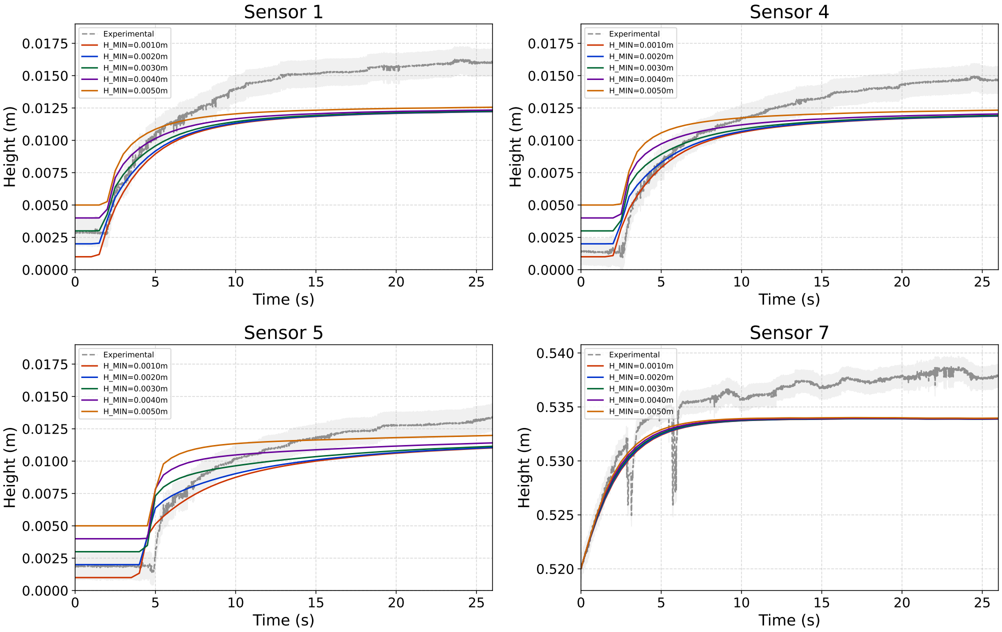

Figure E.1: Comparison of water height evolution at different sensors for various h_{min} values (Q_{mean} = 0.55 $\cdot$ 10^{-3} m^3/s, K = 90 $m^{1/3}/s$, Δx_{tank} = 0.2m

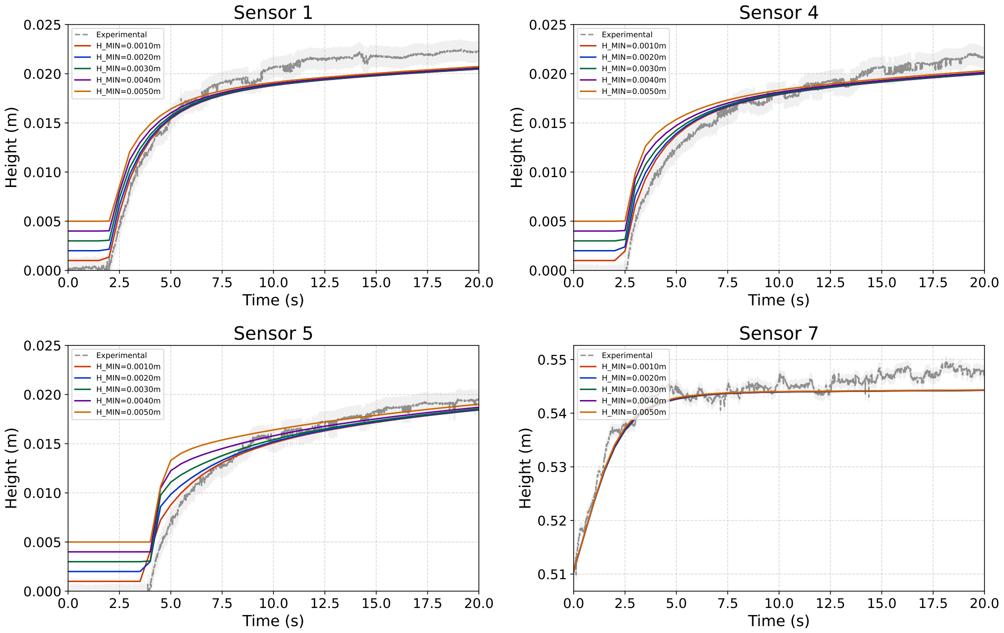

Figure E.2: Comparison of water height evolution at different sensors for various h_{min} values ($Q_{mean} = 1.35 \cdot 10^{-3}$ m^3/s, K = 90 m$^{1/3}$/s, Δx_{tank} = 0.2m

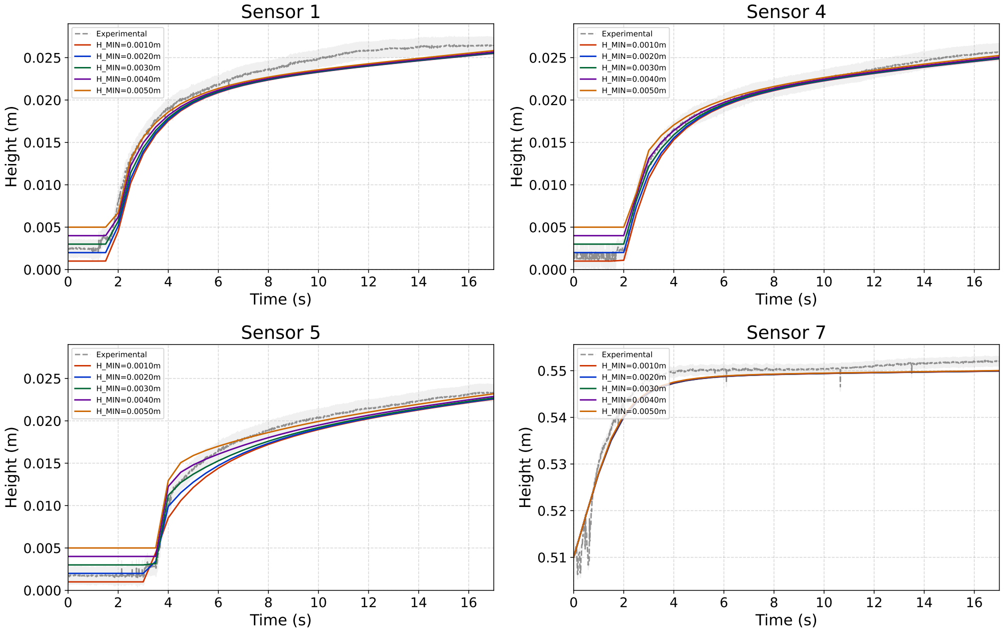

Figure E.3: Comparison of water height evolution at different sensors for various h_{min} values ($Q_{mean} = 1.87 \cdot 10^{-3}$ m^3/s, K = 90 m$^{1/3}$/s, Δx_{tank} = 0.2m

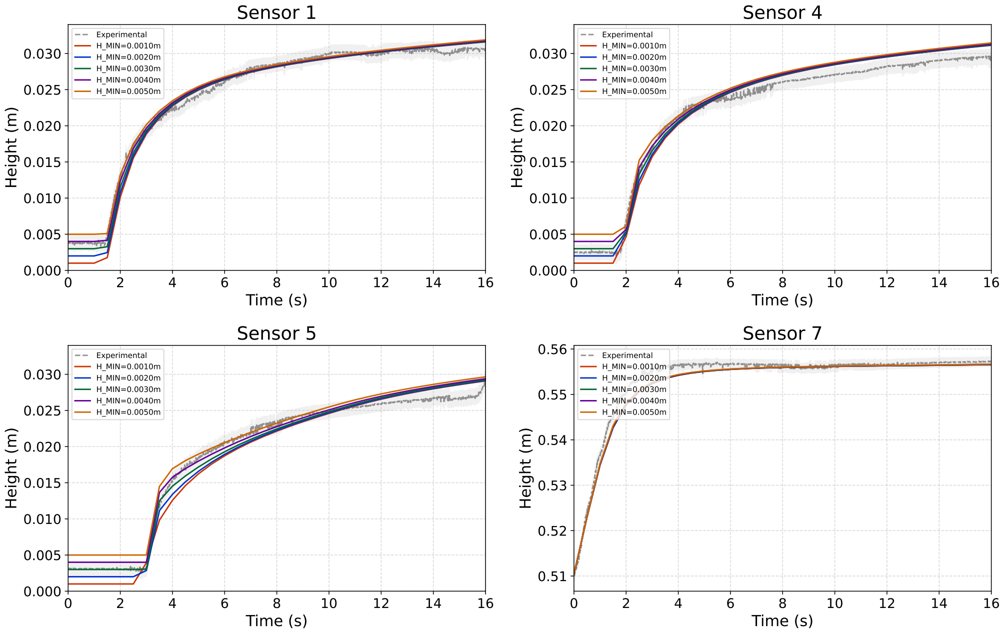

Figure E.4: Comparison of water height evolution at different sensors for various h_{min} values (Q_{mean} = 2.5 · 10^{-3} m^3/s, K = 90 $m^{1/3}$/s, Δx_{tank} = 0.2m

II Friction coefficient sensitivity

Figures E.5 through E.8 illustrate the model sensitivity to the Strickler friction coefficient (K) for each flow rate.

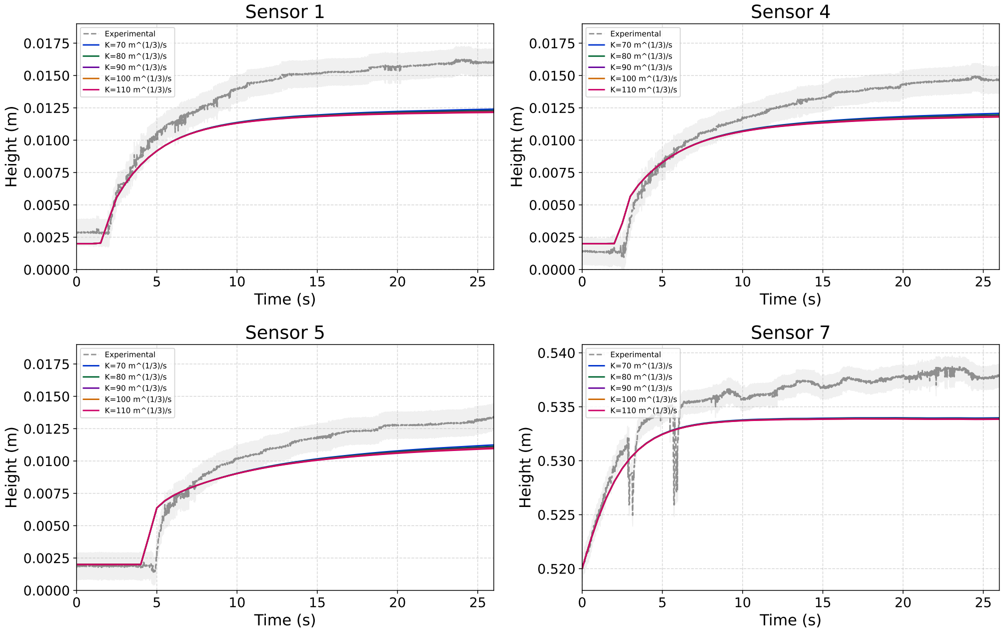

Figure E.5: Comparison of water height evolution at different sensors for various K values ($Q_{mean} = 0.55 \cdot 10^{-3}$ m^3/s, $h_{min} = 0.002$ m, $\Delta x_{tank} = 0.2$ m)

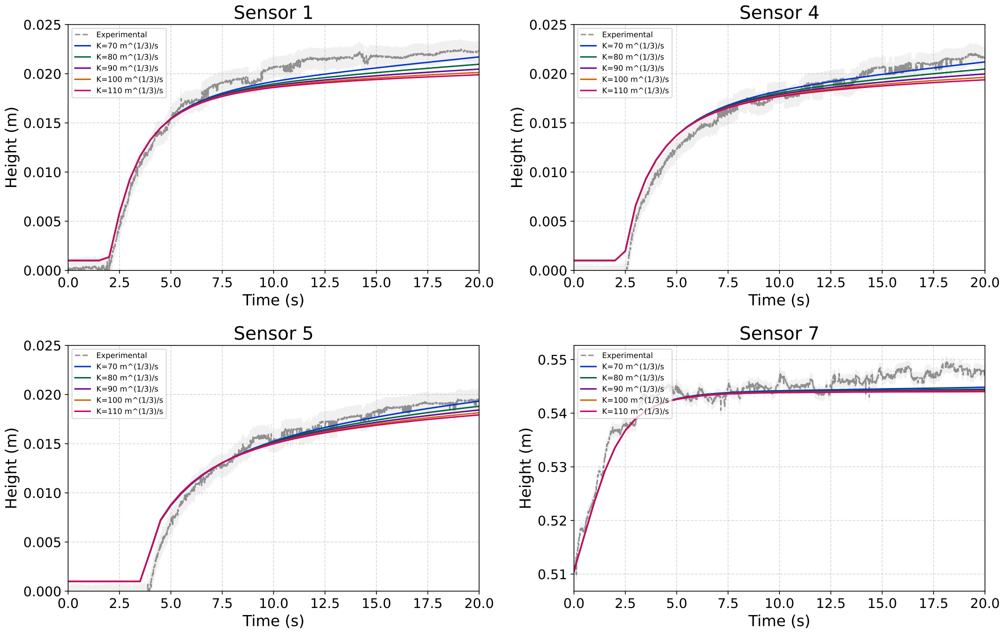

Figure E.6: Comparison of water height evolution at different sensors for various K values ($Q_{mean} = 1.35 \cdot 10^{-3}$ m^3/s, $h_{min} = 0.001$ m, $\Delta x_{tank} = 0.2$ m)

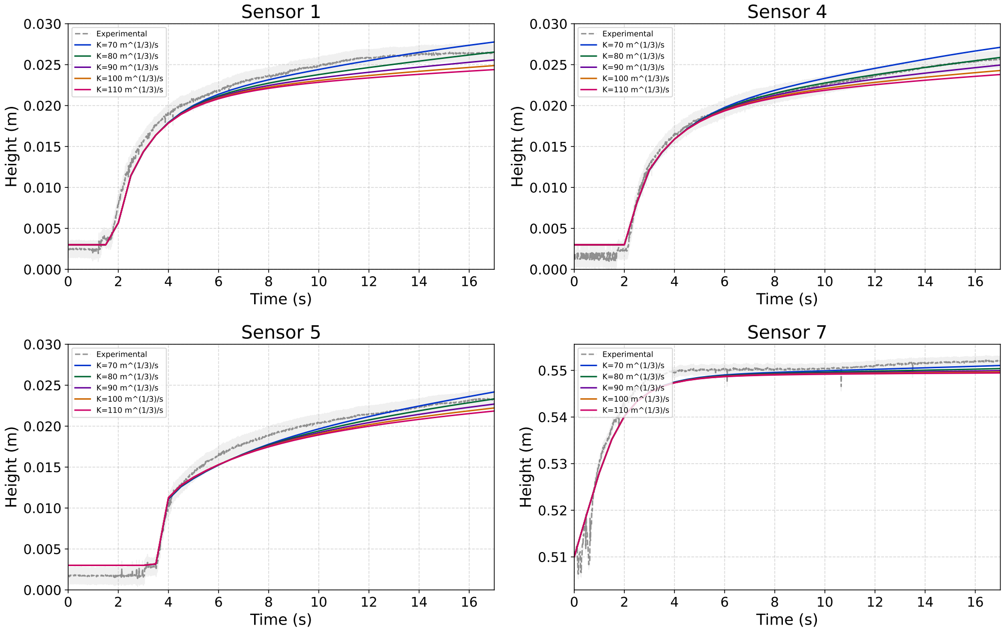

Figure E.7: Comparison of water height evolution at different sensors for various K values ($Q_{mean} = 1.87 \cdot 10^{-3}$ m^3/s, $h_{min} = 0.003$ m, $\Delta x_{tank} = 0.2$ m)

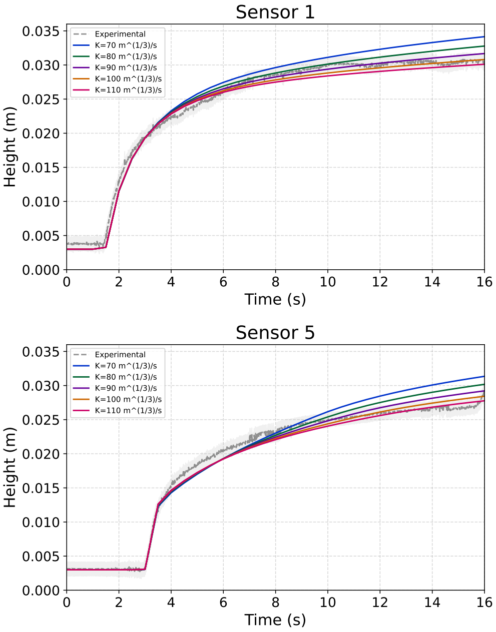

Figure E.8: Comparison of water height evolution at different sensors for various K values ($Q_{mean} = 2.5 \cdot 10^{-3}$ m^3/s, $h_{min} = 0.003$ m, $\Delta x_{tank} = 0.2$ m)

III Injection point cell length (Δx_{tank} sensitivity)

Figures E.9 through E.12 show the sensitivity to the injection point cell length (Δx_{tank}) for each flow rate.

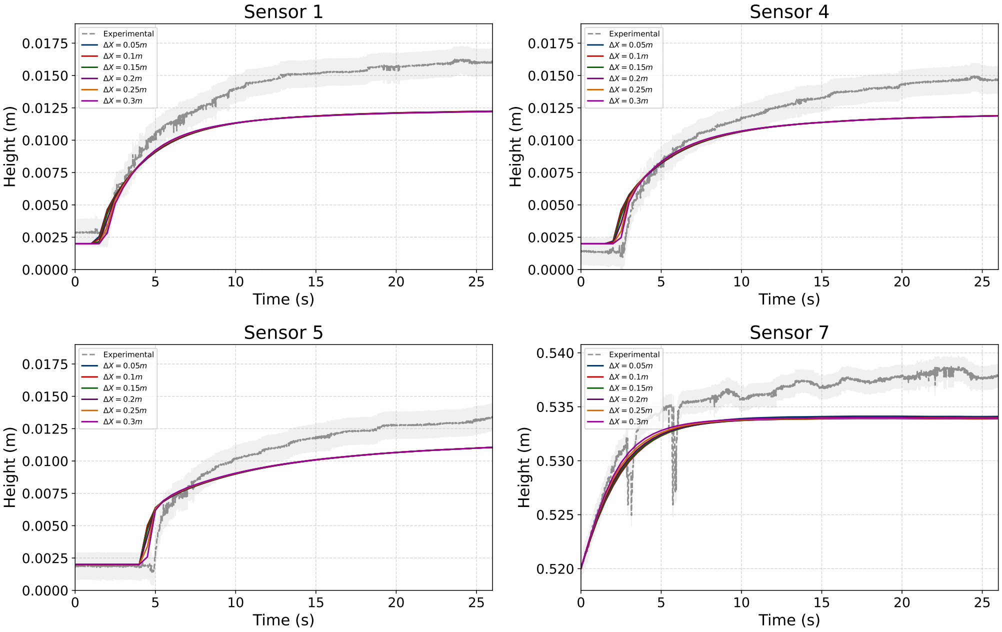

Figure E.9: Comparison of water height evolution at different sensors for various Δx_{tank} values ($Q_{mean} = 0.55 \cdot 10^{-3}$ m^3/s, $h_{min} = 0.002$ m, $K = 90$ m$^{1/3}$/s)

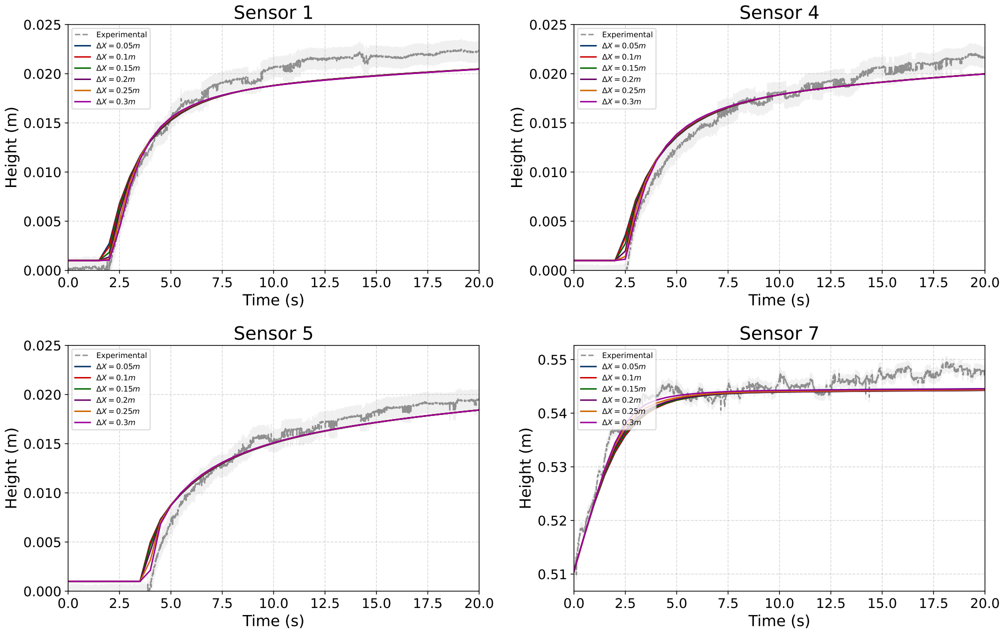

Figure E.10: Comparison of water height evolution at different sensors for various Δx_{tank} values ($Q_{mean} = 1.35 \cdot 10^{-3}$ m^3/s, $h_{min} = 0.001$ m, $K = 90$ m$^{1/3}$/s)

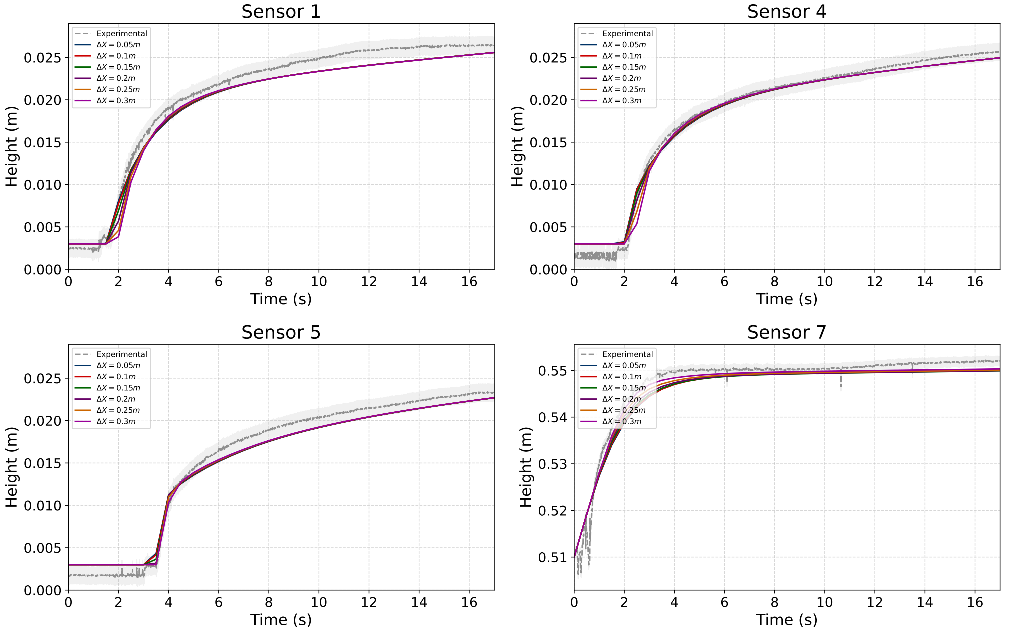

Figure E.11: Comparison of water height evolution at different sensors for various Δx_{tank} values ($Q_{mean} = 1.87 \cdot 10^{-3}$ m^3/s, $h_{min} = 0.003$ m, $K = 90$ m$^{1/3}$/s)

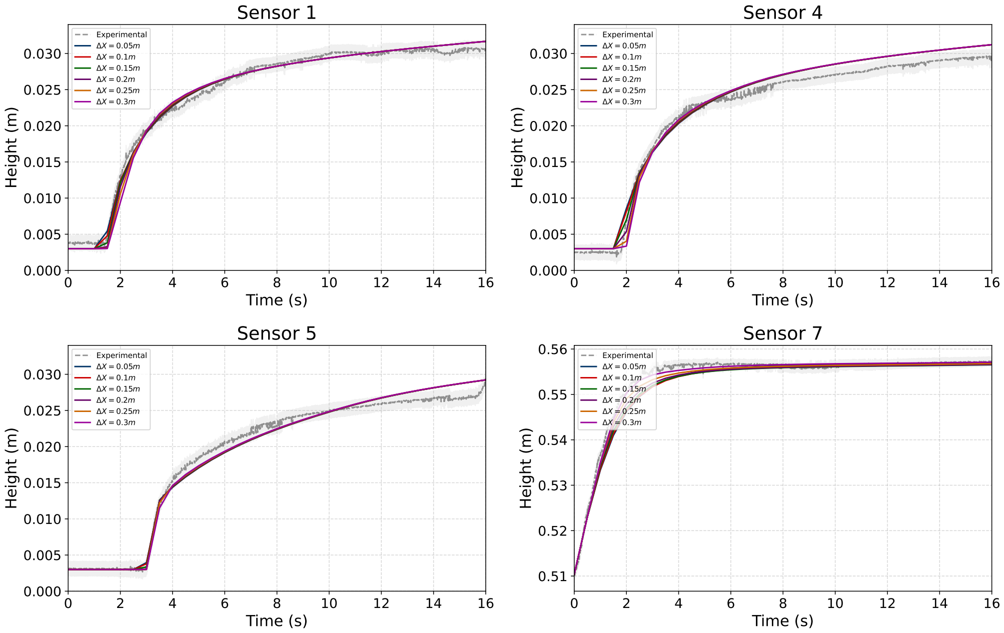

Figure E.12: Comparison of water height evolution at different sensors for various Δx_{tank} values ($Q_{mean} = 2.5 \cdot 10^{-3}$ m^3/s, $h_{min} = 0.002$ m, $K = 90$ m$^{1/3}$/s)

APPENDIX F

COMPARISON WITH EXPERIMENTAL DATA FOR SENSORS LOCATED IN PIPES IN CONTACT WITH THE TANK BEFORE THE FIRST REFLEXION

I Results for $Q_{mean} = 0.55$ L/s

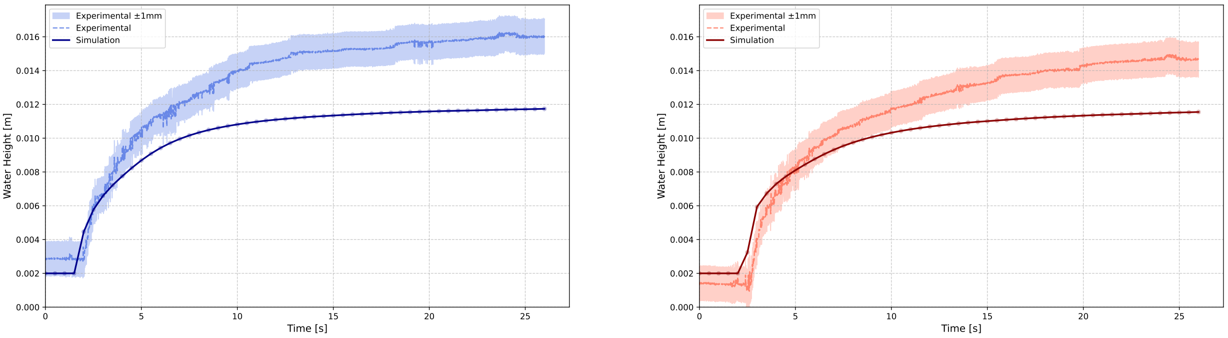

Figure F.1: Evolution of water height over time at sensors 1 (on the left) and 4 (on the right) with a time delay of 66.22 seconds, $h_{min} = 0.002$ m, $\Delta x_{tank} = 0.2$m, $K = 90 m^{1/3}/s$ and a mean flow rate of $0.55 * 10^{-3} m^3/s$

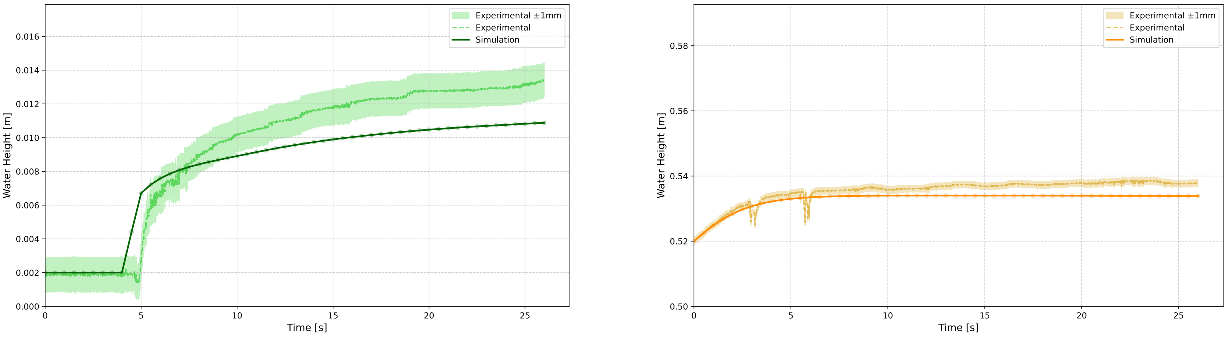

Figure F.2: Evolution of water height over time at sensors 5 (on the left) and 7 (on the right) with a time delay of 66.22 seconds, $h_{min} = 0.002$ m, $\Delta x_{tank} = 0.2$m, $K = 90 m^{1/3}/s$ and a mean flow rate of $0.55 * 10^{-3} m^3/s$

II Results for $Q_{mean} = 1.35$ L/s

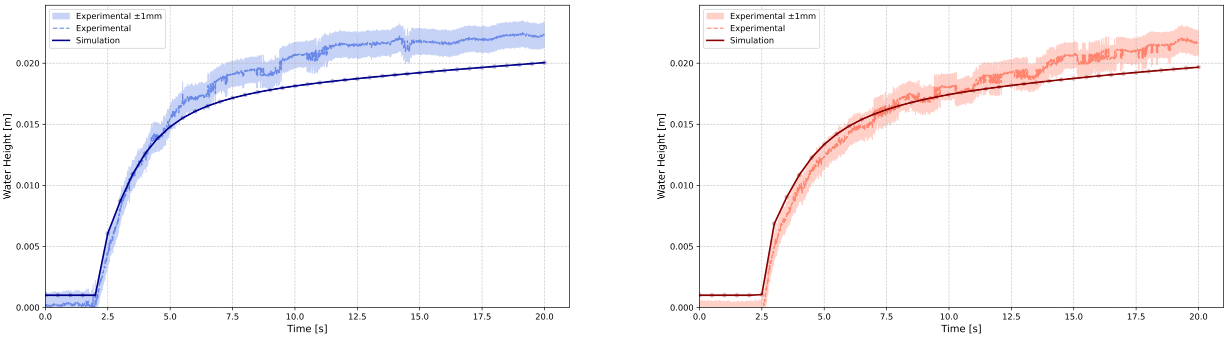

Figure F.3: Evolution of water height over time at sensors 1 (on the left) and 4 (on the right) with a time delay of 27.83 seconds, $h_{min} = 0.001$ m, $\Delta x_{tank} = 0.2$m, $K = 90 m^{1/3}/s$ and a mean flow rate of $1.35 * 10^{-3} m^3/s$

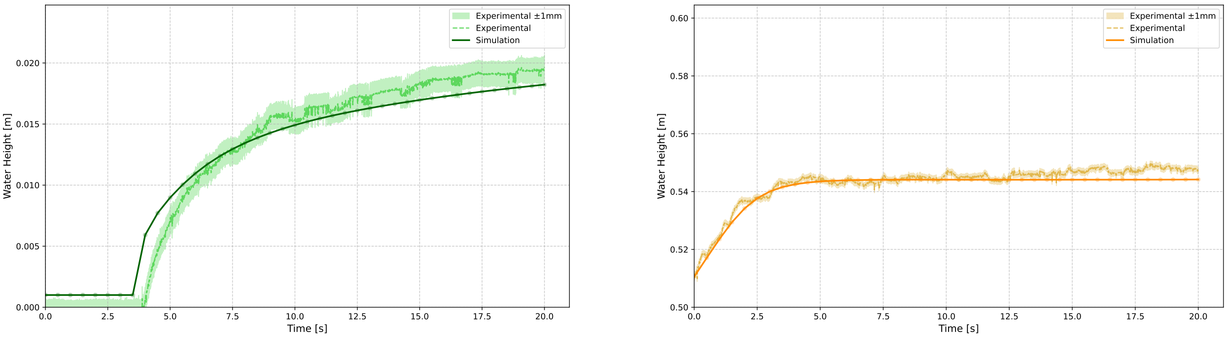

Figure F.4: Evolution of water height over time at sensors 5 (on the left) and 7 (on the right) with a time delay of 27.83 seconds, $h_{min} = 0.001$ m, $\Delta x_{tank} = 0.2$m, $K = 90 m^{1/3}/s$ and a mean flow rate of $1.35 * 10^{-3} m^3/s$

III Results for $Q_{mean} = 1.87$ L/s

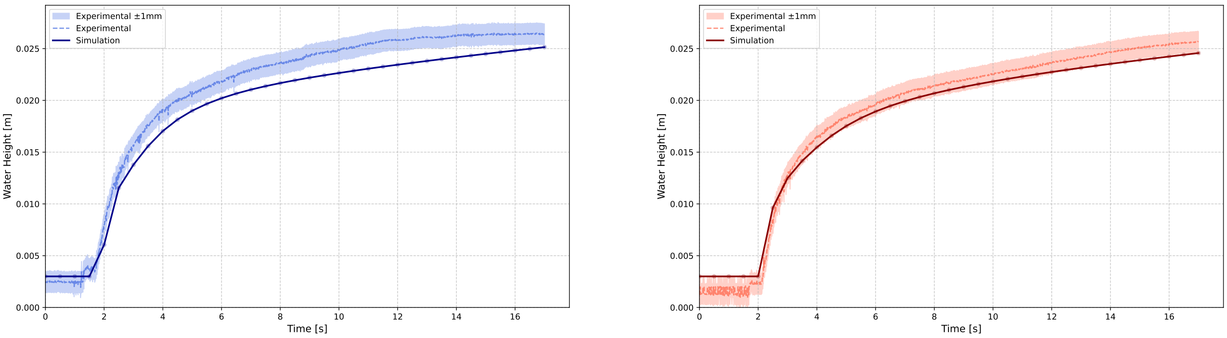

Figure F.5: Evolution of water height over time at sensors 1 (on the left) and 4 (on the right) with a time delay of 22 seconds, $h_{min} = 0.003$ m, $\Delta x_{tank} = 0.2$m, $K = 90 m^{1/3}/s$ and a mean flow rate of $1.87 * 10^{-3} m^3/s$

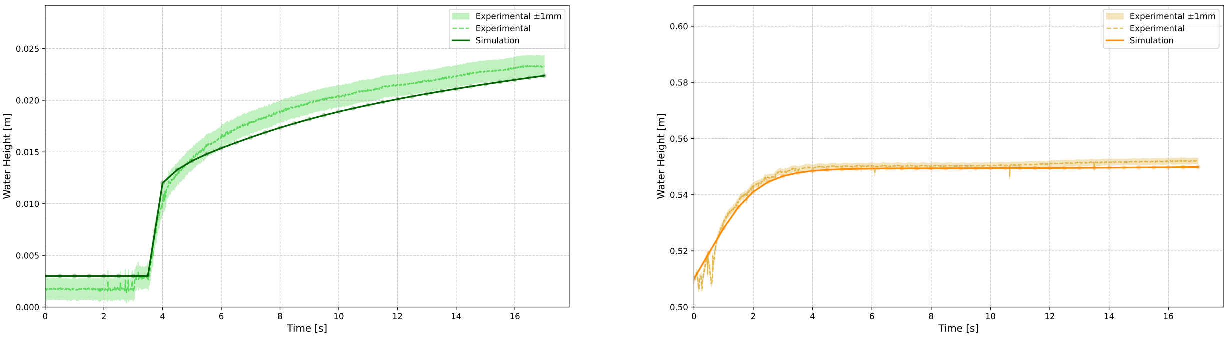

Figure F.6: Evolution of water height over time at sensors 5 (on the left) and 7 (on the right) with a time delay of 22 seconds, $h_{min} = 0.003$ m, $\Delta x_{tank} = 0.2$m, $K = 90 m^{1/3}/s$ and a mean flow rate of $1.87 * 10^{-3} m^3/s$

IV Results for $Q_{mean} = 2.5$ L/s

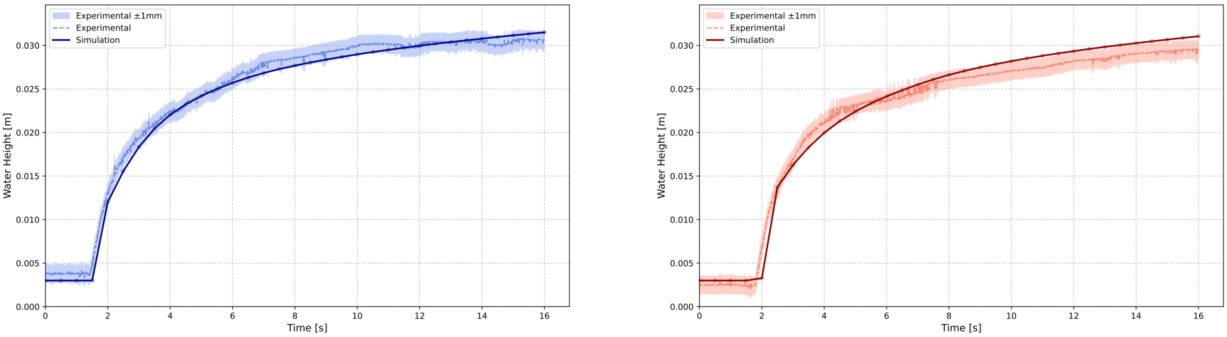

Figure F.7: Evolution of water height over time at sensors 1 (on the left) and 4 (on the right) with a time delay of 17.11 seconds, $h_{min} = 0.003$ m, $\Delta x_{tank} = 0.2$m, $K = 90 m^{1/3}/s$ and a mean flow rate of $2.5 * 10^{-3} m^3/s$

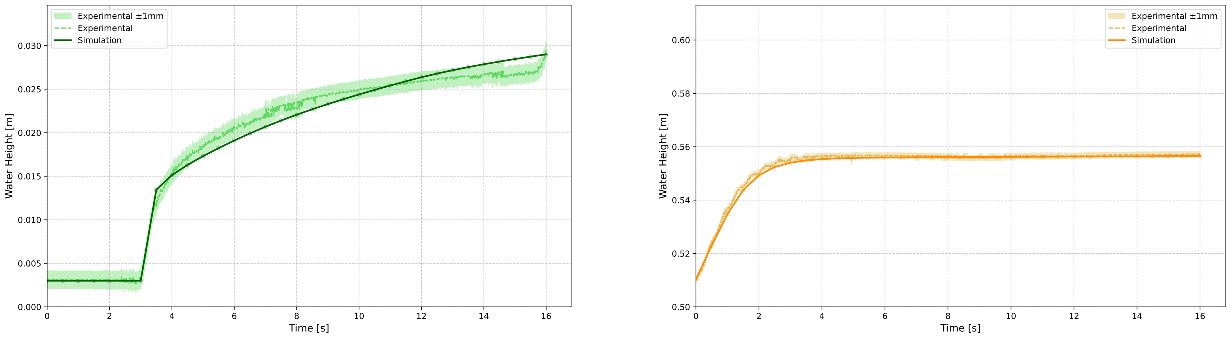

Figure F.8: Evolution of water height over time at sensors 5 (on the left) and 7 (on the right) with a time delay of 17.11 seconds, $h_{min} = 0.003$ m, $\Delta x_{tank} = 0.2$m, $K = 90 m^{1/3}/s$ and a mean flow rate of $2.5 * 10^{-3} m^3/s$

APPENDIX G

MATHEMATICAL DERIVATION OF THE VOLUME FOR A T-JUNCTION

I Geometric configuration of the T-junction

Figure G.1 shows a T-junction formed by the intersection of two circular pipes of equal radius R. One pipe extends along the x-axis, while the second pipe extends along the y-axis. To calculate the total volume of this junction, we need to account for both the straight pipe sections and their intersection.

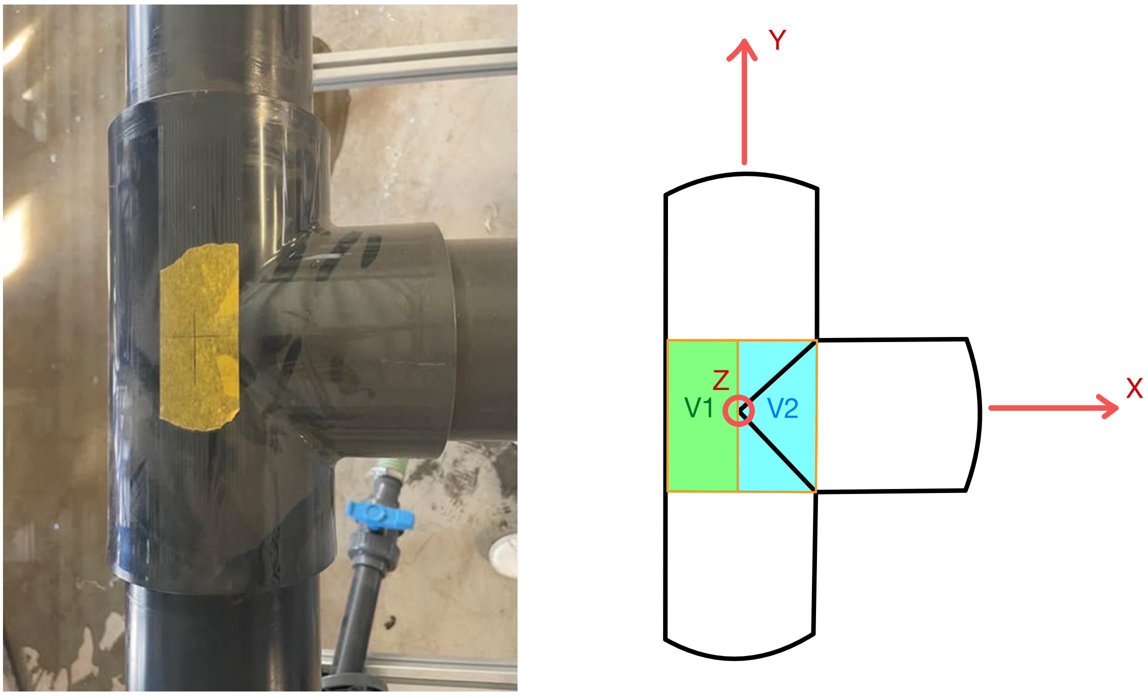

Figure G.1: Geometric representation of a T-junction showing the decomposition into volume V_1 (the non-overlapping pipe sections) and volume V_2 (the intersection region)

II Mathematical derivation

To calculate the total volume of the T-junction, we decompose it into two parts:

- V_1: The volume of the non-overlapping pipe sections.
- V_2: The volume of the intersection region where the pipes overlap.

The total volume is then $V = V_1 + V_2$.

II.1 Volume V_1: Non-overlapping pipe sections

For the non-overlapping sections, we have two pipe segments, each with a semicircular cross-section. The volume of this portion is:

$$V_1 = \frac{1}{2}\pi R^2 * 2R = \pi R^3 \tag{II.1}$$

II.2 Volume V_2: intersection region

For the intersection region, we need to calculate the volume where both pipes overlap. This requires a triple integral over the region of space where both conditions are satisfied:

$$\text{Pipe along } x\text{-axis:} \quad y^2 + z^2 \leq R^2 \tag{II.2}$$

$$\text{Pipe along } y\text{-axis:} \quad x^2 + z^2 \leq R^2 \tag{II.3}$$

We can express this volume using cylindrical coordinates in the z-direction as follows:

$$V_2 = \int_{-R}^{R} \int_{-\sqrt{R^2-z^2}}^{\sqrt{R^2-z^2}} \int_{-\sqrt{R^2-z^2}}^{\sqrt{R^2-z^2}} dx\, dy\, dz \tag{II.4}$$

Let's solve this integral step by step:

$$\begin{aligned}
V_2 &= \frac{1}{2} \int_{-R}^{R} \int_{-\sqrt{R^2-z^2}}^{\sqrt{R^2-z^2}} \int_{-\sqrt{R^2-z^2}}^{\sqrt{R^2-z^2}} dx\, dy\, dz && \text{(II.5)}\\
&= \frac{1}{2} \int_{-R}^{R} \int_{-\sqrt{R^2-z^2}}^{\sqrt{R^2-z^2}} [x]_{-\sqrt{R^2-z^2}}^{\sqrt{R^2-z^2}}\, dy\, dz && \text{(II.6)}\\
&= \frac{1}{2} \int_{-R}^{R} \int_{-\sqrt{R^2-z^2}}^{\sqrt{R^2-z^2}} 2\sqrt{R^2-z^2}\, dy\, dz && \text{(II.7)}\\
&= \frac{1}{2} \int_{-R}^{R} 2\sqrt{R^2-z^2}\, [y]_{-\sqrt{R^2-z^2}}^{\sqrt{R^2-z^2}}\, dz && \text{(II.8)}\\
&= \frac{1}{2} \int_{-R}^{R} 2\sqrt{R^2-z^2} \cdot 2\sqrt{R^2-z^2}\, dz && \text{(II.9)}\\
&= 2 \int_{-R}^{R} (R^2 - z^2)\, dz && \text{(II.10)}\\
&= 2 \left[R^2 z - \frac{z^3}{3} \right]_{-R}^{R} && \text{(II.11)}\\
& && \text{(II.12)}
\end{aligned}$$

$$= 2\left[(R^3 - \frac{R^3}{3}) - (-R^3 + \frac{R^3}{3})\right] \tag{II.13}$$

$$= 2\left[\frac{2R^3}{3} + \frac{2R^3}{3}\right] \tag{II.14}$$

$$= 2\frac{4R^3}{3} \tag{II.15}$$

$$= \frac{8R^3}{3} \tag{II.16}$$

II.3 Total volume of the T-junction

The total volume of the T-junction is therefore:

$$V = V_1 + V_2 \tag{II.17}$$

$$= \pi R^3 + \frac{8R^3}{3} \tag{II.18}$$

$$= R^3\left(\pi + \frac{8}{3}\right) \tag{II.19}$$

For a pipe with radius $R = 0.05$ m, the volume is:

$$V = (0.05)^3\left(\pi + \frac{16}{3}\right) \tag{II.20}$$

$$= 0.000726 \text{ m}^3 \tag{II.21}$$

$$= 726.032 \text{ cm}^3 \tag{II.22}$$

This calculation gives us the precise volume of the T-junction, accounting for both the straight pipe sections and their intersection region.

II.4 Geometric interpretation

The volume of the T-junction exceeds that of three straight pipe segments meeting at a point because the intersection region contributes additional volume. Understanding this additional volume is crucial for accurate hydraulic modeling, as it affects wave propagation and pressure dynamics throughout the pipe network.

The factor $\left(\pi + \frac{8}{3}\right)$ represents the normalized volume of the T-junction in terms of R^3, which is approximately 5.81 times the cube of the radius. This precise volume calculation is essential for accurate numerical simulations of flow dynamics in pipe networks with multiple junctions.

APPENDIX H

FINAL RESULTS FOR THE LAB MODEL

I Results for $Q_{mean} = 0.55$ L/s

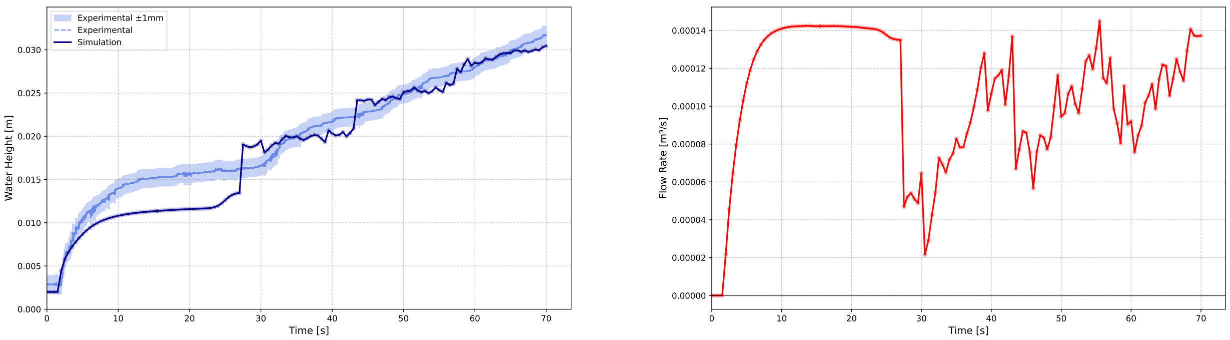

Figure H.1: Evolution of water height and flow rate over time at sensor 1 with a time delay of 66.22 seconds, $h_{min} = 0.002$ m, $\Delta x_{tank} = 0.2$m, $K = 90m^{1/3}/s$ and a mean flow rate of $0.55 \cdot 10^{-3} m^3/s$

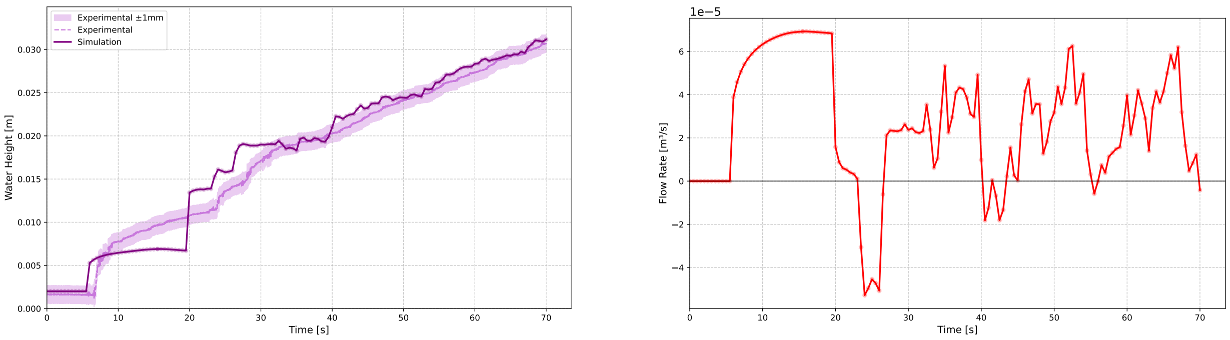

Figure H.2: Evolution of water height and flow rate over time at sensor 2 with a time delay of 66.22 seconds, $h_{min} = 0.002$ m, $\Delta x_{tank} = 0.2$m, $K = 90m^{1/3}/s$ and a mean flow rate of $0.55 \cdot 10^{-3} m^3/s$

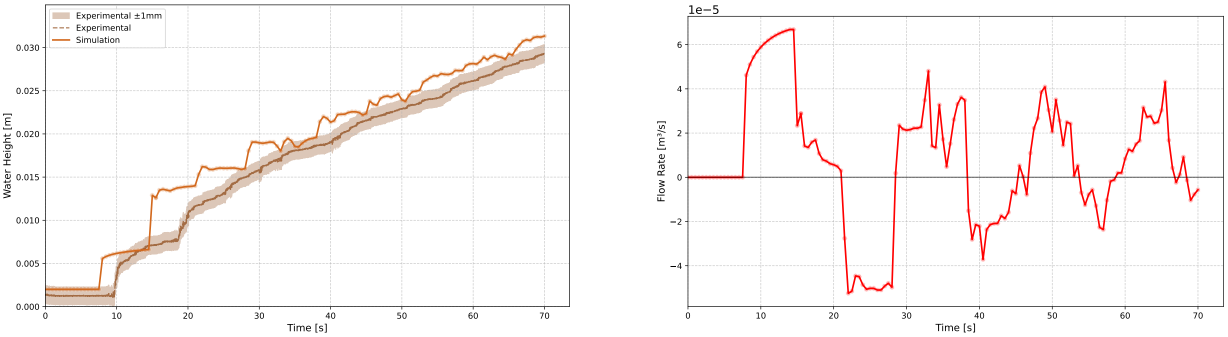

Figure H.3: Evolution of water height and flow rate over time at sensor 3 with a time delay of 66.22 seconds, $h_{min} = 0.002$ m, $\Delta x_{tank} = 0.2$m, $K = 90 m^{1/3}/s$ and a mean flow rate of $0.55 \cdot 10^{-3} m^3/s$

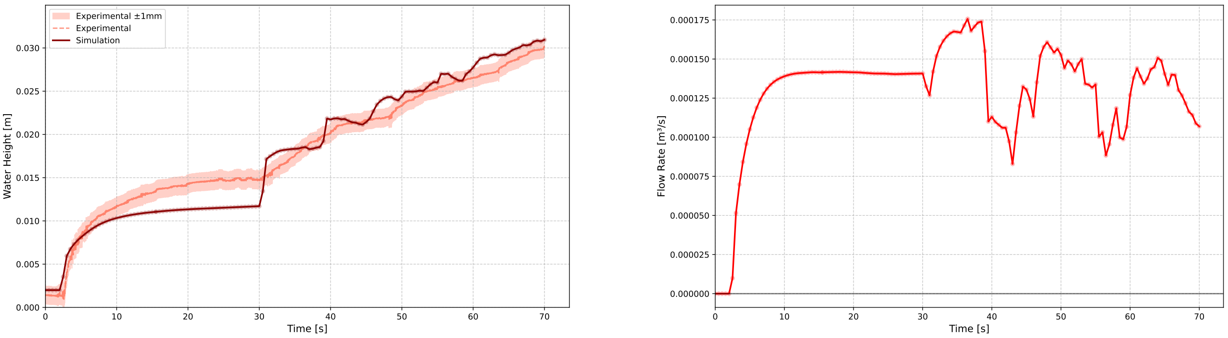

Figure H.4: Evolution of water height and flow rate over time at sensor 4 with a time delay of 66.22 seconds, $h_{min} = 0.002$ m, $\Delta x_{tank} = 0.2$m, $K = 90 m^{1/3}/s$ and a mean flow rate of $0.55 \cdot 10^{-3} m^3/s$

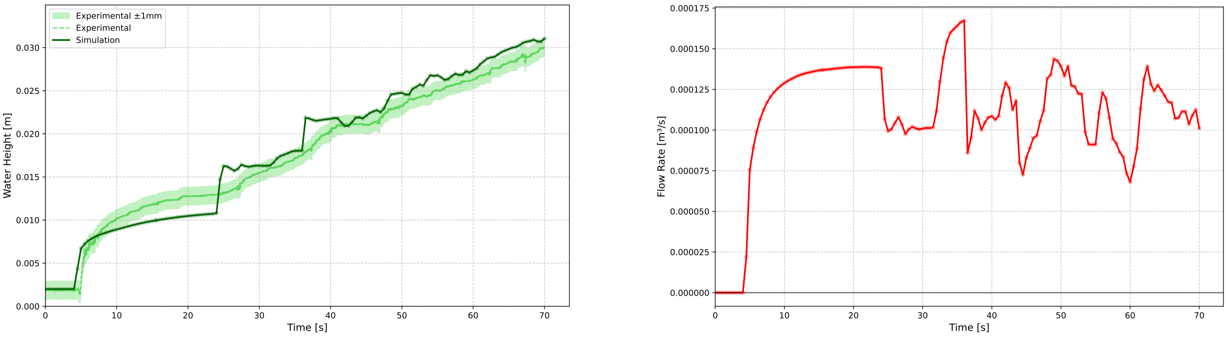

Figure H.5: Evolution of water height and flow rate over time at sensor 5 with a time delay of 66.22 seconds, $h_{min} = 0.002$ m, $\Delta x_{tank} = 0.2$m, $K = 90 m^{1/3}/s$ and a mean flow rate of $0.55 \cdot 10^{-3} m^3/s$

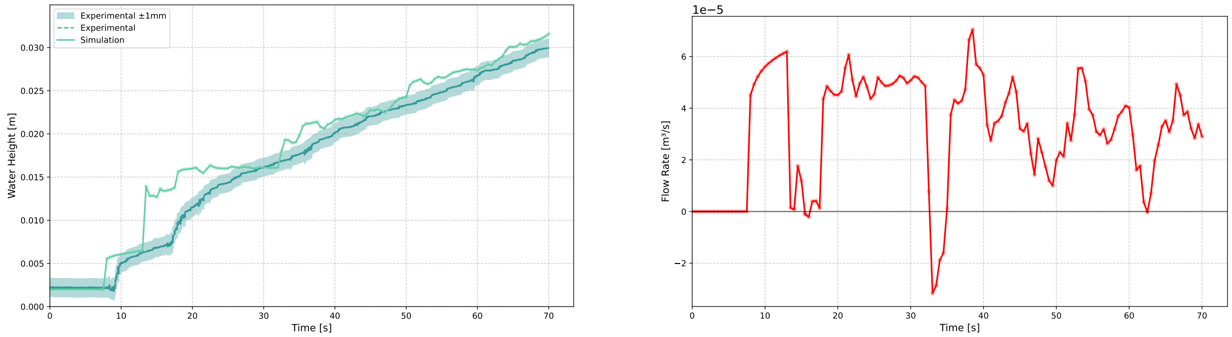

Figure H.6: Evolution of water height and flow rate over time at sensor 6 with a time delay of 66.22 seconds, $h_{min} = 0.002$ m, $\Delta x_{tank} = 0.2$m, $K = 90m^{1/3}/s$ and a mean flow rate of $0.55 \cdot 10^{-3}m^3/s$

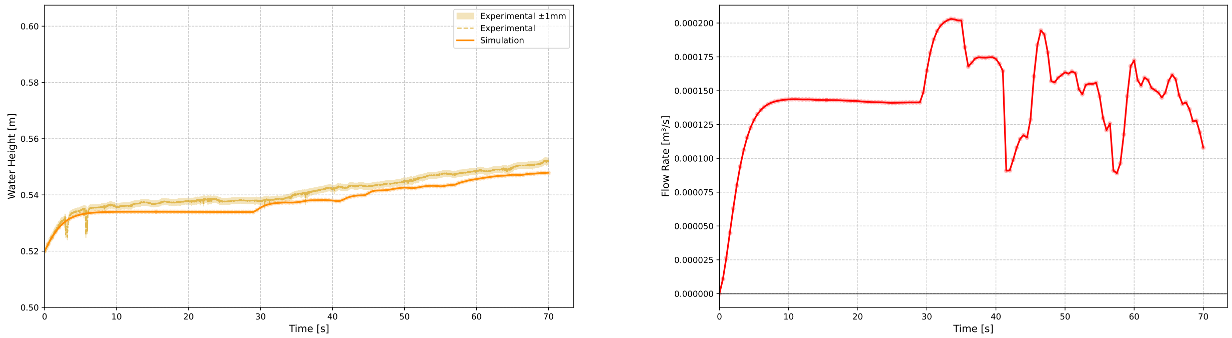

Figure H.7: Evolution of water height and flow rate over time at sensor 7 with a time delay of 66.22 seconds, $h_{min} = 0.002$ m, $\Delta x_{tank} = 0.2$m, $K = 90m^{1/3}/s$ and a mean flow rate of $0.55 \cdot 10^{-3}m^3/s$

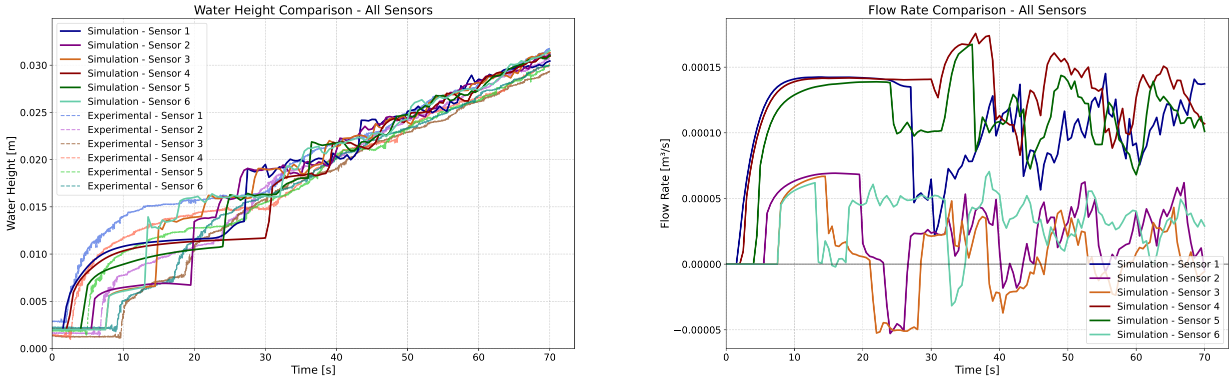

Figure H.8: Evolution of water height and flow rate over time at all sensors with a time delay of 66.22 seconds, $h_{min} = 0.002$ m, $\Delta x_{tank} = 0.2$m, $K = 90m^{1/3}/s$ and a mean flow rate of $0.55 \cdot 10^{-3}m^3/s$

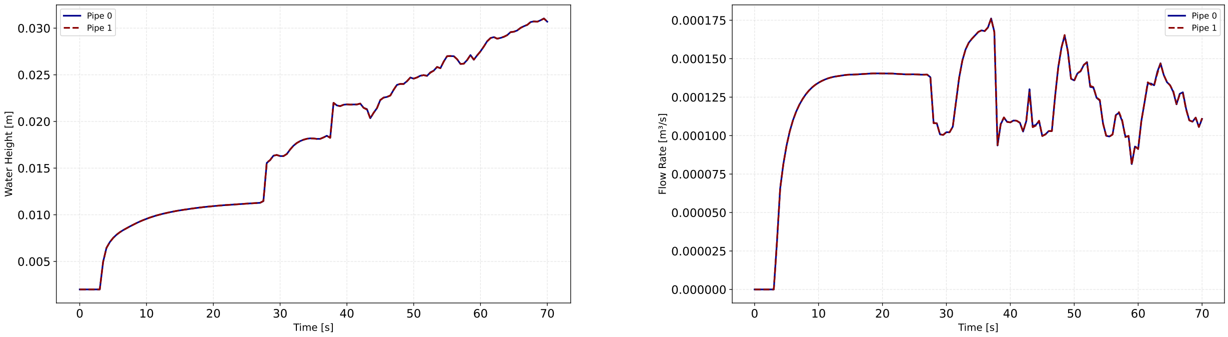

Figure H.9: Evolution of water height and flow rate over time in pipes 0 and 1 with a time delay of 66.22 seconds, $h_{min} = 0.002$ m, $\Delta x_{tank} = 0.2$m, $K = 90 m^{1/3}/s$ and a mean flow rate of $0.55 \cdot 10^{-3} m^3/s$

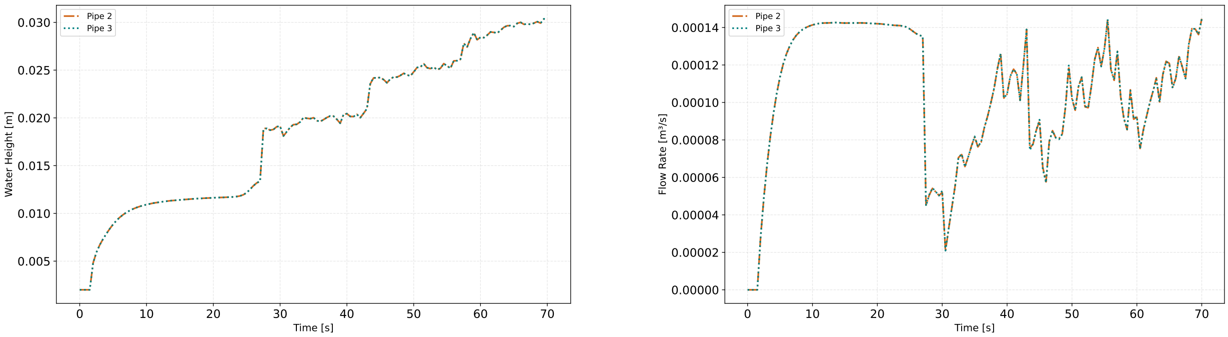

Figure H.10: Evolution of water height and flow rate over time in pipes 2 and 3 with a time delay of 66.22 seconds, $h_{min} = 0.002$ m, $\Delta x_{tank} = 0.2$m, $K = 90 m^{1/3}/s$ and a mean flow rate of $0.55 \cdot 10^{-3} m^3/s$

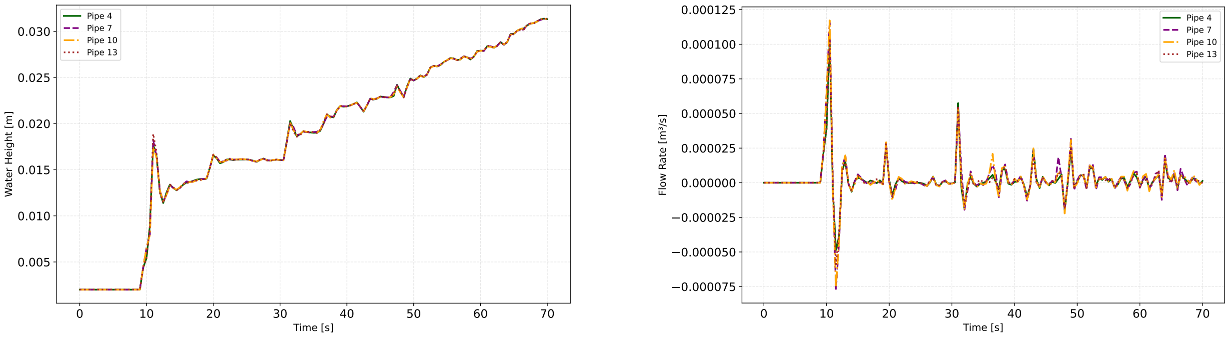

Figure H.11: Evolution of water height and flow rate over time in pipes 4, 7, 10 and 13 with a time delay of 66.22 seconds, $h_{min} = 0.002$ m, $\Delta x_{tank} = 0.2$m, $K = 90 m^{1/3}/s$ and a mean flow rate of $0.55 \cdot 10^{-3} m^3/s$

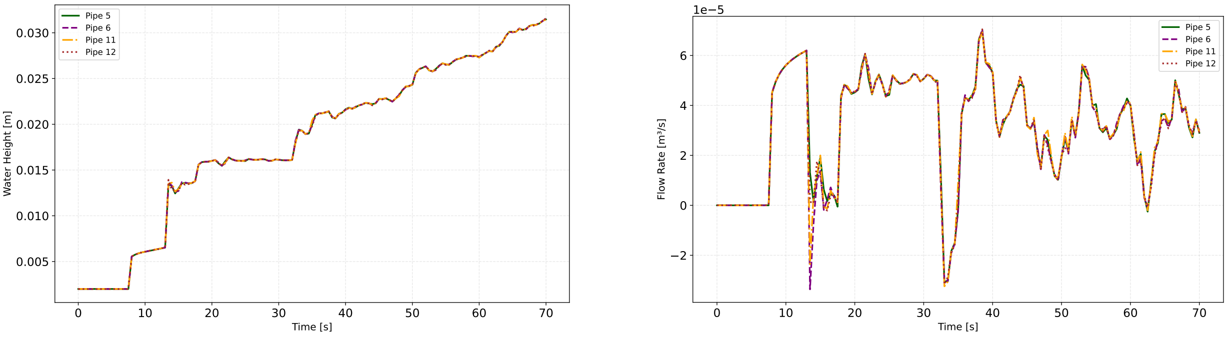

Figure H.12: Evolution of water height and flow rate over time in pipes 5, 6, 11 and 12 with a time delay of 66.22 seconds, $h_{min} = 0.002$ m, $\Delta x_{tank} = 0.2$m, $K = 90m^{1/3}/s$ and a mean flow rate of $0.55 \cdot 10^{-3} m^3/s$

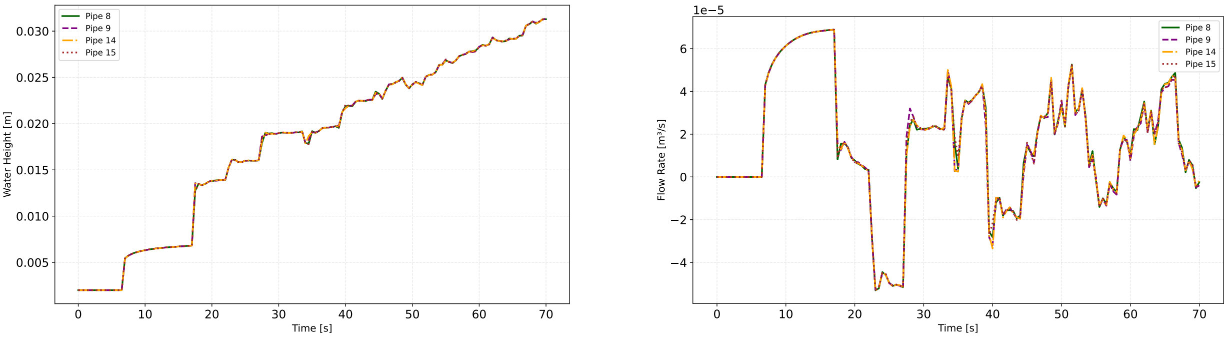

Figure H.13: Evolution of water height and flow rate over time in pipes 8, 9, 14 and 15 with a time delay of 66.22 seconds, $h_{min} = 0.002$ m, $\Delta x_{tank} = 0.2$m, $K = 90m^{1/3}/s$ and a mean flow rate of $0.55 \cdot 10^{-3} m^3/s$

II Results for $Q_{mean} = 1.35$ L/s

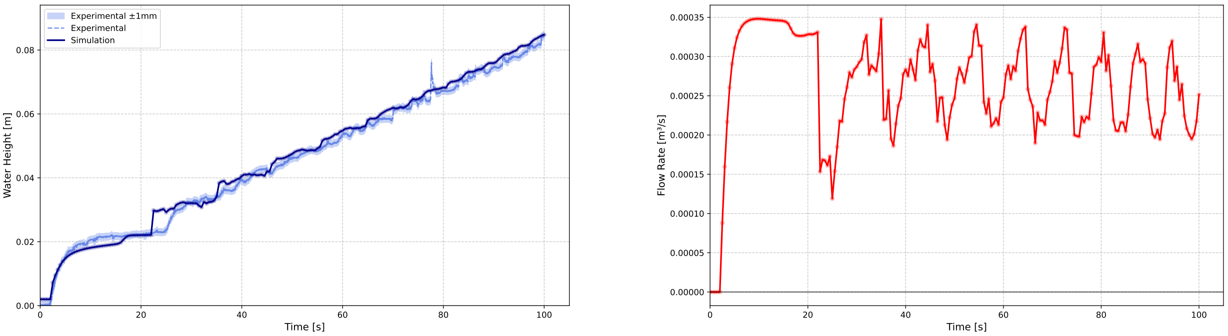

Figure H.14: Evolution of water height and flow rate over time at sensor 1 with a time delay of 27.83 seconds, $h_{min} = 0.001$ m, $\Delta x_{tank} = 0.2$m, $K = 90m^{1/3}/s$ and a mean flow rate of $1.35 \cdot 10^{-3} m^3/s$

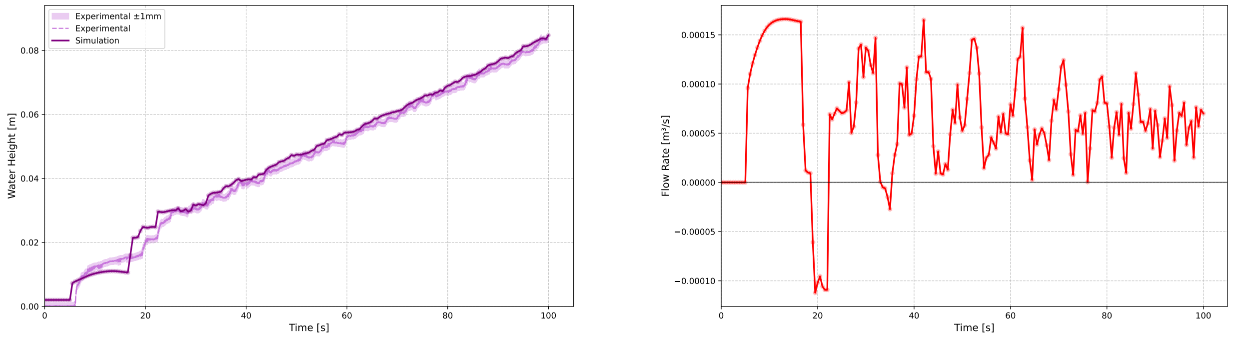

Figure H.15: Evolution of water height and flow rate over time at sensor 2 with a time delay of 27.83 seconds, $h_{min} = 0.001$ m, $\Delta x_{tank} = 0.2$m, $K = 90m^{1/3}/s$ and a mean flow rate of $1.35 \cdot 10^{-3} m^3/s$

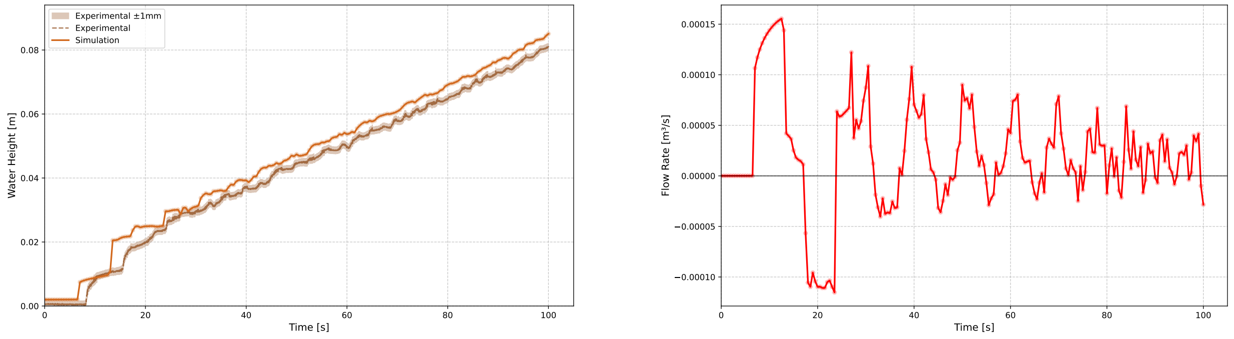

Figure H.16: Evolution of water height and flow rate over time at sensor 3 with a time delay of 27.83 seconds, $h_{min} = 0.001$ m, $\Delta x_{tank} = 0.2$m, $K = 90m^{1/3}/s$ and a mean flow rate of $1.35 \cdot 10^{-3} m^3/s$

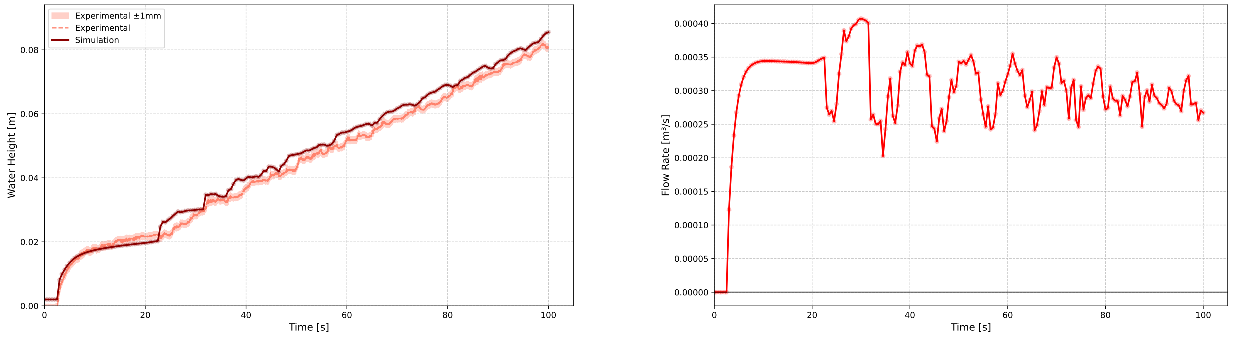

Figure H.17: Evolution of water height and flow rate over time at sensor 4 with a time delay of 27.83 seconds, $h_{min} = 0.001$ m, $\Delta x_{tank} = 0.2$m, $K = 90m^{1/3}/s$ and a mean flow rate of $1.35 \cdot 10^{-3} m^3/s$

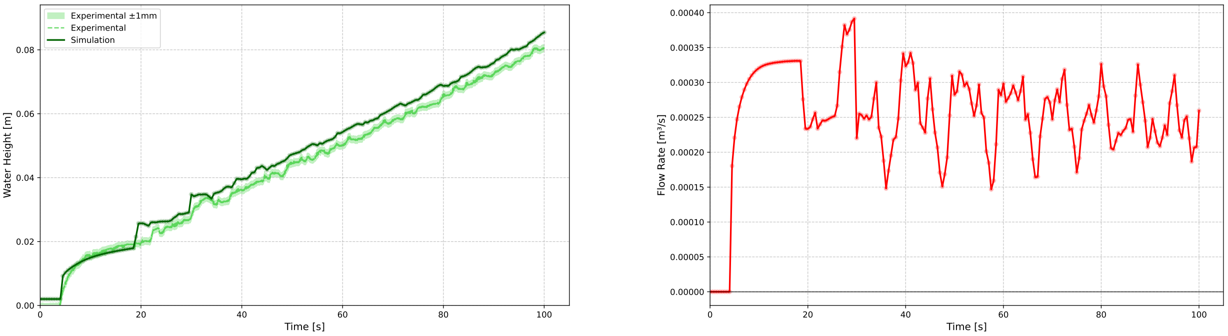

Figure H.18: Evolution of water height and flow rate over time at sensor 5 with a time delay of 27.83 seconds, $h_{min} = 0.001$ m, $\Delta x_{tank} = 0.2$m, $K = 90 m^{1/3}/s$ and a mean flow rate of $1.35 \cdot 10^{-3} m^3/s$

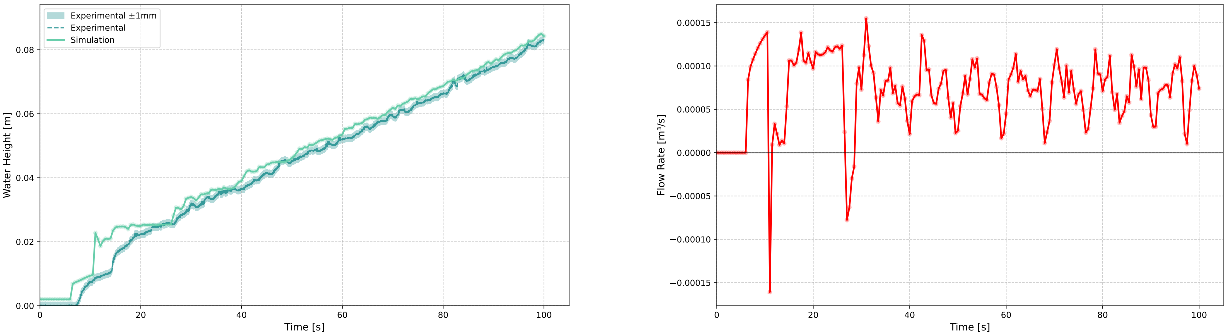

Figure H.19: Evolution of water height and flow rate over time at sensor 6 with a time delay of 27.83 seconds, $h_{min} = 0.001$ m, $\Delta x_{tank} = 0.2$m, $K = 90 m^{1/3}/s$ and a mean flow rate of $1.35 \cdot 10^{-3} m^3/s$

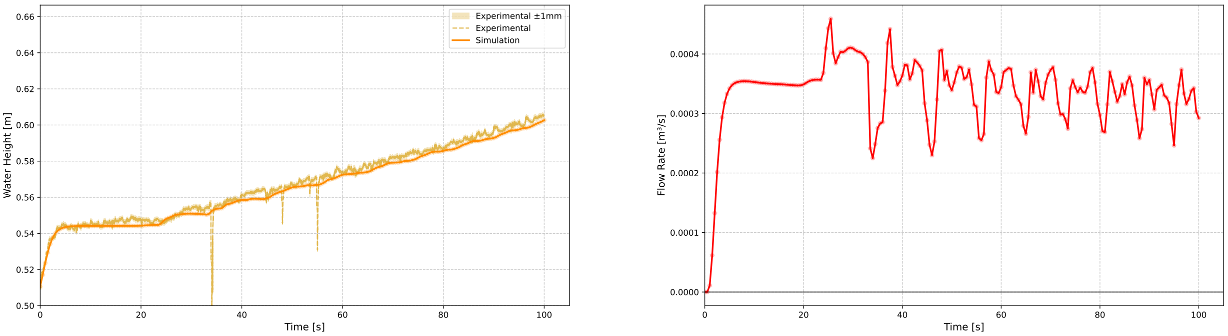

Figure H.20: Evolution of water height and flow rate over time at sensor 7 with a time delay of 27.83 seconds, $h_{min} = 0.001$ m, $\Delta x_{tank} = 0.2$m, $K = 90 m^{1/3}/s$ and a mean flow rate of $1.35 \cdot 10^{-3} m^3/s$

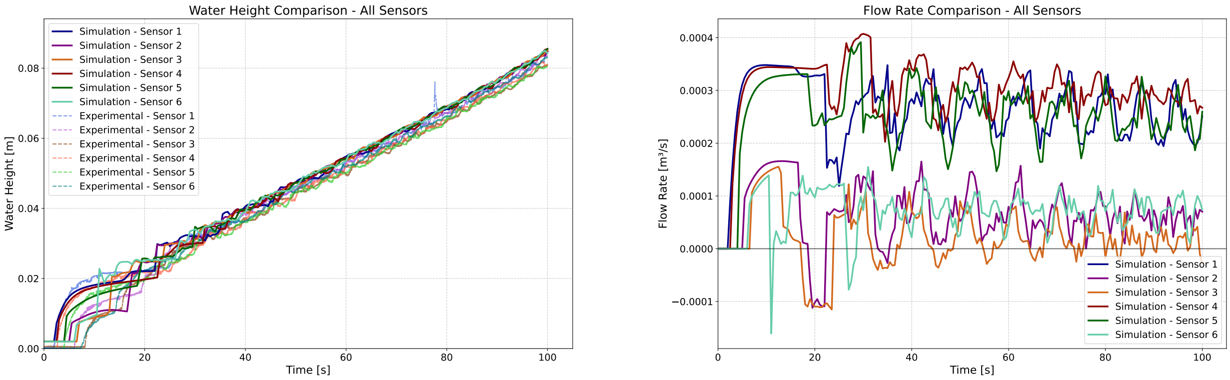

Figure H.21: Evolution of water height and flow rate over time at all sensors with a time delay of 27.83 seconds, $h_{min} = 0.001$ m, $\Delta x_{tank} = 0.2$m, $K = 90m^{1/3}/s$ and a mean flow rate of $1.35 \cdot 10^{-3}m^3/s$

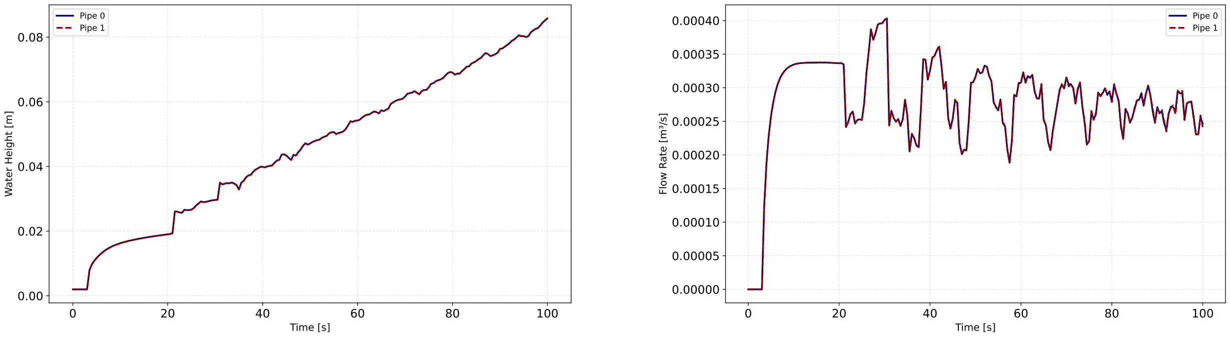

Figure H.22: Evolution of water height and flow rate over time in pipes 0 and 1 with a time delay of 27.83 seconds, $h_{min} = 0.001$ m, $\Delta x_{tank} = 0.2$m, $K = 90m^{1/3}/s$ and a mean flow rate of $1.35 \cdot 10^{-3}m^3/s$

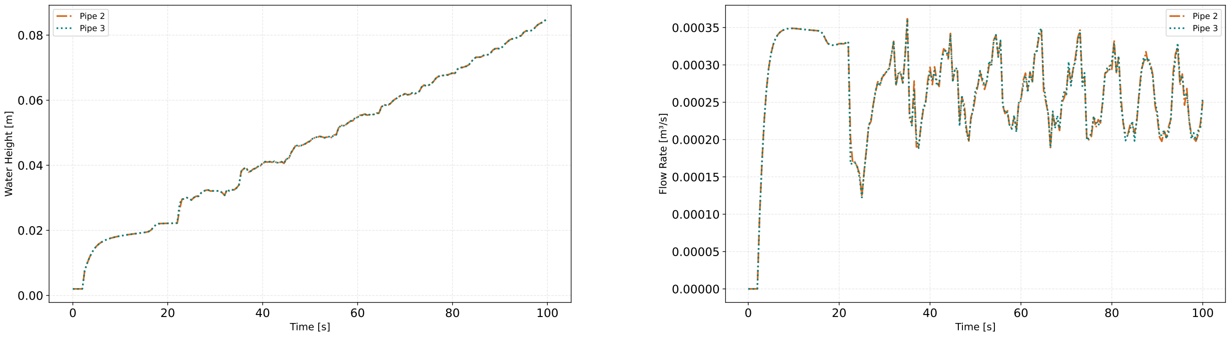

Figure H.23: Evolution of water height and flow rate over time in pipes 2 and 3 with a time delay of 27.83 seconds, $h_{min} = 0.001$ m, $\Delta x_{tank} = 0.2$m, $K = 90m^{1/3}/s$ and a mean flow rate of $1.35 \cdot 10^{-3}m^3/s$

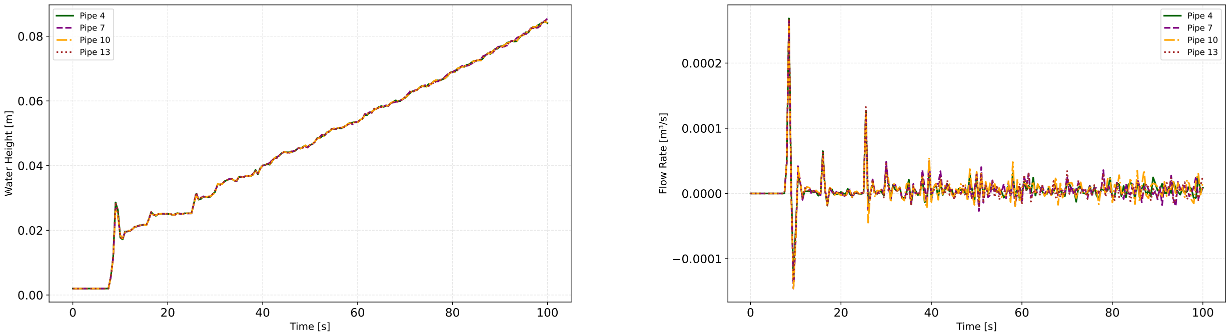

Figure H.24: Evolution of water height and flow rate over time in pipes 4, 7, 10 and 13 with a time delay of 27.83 seconds, $h_{min} = 0.001$ m, $\Delta x_{tank} = 0.2$m, $K = 90 m^{1/3}/s$ and a mean flow rate of $1.35 \cdot 10^{-3} m^3/s$

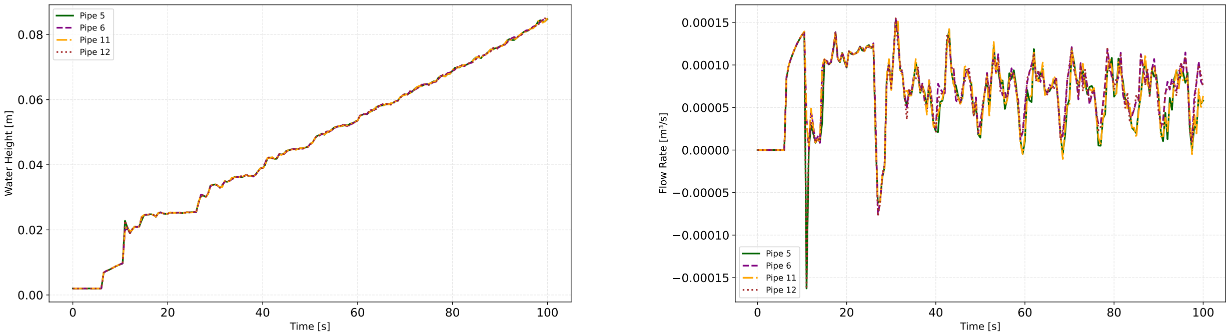

Figure H.25: Evolution of water height and flow rate over time in pipes 5, 6, 11 and 12 with a time delay of 27.83 seconds, $h_{min} = 0.001$ m, $\Delta x_{tank} = 0.2$m, $K = 90 m^{1/3}/s$ and a mean flow rate of $1.35 \cdot 10^{-3} m^3/s$

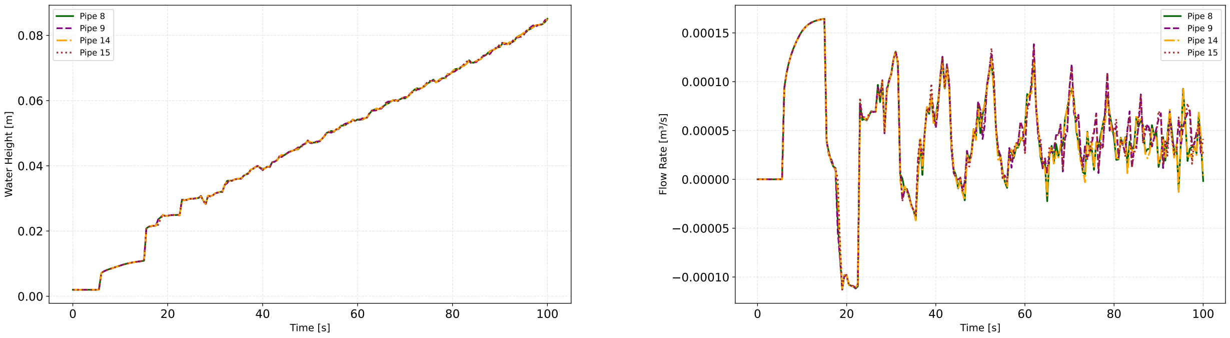

Figure H.26: Evolution of water height and flow rate over time in pipes 8, 9, 14 and 15 with a time delay of 27.83 seconds, $h_{min} = 0.001$ m, $\Delta x_{tank} = 0.2$m, $K = 90 m^{1/3}/s$ and a mean flow rate of $1.35 \cdot 10^{-3} m^3/s$

III Results for $Q_{mean} = 2.5$ L/s

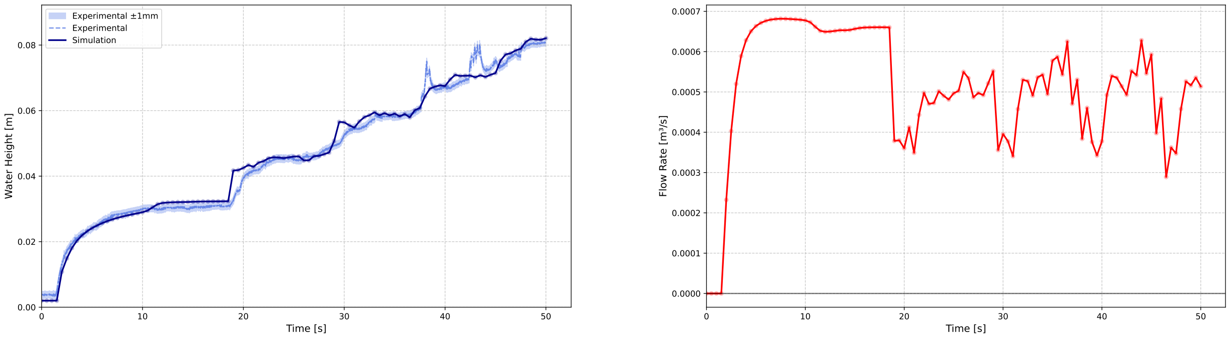

Figure H.27: Evolution of water height and flow rate over time at sensor 1 with a time delay of 17.11 seconds, $h_{min} = 0.003$ m, $\Delta x_{tank} = 0.2$m, $K = 90 m^{1/3}/s$ and a mean flow rate of $2.5 \cdot 10^{-3} m^3/s$

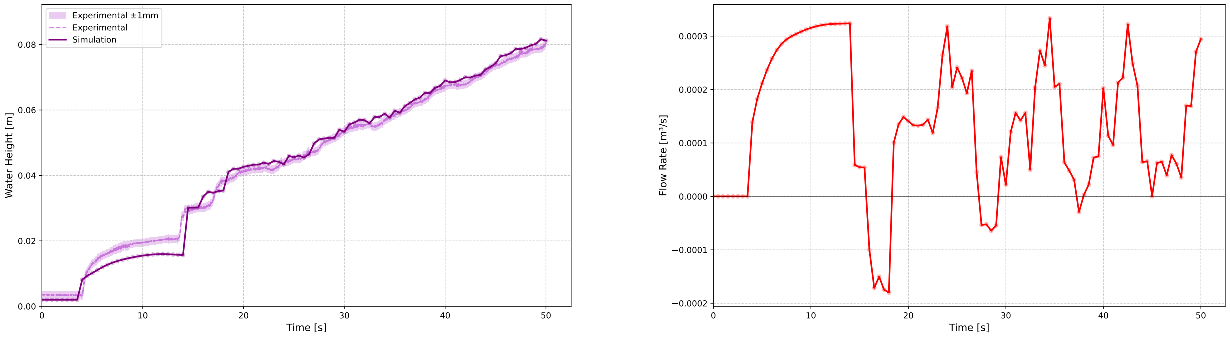

Figure H.28: Evolution of water height and flow rate over time at sensor 2 with a time delay of 17.11 seconds, $h_{min} = 0.003$ m, $\Delta x_{tank} = 0.2$m, $K = 90 m^{1/3}/s$ and a mean flow rate of $2.5 \cdot 10^{-3} m^3/s$

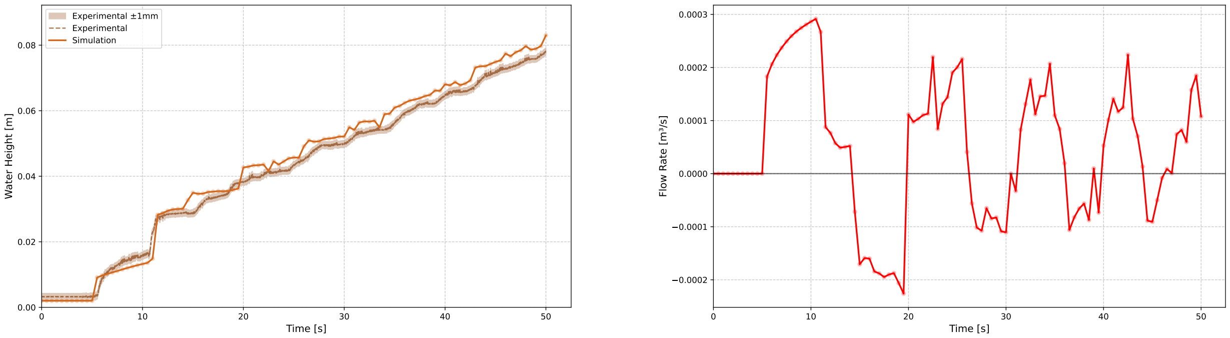

Figure H.29: Evolution of water height and flow rate over time at sensor 3 with a time delay of 17.11 seconds, $h_{min} = 0.003$ m, $\Delta x_{tank} = 0.2$m, $K = 90 m^{1/3}/s$ and a mean flow rate of $2.5 \cdot 10^{-3} m^3/s$

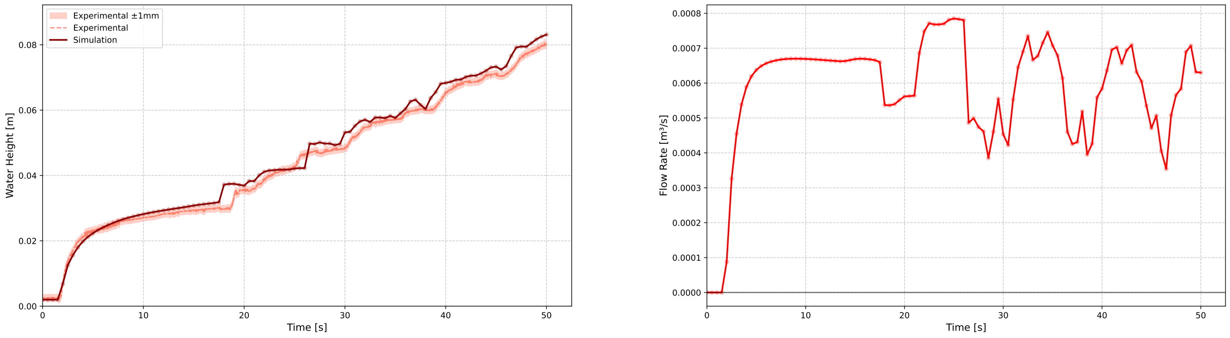

Figure H.30: Evolution of water height and flow rate over time at sensor 4 with a time delay of 17.11 seconds, $h_{min} = 0.003$ m, $\Delta x_{tank} = 0.2$m, $K = 90 m^{1/3}/s$ and a mean flow rate of $2.5 \cdot 10^{-3} m^3/s$

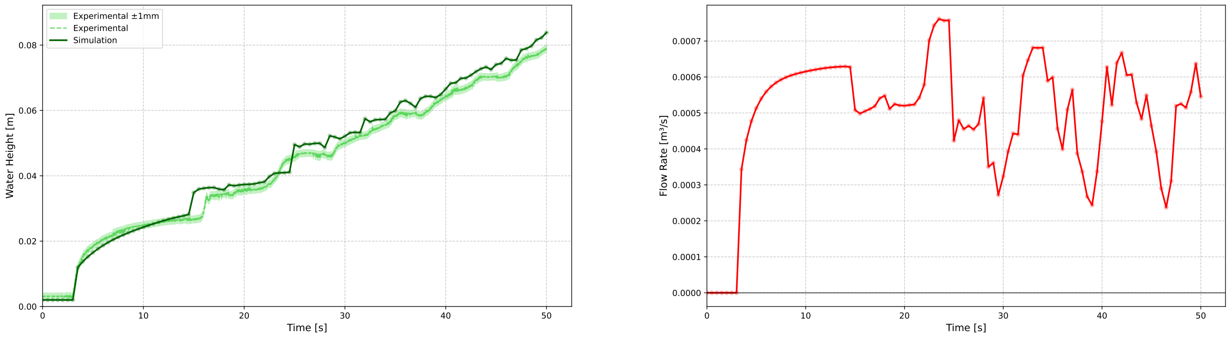

Figure H.31: Evolution of water height and flow rate over time at sensor 5 with a time delay of 17.11 seconds, $h_{min} = 0.003$ m, $\Delta x_{tank} = 0.2$m, $K = 90 m^{1/3}/s$ and a mean flow rate of $2.5 \cdot 10^{-3} m^3/s$

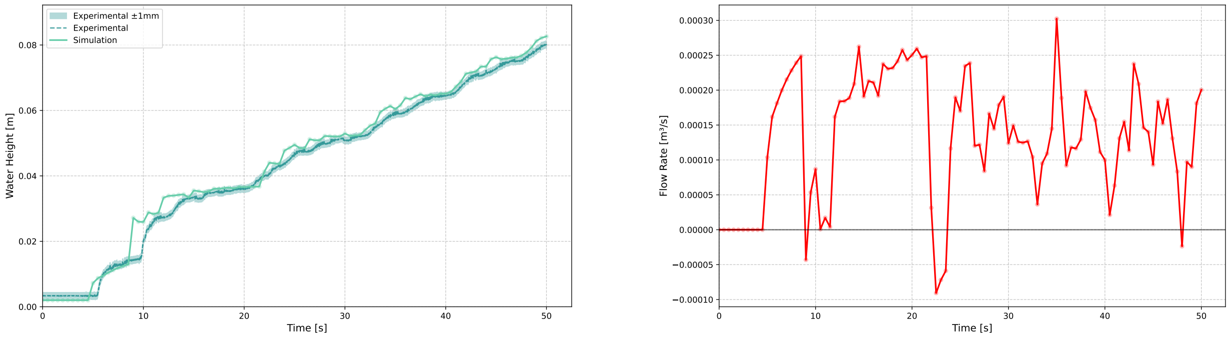

Figure H.32: Evolution of water height and flow rate over time at sensor 6 with a time delay of 17.11 seconds, $h_{min} = 0.003$ m, $\Delta x_{tank} = 0.2$m, $K = 90 m^{1/3}/s$ and a mean flow rate of $2.5 \cdot 10^{-3} m^3/s$

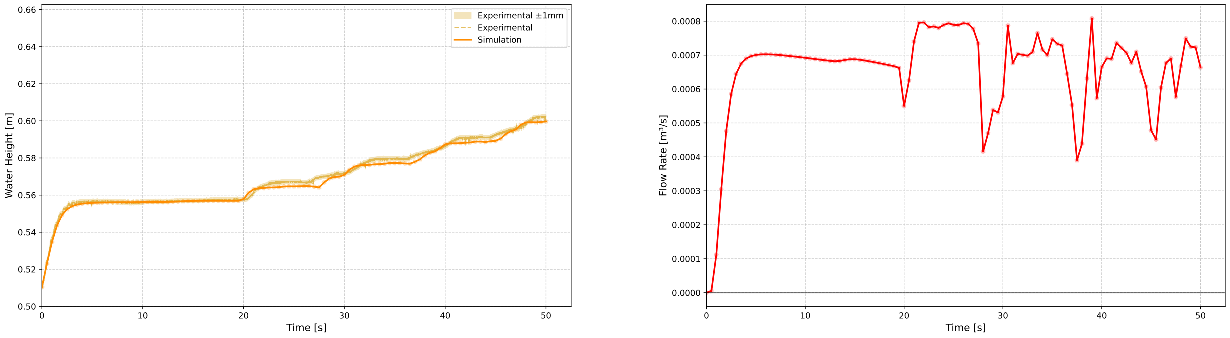

Figure H.33: Evolution of water height and flow rate over time at sensor 7 with a time delay of 17.11 seconds, $h_{min} = 0.003$ m, $\Delta x_{tank} = 0.2$m, $K = 90 m^{1/3}/s$ and a mean flow rate of $2.5 \cdot 10^{-3} m^3/s$

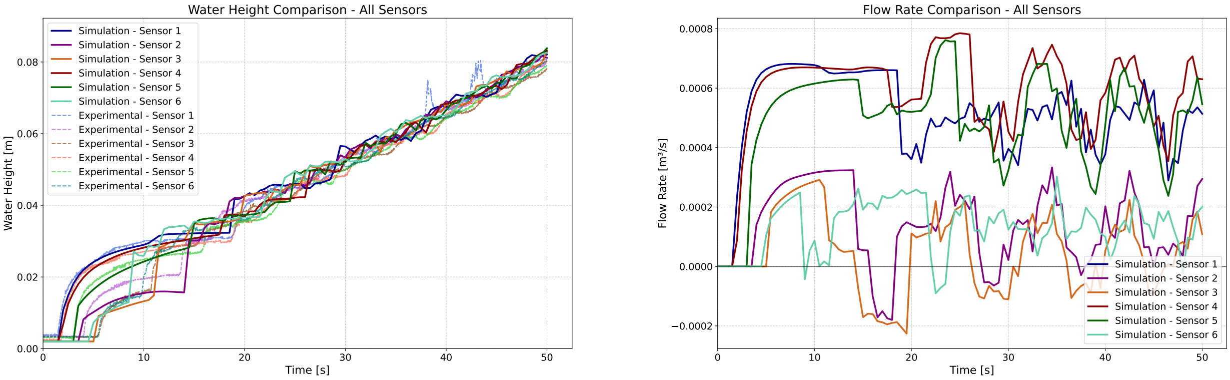

Figure H.34: Evolution of water height and flow rate over time at all sensors with a time delay of 17.11 seconds, $h_{min} = 0.003$ m, $\Delta x_{tank} = 0.2$m, $K = 90 m^{1/3}/s$ and a mean flow rate of $2.5 \cdot 10^{-3} m^3/s$

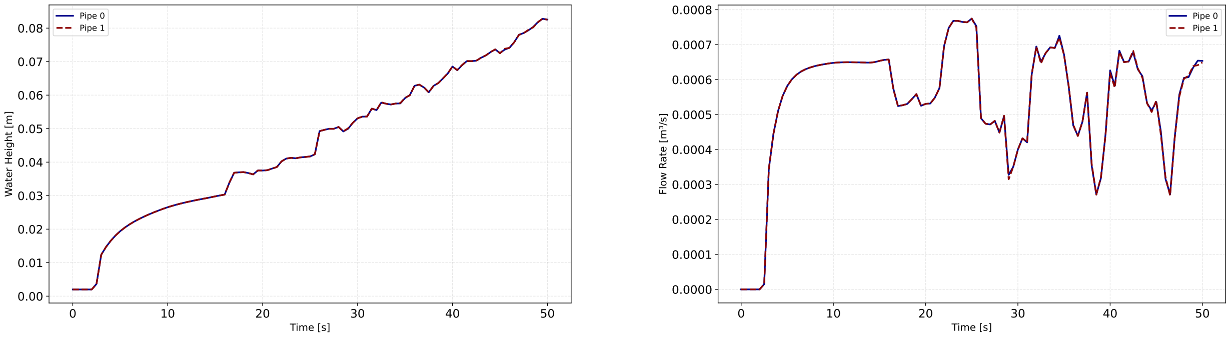

Figure H.35: Evolution of water height and flow rate over time in pipes 0 and 1 with a time delay of 17.11 seconds, $h_{min} = 0.003$ m, $\Delta x_{tank} = 0.2$m, $K = 90 m^{1/3}/s$ and a mean flow rate of $2.5 \cdot 10^{-3} m^3/s$

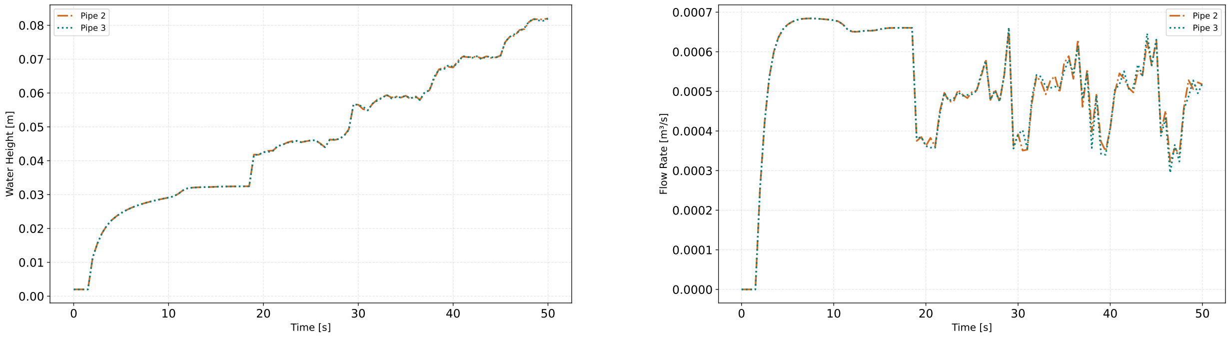

Figure H.36: Evolution of water height and flow rate over time in pipes 2 and 3 with a time delay of 17.11 seconds, $h_{min} = 0.003$ m, $\Delta x_{tank} = 0.2$m, $K = 90 m^{1/3}/s$ and a mean flow rate of $2.5 \cdot 10^{-3} m^3/s$

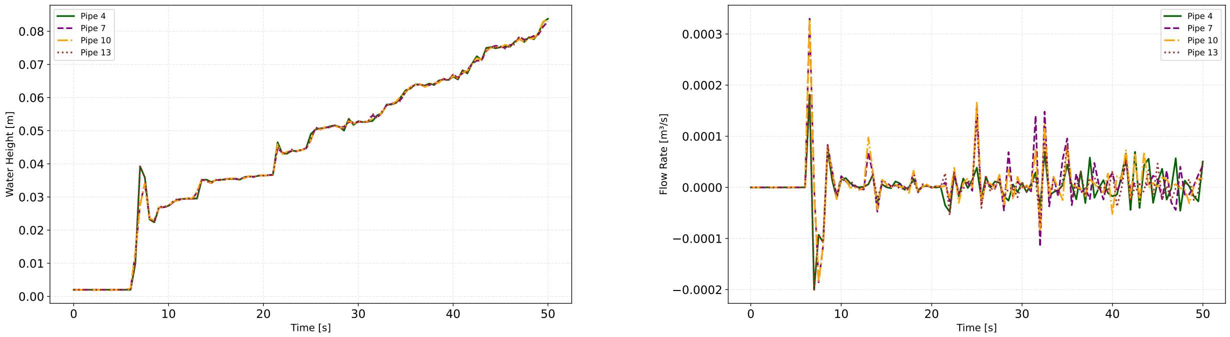

Figure H.37: Evolution of water height and flow rate over time in pipes 4, 7, 10 and 13 with a time delay of 17.11 seconds, $h_{min} = 0.003$ m, $\Delta x_{tank} = 0.2$m, $K = 90 m^{1/3}/s$ and a mean flow rate of $2.5 \cdot 10^{-3} m^3/s$

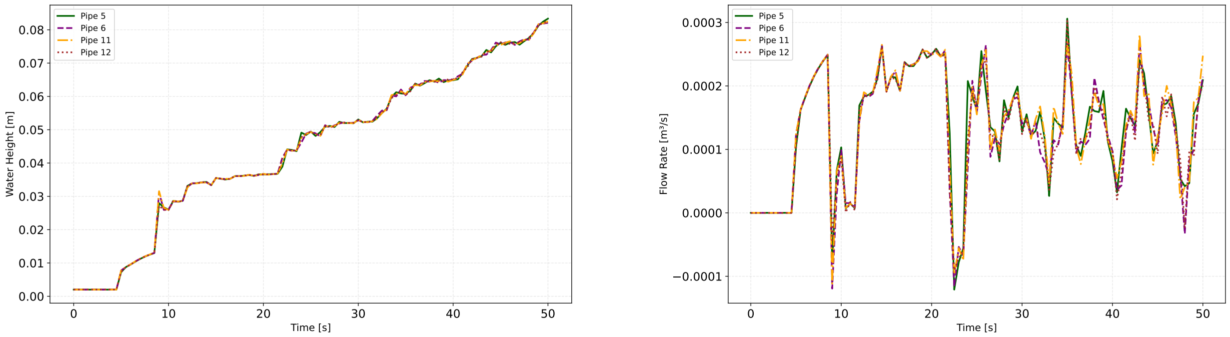

Figure H.38: Evolution of water height and flow rate over time in pipes 5, 6, 11 and 12 with a time delay of 17.11 seconds, $h_{min} = 0.003$ m, $\Delta x_{tank} = 0.2$m, $K = 90 m^{1/3}/s$ and a mean flow rate of $2.5 \cdot 10^{-3} m^3/s$

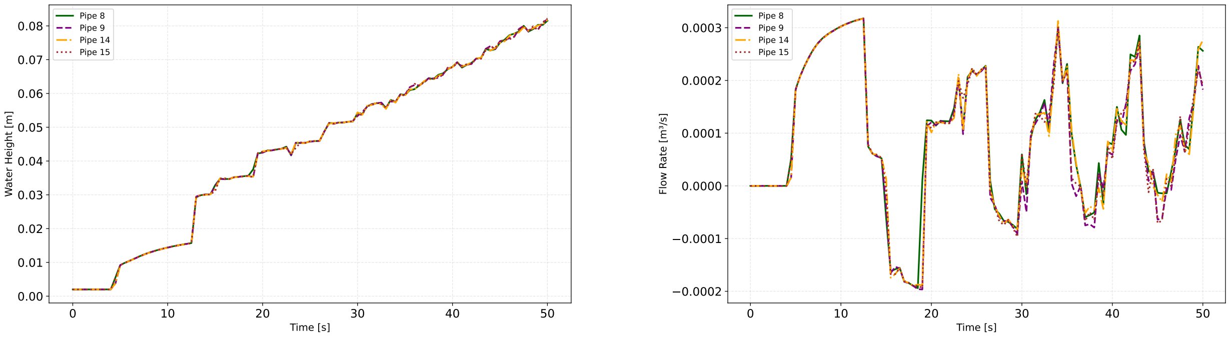

Figure H.39: Evolution of water height and flow rate over time in pipes 8, 9, 14 and 15 with a time delay of 17.11 seconds, $h_{min} = 0.003$ m, $\Delta x_{tank} = 0.2$m, $K = 90 m^{1/3}/s$ and a mean flow rate of $2.5 \cdot 10^{-3} m^3/s$

APPENDIX I

EFFECT OF PIPE SPACING ON FLOW DYNAMICS

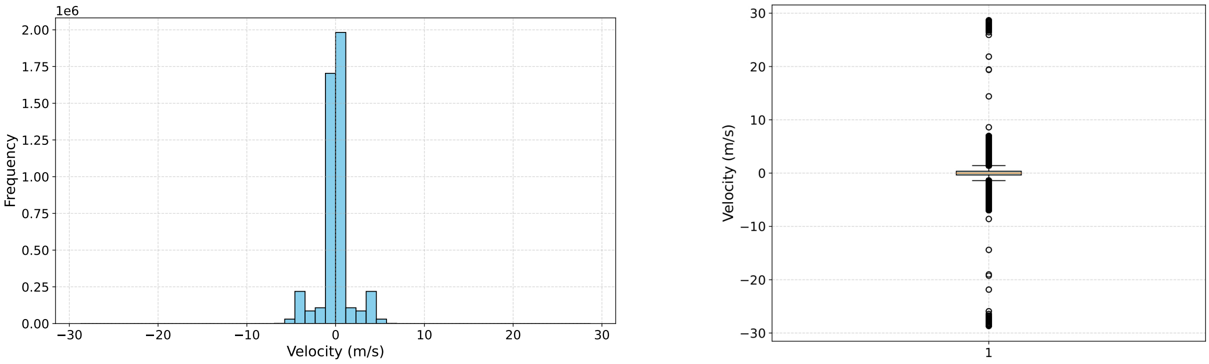

Figure I.1: Velocity distribution (histogram and boxplot) for modified model 1

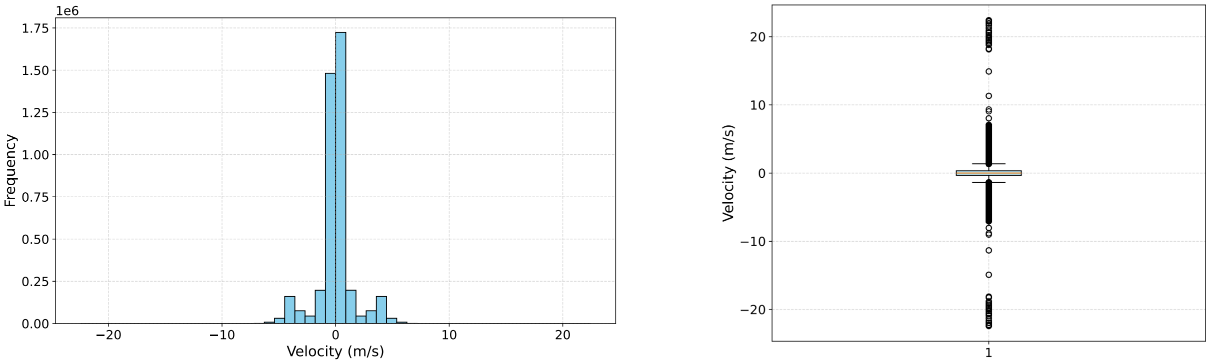

Figure I.2: Velocity distribution (histogram and boxplot) for modified model 2

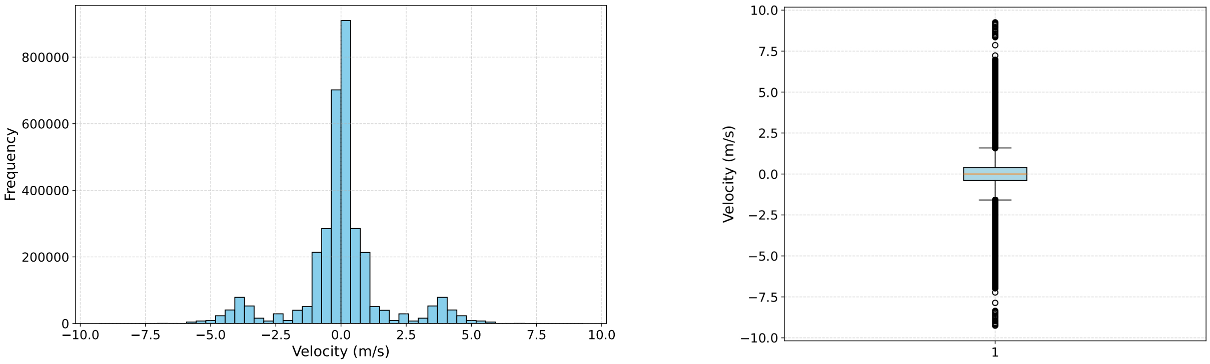

Figure I.3: Velocity distribution (histogram and boxplot) for modified model 3

I Flow reversal analysis

To quantify flow direction changes, the number of velocity sign reversals was computed for each pipe. At every time step, the velocity values along the pipe segments were examined. A flow reversal was detected whenever the product of two consecutive velocity values was negative (i.e., v[i] * v[i+1] < 0), indicating a change in sign and therefore a change in flow direction. This simple and robust method allows for consistent tracking of bidirectional flow behavior across all network configurations.

The frequency of flow reversals (zero-crossings) provides crucial insights into the dynamic behavior of different pipe groups across varying network configurations. Table I.1 presents the number of flow direction changes for each pipe across all spacing configurations.

Pipe	Network Configuration (Width x Length)			
	70x400 m	100x400 m	150x400 m	200x400 m
Primary pipes				
0, 1	14	14	14	14
2	53	5	6	6
3	79	5	6	6
Terminal dead-end pipes				
4	3387	5134	5368	4287
7	3294	5129	5279	3685
10	3183	4827	4927	3838
13	3074	4998	4973	4072
Short interconnecting pipes				
5	158	364	475	822
6	139	439	502	817
11	185	336	466	804
12	111	448	496	853
Long interconnecting pipes				
8	5808	7901	5467	3714
9	6397	7178	5323	3587
14	5311	7771	5553	3649
15	5998	7077	5537	5734

Table I.1: Number of flow reversals across different network spacings

REFERENCES

Alvarado Montero, Rodolfo, Andre Niemann, and Dirk Schwanenberg (2013). "Concepts for Pumped-Storage Hydro-Electricity Using Underground Coal Mines". in: Proceedings of the IAHR World Congress. URL: `https://www.iahr.org/library/infor?pid=15090`.

Ceresetti, Sara (2023). "Hydraulic modelling of a network of mining galleries used as a lower reservoir of a pumping-turbining scheme". MA thesis. Université de Liège. URL: `https://matheo.uliege.be/bitstream/2268.2/17718/6/TFE_Sara_Ceresetti.pdf`.

Dewals, Benjamin (2023). Fundamentals of Sediment Transport, Morphodynamics & Sediment Management. Hydrodynamic and Sediment Transport Course. Lecture notes, Master 1 in Civil Engineering (Constructions), University of Liège.

Erpicum, Sébastien (2003). "Modélisation des écoulements à surface libre dans les bassins de dessablage : couplage entre l'hydraulique à surface libre et le transport des sédiments". PhD thesis. Université de Liège. URL: `https://orbi.uliege.be/bitstream/2268/24835/1/Th%C3%A8se%20Erpicum%20S.pdf`.

Kitsikoudis, Vasileios, Pierre Archambeau, Benjamin Dewals, et al. (2020). "Underground Pumped-Storage Hydropower (UPSH) at the Martelange Mine (Belgium): Underground Reservoir Hydraulics". in: Energies 13.14, p. 3512. DOI: `10.3390/en13143512`. URL: `https://orbi.uliege.be/handle/2268/249526`.

Menendez, Javier et al. (2019). "Pumped-storage hydropower plants with underground reservoir: Influence of air pressure on the efficiency of the Francis turbine and energy production". in: Renewable Energy 143, pp. 1427–1438. DOI: `10.1016/j.renene.2019.05.099`. URL: `https://www.researchgate.net/publication/333367504_Pumped-storage_hydropower_plants_with_underground_reservoir_Influence_of_air_pressure_on_the_efficiency_of_the_Francis_turbine_and_energy_production`.

Morabito, Alessandro et al. (2020). "Underground Pumped Storage Hydropower Case Studies in Belgium: Perspectives and Challenges". in: Energies 13.15, p. 4000. DOI: `10.3390/en13154000`. URL: `https://www.researchgate.net/publication/343399998_Underground_Pumped_Storage_Hydropower_Case_Studies_in_Belgium_Perspectives_and_Challenges`.

Pirotton, Michel (2022). Free Surface Flow Course. Lecture Notes. Given at the University of Liège, Faculty of Applied Sciences, in 2022-2023. Liège, Belgium.

Pujades, Estanis, Philippe Orban, Pierre Archambeau, et al. (2018). “Numerical study of the Martelange mine to be used as lower reservoir for constructing an Underground Pumped Storage Hydropower plant”. in: Advances in Geosciences 45, pp. 51–56. DOI: `10.5194/adgeo-45-51-2018`. URL: `https://orbi.uliege.be/handle/2268/226770`.

Pujades, Estanislao et al. (2016). “Underground pumped storage hydroelectricity using abandoned works (deep mines or open pits) and the impact on groundwater flow”. in: Hydrogeology Journal 24.6, pp. 1291–1306. DOI: `10.1007/s10040-016-1413-z`. URL: `https://www.researchgate.net/publication/301716670_Underground_pumped_storage_hydroelectricity_using_abandoned_works_deep_mines_or_open_pits_and_the_impact_on_groundwater_flow`.

Pummer, Elena and Holger Schüttrumpf (2018). “Reflection Phenomena in Underground Pumped Storage Reservoirs”. in: ResearchGate, p. 14. DOI: `10.3390/w10040504`. URL: `https://www.researchgate.net/publication/324603667_Reflection_Phenomena_in_Underground_Pumped_Storage_Reservoirs`.